DOE-ER-0313/57
Distribution
Categories
UC-423, -424

FUSION MATERIALS
SEMIANNUAL PROGRESS REPORT
FOR THE PERIOD ENDING

December 31, 2014

Prepared for
DOE Office of Fusion Energy Sciences
(AT 60 20 10 0)

DATE PUBLISHED: March 2015

Prepared by
OAK RIDGE NATIONAL LABORATORY
Oak Ridge, Tennessee 37831
Managed by
UT-Battelle, LLC
For the
U.S. DEPARTMENT OF ENERGY

FOREWORD

This is the fifty-seventh in a series of semiannual technical progress reports on fusion materials science activity supported by the Fusion Energy Sciences Program of the U.S. Department of Energy. It covers the period ending December 31, 2014. This report focuses on research addressing the effects on materials properties and performance of exposure to the neutronic, thermal and chemical environments anticipated in the chambers of fusion experiments and energy systems. This research is a major element of the national effort to establish the materials knowledge base for an economically and environmentally attractive fusion energy source. Research activities on issues related to the interaction of materials with plasmas are reported separately.

The results reported are the products of a national effort involving a number of national laboratories and universities. A large fraction of this work, particularly in relation to fission reactor irradiations, is carried out collaboratively with partners in Japan, Russia, and the European Union. The purpose of this series of reports is to provide a working technical record for the use of program participants, and to provide a means of communicating the efforts of fusion materials scientists to the broader fusion community, both nationally and worldwide.

This report has been compiled under the guidance of F. W. (Bill) Wiffen and Susan Noe, Oak Ridge National Laboratory. Their efforts, and the efforts of the many persons who made technical contributions, are gratefully acknowledged.

Peter J. Pappano
Research Division
Office of Fusion Energy Sciences

TABLE OF CONTENTS

TABLE OF CONTENTS

TABLE OF CONTENTS

TABLE OF CONTENTS

TABLE OF CONTENTS

TABLE OF CONTENTS

TABLE OF CONTENTS

TABLE OF CONTENTS

TABLE OF CONTENTS

TABLE OF CONTENTS

TABLE OF CONTENTS

TABLE OF CONTENTS

TABLE OF CONTENTS

1.1 DEVELOPMENT OF ADVANCED REDUCED ACTIVATION FERRITIC/MARTENSITIC STEELS - L. Tan, X. Chen (Oak Ridge National Laboratory)

OBJECTIVE

Traditional reduced activation ferritic/martensitic (RAFM) steels suffer noticeable strength reduction at temperatures above ~500°C, which limits their high temperature applications. This project is to develop manufacturable and affordable advanced RAFM steel having an optimized alloy composition and thermomechanical treatment (TMT) to produce high density of stable nanoprecipitates for superior high temperature performance.

SUMMARY

The effect of different TMTs on microstructures has been characterized by electron backscattered diffraction (EBSD). The increased interweaving of the microstructures with refined local misorientation zones may be responsible for the improved ductility and Charpy impact resistance. A new RAFM steel has been designed to favor the formation of a high density of MC (M = metal) carbides. The preliminary result of optical images exhibited the presence of a large amount of precipitates in the matrix. Mechanical testing and detailed microstructural characterization of the new alloy will be conducted. Microstructural characterization of the high-dose Fe^{2+} ion irradiated TaC, TaN, and VN specimens has shown different evolutions of the particles as compared to evolution under low-dose irradiation.

PROGRESS AND STATUS

Introduction

Alloy TT1 in the normalized and tempered (N&T) condition has shown excellent yield and tensile strength but mediocre ductility at temperatures up to 800°C. To improve ductility, four types of TMT conditions, involving the application of warm-rolling (WR) and tempering, have been explored using Grade 92 that has a basic tempered martensitic microstructure similar to the TT1 alloy. The major composition difference from Grade 92 is the elimination of Mo, Nb and N and the alloying of Ta and Ti in alloy TT1 to reduce long-term alloy activation and manage the amount of MC precipitates. The best TMT condition, determined by tensile performance and Charpy impact resistance, has been selected and applied to the alloy. This report describes the effect of TMTs on microstructures and preliminary results of the alloy. Additionally, high-dose Fe^{2+} ion irradiated samples bearing TaC, TaN and VN nano-precipitates, respectively, have been characterized using TEM, which are to be briefly reported here.

Experimental Procedure

Computational thermodynamics was employed to optimize alloy composition of RAFM steels with an increased amount of MC-type precipitates. A new alloy, TT3M, has been fabricated using vacuum arc melting and drop casting, yielding a small experimental heat (~1 lb.). Part of the cast alloy was subjected to hot rolling followed by standard normalization (N) and tempering (T) heat treatment. One route of TMTs involved WR after normalization, followed by tempering, has been applied to alloy TT1.

Tensile testing was conducted using miniature specimens (type SS-3: 25.4 x 4.95 x 0.76 mm), machined along the rolling direction of the plate, at a nominal strain rate of 0.001 s^{-1}. Half-size Charpy specimens were extracted from the alloy plates in two orientations along the longitudinal (rolling) and transverse directions. The microstructures of the samples were characterized using optical microscopy, scanning electron microscopy (SEM), EBSD, and transmission electron microscopy (TEM). A FEI CM200 field-emission-gun TEM/STEM equipped with an EDAX energy dispersive X-ray spectroscopy (EDS) detector was primarily used to characterize the Fe^{2+}-irradiated samples. TEM specimens, perpendicular to the surfaces, were lifted out and thinned to electron-transparent using focused ion beam (FIB) on a Hitachi NB5000. Specimen thickness of the characterized regions was estimated using convergent beam electron diffraction (CBED) technique.

Results

The EBSD inverse pole figure (IPF) of the F2 TMT condition, namely N+WR+2T, of Grade 92 is shown in Figure 1, together with the IPF of the N&T condition for comparison. The orientation of the grain components is illustrated according to the color code in Figure 1. Regular prior-austenite grain structures and tempered martensite packets and blocks, which are clearly shown in the N&T condition, are significantly deformed by the TMT, leading to increased interweaving of the microstructures with refined local misorientations. The observed improvements in ductility and Charpy impact resistance of the samples in the TMT condition may be attributable to these changes. The F2 TMT has been applied to alloy TT1 and yielded slightly reduced yield and tensile strength but noticeably improved ductility as compared to the N&T condition of alloy TT1. However, the preliminary creep test at 650°C and 110 MPa exhibited a short creep life of 11.7 h with necking rupture close to the shoulder of type SS-3 specimen. The short creep life of the TMT sample may have resulted from misalignment and/or the specific features induced by the TMT. New creep tests will be conducted to eliminate the cause of misalignment.

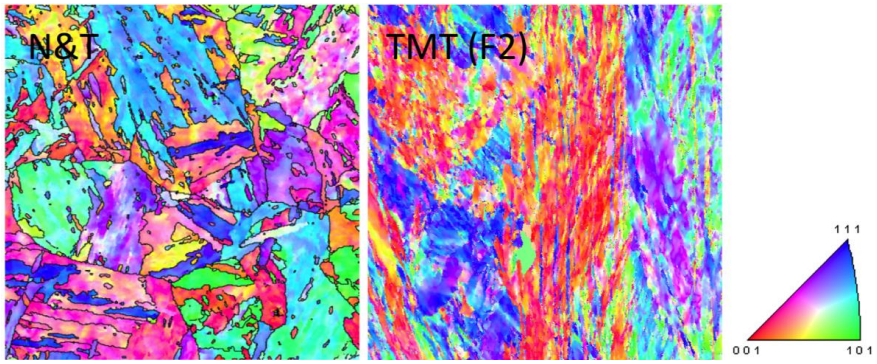

Figure 1. EBSD IPF maps (100×100 μm^2) of Grade 92 samples in the N&T and TMT conditions.

Based on the preliminary studies on the developed alloys TT1 and TT2, a new RAFM steel, TT3M, has been developed and fabricated. The major composition difference from alloy TT1 is the slightly increased amount of Mn and reduced V in alloy TT3M to optimize austenite temperature regime for improved efficiency of heat treatment. The optical micrograph of TT3M as compared to P92 is shown in Figure 2. The new alloy exhibits a large amount of precipitates in matrix, which is different from the observed precipitates in P92, primarily pinning lath/packet/block/prior-austenite boundaries. Further microstructural characterization will be conducted using SEM and TEM.

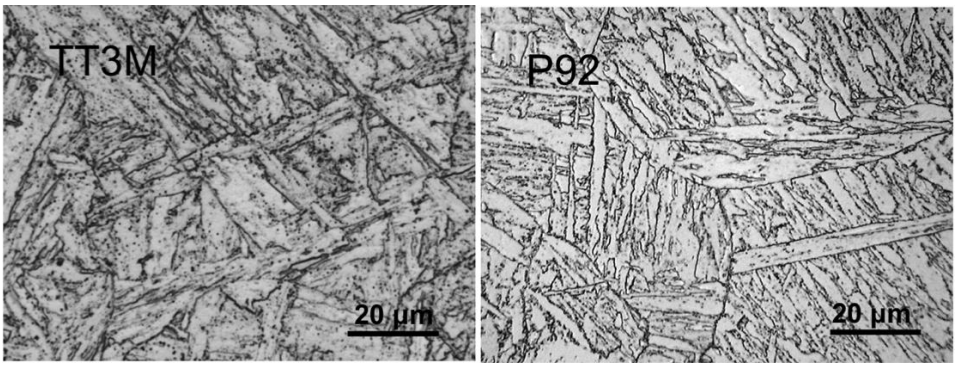

Figure 2. Optical micrographs comparison between alloy TT3M and P92.

The stability of TaN nanoprecipitates in a ferritic steel under Fe^{2+} ion irradiation to ~246 dpa at 500°C was characterized using TEM in dark-field (DF) mode. Figure 3 shows the DF image of TaN nanoprecipitates overlaid with the simulated irradiation dose depth profile using SRIM-2013 [3] using the parameters suggested in Ref. [4]. As compared to the low-dose irradiated sample that was reported earlier [1,2], the high-dose irradiation resulted in reduction in size and reduction in number density of TaN particles,

suggesting the dissolution of TaN particles. Unlike previously observed cavities in the TaC specimens subjected to the same high-dose irradiation, cavities were not observed in the TaN specimens. Characterization of the VN specimens has also completed. Statistical analysis of the collected images will be conducted.

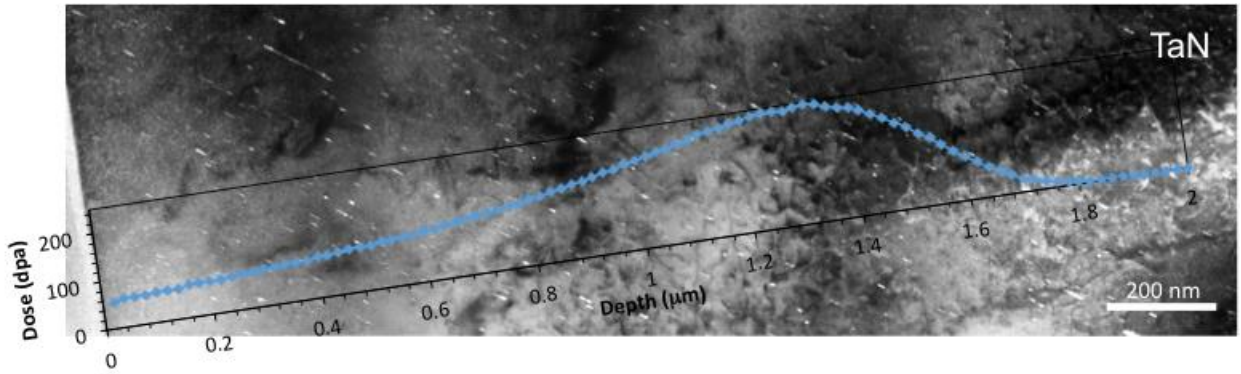

Figure 3. DF image showing the evolution of TaN nanoprecipitates as a function of the depth of Fe^{2+} ion irradiation at 500°C from surface on left, together with the overlaid SRIM simulation of irradiation dose depth profile.

References

[1] L. Tan, Y. Katoh, L.L. Snead, Stability of the strengthening nanoprecipitates in reduced activation ferritic steels under Fe^{2+} ion irradiation, Journal of Nuclear Materials 445 (2014) 104-110.
[2] L. Tan, T.S. Byun, Y. Katoh, L.L. Snead, Stability of MX-type strengthening nanoprecipitates in ferritic steels under thermal aging, stress and ion irradiation, Acta Materialia 71 (2014) 11-19.
[3] The Stopping and Range of Ions in Matter (SRIM) (http://www.srim.org).
[4] R.E. Stoller, M.B. Toloczko, G.S. Was, A.G. Certain, S. Dwaraknath, F.A. Garner, On the use of SRIM for computing radiation damage exposure, Nuclear Instruments and Methods in Physics Research B 310 (2013) 75-80.

1.2 IRRADIATION HARDENING BEHAVIOR OF F82H AND NICKEL-DOPED F82H - M. Ando, H. Tanigawa, E. Wakai (Japan Atomic Energy Agency), J. P. Robertson and Y. Katoh (Oak Ridge National Laboratory)

OBJECTIVE

It is important to predict the helium effects on mechanical properties of reduced activation ferritic/martensitic (RAFM) steels in fusion blanket structural materials. For example, isotope ^{58}Nickel can generate helium atoms by the ^{58}Ni(n, γ)^{59}Ni(n, α)^{56}Fe reaction. However, it is also reported that heavy irradiation hardening occurs in Nickel-doped ferritic/martensitic steels. The objective of this JAEA-USDOE collaborative study is to compare the irradiation hardening behavior of F82H with that of Nickel-doped F82H after ion irradiation or neutron irradiation experiments.

SUMMARY

For ion irradiation, the irradiation hardening behavior of Nickel-doped F82H steels is similar to that of F82H for 633 K irradiation. However, heavy hardening resulted in Nickel-doped F82H steels irradiated at 543 K. This heavy hardening was especially remarkable after only low dose irradiation. For neutron irradiation, heavy irradiation hardening occurred in the 1.4% Nickel-doped F82H up to 20 dpa; however irradiation hardening of 1.4% Nickel-doped F82H after 80 dpa irradiation is the same level for that of F82H. These results show that the helium effect of mechanical properties in F82H can be examined using F82H and Nickel-doped F82H after high-dose irradiation.

PROGRESS AND STATUS

Introduction

Reduced activation ferritic/martensitic steels (RAFM) are the most promising candidates for blanket structural materials of fusion reactors. Some transmutation products (mainly helium atoms) are produced by high-energy neutrons in the first wall of a fusion reactor. Thus it is important to understand the effects of helium production on material properties. However, helium atoms are rarely produced in F82H by neutron irradiation in a fission reactor. Therefore, to investigate the effects of helium on material properties for RAFM, some results of isotope tailoring experiments using the reaction of ^{10}B(n, α)^{7}Li or ^{58}Ni(n, γ)^{59}Ni(n, α)^{56}Fe in RAFM doped with ^{10}B or ^{58}Ni have been reported [1-4]. It is well known that heavy irradiation hardening occurs in Nickel-doped F82H at low dose at ~573K in spite of a low helium production rate. For this reason, it is difficult to separate the effects of nickel-doping from helium generation after high-dose irradiation.

The objectives of this study are to examine the irradiation hardening behavior of F82H and Nickel-doped F82H using ion irradiation experiments and high-dose neutron irradiation.

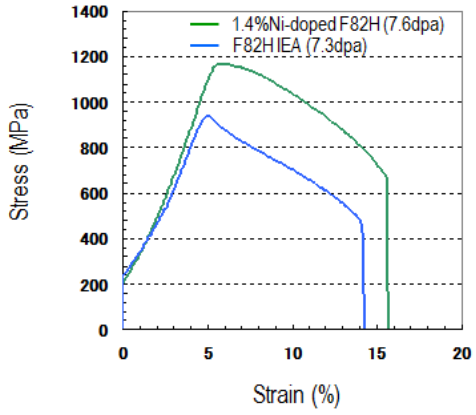

Figure1. Tensile result of F82H IEA and 1.4%Ni-doped F82H neutron irradiated at ~573 K, then tested at room temperature.

Experimental

The materials used in this study were RAFM steel (F82H IEA; Fe-8Cr-2W-0.2V-0.04Ta-0.1C [5]), and 0.5, 1.0 and 1.4%Nickel-doped F82H [6]. Each material was cut into small coupon type specimens (dimensions are 6×3×0.8 mm^3, Figure 2). One of the 6x0.8 mm^2 sides was irradiated after polishing with SiC paper #4000, 0.3 μm alumina powder, and finally to an electrolytic surface polishing. These specimens were irradiated at 543 or 633 K in the TIARA facility (JAEA Takasaki in Japan) by 10.5 MeV Fe^{3+} ions. Figure 3 shows a depth profile of displacement damage in F82H. The irradiation was performed up to ~43 dpa at the depth of ~0.6 μm from surface and the damage rate was about 10^{-3} dpa/s at this depth. Micro-indentation tests were performed at about 30points for each specimen and test condition with a load to penetrate up to 0.4 μm using an UMIS-2000 (CSIRO). The shape of the indenter tip was a Berkovich tip.

Neutron irradiation was performed in the High Flux Isotope Reactor (HFIR) to atomic displacement levels up to 80 dpa in JP28/29 capsules [7]. In this experiment, F82H IEA and two types of 1.4%Nickel-doped F82H were prepared. One was 1.4%^{58}Nickel-doped F82H which produced helium atoms during irradiation. The other was 1.4%^{60}Nickel-doped F82H which did not produce helium atoms. The hardness of some specimens irradiated at ~573 or ~673 K was measured by a Vickers hardness tester (Mitsutoyo AAV-500) at cell 2 in Building 3025E [8].

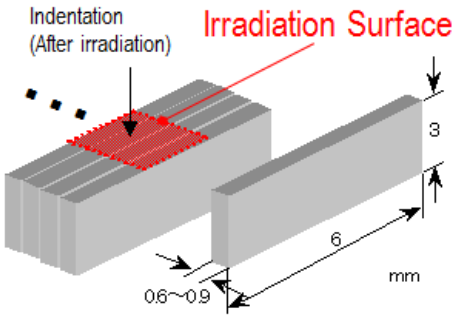

Figure 2. Illustration of coupon type specimens for ion irradiation

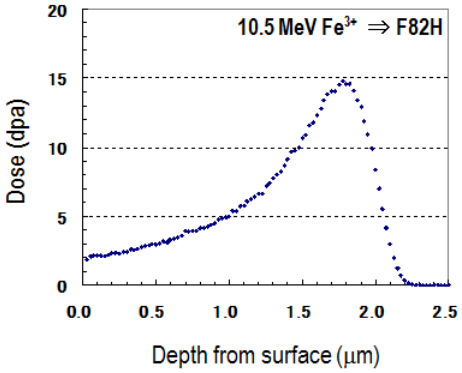

Figure 3. The depth profile of displacement damage in F82H at TIARA Facility

Results and Discussion

Figure 4a) and b) show the relationship between irradiation hardening ($100x\Delta H_m/H_m$) and irradiation dose of F82H and Nickel-doped F82H steels after ion irradiation. As the irradiation dose increases, the irradiation hardening increases for F82H irradiated at 543 and 633 K. The irradiation hardening behavior of each of the Nickel-doped F82H steels is similar to that of F82H for 633 K irradiation. However, a heavy hardening resulted in the Nickel-doped F82H steels irradiated at 543 K. This heavy hardening is especially remarkable for low dose irradiation. These results show the irradiation hardening results from a similar mechanism in F82H and Nickel-doped F82H steels irradiated at 633 K; however another hardening mechanism is possibly included in the Nickel-doped F82H steels irradiated at 543 K.

After high-dose ion irradiation, the irradiation hardening in F82H and Nickel-doped F82H was close to the same level. Therefore, it seems suitable to determine helium effects on mechanical properties of these F82H steels at higher neutron doses. Finally, 1.4% Nickel-doped F82H was selected for the neutron irradiation experiment because the irradiation hardening behavior was almost the same in 0.5-1.4% Nickel-doped F82H.

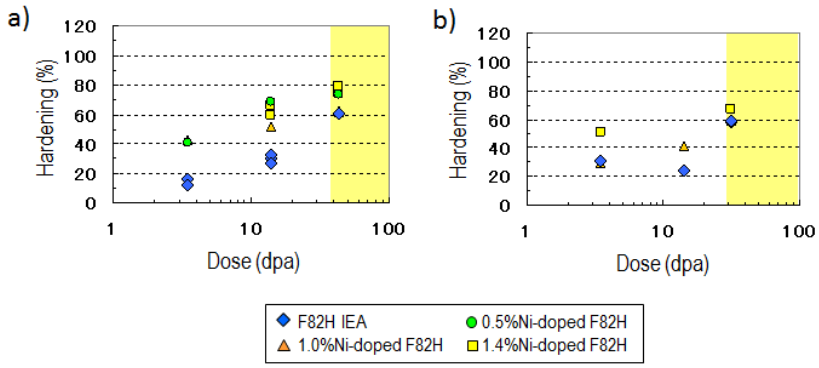

Figure 4. Dose dependence of irradiation hardening ($100x\Delta H_m/H_m$) for F82H IEA, 0.5, 1.0 and 1.4% Ni-doped F82H ion irradiated at TIARA. a) After 543 K irradiation. b) After 633 K irradiation.

Figure 5a) and b) show the dose dependence of irradiation hardening (100xΔHv/Hv) of F82H and 1.4% Nickel-doped F82H after neutron irradiation. It seems to be qualitatively similar to the behavior of ion irradiated specimens. Heavy irradiation hardening is observed in the 1.4% ^{58}Nickel-doped and ^{60}Nickel-doped F82H up to 20 dpa at ~573K, however irradiation hardening of 1.4%Nickel-doped F82H after 80 dpa (~800 appm helium) irradiation is at the same level as for that of F82H. For ~673K irradiation, 1.4% ^{58}Nickel-doped F82H, which produced helium (~200 appm helium), shows slightly more irradiation hardening than 1.4%^{60}Nickel-doped F82H. It is possible that the extra-hardening in this temperature range was caused by the production of small helium bubbles.

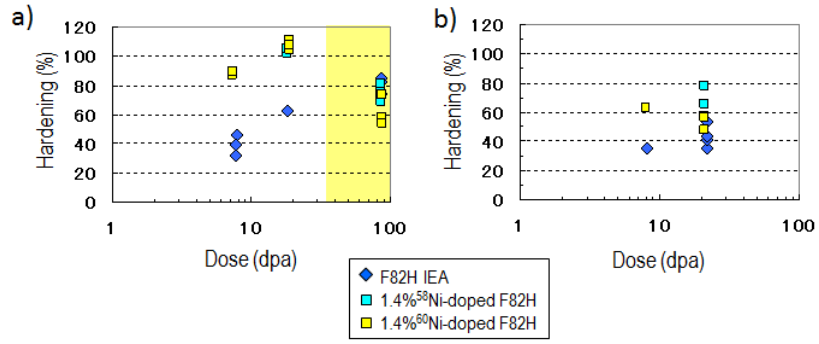

Figure 5. Dose dependence of irradiation hardening (100xΔHv/Hv) for F82H IEA and 1.4% Ni-doped F82H neutron irradiated in HFIR. a) After ~573K irradiation. b) After ~673K irradiation (No tests at ~80 dpa).

These results show that the helium effects on mechanical properties of F82H can be examined using F82H and Nickel-doped F82H after high-dose irradiation because heavy irradiation hardening decreases in Nickel-doped F82H. Future plans are for tensile and fracture toughness tests of these specimens after completion of Vickers hardness testing.

Acknowledgement

This research was sponsored by Japan Atomic Energy Research Institute and the Office of Fusion Energy Sciences, U.S. Department of Energy, under contracts NFE-10-02779 and DE-AC05-00OR22725 with UT-Battelle, LLC., respectively. The authors would like to acknowledge the assistance of Patrick S. Bishop, R.G. Bowman and G.C. Morris in Building 3025 hot cell facility with the

experimental work. Some of the hardness data were obtained by Drs. T. Hirose and N. Okubo under this collaboration program.

References

[1] K. Shiba, et al., J. Nucl. Mater. 283-287 (2000), 474-477.
[2] A. Kimura, et al., J. Nucl. Mater. 307-311 (2002) 521-526.
[3] N. Hashimoto, et.al., J. Nucl. Mater. 307-311 (2002) 222-228.
[4] E. Wakai, et.al., J. Nucl. Mater. 283-287 (2000) 217-221.
[5] K. Shiba, et al., JAERI-Tech 97-038 (1997).
[6] T. Sawai et al., Fusion Science & Technology 44 (2003), 201-205.
[7] D. K. Felde et al., DOE/ER-0313/38 (2005) 164-182.
[8] M. Ando et al., DOE/ER-0313/56 (2014) 15-18.

1.3 ON THE EFFECTS OF HELIUM-DPA INTERACTIONS ON CAVITY EVOLUTION IN TEMPERED MARTENSITIC STEELS AND NANOSTRUCTURED FERRITIC ALLOYS UNDER DUAL ION-BEAM IRRADIATION - G. Robert Odette, Takuya Yamamoto, Yuan Wu, (University of California Santa Barbara), Sosuke Kondo, Akihiko Kimura (Kyoto University)

OBJECTIVE

The objective of this research is to characterize how cavity and other microstructural evolutions in irradiated candidate 9Cr tempered martensitic steels and nanostructured ferritic alloys are influenced by the starting microstructure and irradiation variables, including temperature, displacements per atom (dpa), dpa rate and the helium/dpa (He/dpa) ratio.

SUMMARY

Cavity evolution in normalized and tempered 9Cr martensitic steels (TMS) F82H under Fe^{3+} and He^{+} dual ion beam irradiation (DII) at 500°C was characterized for new dpa and He conditions. The cavity evolution TMS alloy database at 500°C now includes 88 dpa-He-dpa rate DII conditions. The data indicate there may be two swelling trends. This may partly be due to slightly different irradiation flux and/or temperature conditions plus simply natural scatter that is enhanced by local microstructural variations. The fact that swelling under neutron irradiation conditions at low He levels tends to be highly inhomogeneous is well established. The higher swelling rate upper bound data reaches more than ≈ 3% swelling. In the high swelling rate case, the incubation dpa for the onset of void swelling (dpa_i) decrease linearly with increasing He/dpa, and the data can be collapsed on an incubation-adjusted dpa' (= dpa-dpa_i) master trend band. In the low swelling rate case, the incubation dose is ≈ 20 dpa and the post incubation swelling is much more gradual, and approximately linear, with slopes that increase with He/dpa.

BACKGROUND

As reported previously[1-4] we have been carrying out DII studies at 500°C in DuET facility in Kyoto University at various nominal He/dpa and dpa rates (defined at the depth of 600 nm) in TMS and Nanostructured Ferritic Alloys (NFAs). Here we update the DII database and analyze cavity evolution (and swelling) trends in F82H Mod.3 and IEA heats encompassing a very wide range of DII dpa, He and He/dpa. We also compare the behavior of F82H to that in the NFA MA957.

Experimental Procedure

While details of alloys and DII experiments can be found in [2], Table 1 summarizes nominal He and dpa conditions at two reference depth locations encompassed by the current database. The irradiations targeted two nominal doses, three He/dpa and two dpa rate conditions. Taking advantages of the varying spatial distributions of dpa, He and He/dpa as shown Figure 1a for the latest DI14B irradiation, we characterized the microstructures over a very wide range of He-dpa conditions. Figure 1b shows all the available conditions for F82H IEA and Mod.3 in terms of He to dpa rations, where quantitative analyses of microstructure were performed for the series of depth regions in 100nm increments. The conditions shown in Fig.1b represent the average dpa, He and He/dpa in each 100nm section. The dpa are based on SRIM using the Kinchin-Pease with Fe displacement energy of 40 eV [5,6].

RESULTS

Swelling Trends

We have quantitatively characterized the cavity evolution trend as a function of dpa, He and He/dpa in terms of their average size, <d>, number density, N, and volume fractions f. In the previous analysis [1,2], notably <d> and N vary significantly for similar irradiation conditions. This is largely due to the effects of the local microstructure. However, the corresponding variations in f are less. This reflects the fact that variations in the corresponding void $<d_v>$ and N_v are also less, and that the total $f \approx f_v$. Here we assume separation of voids from bubbles at a (≈ critical) size of 4 nm, corresponding to the dip between the two peaks in the cavity size distributions at various conditions.

Table 1. Irradiation conditions analyzed in this report

Exp ID	Alloys	T (°C)	Nominal Condition (@550-650nm)				Peak He (@1000-1100nm)		
			dpa	He (appm)	He/dpa	dpa/s	dpa	He (appm)	He/dpa
DI10B1	F82H mod.3, MA957	500	26	1210	47	5.0×10^{-4}	45	2100	47
DI10B2			9.9	457	46	5.2×10^{-4}	17	795	46
DI10B3			10	480	47	5.1×10^{-4}	18	840	47
DI13A1	F82H mod.3	500	26	390	15	5.1×10^{-4}	44	670	15
DI12A1	MA957	650	48	2230	47	1.1×10^{-3}	83	3860	47
DI13B1	F82H mod.3, F82H IEA (AT)	500	30	848	29	1.5×10^{-3}	51	1467	29
DI13B1+2	MA957	500	57	1578	28	1.5×10^{-3}	97	2729	28
DI14A1	F82H mod.3, F82H IEA (AT)	500	26	1200	47	1.5×10^{-3}	45	2100	47
DI14A1+2	MA957	500	52	2400	47	1.5×10^{-3}	90	4200	47
DI14B	F82H mod.3, F82H IEA (AT)	500	45	1290	28	8×10^{-4}	79	2230	28

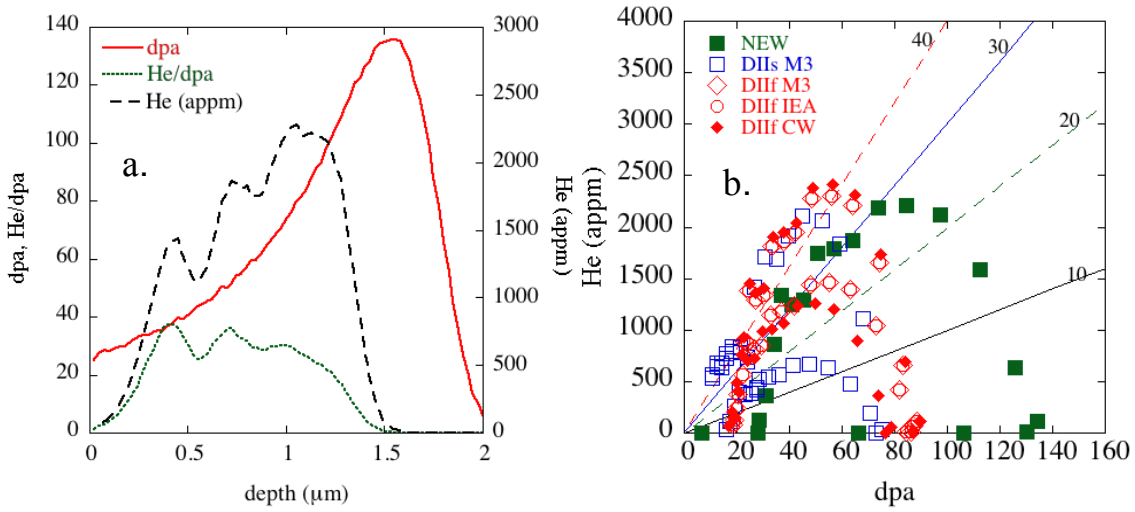

Figure 1. a) The dpa, He (appm) and He/dpa profile of the latest DI14B irradiation, and b) He/dpa - dpa conditions for all the DI runs for TMS materials.

We have updated our database with newly analyzed cavity microstructural data for F82H IEA and Mod.3. To date we have collected data on 88 dpa-He-dpa rate DII conditions for F82H Mod.3 and 48 conditions for F82H IEA. Figure 2 shows a) The number density, b) average diameter, and c) volume fraction of "voids" observed in F82H IEA in dual ion-beam irradiation experiments, as a function of dpa for the groups by nominal He/dpa ratio (SRIM estimated ratio over the analyzed region rounded to the nearest 10s). As shown in Fig.2a the N_v seems to increase monotonously with some scatter for He/dpa of 20 or more, while at lower He/dpa conditions the trend seems to have distinctly 2 groups; one rises sharply around 80 dpa, while the other stays lower until ≈ 130 dpa. The average diameter $\langle d_g \rangle$ seems less scattered within each He/dpa group. The $\langle d_g \rangle$ seems to show a steeper initial increase higher He/dpa, followed by gradual decrease. The decrease may be due to continuing nucleation of smaller voids. As a

result of the increasing N_v and $<d_g>$, the f_v show monotonic increases as a single group with significant scatter for He/dpa of 20 or more. However, in one trend for lower He/dpa of 10 the voids continue to remain in the incubation regime, rather than steeply rising at ≈ 80 dpa. These two trends are associated with different DII runs. The results showing higher f_v are from DI14A1, while the lower f_v are from DI14B. The differences in the irradiation conditions are the dpa and He injection rates, which for larger f_v are both about twice as high as that for lower f_v. Higher He and vacancy concentrations may cause higher N_v voids forming on a higher number density of bubbles along with a theoretically smaller critical size for bubble to void conversion. Another factor is a possible difference in irradiation temperature. Temperature was measured using a pyrometer. A rough estimate of the temperature uncertainty is ±25°C.

Figure 3 shows the corresponding a) number density, b) average diameter, and c) volume fraction of "voids" vs. dpa plots for F82H Mod.3. In this case the two groups of trend is even more enhanced, and is observed even at highest He/dpa. The similar split of trends in two alloys that were irradiated side-by-side supports the hypothesis that the differences may be partly related to the irradiation conditions.

Reiterating the data showing faster f_v versus dpa trend in F82H IEA as summarized in a previous report [1], shows that the swelling incubation dose, dpa_i, linearly decreases with He/dpa ratio as shown in Figure 4a. Using the dpa – dpa_i(He/dpa) gives more unified trend of swelling vs. dose in post-incubation swelling trend. Figure 4b shows the f_v trend for F82H IEA irradiated in the DII experiments compared with f_b for bubbles in MA957 (since no voids are present) on thus modified dpa scale (dpa') normalized at He/dpa = 30, which corresponds to dpa_i = 40. Thus we define dpa' = dpa - dpa_i(He/dpa) + 40. The post incubation swelling in the F82H IEA (filled symbols) occurs at a high rate in a scatter band that averages ≈ 0.1%/dpa. In contrast, the f in the NFA are low up to dpa' ≈ 140 dpa. Note that at ultra high helium levels of ≈ 5000 appm most of the nominal f_b is actually occupied within the nano-feature (NF) oxides that are enveloped by the bubble. The volume fraction of the oxides is ≈ 0.5% shown by the horizontal blue box, thus the f_v for the helium itself is estimated to be less than ≈ 0.3%. This result is reasonably consistent with recent measurement of the helium density in small bubbles, which is ≈ 60/nm^3 are r_b = 1.4 nm [7]. These results also confirm approximate predictions of an older equation of state for helium [8] as well as one based on a new atomistic model [9].

As noted previously, these results can be used to estimate the upper bound swelling in the TMS. For example, at He/dpa = 10, dpa_i ≈ 70 and assuming a post incubation rate of ≈ 0.1%/dpa, the estimated swelling at 200 dpa is ≈ 13%. The corresponding bubble swelling in the NFA at 2000 appm helium is estimated to be less than 0.3%. These dual ion data cannot be translated to different temperatures or neutron irradiation conditions. However, Figure 5 also includes data from in-situ helium injection (ISHI) experiments in High Flux Isotope Reactor (HFIR) at fusion relevant conditions as the large crosshatched symbols. Details of the ISHI technique are given elsewhere. Briefly Ni (or B or Li)-bearing implanter layers are used to inject high-energy α particles into an adjacent material that is simultaneously undergoing fast neutron induced displacement damage. Notably, based on an estimated neutron incubation dpa_i ≈ 5dpa at He/dpa≈50, the ISHI swelling data falls in the trend band for the DII. Note that the ISHI database is being extended from 21 to ≈ 35 dpa, that extrapolates to a more significant level of ≈ 1.9% swelling if the lower dose trends persist.

Even in the low swelling rate regime, the void f_v alone exceeds the corresponding bubble f_b in MA957. However, in the low swelling rate case of F82H, f_v is closer to f_b in MA957. The low swelling rate data can be best treated with linear f_v versus dpa fits with a slope M and intercept f_{vo}. These fits have a roughly constant incubation dose of dpa_i ≈ 20 dpa. However, at higher post incubation dpa, the slopes M increase systematically with He/dpa, as M ≈ C[He/dpa]. Fits to both F82H variants slopes yield a C ≈ 0.00018±0.00001. In this case swelling is approximately represented by f_v = 0.00018[He/dpa][dpa - 20]. It is inappropriate to extrapolate this relation. But if this is done for a He/dpa = 10, f_v is 0.36% at 200 dpa does and not reach 1% until ≈ 555 dpa. Finally, it is very important to emphasize that we are not suggesting these estimates that are based on DII irradiations should be considered as being representative of neutron irradiation conditions.

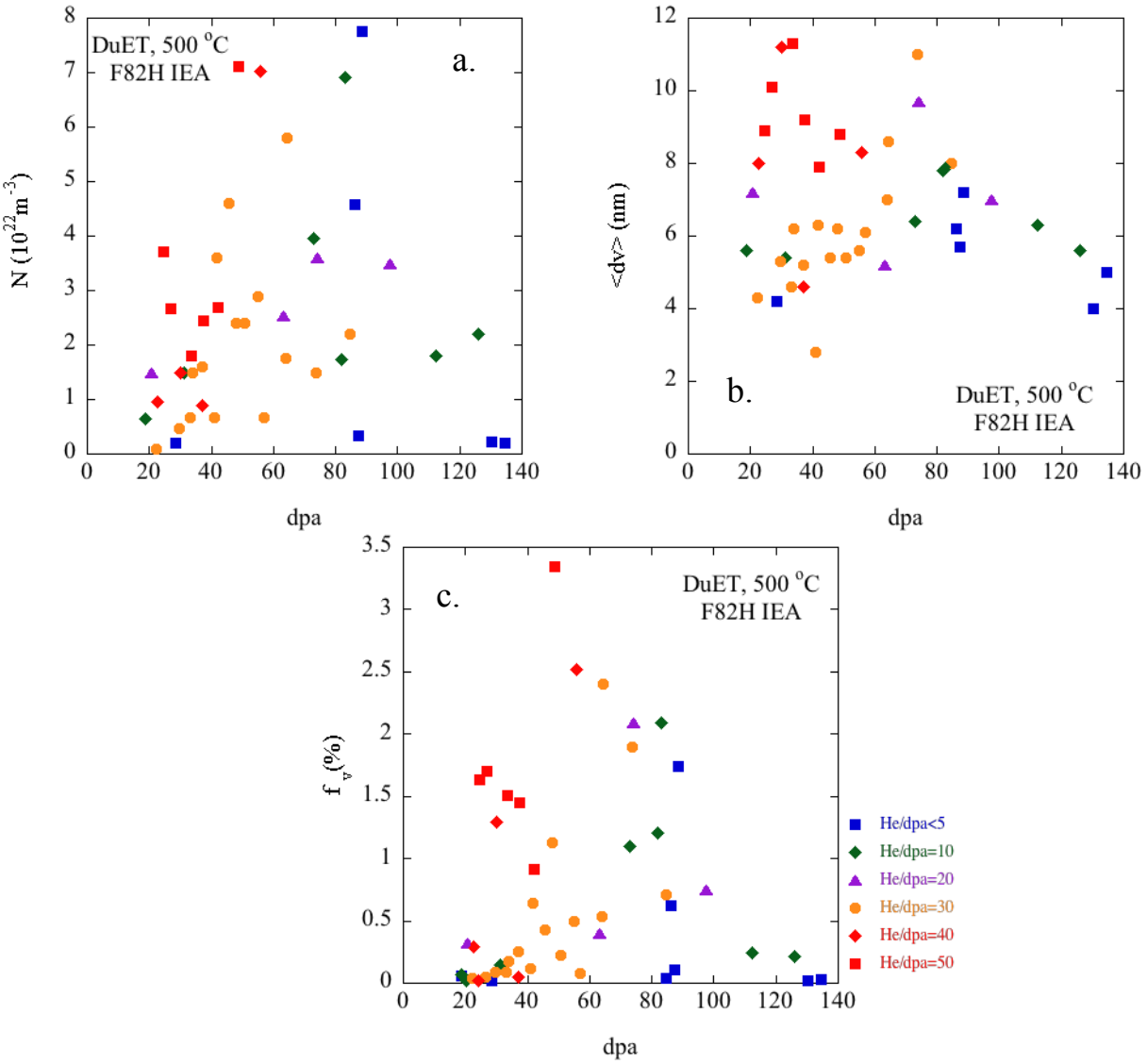

Figure 2. a) The number density, b) average diameter, and c) volume fraction of "voids" observed in F82H IEA in dual ion-beam irradiation experiments, as a function of dpa for the groups by nominal He/dpa ratio.

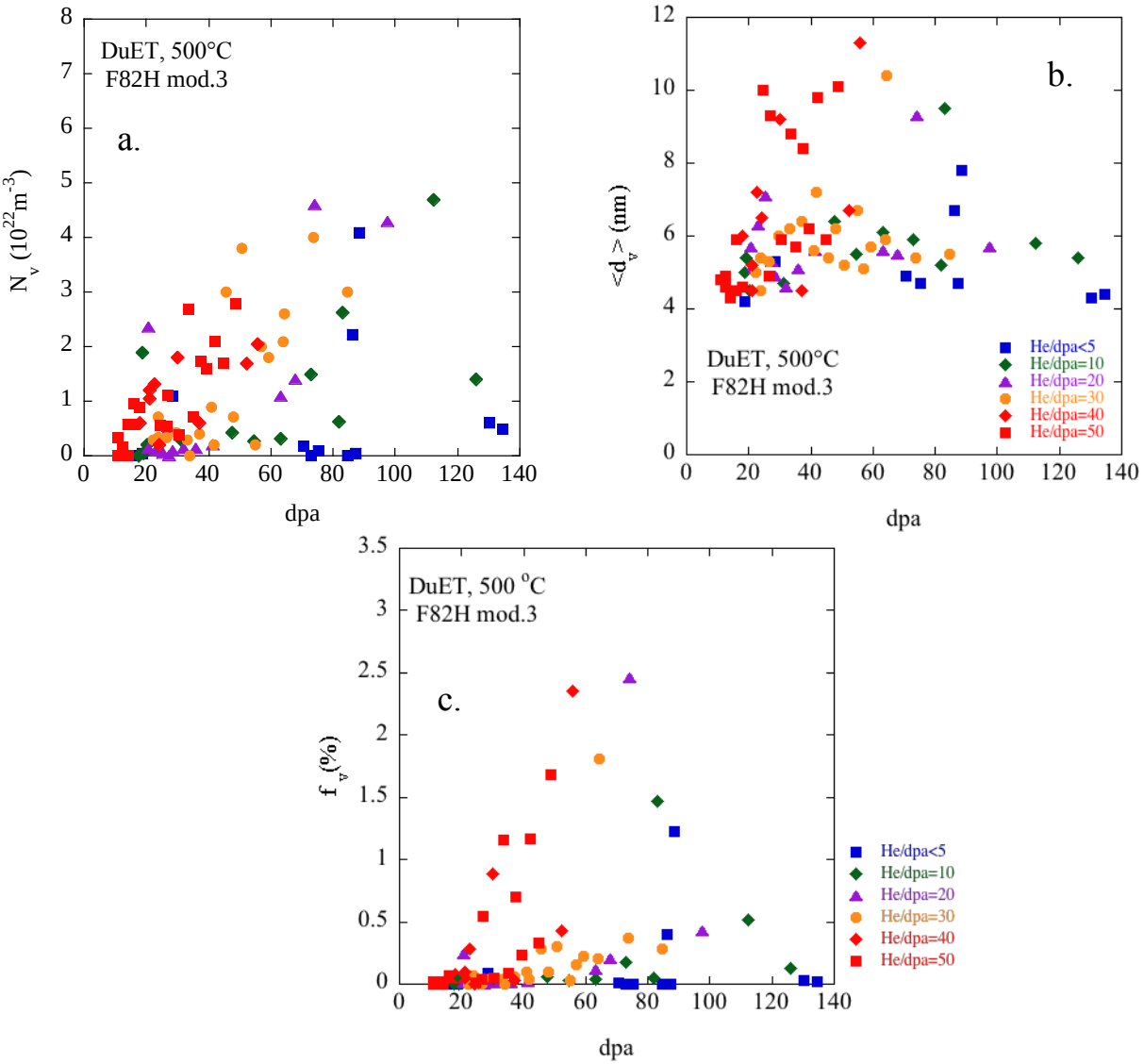

Figure 3. a) The number density, b) average diameter, and c) volume fraction of "voids" observed in F82H Mod.3 in dual ion-beam irradiation experiments, as a function of dpa for the groups by nominal He/dpa ratio.

Summary

Cavity evolutions in normalized and tempered martensitic steel (TMS) F82H under Fe^{3+} and He^{+} dual ion beam irradiations (DII) at 500°C have been characterized over a wide range of dpa, He and He/dpa. The cavity evolution database, that includes 88 dpa-He-dpa rate DII conditions for TMS alloys, shows that the swelling is highly scattered and may manifest two swelling trends. The differences may be partly related to slightly different dpa rates and irradiation temperatures. In the high swelling rate trend case, the incubation dpa_i for the onset of rapid void swelling decreases linearly with increasing He/dpa. In the low swelling rate case the dpa_i are all ≈ 20 and the slopes of f_v versus dpa (>dpa_i)_are the roughly linear and increase, also roughly linearly, with He/dpa. The bubble swelling in the nano-structured ferritic alloy MA957 is smaller compared to the void swelling alone In F82H.

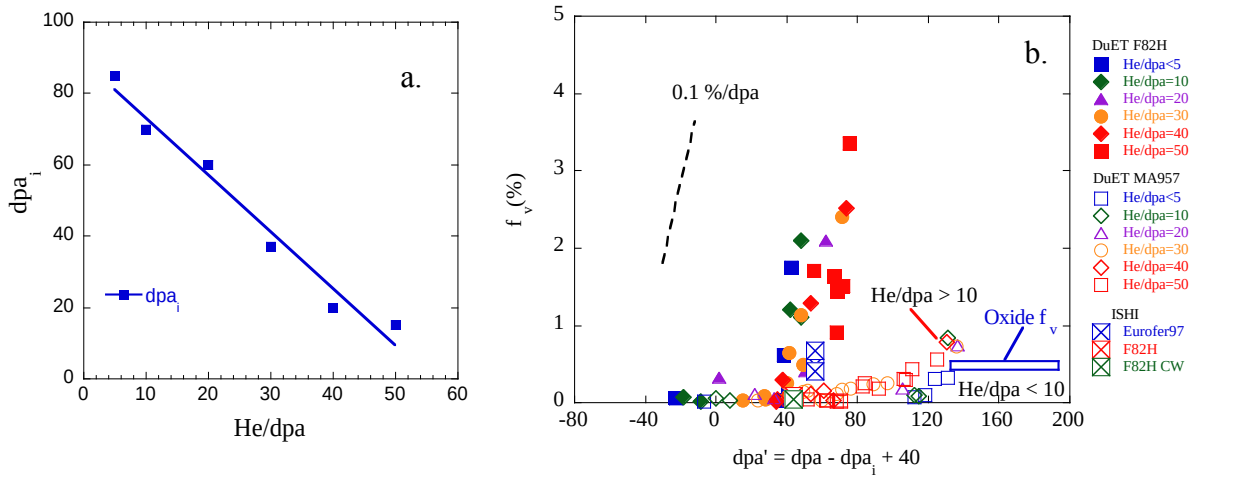

Figure 4. a) swelling incubation dose (dpa_i) versus He/dpa in DII F82H IEA; b) swelling, fv, for F82H IEA compared with NFA, MA957 in DII experiments, as well as with TMS data in in-situ He injection experiments in HFIR.

Acknowledgements

The dual ion-beam irradiations were conducted under the support of the "Joint Research Program on Zero-Emission Energy Research, Institute of Advanced Energy, Kyoto University (ZE26A-16, 25A-19, 24A-13 and 23B-3). The work performed at UCSB was supported by the U. S. Department of Energy, Office of Fusion Energy Sciences, under contract DE-FG03-94ER54275. We acknowledge the contributions of the NSF sponsored UCSB Microstructure and Microanalysis Facility. We are also grateful for generous support of research materials, F82H mod.3 from Dr. K. Shiba, (JAEA, Japan).

References

[1] T. Yamamoto, Y. Wu, G.R. Odette, S. Kondo, A. Kimura, *Fusion Materials Semiannual Report 6/30/2014* DOE/ER-313/56 (2014) 194

[2] T. Yamamoto, Y.Wu, G.R. Odette, K. Yabuuchi, S. Kondo, A. Kimura, J. Nucl. Mater. 449 (2014) 190

[3] T. Yamamoto, Y.Wu, G.R. Odette, S. Kondo, A. Kimura, *Fusion Materials Semiannual Report 6/30/2013* DOE/ER-313/54 (2013) 6.

[4] T. Yamamoto, Y. Wu, G.R. Odette, K. Yabuchi, A. Kimura, *Fusion Materials Semiannual Report 12/31/2010* DOE/ER-313/49 (2011) 1.

[5] ASTM E521-96 (2009), ASTM

[6] R.E. Stoller, M.B. Toloczko, G.S. Was, A.G. Certain, S. Dwaraknath, F.A. Garner, Nuc Instr Mehtods Phys Res B 310 (2013) 75.

[7] Y. Wu, G.R. Odette, T. Yamamoto, J. Ciston, P. Hosemann, Fusion Materials Semiannual, Report 6/30/2013 DOE/ER-0313/54, 2013, pp. 172

[8] R. E. Stoller and G. R. Odette, J. Nucl. Mater. 131 (1985) 118..

[9] R. E. Stoller and Y. N. Osetskiy, *Fusion Materials Semiannual Report June. 30, 2014*,. DOE/ER-0313/56 (2014) 217.

2.1 DEVELOPMENT OF ODS FeCrAl FOR FUSION REACTOR APPLICATIONS – B. A. Pint, K. A. Unocic, S. Dryepondt and D. T. Hoelzer (Oak Ridge National Laboratory, USA)

OBJECTIVE

The dual coolant lead-lithium (DCLL) blanket concept requires improved Pb-Li compatibility with ferritic steels in order to demonstrate viable blanket operation in a DEMO-type fusion reactor. The goal of this work is to develop an oxide dispersion strengthened (ODS) alloy with improved compatibility with Pb-Li and excellent mechanical properties. The current focus is characterizing the performance of a group of ODS alloys based on Fe-12Cr-5Al.

SUMMARY

Characterization of the first four experimental ODS FeCrAl heats (based on Fe-12Cr-5Al) is nearing completion. Creep testing of the alloys containing Y_2O_3 + ZrO_2 and Y_2O_3 + HfO_2 at 800°C/100 MPa has shown exceptional lifetimes for these materials. Additional Pb-Li compatibility experiments were completed at 700°C including similar composition ODS FeCrAl alloys made for a nuclear energy project. All of the alloys showed low mass changes in these experiments. suggesting superior Pb-Li compatibility compared to wrought and ODS Fe-Cr compositions. A thin (~1 μm) reaction product of $LiAlO_2$ was observed in all cases and additional characterization is in progress. The final phase of this project will examine two new alloys made with the same Fe-12Cr-5Al powder and several new alloys where Zr was added as an alloy addition rather than an oxide dispersion.

PROGRESS AND STATUS

Introduction

The DCLL blanket concept (Pb-Li and He coolants) is the leading U.S. design for a test blanket module (TBM) for ITER and for a DEMO-type fusion reactor.[1] With reduced activation ferritic-martensitic (FM) steel as the structural material, the DCLL is limited to ~475°C metal temperature because Fe and Cr readily dissolve in Pb-Li above 500°C and Eurofer 97 plugged a Pb-Li loop at 550°C.[2-3] For a higher temperature blanket for DEMO, structural materials with enhanced creep and compatibility are needed. ODS FeCrAl alloys are one possibility to meet this objective and considerable research on ODS FeCr alloys has shown an excellent combination of creep strength and radiation resistance.[4-7] However, these ODS FeCr alloys do not have adequate compatibility with Pb-based coolants, such as Pb-Bi eutectic (LBE) [8-11]. With the addition of Al, isothermal compatibility tests have shown low mass losses at up to 800°C [12] and a recent thermal convection loop was operated for 1000h at 550°C with only small mass changes measured for the commercial Fe-21Cr-5Al-3Mo alloy (Kanthal APMT) specimens in the hot and cold legs [13] . Therefore, a materials development effort is underway, specific to this application. ODS FeCrAl was commercialized in the 1970's for its high temperature (>1000°C) creep and oxidation resistance [14] and other research groups are currently investigating new FeCrAl alloy compositions for fission and fusion applications with liquid metals [15-17].

Previous initial work [18-21] had identified Fe-12wt.%Cr-5Al as a target composition with low Cr to minimize α' formation during irradiation [22], while maintaining 5%Al for Pb-Li compatibility.[18,21] Using diffusion couples, combinations of oxides also were identified that could form stable ternary compounds. The microstructure and property assessment of this first generation of composition is nearly complete [23,24] and a second generation is being designed based on the information learned.

Experimental Procedure

Four experimental ODS FeCrAl ferritic alloys were produced by mechanical alloying (MA). Powder of specified composition Fe-12.1wt.%Cr-5.0Al and particle size range ~45-150 μm was prepared by Ar gas atomization by ATI Metal Powders. The FeCrAl powder was blended with 0.3%Y_2O_3 powder (17-31 nm crystallite size, produced by Nanophase, Inc.) and subsequent 1kg batches included additions of 0.4ZrO_2, 0.22HfO_2 and 0.2TiO_2 powders (<100 nm diameter from American Elements). Each batch was ball milled for 40 h in Ar gas atmosphere using the Zoz CM08 Simoloyer ball mill. After ball milling, the powders were placed in mild steel cans, degassed at 300ºC under vacuum and sealed. The cans were equilibrated at 950ºC for 1 h and then extruded through a rectangular shaped die. Table 1 shows the as-extruded compositions of each alloy. The alloys with additional ZrO_2, HfO_2 and TiO_2 oxide additions showed higher O contents and the Cr and Al contents were lower than the starting powder. Other typical impurities were Co, Cu, Ni and Mn at the 0.01-0.02% level and the C and N pickups from the milling process were acceptable. Table 1 also includes several additional alloys with higher Cr contents that were produced for a nuclear energy project. These alloys were made by a similar process but with only Y_2O_3 additions. For comparison, a commercial ODS (PM2000) and a powder metallurgy (APMT) FeCrAl alloy are shown.

Because of the relatively small amount of material fabricated, creep testing of the new alloys was performed at 800°C using 25mm long specimens parallel to the extrusion axis and with a 2 x 2 mm gauge section that was 7.6mm long. Static Pb-Li capsule tests were performed using Mo (inert to Pb-Li) inner capsules and type 304 stainless steel (SS) outer capsules to protect the inner capsule from oxidation. The ODS FeCrAl specimens were ~1.5 mm thick and 4-5 cm^2 in surface area with a 600 grit surface finish and were held with 1 mm diameter Mo wire. The capsules were loaded with 125 g of Pb-Li in an Ar-filled glove box. The most recent capsule tests were conducted with commercial Pb-Li from the same supplier used for the loop experiment [13]. The Mo and SS capsules were welded shut to prevent the uptake of impurities during the isothermal exposure. After exposure, residual Pb-Li on the specimen surface was removed by soaking in a 1:1:1 mixture of acetic acid, hydrogen peroxide and ethanol for up to 72 h. Mass change was measured with a Mettler-Toledo balance with an accuracy of ±0.04 mg or 0.01 mg/cm^2.

Post-test specimen surfaces were examined using x-ray diffraction (XRD) and secondary electron microscopy (SEM) equipped with energy dispersive x-ray (EDX) analysis. After surface characterization, the specimens were metallographically sectioned and polished and examined by light microscopy, SEM and transmission electron microscopy (TEM). Specimens for TEM analysis were prepared by Focused Ion Beam (FIB, Hitachi model NB500) using the in-situ lift-out method. A Philips model CM200 FEG-TEM/STEM (Scanning TEM) with XEDS was used for analysis. Bright-Field (BF) and High Angle Annular Dark Field (HAADF) STEM imaging methods were used in the microstructural investigations.

Table 1. Alloy chemical compositions (mass% or ppmw) by inductively coupled plasma analysis and combustion analysis.

Material	Fe%	Cr%	Al%	Y%	O	C	N	S	Other
Powder	82.8	12.1	5.0	<	64	31	11	<3	0.004Si
125Y	83.3	11.4	4.8	0.19	842	380	455	20	0.05W, 0.02Si, 0.01Ti
125YZr	82.8	11.5	4.9	0.18	1920	250	160	10	0.30Zr, 0.01Hf, 0.01Si
125YHf	82.3	11.7	4.8	0.17	2280	220	110	10	0.68Hf, 0.01Zr, 0.01Si
125YTi	82.4	12.0	4.9	0.16	2220	350	135	30	0.20Ti,0.01Si
134Y	82.5	12.8	4.4	0.17	1360	310	140	10	0.01Si
155YT	79.9	14.6	4.7	0.16	950	340	240	10	0.44Ti, 0.02Si
155YMT	79.0	14.6	4.8	0.16	830	370	130	<10	0.44TI,0.88Mo,0.02Si
PM2000	74.1	19.1	5.5	0.39	2480	14	86	8	0.48Ti, 0.02Si
APMT	69.8	21.2	4.8	0.21	519	360	530	<3	2.8Mo,0.1Zr,0.2Hf,0.5Si

< indicates below the detectability limit of <0.01%

Table 2. Measurements of the grain size and grain aspect ratio (GAR) of the ODS FeCrAl ferritic alloys.

Alloy	Grain Size (μm)		GAR
	Parallel to Extrusion Axis	Normal to Extrusion Axis	(Parallel/Normal)
125Y	0.83 ± 0.17	0.56 ± 0.09	1.48
125YZ	0.27 ± 0.06	0.17 ± 0.02	1.59
125YH	0.70 ± 0.16	0.39 ± 0.06	1.79
125YT	0.14 ± 0.02	0.12 ± 0.01	1.17

Results and Discussion

A large amount of microstructural information has been reported previously on the ODS Fe-12Cr-5Al alloys as well as aging and hardness data [20,23-25]. Table 2 summarizes the completed comparison of grain size for each of the four alloys.

Figure 1 compares the creep performance at 800°C of the ODS Fe-12Cr-5Al alloys to the commercial alloys PM2000 and APMT. Data from Plansee for fine grain (FG) PM2000 are also included. One PM2000 specimen failed during loading at 80 MPa, while an on-going 125YT test has reached 285 h with the same applied stress. For testing at 100 MPa, one 125YH specimen failed after 1242 h and one 125YZ specimen has passed 4000 h without failure. To reach a minimum lifetime of 1000h at 800ºC, alloys APMT and FG PM2000 are limited to ~25 MPa and ~45 MPa, respectively. For the new 12Cr-5Al alloys, the stress can be increased to at least 80MPa. A 100MPa test is planned for 125YT and further work is needed to confirm that 125YZ exhibits the best creep properties among the new alloys.

For the Pb-Li compatibility assessment, the most recent mass change data after 1000 h at 700°C in static Pb-Li is summarized in Figure 2 with the previous result for a 125YZ specimen. In the initial set of capsule experiments under the same conditions, a 125YH specimen lost 1.3 mg/cm^2, but showed no visual indication of attack. A second 125YH specimen was exposed in this set of experiment and showed a low

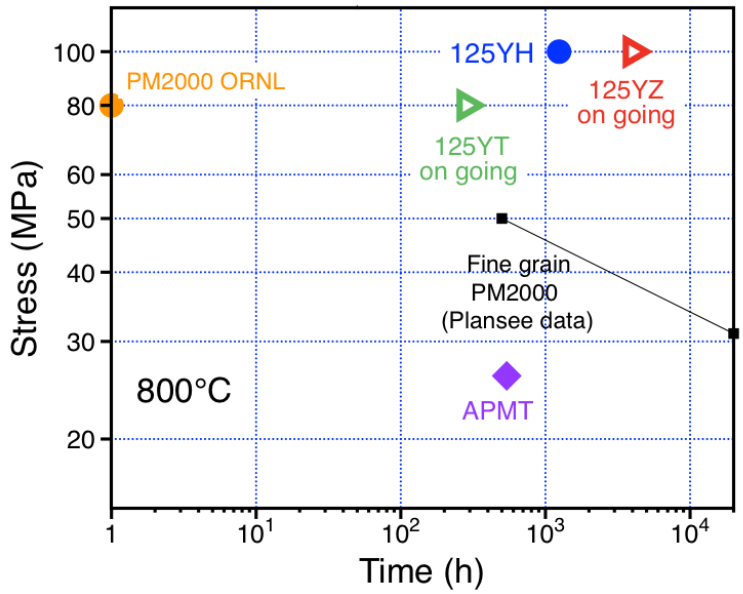

Figure 1. Lifetime at 800°C versus applied stress for the ODS Fe-12Cr-5Al, PM2000 and APMT alloys.

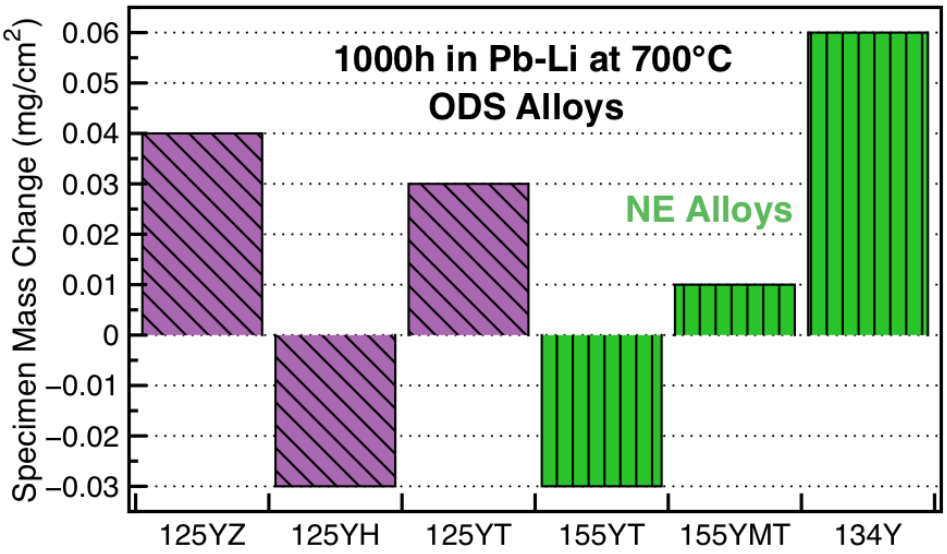

Figure 2. Specimen mass change for alloy specimens exposed for 1000h at 700°C in static Pb-Li.

mass change like the other specimens. In addition to the 12Cr-5Al specimens, ODS FeCrAl alloy specimens from another project were included that contained higher Cr contents, Table 1. These specimens also showed low mass changes after exposure and cleaning, consistent with prior work on commercial FeCrAl alloys PM2000 and APMT [12,26]. Also consistent with these prior studies, XRD identified the reaction products as $LiAlO_2$ in all cases. This oxide formed due to O impurities in the Pb-Li and presumably inhibited dissolution of the alloy into the liquid metal. However, the mass losses observed in the recent loop test at ~450-550°C suggest that this layer does not prevent dissolution.

Figure 3 shows cross-sections of the 12Cr-5Al ODS alloy specimens exposed in Pb-Li. In several cases, the ~1μm thick $LiAlO_2$ layer fractured or delaminated during specimen preparation. Previously, the Al content in the alloy was measured using electronprobe microanalysis but only minor Al depletion was observed in the 125YH and 125YZ specimens [23,25]. In order to further study the reaction product, TEM cross-sections were made. Figures 4 and 5 show initial results for the 125YZ specimen. The oxide appeared to have a columnar grain structure, Figure 4. At higher magnification, voids and oxide precipitates could be observed in the $LiAlO_2$ layer. Voids appear light in the bright field image and dark in the HAADF image. Oxides rich in Zr should appear bright in the HAADF image and dark in the bright field image, Figure 5. The incorporation of oxides into the reaction product suggests that the layer grew by the inward transport of O, rather than outward transport of Al. Unfortunately, $LiAlO_2$ was easily damaged by the electron beam (as was found earlier [26]) and only limited analysis has been possible of this specimen.

In the final year of this 3-year effort, several new alloys will be briefly investigated. Two new alloys have been extruded with the same Fe-12Cr-5Al powder with additions of La_2O_3-ZrO_2 and Y_2O_3-Fe_2O_3. The former was selected to examine the oxide precipitates formed in the alloy with La rather than Y and the latter was made to replace the 125Y alloy baseline alloy that had a lower O content than the other alloys (Table 1) and was contaminated with Fe-Cr powder resulting in questionable mechanical properties and Pb-Li compatibility [25]. In addition, new powder was ordered with Fe-12Cr-5.6Al and Fe-10Cr-6Al base compositions and alloys additions of Zr, Hf or Zr and Ti. The primary goal with these powders is to determine if different oxides form if, for example, the Zr is added as an alloy addition rather than as ZrO_2.

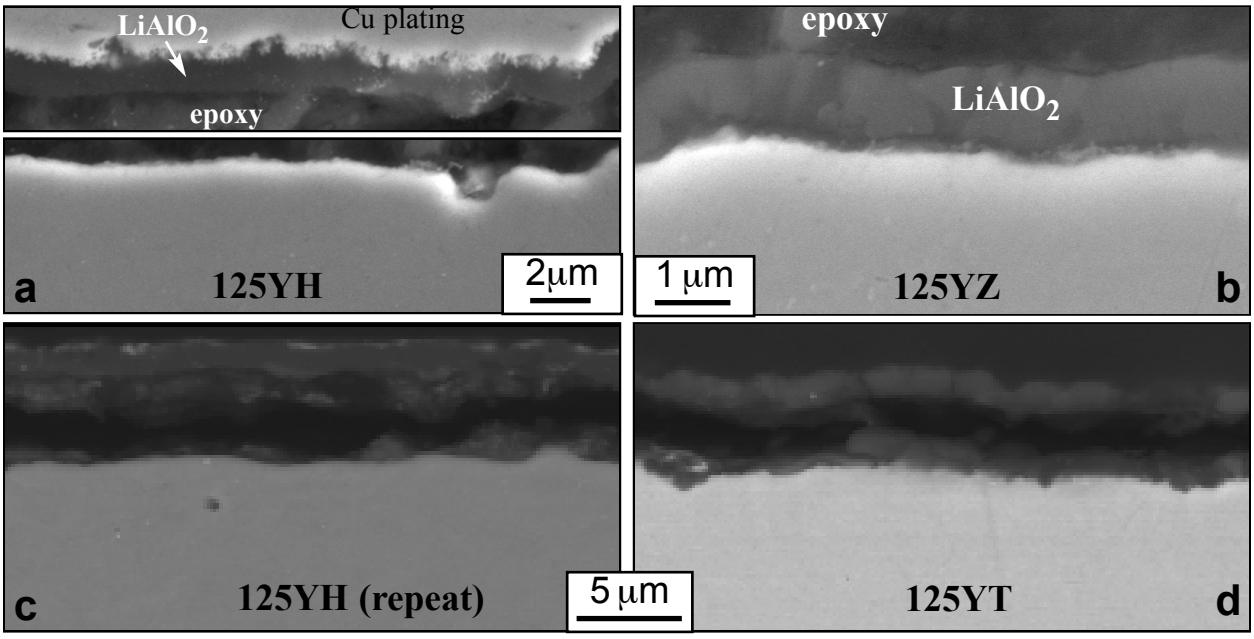

Figure 3. SEM backscattered electron images of polished cross-sections after 1000 h in Pb-Li at 700°C of (a) 125YH, (b) 125YZ, (c) 2nd 125YH specimen and (d) 125YT. In (a), (c) and (d) the oxide delaminated during specimen preparation.

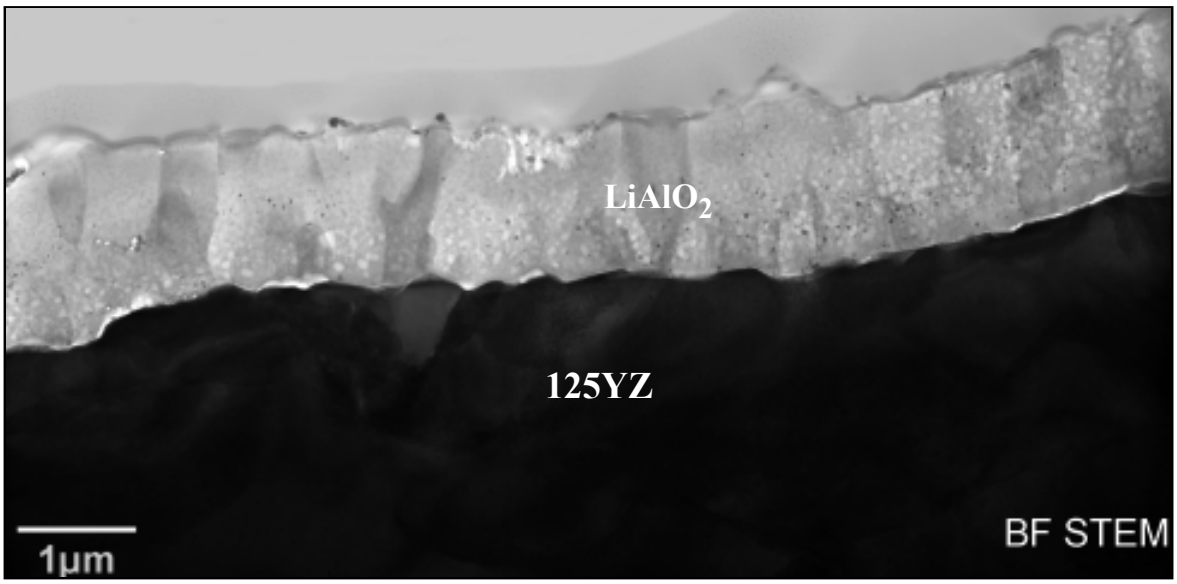

Figure 4. Bright field STEM image of the oxide formed on 125YZ after 1000h at 700°C in PbLi.

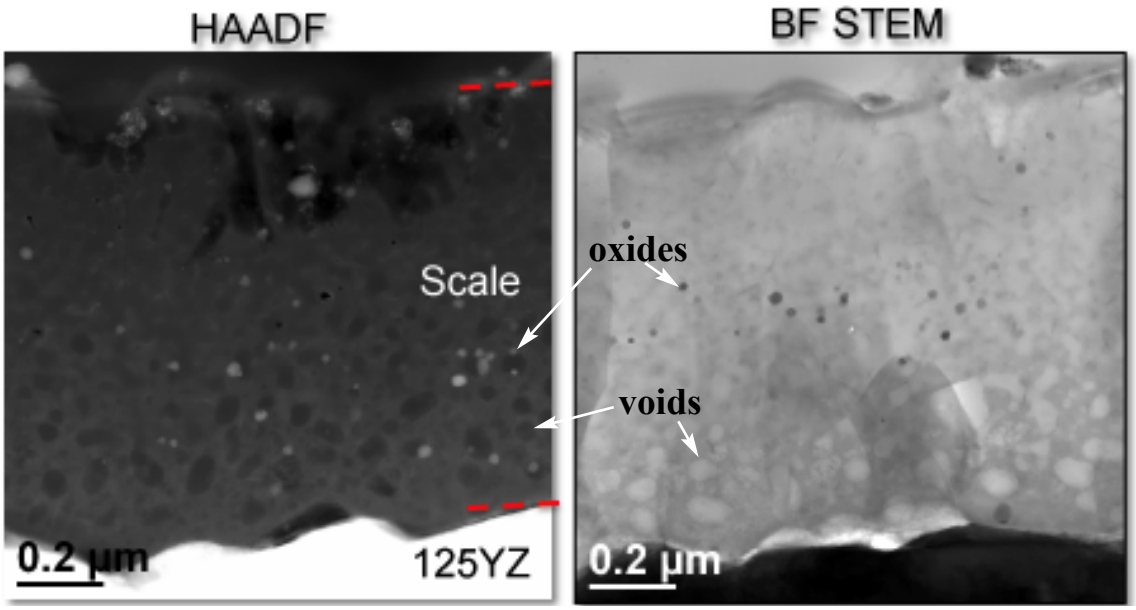

Figure 5. STEM cross-sectional images of the oxide formed on 125YZ after 1000h at 700°C in PbLi.

References

[1] M. Abdou, D. Sze, C. Wong, M. Sawan, A. Ying, N. B. Morley and S. Malang, Fus. Sci. Tech., 47 (2005) 475.
[2] O. K. Chopra, D. L. Smith, P. F. Tortorelli, J. H. DeVan and D. K. Sze, Fusion Technol., 8 (1985) 1956.
[3] J. Konys, W. Krauss, J. Novotny, H. Steiner, Z. Voss and O. Wedemeyer, J. Nucl. Mater. 386-88 (2009) 678.
[4] S. Ukai and M. Fujiwara, J. Nucl. Mater. 307 (2002) 749.
[5] G. R. Romanowski, L. L. Snead, R. L. Klueh, D. T. Hoelzer, J. Nucl. Mater., 283-287 (2000) 642.
[6] R. L. Klueh, J. P Shingledecker, R. W. Swindeman, D. T. Hoelzer, J. Nucl. Mater. 341 (2005) 103.
[7] D. A. McClintock, M. A. Sokolov, D. T. Hoelzer and R. K. Nanstad, J. Nucl. Mater., 392 (2009) 353.
[8] T. Furukawa, G. Müller, G. Schumacher, A. Weisenburger, A. Heinzel and K. Aoto, J. Nucl. Mater. 335 (2004), 189.
[9] P. Hosemann, H.T. Thau, A.L. Johnson, S.A. Maloy and N. Li, J. Nucl. Mater. 373 (2008) 246.
[10] C. Schroer, J. Konys, T. Furukawa and K. Aoto, J. Nucl. Mater. 398 (2010) 109.
[11] A. Weisenburger, K. Aoto, G. Müller, A. Heinzel, G. Schumacher and T. Furukawa, J. Nucl. Mater. 358 (2006) 69.
[12] B. A. Pint, L. R. Walker and K. A. Unocic, Mater. High Temp. 29 (2012) 129.
[13] S. J. Pawel, DOE-ER-0313/56 (2014) 178.
[14] J. D. Whittenberger, Met. Trans. 9A (1978) 101.
[15] J. Lim, H.O. Nam, I.S. Hwang and J.H. Kim, J. Nucl. Mater. 407 (2010) 205.
[16] A. Kimura, et al., J. Nucl. Mater. 417 (2011) 176.
[17] S. Takaya, et al., J. Nucl. Mater. 428 (2012) 125.
[18] B. A. Pint, D. T. Hoelzer, D. Shin, J. O. Kiggans, Jr., K. A. Unocic, DOE/ER-0313/53 (2012) 10.
[19] B. A. Pint, D. T. Hoelzer and K. A. Unocic, DOE/ER-0313/54 (2013) 27.
[20] D. T. Hoelzer, K. A. Unocic, S. Dryepondt and B. A. Pint, DOE/ER-0313/55 (2013) 5.
[21] K. A. Unocic and B. A. Pint, J. Nucl. Mater. 455 (2014) 330.

[22] C. Capdevila, M.K. Miller, K.F. Russell, J. Chao, J.L. González-Carrasco, Mater. Sci. Eng. A 490 (2008), 277.
[23] B. A. Pint, S. Dryepondt, K. A. Unocic and D. T. Hoelzer, JOM 66 (2014) 2458.
[24] K. A. Unocic, D. T. Hoelzer and B. A. Pint, Mater. High Temp. 32 (2015) 123.
[25] B. A. Pint, K. A. Unocic, S. Dryepondt and D. T. Hoelzer DOE-ER-0313/56 (2014) 31.
[26] B. A. Pint and K. L. More, J. Nucl. Mater. 376 (2008) 108.

2.2 TEM CHARACTERIZATION OF 14YWT AND 12YWT ODS FERRITIC ALLOYS NEUTRON IRRADIATED AT 500°C USING IN-SITU HELIUM INJECTION - H.J. Jung, D. J. Edwards, R. J. Kurtz (Pacific Northwest National Laboratory), G. R. Odette, Y. Wu, T. Yamamoto (University of California Santa Barbara)

OBJECTIVE

The objective is to characterize the microstructure and chemical evolution in two oxide dispersion strengthened (ODS) ferritic alloys, 14YWT and 12YWT, containing 14 and 12 Cr wt % respectively, irradiated with neutrons to 21.2 dpa at 500°C. Samples were injected with 1230 appm of helium via an in situ He injection (ISHI) technique.

SUMMARY

This report summaries TEM characterization of 14YWT and 12YWT, ODS ferritic alloys with 14 and 12 wt % Cr, respectively, to compare the effect of neutron irradiation with and without concurrent He injection using in situ He injection. The density and average size of <100>/{100} type dislocation loops are always larger than those of 1/2<111>/{111} type, but this difference is significantly affected by He implantation. The density of dislocation loops of both types ranges from ~1 to $4x10^{21}$ m^{-3} with average size ranging from 5~20 nm. 14YWT has lower density but larger size dislocation loops than 12YWT, while the line dislocation density of 14YWT is 3 times lower than that of 12YWT. Helium bubble densities of both 14YWT and 12YWT are $1.9x10^{23}$ m^{-3}, the average He bubbles size of 14YWT and 12YWT are 1.4 and 1.2 nm, respectively. 14YWT exhibits α-α' phase separation, Y-rich particles and uniformly distributed W. In addition to those features, 12YWT exhibits Y-Ti-O particles (not Y-O rich) and elongated Cr-rich phases.

PROGRESS AND STATUS

Introduction

Oxide-dispersed strengthened (ODS) alloys provide excellent high-temperature mechanical properties with high swelling-resistance for first-wall materials for future fusion reactors [1,2]. The materials for the first wall will inescapably endure a severe thermal and neutron-irradiation environment, with the presence of high levels of He production (10 appm He per dpa) from transmutation creating an even more challenging environment [3]. The high levels of He impacts the mechanical properties of ferritic alloys through He embrittlement and the formation of He bubbles and voids in the matrix, at lath boundaries, grain boundaries, and at particle-matrix interfaces [4], which can lower the high-temperature tensile and creep properties. A further consequence of the He accumulation is that the small bubbles (d<2 nm) can increase in size and convert to large unstably growing voids, thereby causing significant swelling [5]. In order to prevent the transition of He bubbles to voids, microstructures are being designed to provide a high density of nanoscale trapping sites such as nano-size oxide particles to broadly disperse He gas atoms [1] so that bubbles do not reach the critical size. We are currently examining the effectiveness of oxide dispersions, as well as elucidating the mechanisms of He movement, trapping, and interaction with various defects and interfaces in ferritic alloys under irradiation.

Due to practical difficulties in realizing material performance under a fusion-relevant irradiation environment, the in-situ He injection (IHSI) technique has been developed to explore the effects of simultaneous neutron irradiation and He injection on microstructural evolution of candidate materials, as detailed in the literature [7]. Here we present analytical transmission electron microscopy (TEM) characterization of neutron-irradiated and He/neutron-irradiated effects on 14YWT and 12YWT ferritic alloys with a nominally 4 μm thick NiAl layer deposited to one surface. When irradiated with neutrons, the ^{59}Ni isotope undergoes a ^{59}Ni (n, α) reaction and injects some fraction of the energetic He into the ferritic alloy. The samples were irradiated to a dose of 21.2 dpa at 500°C in the JP-27 experiment in the HFIR reactor for several operating cycles over a span of years, leading to an estimated 1230 appm of He in the sample over a uniform depth of about 6 μm. Cross-sectional TEM samples were prepared by the focus

ion beam (FIB) technique to characterize microstructure related features such as He bubbles/voids, dislocation loops/line dislocations, and oxide or carbide particles.

Experimental Procedure

The compositions of the 14YWT and 12YWT ODS alloys in this report are listed in Table 1. Both 14YWT and 12YWT are powder metallurgy products, but 14YWT was hot isostatically pressed at 1150°C and 12YWT was hot extruded at 1150°C. All samples were neutron irradiated to a dose of 21.2 dpa at 500°C in the High Flux Isotope Reactor (HFIR) at Oak Ridge National Laboratory (ORNL). A 4 μm NiAl coating used for the ISHI was applied to one side of a 3-mm TEM disc, which allows a FIB lamella to be extracted from either side of the TEM discs to explore the impact of neutron irradiation with or without concurrent helium injection. The NiAl coating produces a He concentration of about 1230 appm in the ferritic matrix extending to a depth of ~6 μm below the coating. Cross-sectional TEM samples, prepared by a FIB (FEI Quanta 3D), were finalized with low-energy surface cleaning (2 keV Ga^+ ion) at ±2° tilt angles. The TEM lamellae were extracted from each side of the TEM disc.

Table 1. Composition of examined ODS alloys

Alloy	Composition (wt.%) with Fe balance											
	Cr	Y(Y2O3)	W	Ti	Al	Mg	Si	V	Mo	Mn	Re	Os
14YWT	13.76	0.13	2.04	0.41	0.82	0.09	0.22	0.24	0.07	2.16	0.21	0.54
12YWT	11.98	0.15	1.74	0.35	0.84	0.17	0.14	0.21	0.32	2.10	0.15	0.49

The analytical TEM characterization was performed using a newly installed Cs-corrected JEOL ARM 200cF microscope equipped with various detectors, including a Centurio silicon drift detector (SDD) for energy dispersive X-ray spectroscopy (EDS), a Gatan Quantum 965 Dual EELS system, and high angle annular dark field (HAADF) and bright field (BF) STEM detectors. This instrument can produce a Cs-corrected sub-Å STEM probe with high electron current because of the cold field emission gun (CFEG), allowing enhanced spatial resolution of EDS mapping over shorter times. TEM sample thickness was determined through convergent-beam electron diffraction (CBED). Bright-field TEM (BFTEM) images of He bubbles and voids were acquired using an over/under-focus technique, and measured bubble sizes are about 87% of the actual bubble size at an under-defocus of 750 nm as determined from a previous modeling study [7,8]. The dislocation loops and line dislocations were imaged using a specific diffraction vector of g=200 at two-beam conditions near a 001 zone axis in bcc matrix [9].

Results and Discussion

First, the effect of neutron-irradiation at 500°C with and without helium injection on dislocation loops and line dislocations of 14YWT and 12YWT was investigated from BFTEM images (Fig. 1a~d) taken from a slightly weak two-beam condition to g=200 direction near a 001 zone axis in bcc matrix. Density and size measurements of <100>/{100} and 1/2<111>/{111} type loops, examples of which are shown in Fig. 1e and 1f, show that the injection of He under neutron increases the density and size of each dislocation loop type compared to those measured in the neutron-only irradiated side of the disc, while line dislocation densities are almost same in 14YWT and 12YWT (slightly lowered though by He injection). Interestingly, the density and average size of <100>/{100} loops are always larger than those of 1/2<111>/{111} loops irrespective of the presence of helium, leading to the question of why <100>/{100} loops are more dominant. Careful long-term simulation of the nucleation, growth and mobility of each type loop is needed to elucidate this phenomenon, requiring careful consideration of several factors such as physical distribution of ODS particles, the role of grain boundaries and pre-existing dislocation sinks, chemical changes in the microstructure like α-α' phase separation, second phase formation, and segregation of certain elements (ex. Cr, Ti). The density range of each dislocation loop is roughly 1 to $4x10^{21}$ m^{-3} with average size ranging from 5~20 nm. 14YWT has lower density but larger size dislocation loops than those in 12YWT under the same conditions, while line dislocation density of 14YWT is about 3 times lower than that of 12YWT.

Interestingly, size distribution histograms of <100>/{100} and 1/2<111>/{111} loops in Fig. 2 provide detailed data on how loops grow under the influence of He. Please note that the histograms have the

same population scale (Y-axis) to facilitate a comparison between histograms from the neutron-only irradiated side (left) versus histograms for the loops on the He-injected side (right). While the neutron-only irradiated cases of each type of loop usually have one dominant peak at a small size, the dual He/neutron-irradiation cases display bimodal histograms with a broader distribution at larger sizes (> 30 nm). It is significant that in the 14YWT alloy the densities of the <100>/{100} loops are higher and the loops extend to larger sizes compared to the 1/2<111>/{111} loops under He injection. The loop characteristics suggest that the histogram shapes are fairly similar when comparing the two alloys, however, 12YWT in general has a higher density of smaller loops. The reasons for this are not presently understood.

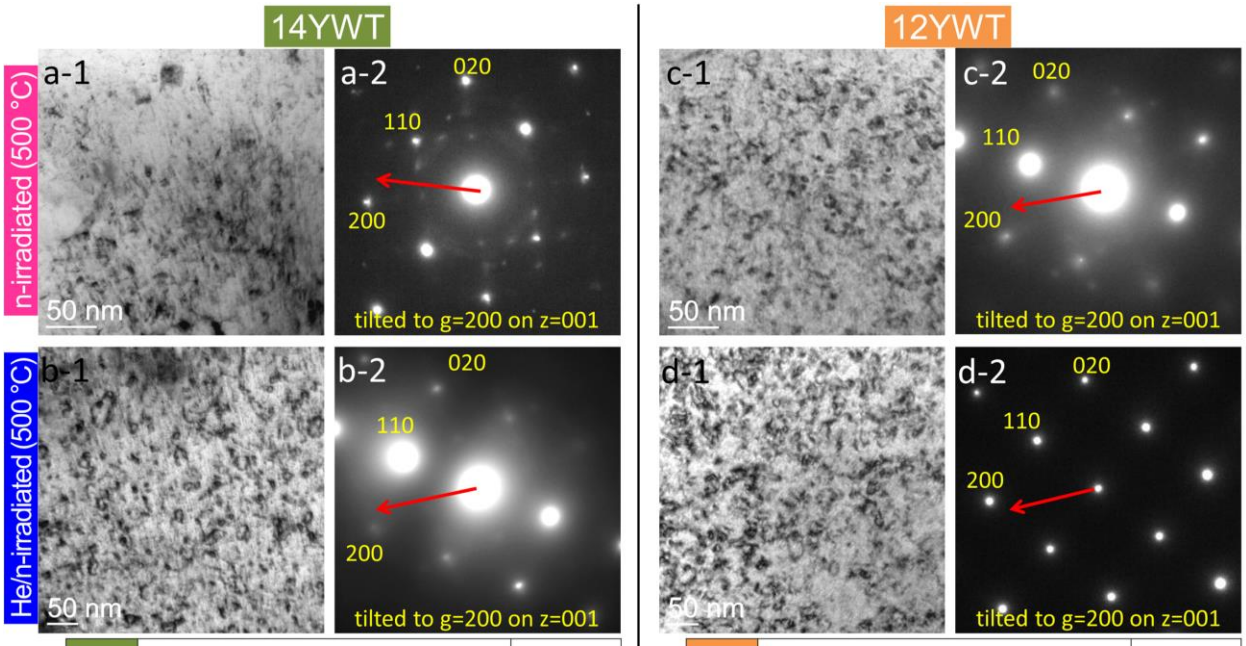

e

14YWT	Dislocation Loops				Line Dislocations
	<100>/{100} type		½<111>/{111} type		
	density [10^{21}/m^3]	size (stdev) [nm]	density [10^{21}/m^3]	size (stdev) [nm]	density [10^{13}/m^3]
n	1.8	11.2 (7.1)	1.5	8.9 (6.6)	6.3
He/n	3.6	17.1 (11.2)	1.8	16.4 (9.2)	5.6

f

12YWT	Dislocation Loops				Line Dislocations
	<100>/{100} type		½<111>/{111} type		
	density [10^{21}/m^3]	size (stdev) [nm]	density [10^{21}/m^3]	size (stdev) [nm]	density [10^{13}/m^3]
n	2.9	6.1 (2.8)	2.0	6.9 (3.7)	18
He/n	3.3	14.5 (8.8)	2.8	10.5 (3.8)	17

Figure 1. Dislocation loops and line dislocations of 14YWT (a and b) and 12YWT (c and d) under neutron-irradiation and He/neutron-irradiation at 500 °C from four sets of BFTEM images (left) and SAD patterns (right) and statistics (e and f) of <100>/{100} and 1/2<111>/{111} type loops and line dislocations measured from 3 different images of each sample. Please note that each BFTEM (denoted as 1) was taken from each diffraction condition (denoted as 2), which is a slightly weak g=200 two-beam condition near the 001 zone axis of bcc matrix to show better diffraction contrast of dislocations. Interestingly, the density and size of <100>/{100} and 1/2<111>/{111} dislocation loops in both 14YWT and 12YWT increase under irradiation from only neutron to dual He and neutron, while line dislocation densities are similar.

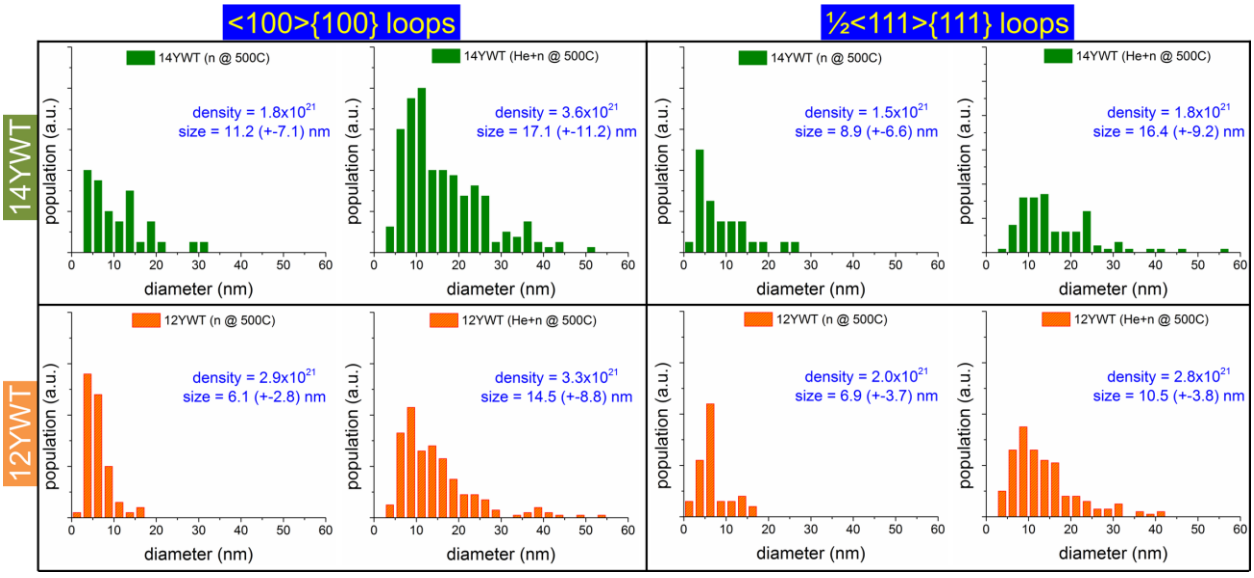

Figure 2. Histograms of <100>/{100} and 1/2<111>/{111} loop sizes in 14YWT (top green) and 12YWT (bottoms orange) under only neutron-irradiation (left) and He/neutron-irradiation (right) at 500 °C.

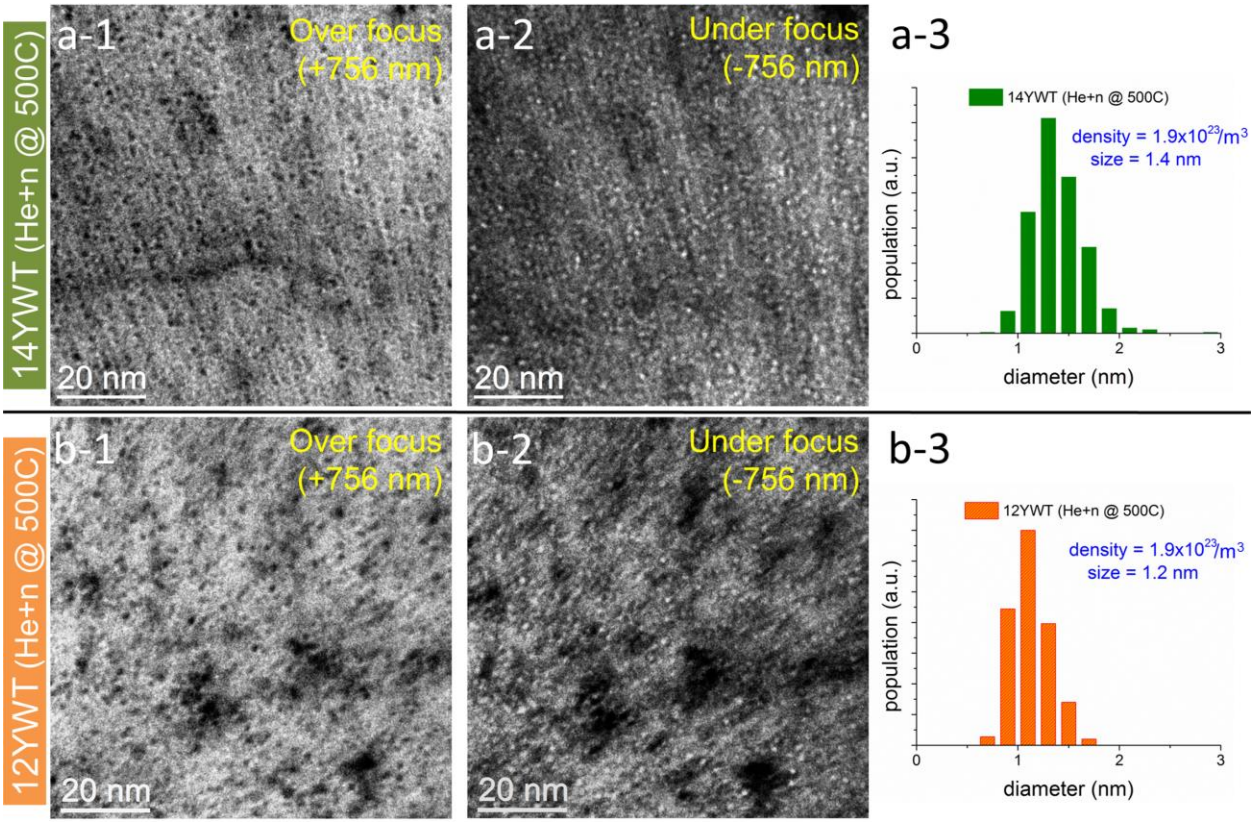

Figure 3. Two sets of BFTEM images at over-focus (denoted as 1 at right) and under-focus (denoted as 2 at left) of the He/neutron-injected side of 14YWT (a) and 12YWT (b) with summary histograms of He bubbles in matrix. Please note that He bubble densities of 14YWT and 12YWT are similar at 1.9×10^{23} m^{-3} and average He bubble size of 12YWT is slightly smaller than 14YWT by ~0.2 nm, as confirmed by the histogram peak positions.

Second, we examined small He bubbles in the matrix of the He-implanted sides as can be seen in Fig. 3. A notable observation is that the matrix of both 14YWT and 12YWT contain only very small He bubbles (d < 2 nm) without any larger voids unlike 14YW and F82H-mod.3 [10]. From a direct comparison of 14YW with 14YWT and 12YWT under the same irradiation environment, it can be deduced that Ti has an important role in keeping He dispersed into small bubbles via refinement of the oxide particles that serve as effective traps for helium. He bubble densities of both 14YWT and 12YWT are the same at 1.9×10^{23} m^{-3}, but the average He bubble size in the 12YWT is slightly smaller than that of 14YWT (1.2 nm versus 1.4 nm, respectively). It is unclear if the chemical changes in the matrix have any direct, measureable effect on the helium distribution.

In order to identify the particle type (or composition) and explore chemical evolution during irradiation, STEM-EDS elemental maps of Fe, Cr, C, W, Y, T, and O with a comparable set of BF/HAADF STEM images at various magnifications were taken, the results are presented in Figs. 4 & 5. In the case of He/neutron-irradiated 14YWT, Fig. 4-a presents an overview of large particle (50~200 nm) distributed predominantly on grain boundaries; these are Ti-rich particles. While only a few large particles (50~200 nm) are observed inside grains, an unusual Cr-Ti-rich particle is found. At low magnification, Y-rich particles are not clearly detected, and W is distributed evenly throughout the matrix without significant segregation. Interestingly, an intermediate magnification of elemental mapping in Fig. 4b displays distinctive Cr-segregation along a grain boundary passing through a large Ti-rich particle and obvious phase separation of α (Fe-rich) and α' (Cr-rich). Observed Y-O particles and Cr-rich phases tend to segregate to Ti-rich particles located at grain boundaries. Preferential chemical binding of Cr-C and Y-O is observed, while W is independently distributed.

In case of neutron-irradiated 12YWT, Fig. 5a and 5b at low and intermediated magnification maps show Y-Ti-O particles, elongated Cr-rich phases (probably chromium carbide) and phase separation of α (Fe-rich) and α' (Cr-rich) with spherical morphologies. A higher magnification map in Fig. 5c shows that Y-Ti-O particles are attached to Cr-rich phases, suggesting a tendency for Cr segregation toward these particles. W is distributed uniformly as in the case of 14YWT regardless of other present in 12YWT. Y-Ti-O particles are observed in the EDS maps ranging roughly in size from 5~70 nm. Fine Y-rich particles (< 5 nm) should be clearly observed in a much thinner TEM sample (10~20 nm thick) in STEM-EDS/EELS mapping and high-resolution S/TEM images to investigate the role of Ti.

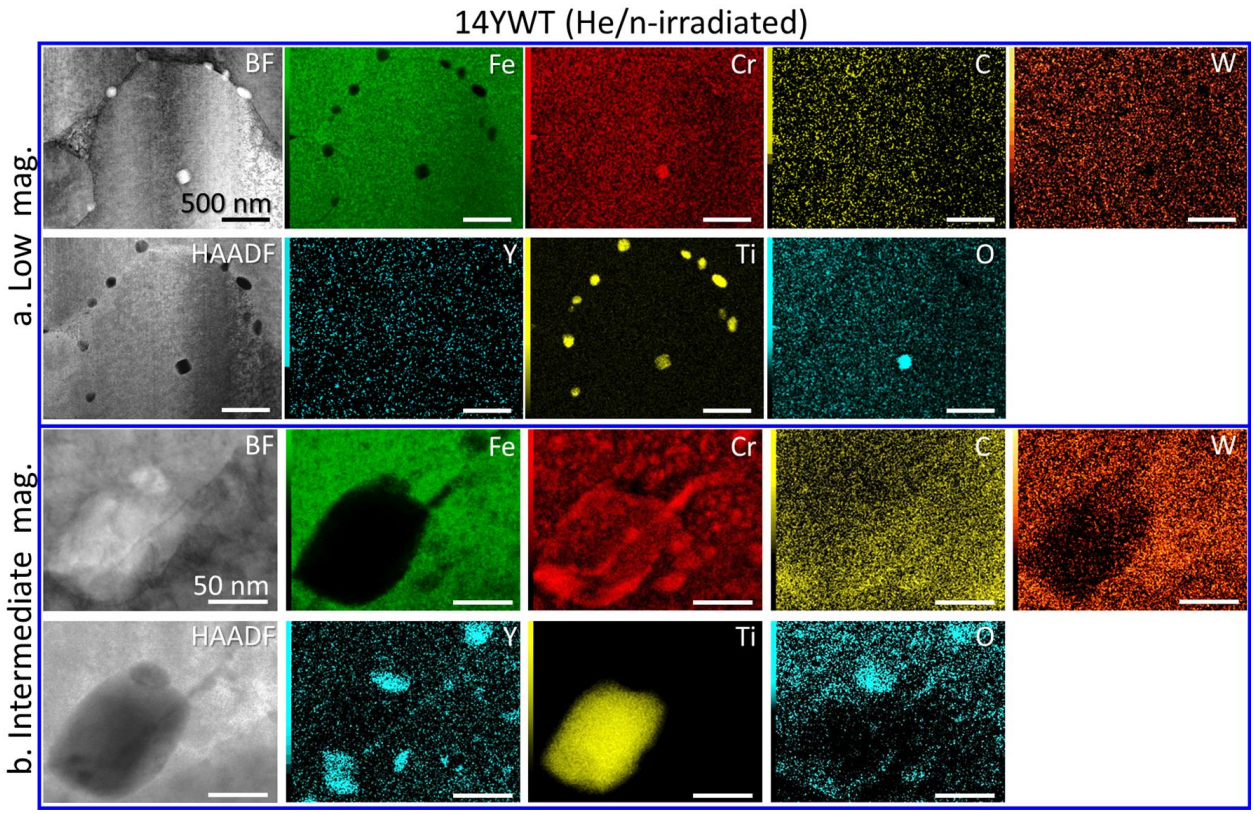

Figure 4. STEM-EDS maps of He/neutron-irradiated 14YWT at 500 °C at low (a) and intermediate (b) magnifications composed of BF and HAADF STEM images and elemental maps of Fe, Cr, C, W, Y, T, and O. (a) Low magnification map shows Ti-rich particles dominantly are located at grain boundaries, and unusual Cr-Ti segregation. Low magnification does not have enough resolution to show small Y-rich particles. (b) Intermediate magnification shows Cr-segregation along a grain boundary crossing a large Ti-rich particle (yellow) and also clear phase separation of α (Fe-rich) and α' (Cr-rich). Y-O particles and Cr-rich phases tend to segregate to the Ti-rich particles. Preferential chemical associations of Cr-C and Y-O are observed, while W is uniformly distributed. Please note that Y-Ti-O nano-oxide particles are not directly observed in this 14YWT, however it has very small He bubble (d_{ave}=~1.4 nm) with a density of 1.9×10^{23} m^{-3} similar to 12YWT. Care must be taken in interpreting the oxygen map because of overlap between the O K_α peak overlapping with the Cr L_α peaks.

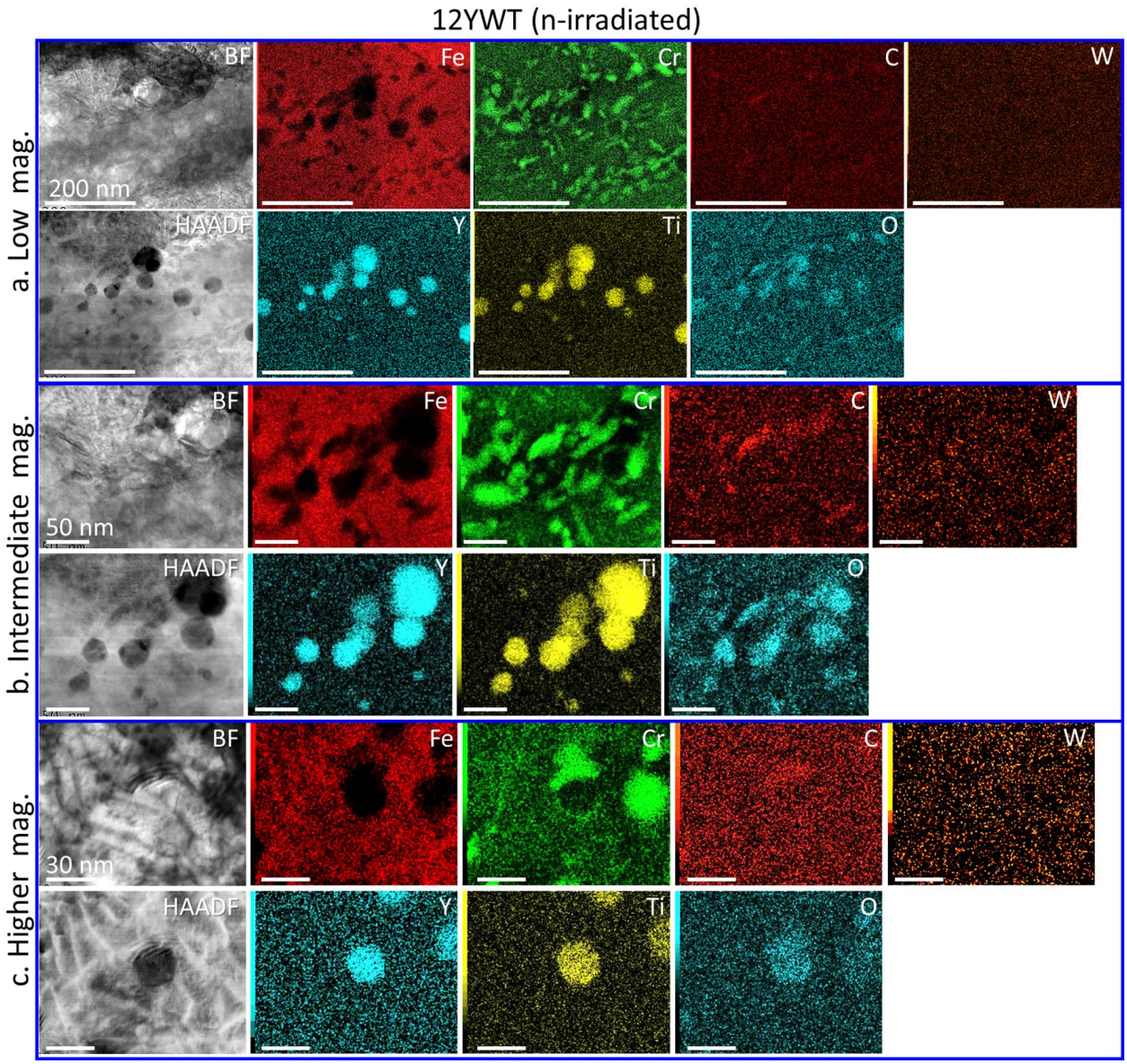

Figure 5. STEM-EDS maps of neutron-irradiated 12YWT at 500 °C at low (a), intermediate (b) and higher (c) magnifications composed of BF and HAADF STEM images and elemental maps of Fe, Cr, C, W, Y, T, and O. Low and intermediated magnification maps (a and b) show Y-Ti-O particles unlike 14YWT and clear elongated Cr-rich phases (probably Chromium carbide) and phase separation of α(Fe-rich) and α' (Cr-rich) with spherical shape. Higher magnification map (c) displays Y-Ti-O particles are attached to Cr-rich phases, inferring that Cr preferentially segregates to these particles, more precisely Y-rich particles considering the 14YWT case. W is uniformly distributed.

Acknowledgements

This research was supported by the U. S. Department of Energy, Office of Fusion Energy Sciences, under contract DE-AC06-76RLO1830. A portion of the research was performed using EMSL, a national scientific user facility sponsored by the DOE's Office of Biological and Environmental Research and located at PNNL.

References

[1] G.R. Odette, M.J. Alinger, and B.D. Wirth, Annu. Rev. Mater. Res. 38 (2008) 471.
[2] R.J. Kurtz, A. Alamo, E. Lucon, Q. Huang, S. Jitsukawa, A. Kimura, R.L. Klueh, G.R. Odette, C. Petersen, M.A. Sokolov, P. Spätig, J.W. Rensman, J. Nucl. Mater. 386-388 (2009) 411.
[3] N. Baluc, K. Abe, J.L. Boutard, V.M. Chernov, E. Diegele, S. Jitsukawa, A. Kimura, R.L. Klueh, A. Kohyama, R.J. Kurtz, R. Lässer, H. Matsui, A. MÖslang, T. Muroga, G.R. Odette, M.Q. Tran, B. van der Schaaf, Y. Wu, J. Yu, and S.J. Zinkle, Nucl. Fusion 47 (2007) S696.
[4] H. Ullmaier, Nuclear Fusion. 24 (1984) 1039.
[5] R.E. Stoller, G.R. Odette, J. Nucl. Mater. 131 (1985) 118.
[6] R. Schäeublin, Y.L. Chiu, J. Nucl. Mater. 362 (2007) 152.
[7] B. Yao, D. J. Edwards, R. J. Kurtz, G. R. Odette, and T. Yamamoto, Fusion Reactor Materials Program 51 (2011), 85.
[8] B. Yao, D. J. Edwards, R. J. Kurtz, G. R. Odette, and T. Yamamoto, J. Electron Microsc. 61(6) (2012) 393.
[9] B. Yao, D. J. Edwards, and R. J. Kurtz, J. Nucl. Mater. 434 (2012) 402.
[10] H.J. Jung, D. J. Edwards, B. Yao, R. J. Kurtz, G. R. Odette, T. Yamamoto , Fusion Reactor Materials Program 56 (2014) 19.

2.3 IRRADIATION-DAMAGE BEHAVIOR IN ADVANCED STEELS - C. M. Parish, Y. Katoh (Oak Ridge National Laboratory) and S. Kondo (Kyoto University, Japan)

OBJECTIVE

Determine the irradiation response of the newly developed 9Cr-based ODS/NFA (oxide dispersion strengthened / nanostructured ferritic alloy) steels and compare to F82H.

SUMMARY

A 650°C heavy-ion irradiation was performed on 9YWTV, a new 9Cr NFA. This was compared to F82H as a baseline material. Advanced TEM (transmission electron microscopy)-based methods were used to characterize the irradiated zone, and compare to the unirradiated base material. Broadly speaking, little residual radiation damage in the form of black spots or dislocation loops was observed in either the 9YWTV or F82H material, even at areas of the highest dose (>100 dpa). This is likely a result of the high irradiation temperature causing rapid annealing of the irradiation-induced damage. Elemental mapping using EDS (X-ray energy dispersive spectroscopy) or EFTEM (energy filtered TEM) showed evolution of the fine-scale precipitates.

PROGRESS AND STATUS

Introduction

As a screening experiment to begin understanding 9Cr NFA irradiation effects, a high-dose 650°C irradiation was performed at the Kyoto University DuET facility. Both 9YWTV NFA and F82H RAFM alloy were irradiated. Advanced characterization was used with the intent of analyzing the changes to the microstructure driven by the irradiation, and using the unirradiated material below the ion range as an internal control specimen for comparison of irradiated and unirradiated microstructures. This is intended to begin providing microstructural insight to the irradiation-driven mechanisms that will dominate for fission irradiation tests and possible eventual fusion service.

Experimental Procedure

9YWTV-PM1 material [1] (Fe–9Cr–2W–0.4Ti–0.2V–0.12C–0.3Y_2O_3) and F82H material were subjected to heavy-ion irradiation (6.4 MeV Fe, 1.5×10^{21} ions/m^2, ~150 dpa peak, ~2 μm range) at 650°C, using the DuET facility at Kyoto University. Calculations for dpa used Stoller's method [2]. Scanning TEM (STEM) based methods, particularly imaging and high-efficiency EDS mapping, were performed at the North Carolina State University Analytical Instrumentation Facility (NCSU AIF) using the probe-corrected FEI Titan G2 with ChemiSTEM instrument operated at 200 keV. Analysis of the EDS spectrum images (SIs) used the Sandia National Laboratory AXSIA computer code [3].

Results

Interestingly, low-angle annular dark field (LAADF) imaging in aberration-corrected STEM provides excellent diffraction contrast and well complements the standard bright field (BF) and high-angle annular dark field (HAADF) images. Although significant defect densities (dislocations, small spots) are observed, no gross differences are present between the irradiated and unirradiated regions; Figure 1 illustrates that although defects are visible in BF mode (i.e., red arrows), higher contrast on many of the defects (such as grain boundaries) are present in LAADF mode than in either BF or HAADF. High densities of defects are present in both the irradiated and unirradiated regions (blue and green arrows), indicative of little residual damage in the forms commonly observed at lower irradiation temperatures. (The ultrafine grain sizes

prevent tilting to clear diffraction conditions, so conventional two-beam TEM of defect strain centers is not feasible.) Precipitates, particularly in the F82H, are most easily seen in LAADF mode.

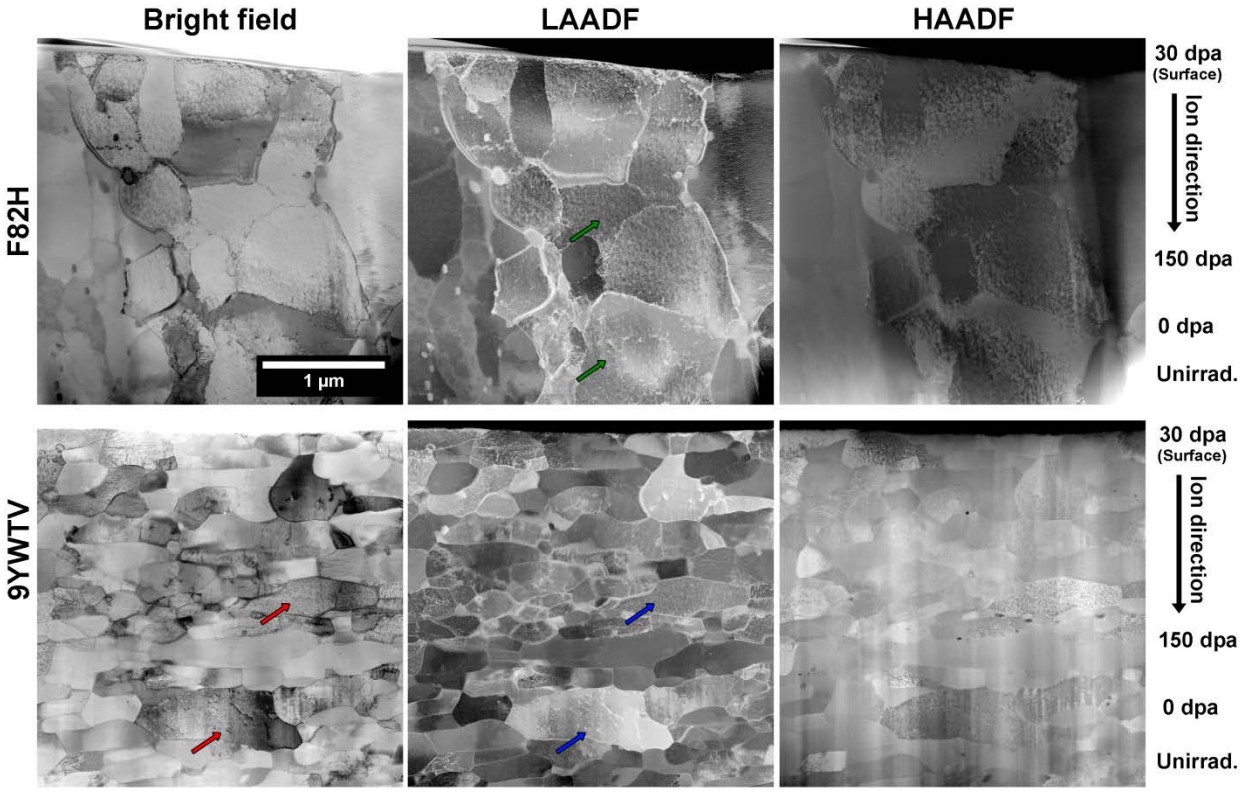

Figure 1. STEM imaging of 650°C, 150 dpa ion-irradiated F82H and 9YWTV. LAADF, low-angle annular dark field. HAADF, high-angle annular dark field.

High-efficiency X-ray mapping indicated multiple populations of precipitates in both alloys; Figure 2 (low magnification, mapping the entire depth of the bombarding particle [4]) where no appreciable differences are visible between the irradiated (shallow) and unirradiated (deep) regions in terms of precipitates present. Additionally, no radiation-induced segregation (RIS) was observed, Figure 3, which is unsurprising at 650°C but experimental confirmation provides greater confidence in material robustness at this temperature.

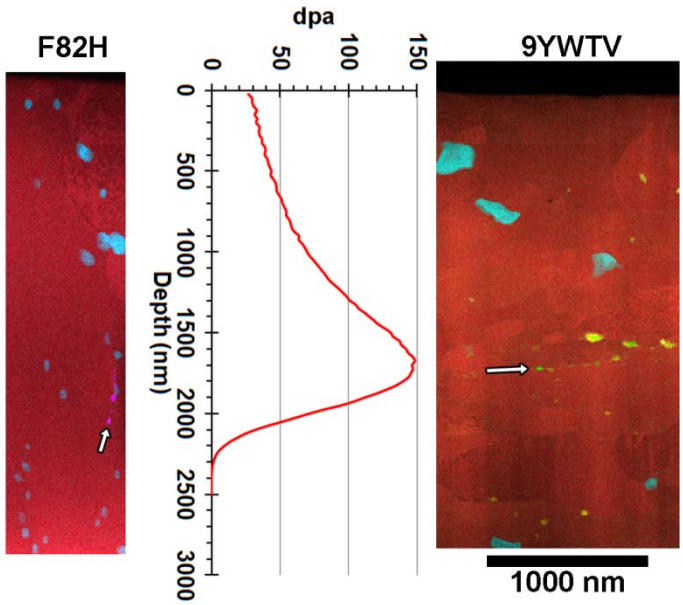

Figure 2. Multivariate statistical analysis (MVSA) decompositions of X-ray spectrum images 650°C-irradiated specimens. Chart shows SRIM-calculated dpa. Colors indicate the identity of the precipitates. Both specimens: red, Fe-Cr matrix; cyan, Cr-W-carbides. F82H only: magenta (arrowed) V-Ta-carbides. 9YWTV only: Yellow, Ti-Cr-carbides; green: Al-Ti-oxides (arrowed).

Higher magnification maps of F82H (Figure 3, depth ~1000 nm, ~50 dpa) shows no measurable radiation induced segregation (albeit along an inclined boundary, but inclined boundaries in NFA 14YWT with appreciable processing-induced segregation have been measured using the technique [5]).

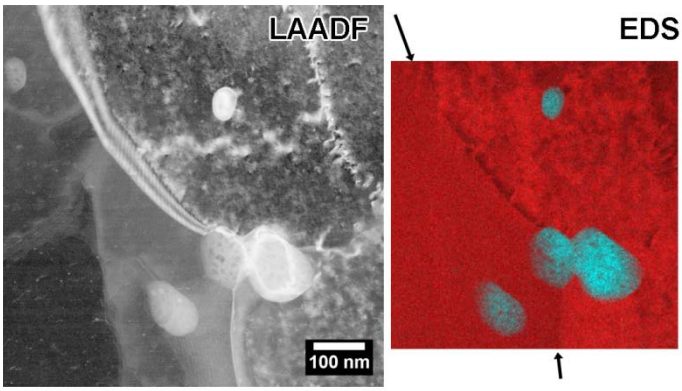

Figure 3. Low-angle annular dark field (LAADF) STEM image and multivariate statistical analysis decomposition of the EDS spectrum image. Red is the Fe-Cr matrix and cyan the Cr-W(-V) rich carbides. Arrows denote a grain boundary; no statistically significant RIS was detected. 650°C, ~50 dpa.

In the 9YWTV NFA material, irradiation was observed to result in a coarser population of the Ti-Y nanoclusters (NCs) that are believed to provide NFAs high creep and irradiation resistance.

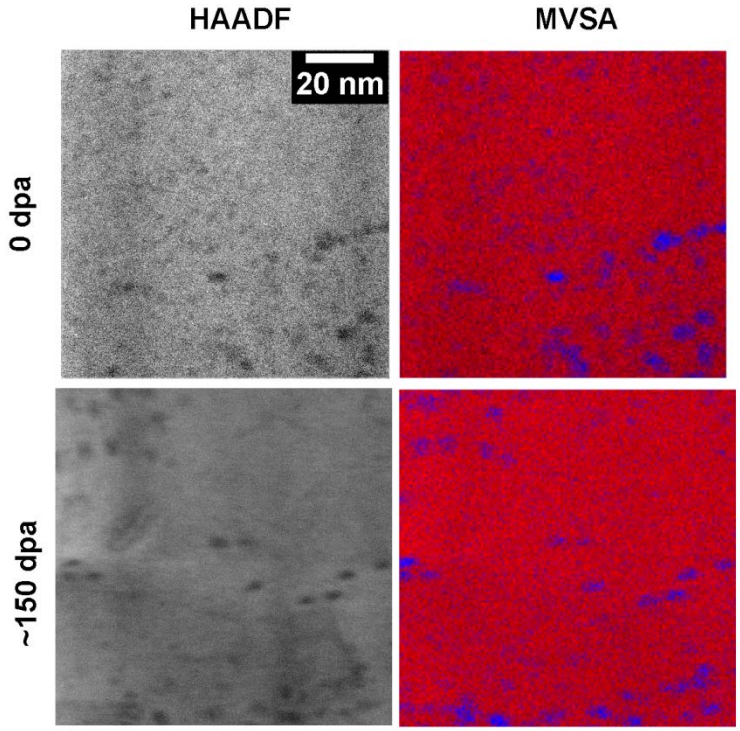

Figure 4. 9YWTV NFA irradiated at 650°C. High-angle annular dark field (HAADF) STEM shows finer precipiates in the unirradiated region than in the irradiated. MVSA decompositions (red: Fe-Cr-W matrix, blue: Y-Ti-O nanoclusters) shows the precipitates visible in HAADF are the nanoclusters.

The lack of large RIS in either material is mostly attributable to the high temperature (650°C). The carbides in the F82H showed damage, however, at higher dose regions (visible in Figure 3, but more clearly in Figure 5) in which the carbides were appearing to fracture or fragment; in unirradiated or lightly-irradiated (deep) areas, this was not observed (Figure 6). This could indicate, at least at this temperature and at the rather high dose rates used in ion irradiation, that the carbides are slowly damaged by the irradiation. (More statistics are needed, however, before this observation can be conclusive.) The NCs in the NFA (Figure 4 above), conversely, although coarsening slightly, maintain their identity (at least to the resolution of STEM-EDS of particles embedded in a matrix foil). This may indicate the NFA will be more stable against high-temperature irradiation at high dose levels.

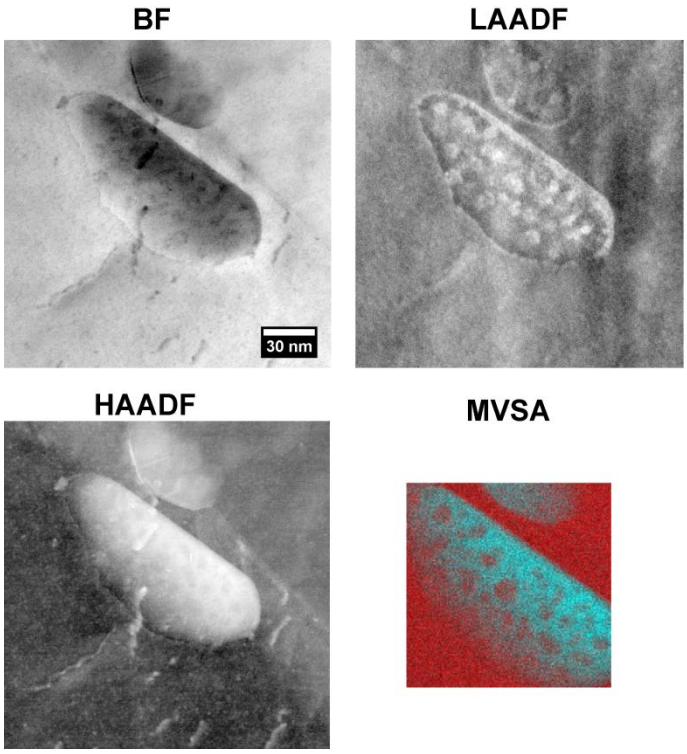

Figure 5. STEM images and MVSA decomposition of EDS data for carbides in F82H. Depth ~700 nm, dose ~50 dpa, 650°C. The carbides appear to be breaking up of fragmenting. MVSA: Red, Fe-Cr matrix, cyan, Cr-W-V(-Ta) carbide.

These results imply good microstructural stability of F82H, and very good stability of 9YWTV, to high-dose heavy-ion irradiation at 650°C. They also illustrate the importance of using the latest generation of analytical electron microscope in order to fully characterize the microstructure. Short-term follow-on work will involve helium+heavy ion irradiations to begin measuring the helium mitigation effects in 9YWTV, and future work involving neutron irradiation may be promising.

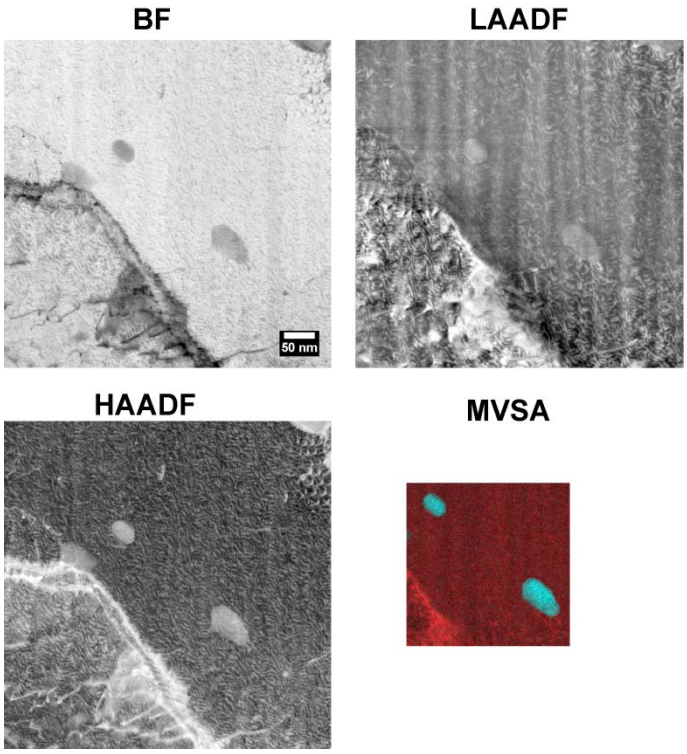

Figure 6. STEM images and MVSA decomposition of EDS data for carbides in F82H. Depth ~2300 nm, dose 0~10 dpa, 650°C. The carbides appear not to be breaking up of fragmenting. MVSA: Red, Fe-Cr matrix, cyan, Cr-W-V(-Ta) carbide.

Acknowledgements

9YWTV material provided by Dr. T. S. Byun. NCSU Titan TEM: We acknowledge the use of the Analytical Instrumentation Facility (AIF) at North Carolina State University, which is supported by the State of North Carolina and the National Science Foundation.

References

[1] T.S. Byun, J.H. Yoon, D.T. Hoelzer, Y.B. Lee, S.H. Kang, S.A. Maloy, Process development for 9Cr nanostructured ferritic alloy (NFA) with high fracture toughness, Journal of Nuclear Materials, 449 (2014) 290-299.

[2] R.E. Stoller, M.B. Toloczko, G.S. Was, A.G. Certain, S. Dwaraknath, F.A. Garner, On the use of SRIM for computing radiation damage exposure, Nuclear Instruments & Methods in Physics Research Section B-Beam Interactions with Materials and Atoms, 310 (2013) 75-80.

[3] P.G. Kotula, M.R. Keenan, J.R. Michael, Automated analysis of SEM X-ray spectral images: a powerful new microanalysis tool, Microscopy and Microanalysis, 9 (2003) 1-17.

[4] C.M. Parish, R.M. White, J.M. LeBeau, M.K. Miller, Response of nanostructured ferritic alloys to high-dose heavy ion irradiation, Journal of Nuclear Materials, 445 (2014) 251-260.

[5] C.M. Parish, M.K. Miller, Aberration-Corrected X-Ray Spectrum Imaging and Fresnel Contrast to Differentiate Nanoclusters and Cavities in Helium-Irradiated Alloy 14YWT, Microscopy and Microanalysis, 20 (2014) 613-626.

2.4 EFFECTS OF SUBSTRATE ETCHING ON Fe - {110} $Y_2Ti_2O_7$ INTERFACES; IMPLICATIONS FOR NANOSTRUCTURED FERRITIC ALLOYS - T. Stan, Y. Wu, S. Kraemer, and G.R. Odette (University of California Santa Barbara)

OBJECTIVE

The objective of this work is to create surrogate bulk Fe – $Y_2Ti_2O_7$ interfaces, with similar characteristics to those found in Nanostructured Ferritic Alloys, which are amenable to conventional characterization techniques and irradiation experiments.

SUMMARY

Nanostructured Ferritic Alloys (NFAs) have a Fe-Cr matrix and are dispersion strengthened by <5 nm Y-Ti-O phases. The interfaces between these Y-Ti-O nanofeatures (NFs), such as $Y_2Ti_2O_7$ (YTO), and the surrounding matrix provide many favorable properties pertinent to fusion environments, such as trapping He in fine scale bubbles. As a supplement to current characterization efforts of the NFs themselves, surrogate bulk Fe-YTO interfaces have been fabricated by electron beam Fe deposition onto un-etched and etched {110}YTO substrates. The observed Fe-{110}YTO orientation relationships (ORs) and interface characteristics are reported. Etching the substrate prior to Fe deposition has yielded interface structures and ORs that are believed to be similar to those found in embedded NFs. These bulk samples are more amenable to conventional characterization techniques and irradiation experiments. The results also support the development of computational models to predict NFA behavior.

PROGRESS AND STATUS

Introduction

The smallest <5 nm features in Nanostructured Ferritic Alloys (NFAs) are composed of the $Y_2Ti_2O_7$ (YTO) complex oxide, fcc pyrochlore phase. The interface between the bcc Fe-Cr matrix and the fcc YTO plays a critical role in the stability, strength and damage tolerance of NFAs [1,2]. In particular, NFAs may turn He from a liability to an asset. For example, He bubbles at Fe-YTO interfaces act as recombination sites for vacancies and interstitials, thus promoting self-healing. The high density of matrix-NF interface traps prevent He from gathering at grain boundaries which would otherwise degrade creep and fracture properties as well as preventing the nucleation of voids.

There is ongoing research to determine NF compositions, structures, and matrix-NF orientation relationships (ORs). A summary of these studies and other NFA properties was recently published by Odette [1]. Determination of the matrix-YTO orientation relationship (ORs) is of interest because they affect characteristics like misfit strains and interface energies, as well as the critical functional properties of NFs. Cube-on-cube[3] and edge-on-cube[4] bulk ORs have been reported for embedded NFs. For example, Dawson et al.[3] observed the following interfacial OR for embedded NFs: $\{110\}_{Fe}||\{110\}_{YTO}$ and $<100>_{Fe}||<100>_{YTO}$. Ciston et al.[4] observed the following interfacial OR for an annealed NF: $\{100\}_{Fe}||\{110\}_{YTO}$ and $<100>_{Fe}||<100>_{YTO}$. These ORs both have {110}YTO planes matching with {110}Fe and {100}Fe, respectively. Other ORs were also observed [3-5].

The experimental approach in this study is to deposit Fe on oriented {110}YTO single crystal substrates to create surrogate mesoscopic-scale interfaces. We recognize that these bilayers may not have the same interfacial characteristics as those found for embedded NFs. A similar characterization of Fe-{111}YTO interfaces was published by T. Stan [6] and some preliminary results from of this Fe-{110}YTO study were mentioned in a previous fusion semiannual report [7]. Even if the mesoscopic interfaces are not the same as the embedded ones, the study will further the general understanding of metal-oxide interfaces. These surrogate interfaces will also be more amenable to irradiation studies such as interactions with point defects and He. Characterization and analysis of Fe-YTO interfaces will help develop and improve current first principles and atomic interface models, and help predict NFA performance in fusion reactor conditions.

Experimental Procedure

The details of how samples were fabricated and what instruments were used for characterization are covered in a previous publication [6]. In summary, a two pure YTO single crystals were {110} oriented and a 2 mm thick wafer was cut using a wire saw. An Allied Multiprep instrument was used to polish the wafers using a sequence of diamond lapping films, followed by a final 15 minute polishing step using a 0.02 μm non-crystallizing silica suspension. One wafer was etched with Aqua Regia for 5 minutes, then annealed in air for 1 hour at 800 °C. The other wafer remained un-etched and un-annealed. An electron beam system was used to deposit Fe on the {110}YTO crystals at $6.2x10^{-6}$ torr and 800 °C. The deposition rate was 8 nm/s for 250 s, producing Fe layer thicknesses of ≈ 2 μm. The samples were then cooled to room temperature at a rate of ≈ 0.16°C/s.

Results

Fe on Un-etched {110}YTO

Scanning Electron Microscope (SEM) and Electron Backscatter Diffraction (EBSD) results for Fe on un-etched {110}YTO were previously reported [7]. In summary, three Fe grain orientations were found. A flat area with a rippled surface was {110}Fe textured. Both pointed and sharp {112}Fe grains were also observed. Neither of these types of grains had an OR with the {110}YTO substrate that is found in embedded NFs. A single large 10 μm grain was found which had the $\{100\}_{Fe}||\{100\}_{YTO}$ and $<100>_{Fe}||<100>_{YTO}$ OR, same as reported for some embedded NFs [6]. This grain is of interest and has been further analyzed.

Scanning Transmission Electron Microscopy (STEM) was carried out on a Focused Ion Beam (FIB) lift-out cross section of the 10 μm grain to observe the interface. The scan is shown in the middle of Figure 1. The orange and blue/white sketches indicate the Fe and YTO orientations, respectively. The black and white STEM image shows the Fe layer in light gray at the top, and the YTO substrate at the bottom. Fe strain in the first deposited layers and/or a thin metallic oxide interlayer is visible in the dark area at the interface (marked with a red bracket). CrystalMaker was used to recreate the interface by matching the oriented Fe and YTO lattices. The results are shown in the right side of Figure 1. Fe, Ti, Y, and O are represented as orange, blue, green and red spheres, respectively. The light blue and dark green circles indicate Ti and Y atomic columns which run through the page, respectively. The purple circles indicate columns of mixed Y and Ti. The contrast in the STEM image allows for column identification, where the brighter substrate spots are indicative of Y columns, the darker spots are Ti columns, and the medium intensity spots are indicative of mixed Y and Ti columns. Note that STEM cannot detect O and thus the YTO chemistry at the interface is not clear.

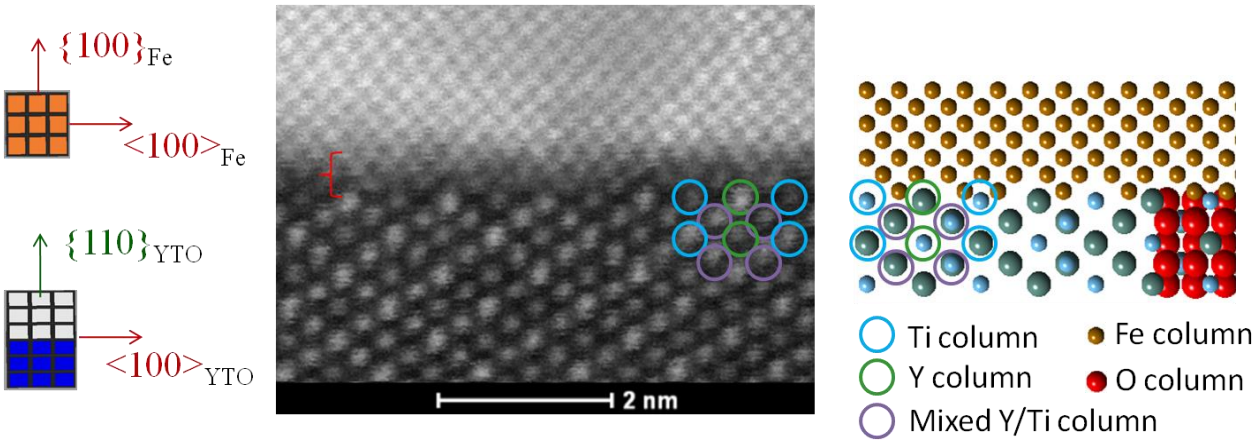

Figure 1. STEM image from the large {100}Fe grain observed on the un-etched {110}YTO substrate. A sketch of the Fe and YTO orientations are shown on the left. A CrystalMaker rendering of the interface is shown on the right.

Fe on Etched {110}YTO

A second {110}YTO substrate was etched with Aqua Regia for five minutes, then annealed for one hour in air at 800 ºC prior to Fe deposition. The EBSD map and associated legend are shown in Figure 2. The Fe film has two types of morphologies. The ~1 micron grains on the left have strong {100}Fe texturing and are shown in red. Pole figures (not shown) indicate that this film has one of the same ORs found in embedded NFs. The right side of the sample shows a polycrystalline film with many grain orientations such as {111}Fe shown in blue and {112}Fe shown in purple. The grains on the right are 1 – 5 microns in size, slightly larger than those on the left. Pole figures from this film (not shown) indicate that the grains have an axiotaxial OR with the substrate. The {100}YTO substrate planes (which are not normal to the sample surface) are parallel to the {100}Fe planes (not normal to the interface plane). These results are relevant since the observed axiotaxial OR for these grains was also reported observed for embedded NFs [4]. Clearly, etching the substrate led to Fe-YTO ORs that are observed in NFAs.

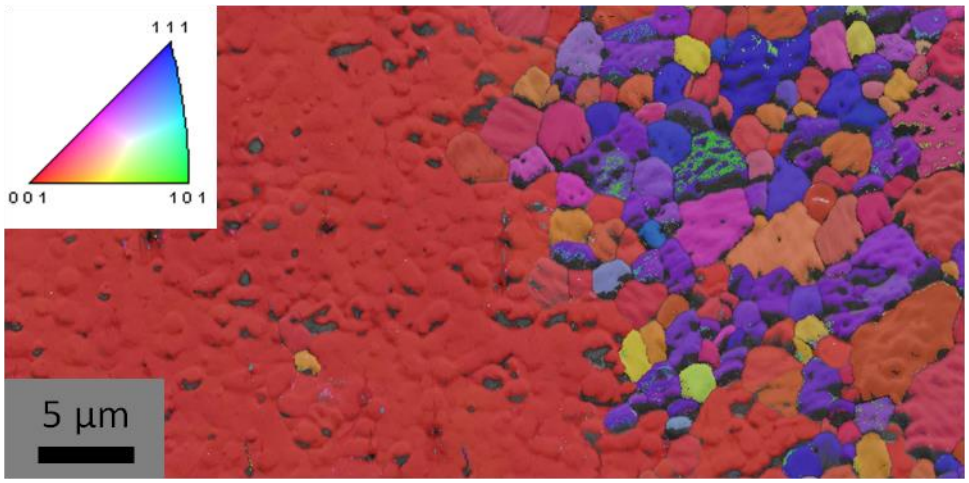

Figure 2. EBSD map of Fe film on etched {110}YTO substrate. The left side of the sample has a continuous {100}Fe oriented film. The right side has a polycrystalline layer with many orientations.

Discussion and Conclusions

Fe deposition on un-etched {110}YTO substrates yielded flat {110}Fe areas with a rippled surfaces, and pointed {112}Fe grains. There was a single 10 micron {100}Fe grain with an OR reported in embedded NFs. Fe deposition on etched {110}YTO led to two types of films. The continuous film on the left side of the sample was {100}Fe textured and had the same OR as the 10 micron grain in the un-etched sample. The polycrystalline side had many Fe orientations including {111}Fe and {112}Fe which are in fact axiotaxially oriented with the substrate to have a different OR found in embedded NFs. Clearly, etching the substrate yielded ORs reported for NFAs.

First principles calculations by Y. Jiang et al.[8] suggest that the deposition conditions used in this experiment should yield O-rich YTO terminations which would promote the growth of an oxidized surface. This was previously shown with depositions on {111}YTO [6] and expected for depositions on the unetched {110}YTO surface used in this experiment. Preliminary TEM and STEM show that the Fe-YTO interface may have strain in the Fe layer and/or a metallic oxide interlayer. These interfaces are still being analyzed.

Future studies include Fe depositions on {110}YTO in a system capable of ultra high vacuum conditions and Reflective High Energy Electron Diffraction (RHEED) monitoring. If the cleaner deposition conditions yield cleaner interfaces, then the work will be extended to Fe depositions on {100}YTO and {111}YTO.

These samples are being prepared for eventual He implantation and dual-beam irradiation studies. The results will help inform first principle models of metallic oxide interfaces, as well as reaction-rate theory models for predicting NFA behavior.

References

[1] G.R. Odette, J. Of Mater., 66, 12, (2014) 2427
[2] G.R. Odette, M.J. Alinger, B.D. Wirth, Annu. Rev. Matter. Res. 38 (2008) 471
[3] K. Dawson, G.J. Tatlock, J. Nuc. Mat. 444 (2014) 252
[4] J. Ciston, Y. Wu, G.R. Odette, et al., Fus. Mat. Semiann. Prog. Rep. (2012) DOE-ER-0313/51
[5] J. Ribis, Y. de Carlan, Acta Mat. 60 (2012) 238
[6] T. Stan, Y. Wu, G.R. Odette. et al., Metal. and Mater. Trans. A, 44, 10 (2013) 4505
[7] T.Stan, Y. Wu, G.R. Odette, Fus. Semiann. 56 (2013) DOE-ER-0313/56
[8] L. Yang, Y. Jiang, G.R. Odette, et al. , Acta Mater. 61 (2013) 7260

2.5 TENSILE PROPERTY CHARACTERIZATION OF 14YWT NANOSTRUCTURED FERRITIC ALLOY NFA1 -

M.E. Alam, K. Fields, G. R. Odette (UCSB), D. T. Hoelzer (ORNL) and S. A. Maloy (LANL)

OBJECTIVES

The main objective of this study is to characterize the high temperature tensile property of a newly developed larger best practice heat of 14YWT nanostructured ferritic alloy, NFA1, indifferent orientations.

SUMMARY

FCRD NFA-1 is a best practice nanostructured ferritic alloy (NFA) produced by ball milling argon atomized Fe-14Cr-3W-0.4Ti-0.2Y (wt.%) and FeO powders, followed by consolidation, extrusion, annealing and cross-rolling. Tensile tests in six orientations at temperatures 23 to 800°C exhibited excellent strength in the extrusion and cross-rolled directions (LT and TL), accompanied by total elongation of ~10%. In contrast, loading in the short plate thickness direction (S) at ambient temperature exhibited much lower strength with a flat, facet fractured surface, and total ductility of less than ~0.5%. The low strength and low total strain in the plate thickness direction can be attributed to the presence of pre-existing microcracks running parallel to the plate surfaces that propagate by brittle cleavage.

BACKGROUND

Background on NFA and further details on NFA-1 are reported elsewhere and will not be reviewed here [1,2].

EXPERIMENTAL

The as fabricated NFA-1 was characterized using a scanning electron microscope (SEM) equipped with energy dispersive spectroscopy (EDS) and electron backscatter diffraction (EBSD). Polished (down to 20 nm colloidal silica) surfaces were observed in a FEI X30 SEM (Netherland) to characterize the surface morphology before testing. EBSD was used to measure the crystallographic grain morphology with respect to extrusion and cross-rolling directions. Tensile tests were performed on SSJ-2 type dog-bone shaped and sub-sized flat specimens with a gage section length, width and thickness of 5.0x1.2x0.5 mm. The tests in air were performed for six orientations, namely LT, TL, LS, TS, SL and ST where L, T and S represent longitudinal (rolling), transverse (cross-rolling) and short thickness directions, respectively (see Fig.1). The tests were conducted at varying temperatures from ambient to 800°C, using a 810 MTS servo-hydraulic universal testing machine equipped with a clam shell furnace. All specimens were sanded down to 1500 grit to remove any surface contamination or residual stresses due to the EDM machining before testing. The specimens were heated to the target temperature in atmosphere environment, and held for 10 minutes before testing. Testing was carried out at a crosshead speed of 0.30 mm/min or a strain rate of $\approx 10^{-3}$/s. Except for the small size of the specimens, the tensile properties were determined in accordance with ASTM Standard E8M-13. Extensive SEM/EDS was carried out on the post-test fracture surfaces.

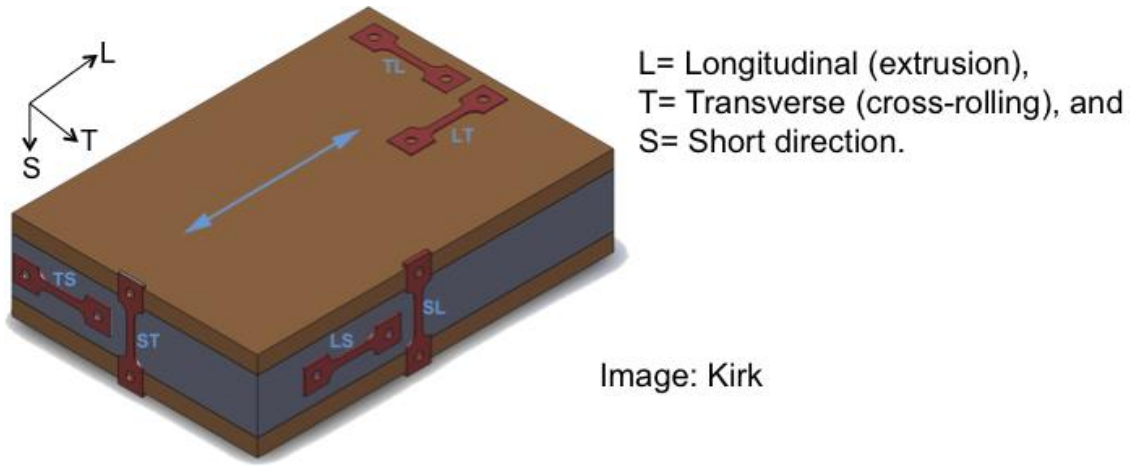

Figure 1. NFA1 specimen orientations labeled with respect to the extrusion, cross-rolling and plate thickness directions.

STATUS AND PROGRESS

Pre-Test Characterization

SEM micrographs on non-deformed polished and etched NFA-1 plate normal surfaces in Fig. 2a do not show any cracks or pores. In contrast, Figs. 2b and c show anisotropic banding in the thickness cross section plane oriented along cross-rolling (plane B) and extrusion (plane C) directions. EBSD used to characterize the grains imaged in all three planes. The inverse pole figure (IPF) maps in Fig. 3 highlight the existence of strong preferential crystallographic fiber texture, with most grains <110> oriented along the extrusion direction. Plane A showed the smallest average grain size of ≈ 235 ± 212 nm, with the lowest grain aspect ratio (GAR) of ≈ 1.7 ± 0.6. Fig. 3b shows the presence of surface cracks along the transverse direction. Most of the grains are extended along the transverse (cross-rolling) direction (Fig. 3b). Very large (2-5 micron) and elongated grains are often observed in the vicinity of the surface cracks. Plane C also reveals relatively larger 349 ± 247 nm grains with the highest GAR ≈ 3.3. Fig. 3c reveals that the elongated grains oriented along the extrusion directions are also often associated with surface cracks.

Tensile Properties

Room temperature tensile tests were conducted in six different orientations shown in Fig. 1. Examples of the results are shown in Fig. 4. The LT orientation showed the highest ambient temperature strength with a YS average of 1144 MPa 0.2% and UTS average of ≈ 1253 MPa, The corresponding ST oriented specimens showed the lowest average strength of ≈ 765 MPa and 832 MPa for the YS and UTS, respectively. The fracture surfaces in all six orientations are shown in Fig. 5. There is a similarity in properties and fracture patterns that fall three different categories: group 1 LT and TL orientations (group 1) with high strength and total strain; LS and TS (group 2) with the highest total strain; and SL and ST (group 3) with the lowest strength with negligible total strain and brittle fracture surfaces.

Delaminations occurred in the group 1 normal to the thickness direction in planes parallel to the plate surfaces.In group 2 delaminations form through the width direction along the gage length normal to the thickness direction, which is basically a 90^{o} rotation from group 1. Stress-strain curves in Fig. 4 show multiple-stage post necking load drops associated with a sequence of delaminations. The load drops are due to the corresponding to reductions in the necking constraint in the width direction. Difference between group 1 and 2 are related to the brittle orientation of the brittle planes with respect to the direction of necking reduction. The LT/TL oriented specimens neck in the thickness direction whether as LS/TS oriented specimens neck in width direction. Specimens loaded in the short directions (group 3) failed almost in a brittle manner, mostly in its elastic regime. In this case the weak planes and laminated layers are perpendicular to the loading direction and easily break during tensile loading at much lower stress compared to other orientations. The Fractured surfaces are quite flat, in this case, with almost

no/minimal area reduction. Group 2 specimens exhibited the highest uniform and total elongations. The LS orientation exhibits an average uniform elongation (UE) of ≈ 8.1% and a total elongation (TE) is as high as 21.8%. Group 1 specimens exhibited lower total strain with averages of ≈ 5.0 % UE and ≈ 10% TE. The higher strength of group 1 specimens comes at the expense of total strain, compared to group 2 specimens. In contrast, group 3 specimens exhibited both lower strength and total strain (≤ 0.5% UE and TE) compared to the other groups. Figure 6 shows higher magnification SEM images of fractured samples that revealed the extensive presence of ductile shear zones in group 1 and ductile dimples in group 2 in contrast to the cleavage brittle fracture features in group 3 specimens.

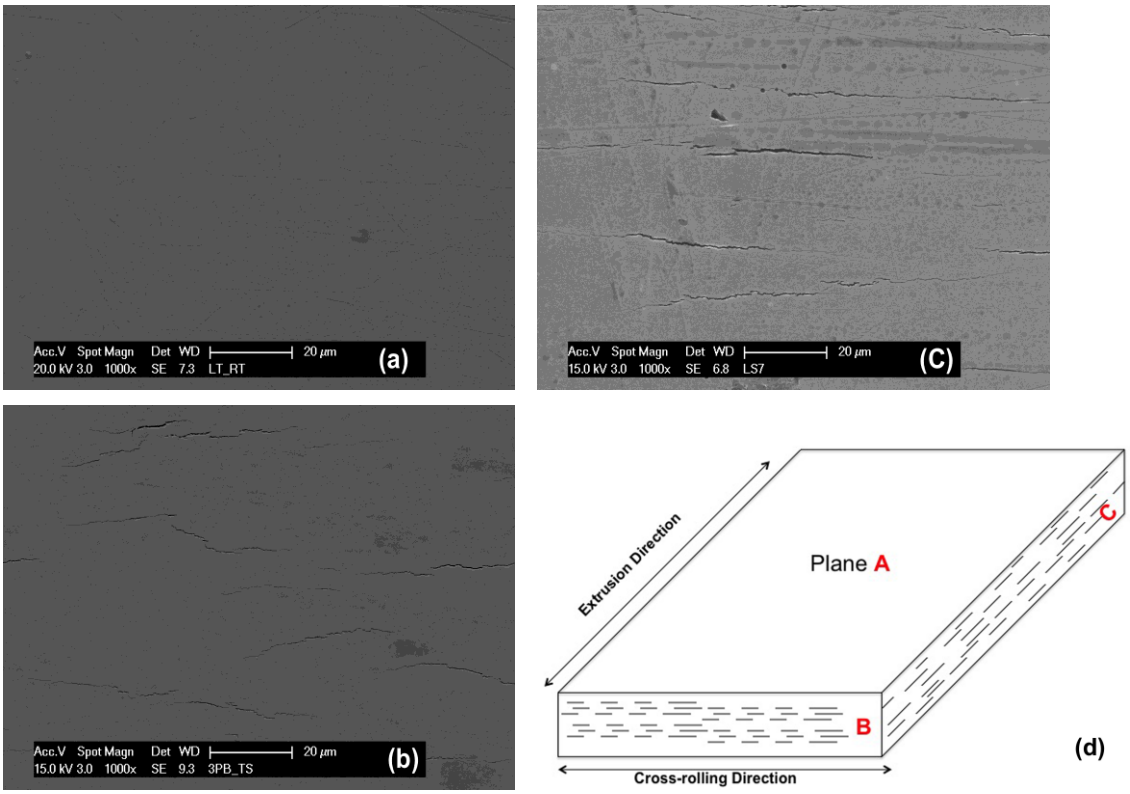

Figure 2. SEM images showing the non-deformed surface morphology of: (a) Plane A, (b) Plane B, and (c) Plane C of 2(d), respectively. 2(d): Schematics of delamination of NFA1.

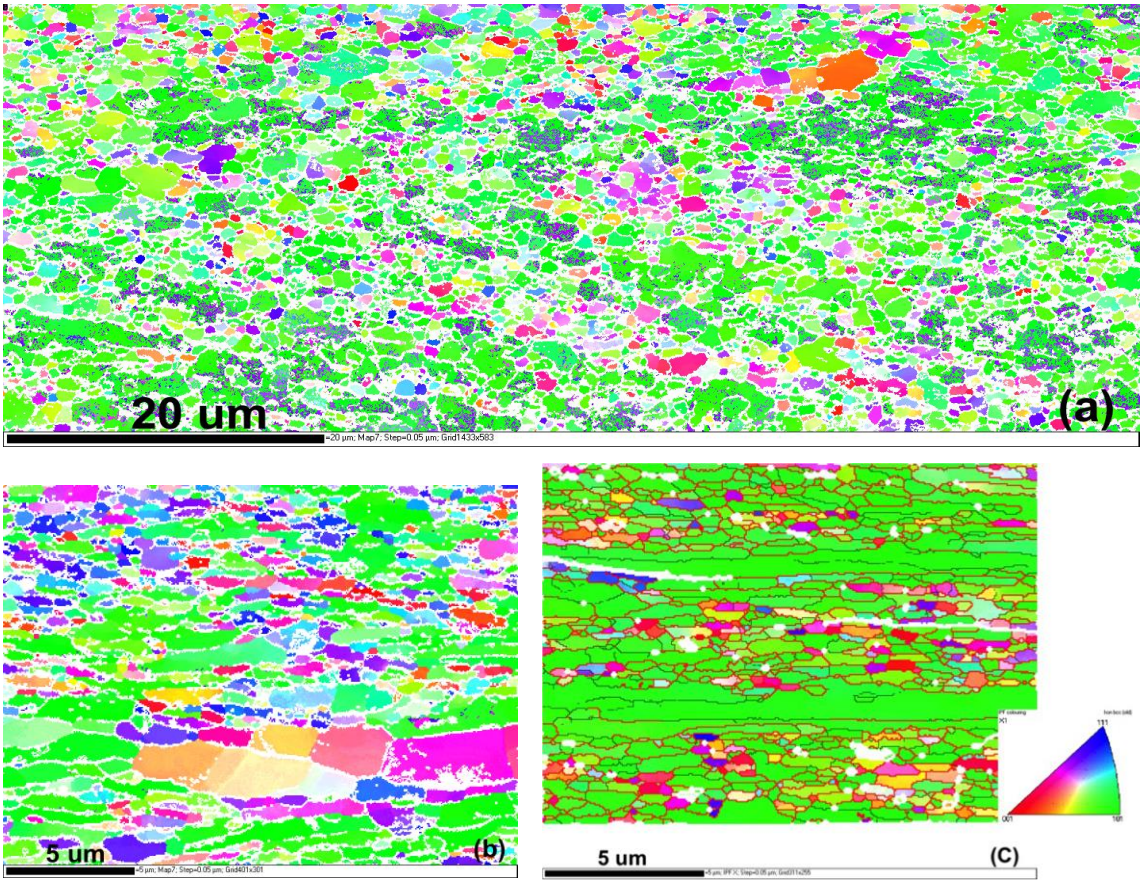

Figure 3. Inverse pole figure (IPF) maps obtained by EBSD on the: (a) Plane A, (b) Plane B, and (c) Plane C of 2(d), respectively.

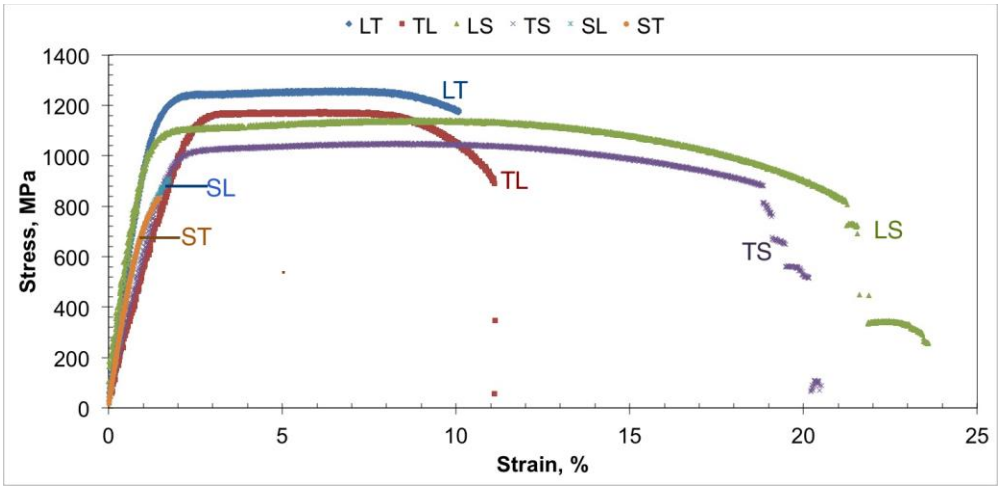

Figure 4. Room temperature engineering stress-strain curves of NFA1 specimens tested ain all six orientations.

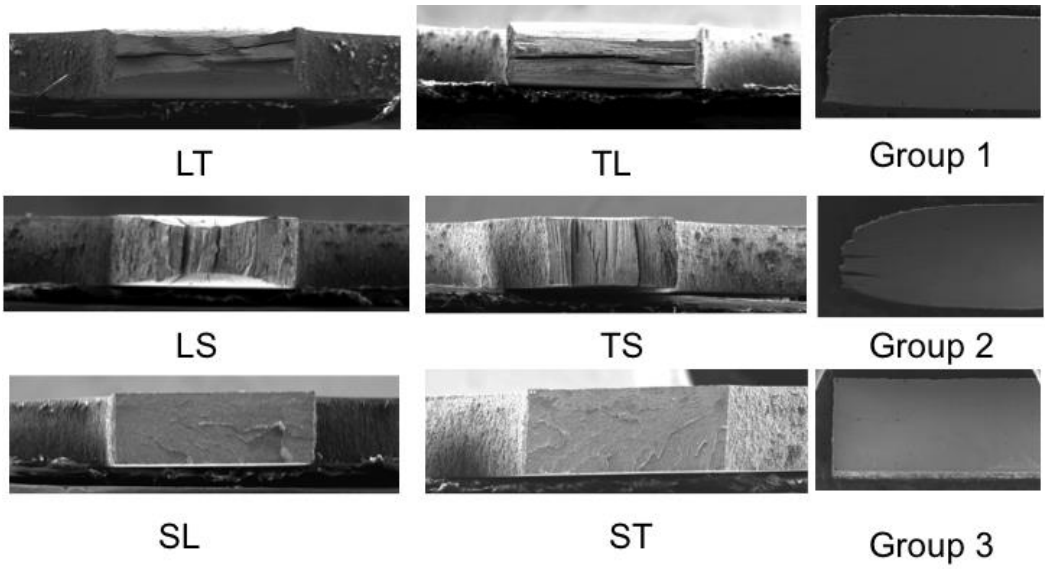

Figure 5. Low magnification SEM fractographs of room temperature tensile fracture surfaces in different orientations.

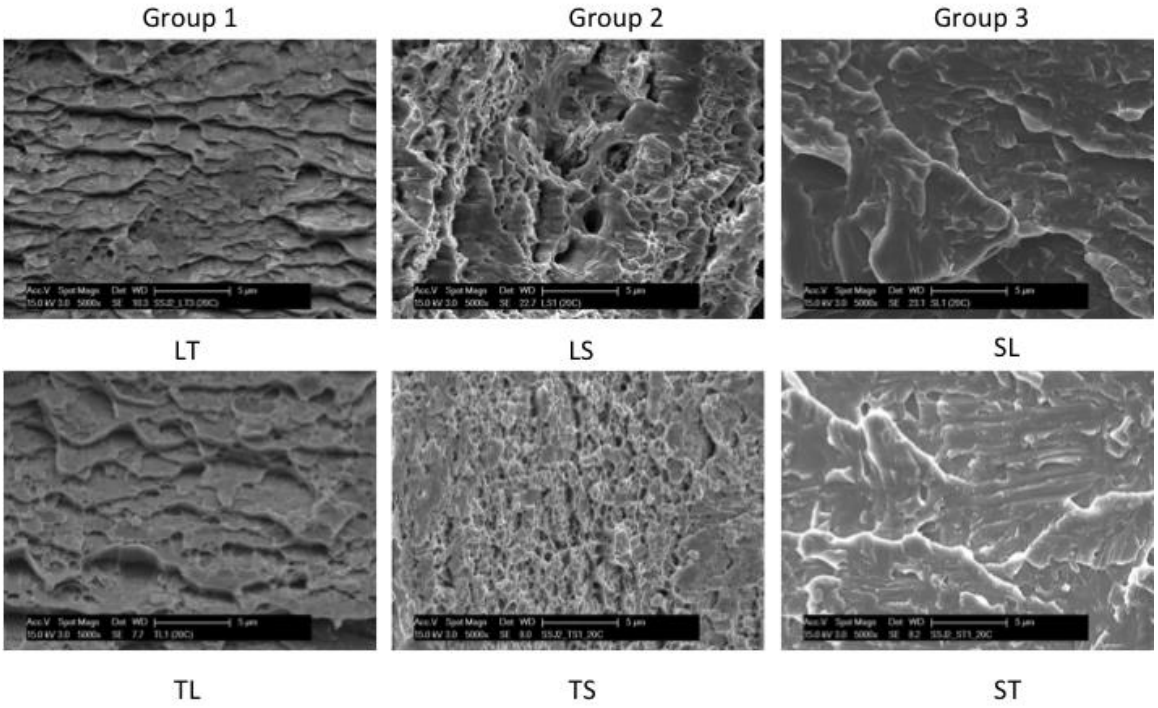

Figure 6. SEM fractographs of NFA-1 tensile specimens showing by group: (1) shear-leaps like features for LT/TL, (2) dimple like features for LS/TS, and (3) cleavage features for SL/ST orientations, respectively.

Tensile curves for tests performed at 600^{o}C in all six orientations are shown in Fig. 7. Like room temperature tensile properties, LT oriented specimen again showed the highest strength with an average value of 584 MPa 0.2% YS and 630 MPa UTS. TL orientations again exhibited similar tensile properties as for LT, but with slightly lower strength. The LS and TS orientations (group 2) have intermediate strength (528-543 MPa 0.2%YS and 555-589 MPa UTS) with the highest total total strain (~23%). Whereas group 3 (SL and ST) specimens failed in a brittle manner with lower strength at room temperature, at 600°C the same orientations exhibited comparable strength (~ 483 MPa 0.2%YS and

~535 MPa UTS) as the other groups. As shown in Figure 8, all the orientations failed in a completely ductile manner with the total elongation as high as 13.5%. In all cases, the uniform elongation is quite low, varying between 1.1-2.3%. No delaminations were observed in any case. Since the overall strength and ductility are comparable at 600°C, an important conclusion is that NFA-1 exhibits nearly isotropic tensile behavior at higher temperature.

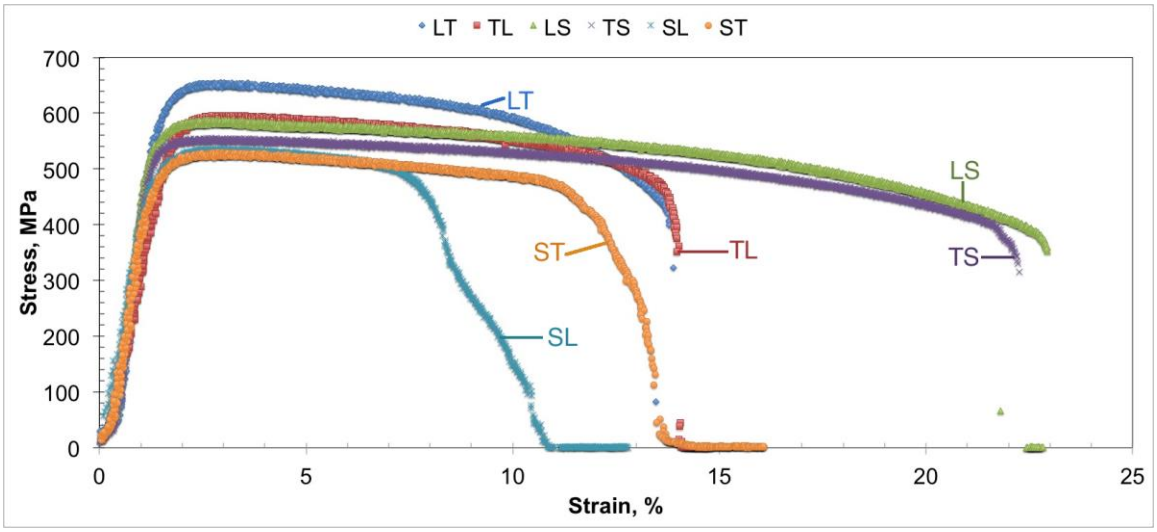

Figure 7. Engineering stress-strain curves of NFA1 tensile specimens tested at 600°C all six orientations.

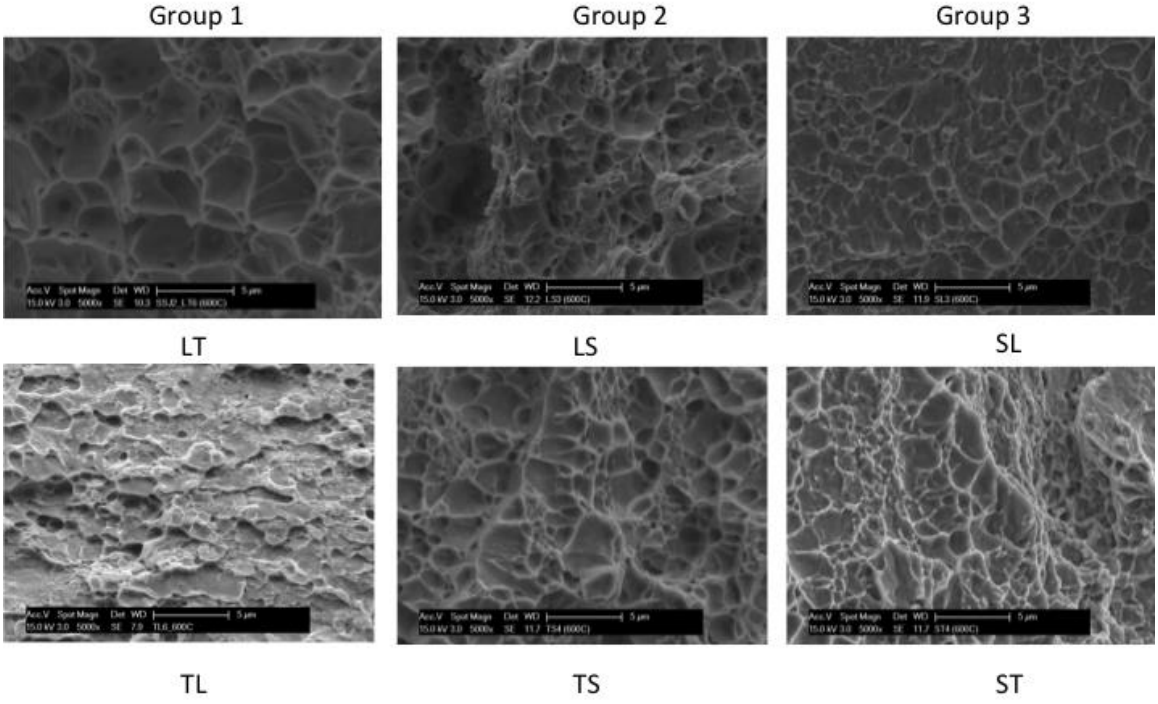

Figure 8. High magnification (x5000) SEM fractographs of NFA-1 tensile specimen fracture surface at 600°C showing dimple like features in all six orientations.

The tensile properties were characterized in the strongest (LT) and the weakest (ST) orientations from ambient temperature to 800°C and the results are shown in Figs. 9 and 10, respectively. Figure 9a is

shows the typical stress-strain curves of LT specimens as a function of temperature and Fig. 9b summarizes the various tensile properties. It can be clearly seen that the strength was decreased with increasing temperature. However, the rate of change of strength is much lower below ≈ 500°C, followed by a sharp decrease from 500°C to 800°C. This might be due to associated with a transition to viscoplastic creep even at the high strain rate of 10^{-3}/s. The strength of the NFA1 material at LT orientation is still high (>250 MPa) at 800°C. Despite the high strength, the material also exhibited relatively high total elongation (10-18%) over the entire temperature range. The uniform and total elongation were almost constant up to 400°C and then followed by a decrease in the uniform elongation up to 700°C while total elongation increased to 18% at 800°C due to the viscoplastic creep behavior.

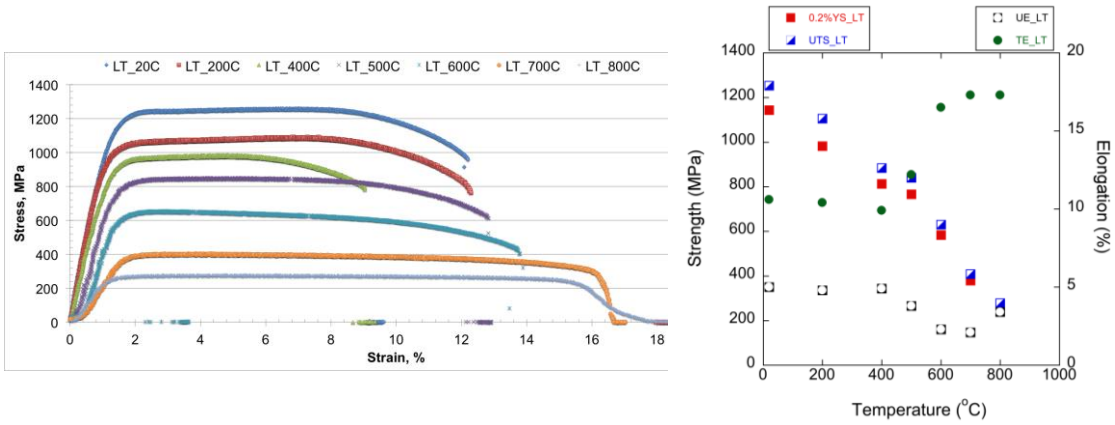

(a) (b)

Figure 9. (a) Engineering stress-strain curves for the LT oriented NFA1 tensile specimens as a function of temperature, and (b) summary of their tensile properties.

Fig. 10a shows the tensile curves for the ST orientation. Fig. 10b plots the various corresponding tensile properties of ST oriented specimen as a function of temperature. A small amount of yielding and strain hardening is observed at 100°C that but the specimen again fails in a brittle manner. Significant strain occurred at 200°C with failure by ductile fracture. The maximum stress was similar in all three cases ranging fro 850 to 900°C. The total elongation increased almost linearly with temperature, from 0.5% at ambient temperature to 16% at 800°C, while the corresponding uniform elongation increased from 0.5% at ambient temperature to 5% at 200°C, then decreasing up to 800°C. The low temperature behavior in the ST orientation can be rationalized by a ductile to brittle transition in the alloy matric toughness that permitted cleavage cracking only between ambient temperature and 100°C.

While not the topic of this report, the corresponding fracture toughness of NFA-1 is also strongly affected by the pre-existing cracks lying in planes parallel to the plat surface and normal to the thickness direction. In this case the delamination actually increase the fracture toughness. The fracture data are shown in Fig. 11 and discussed in some detail elsewhere [1]. We only briefly note that the enhanced toughness and very low ductile to brittle transition temperature In NFA-1 are due to the relaxation of high triaxial crack tip stresses upon delamination accompanied by a transition from a plane strain to a plane stress state condition.

Finally, creep rate and creep rupture time and ductility are also highly anisotropic and affected by the underlying deformation structure. However, as shown in Larson-Miller plot of the minimum creep rate shown in Figure 12, NFA-1 has a high temperature strength that is comparable to other similar alloys such as MA957.

Discussion and Summary

The tensile property of FCRD NFA1 material was fully characterized at six different orientations at varying temperature up to 800°C. In contrast to the LT orientation, NFA-1 failed in the brittle elastic region much

at a much lower stress at ambient temperature when loaded in S (short) direction. The causes of this behavior are under investigation.

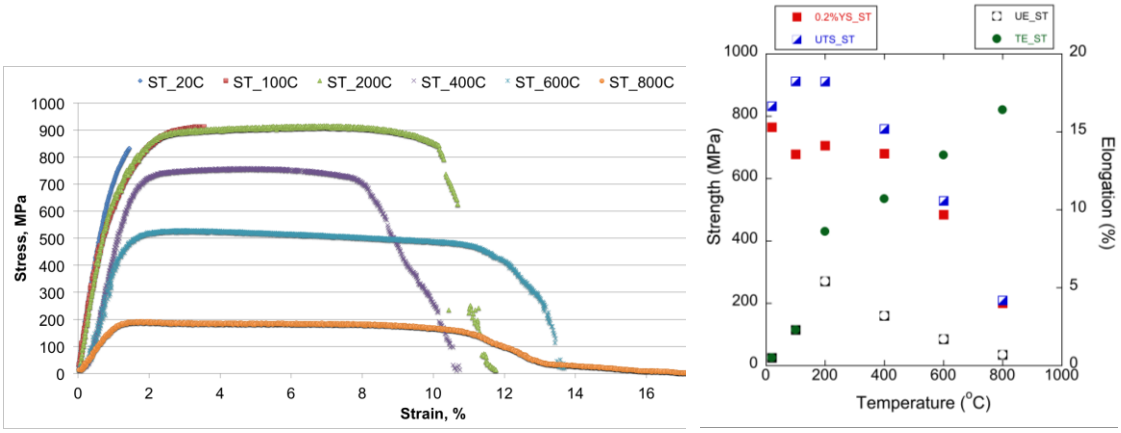

(a) (b)

Figure 10. (a) Engineering stress-strain curves of ST oriented NFA1 tensile specimens as a function of temperature, and (b) summary of their tensile properties.

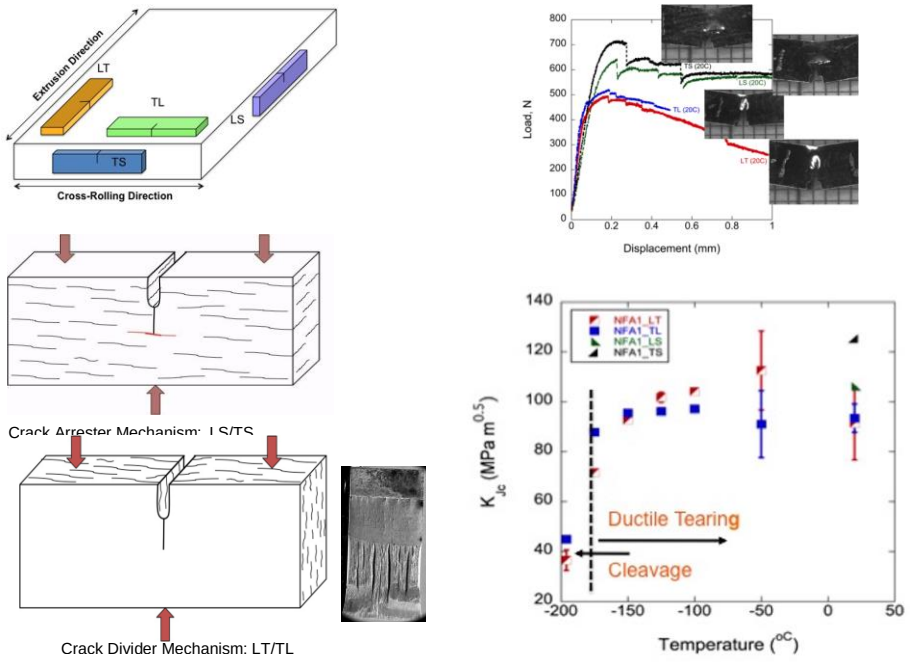

Figure 11, A pictorial summary pictorially illustrating the effect of delamination cracking on the ftactur behavior of NFA-1 as discussed in more detail elsewhere [1]

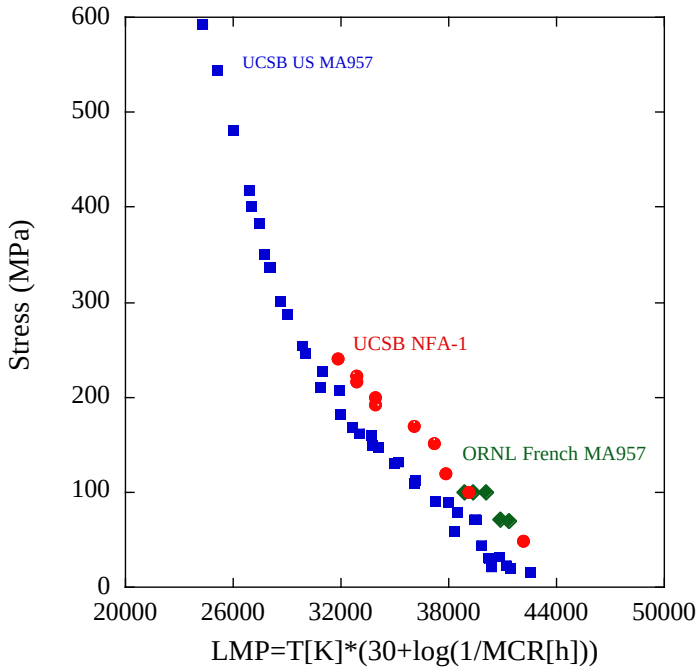

Figure 12. A comparison of the creep strength of NFA-1 with US and French heats of MA957 based on a Larson Miller minimum creep rate plot.

Acknowledgments

This work is part of a multi-laboratory collaboration between LANL, UCSB and ORNL. The DOE Office of Fusion Energy Sciences supported some of the mechanical testing reported here. NFA-1 was produced with the sponsorship of the DOE Office of Nuclear Energy under both a NEUP grant and the FCRD programs.

References

[1] G.R. Odette, “Recent progress in developing and qualifying nanostructured ferritic alloys for advanced fission and fusion applications,” JOM. 66 (2014) 2427.
[2] N.J. Cunningham, Y. Wu, G.R. Odette, D.T. Hoelzer, S.A. Maloy, “ Characterization of a larger best practice heat of 14YWT in annealed powder, HIP consolidated and extruded forms,” DOE/ER-0313/54 (2013), DOE Fusion Reactor Materials Program Semiannual Progress Report (2013).

2.6 FRICTION STIR WELDING OF ODS STEELS AND ADVANCED FERRITIC STRUCTURAL STEELS

- Z. Feng, W. Tang, X. Yu, G. Chen, D. Hoelzer, and L. Tan (Oak Ridge National Laboratory)

OBJECTIVE

This project addresses the critical technology gap of joining oxide dispersion strengthened (ODS) steels, nanostructured ferritic alloys (NFAs), reduced-activation ferritic/martensitic (RAFM) steels, and dissimilar metal joining of ODS/NFAs and RAFM steels through friction stir welding technology. The research focuses on understanding the stability of the strengthening phases in the weld region, and the bonding mechanisms between dissimilar structural steels as a function of FSW process conditions.

Specific project objectives are (i) developing the process parameter space to consistently produce defect-free welds of the same and dissimilar metals, (ii) developing the knowledge base and practical applicable approaches to tailor and optimize the microstructure features in the weld to match the properties of the base metal through process innovation, and (iii) producing representative weld joints and welded components to support future testing and evaluation at high temperature and irradiation environments in collaboration with JAEA and other international teams.

SUMMARY

Research during this period focused on (1) designing and developing a FSW process to join 14YWT ODS steel and an ORNL developed 9Cr steel, referred as modified 9Cr steel in this report, (2) dissimilar materials FSW microstructure characterization and flow pattern interpretation, (3) understanding the effect of FSW process conditions on the nano oxide strengthening particles in 14YWT ODS alloy, and (4) CFD based computer modeling to predict temperature fields and reveal flow fields in FSW. We successfully joined 14YWT ODS alloy and modified 9Cr steel without any defects, found FSW temperatures could be high enough to cause the modified 9Cr quenching in the stir zone. The thermal – mechanical process in FSW resulted in nanoparticle coarsening but the process could be finely tuned to preserve nanoclusters with slight coarsening on the 14YWT side of the stir zone. Computer modeling further revealed FSW thermal – mechanical mechanisms.

PROGRESS AND STATUS

Dissimilar materials ODS alloy and RAFM steel FSW and characterization

Previously, the project team has successfully made various friction stir welds on OSD and RAMF advanced steels, including dissimilar welds between ODS and RAMF. These welds were extensively characterized [1-6]. In this period, a defect free dissimilar material FSW butt joint of 14YWT and the modified 9Cr steel was made with the weld center line skewed with the material interface at 9.6°, see Figure 1 for the welded joint. Three metallographic specimens were cut from the weld at locations shown in Figure 1. Section (A), where the interface between ODS and RAFM steel began to intercept the periphery of the pin and experience the stirring effect of the pin; Section (B), where the interface was coincident with the pin axis, and Section (C), where the pin began to leave the interface. All three specimens were ground, polished and etched with 5 ml HNO3 + 1 ml HF + 50 ml distilled water etchant. Material microstructures at various metallurgical zones were observed under an optical microscope and Vickers hardness mapping test was applied on the joint cross section. All three joint cross sections with the scaled FSW tool shoulder diameter and pin shape are shown in Figure 2.

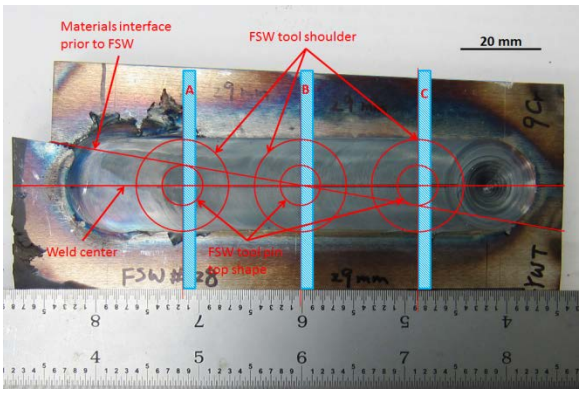

Figure 1. Dissimilar materials 14YWT ODS alloy & modified 9Cr steel FSW joint

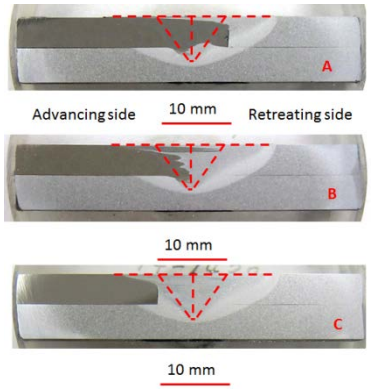

Figure 2. 14YWT ODS alloy & modified 9Cr steel FSW joint cross sections at various locations

As shown in Figure 2, materials mainly stayed at their own sides under the actions of the rotating tool, but some mixing in both horizontal and vertical directions is observed. It is clear that this material mixing neither random nor total mixing, but like a laminar overlap with a specific pattern, i.e., materials close to the top surface flowed and mixed more on the horizontal plane affected by the tool shoulder motion, while materials away from the top surface flowed and mixed both in vertical and horizontal planes influenced by the tool pin. Detailed flow patterns are shown in Figure 3 for Section B, where 14YWT is represented by dark color in the scanned cross section but by white color in microstructure pictures. In Figure 3, the modified 9Cr steel, which was located on the retreating side of the joint, flowed up and towards the advancing side, while 14YWT, which was located on the advancing side of the joint, flowed down and towards the retreating side. As a result, the first layer material at the top of the stir zone under the shoulder influence is always the modified 9Cr steel.

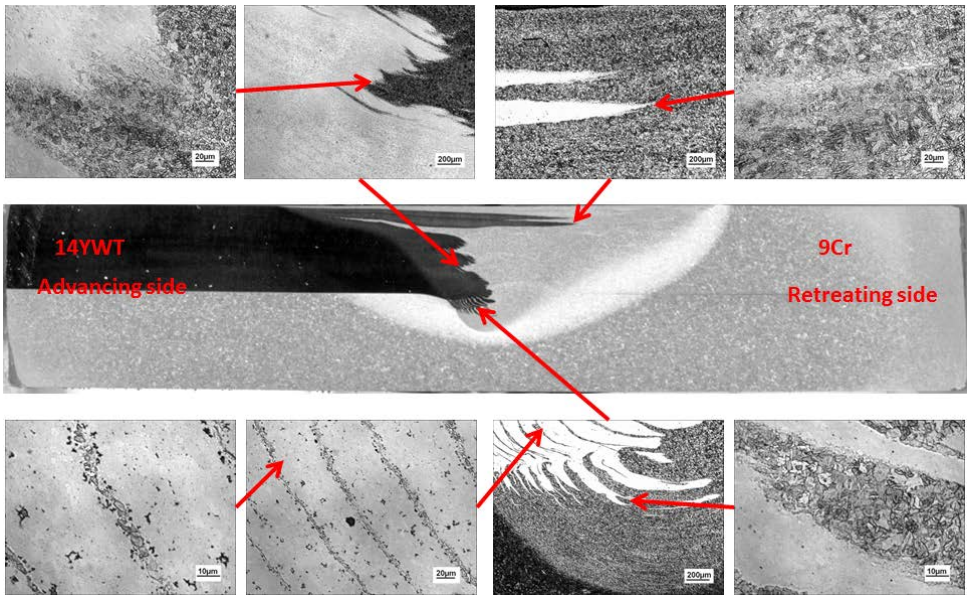

Figure 3. Materials flow pattern in dissimilar materials 14YWT – modified 9Cr FSW joint

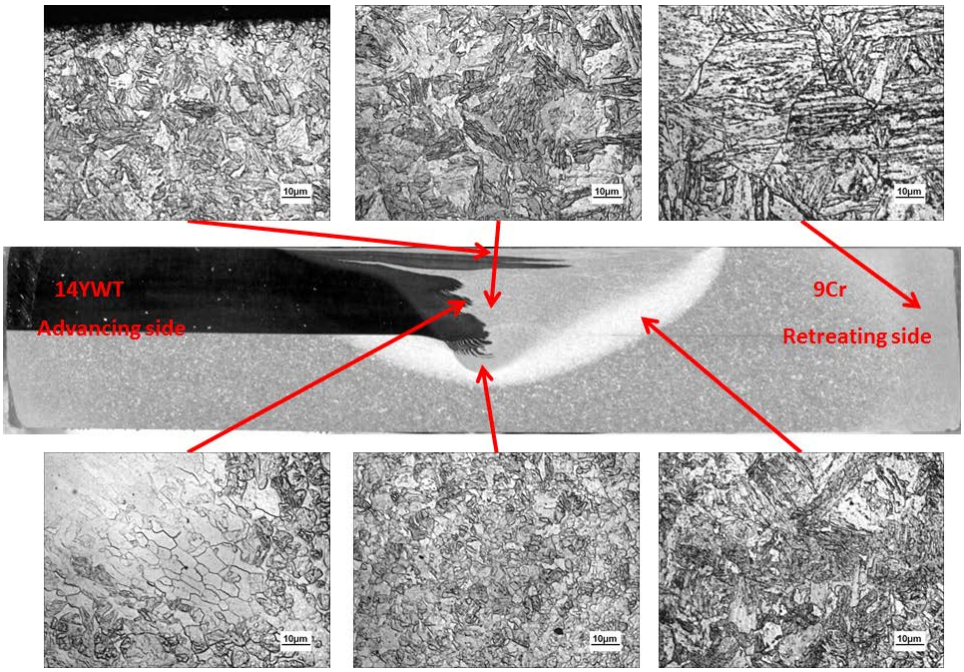

Figure 4. Microstructure of dissimilar materials 14YWT – modified 9Cr FSW joint

Optical microscope observation showed the FSW joint is free from defects for specimen B, where the original interface is aligned with the welding centerline, and microstructures in various metallurgical zones are shown in Figure 4. For base metals, a martensitic microstructure was observed with modified 9Cr steel but 14YWT grain structure can't be recognized under optical microscope due to its submicron size. In the stir zone, modified 9Cr remains martensitic and grain size at the bottom is obvious smaller than that in the middle or at the top due to the FSW temperature distributions. 14YWT grains are observed in the stir zone because they have enlarged from submicron to micron size due to the FSW heat input. In

addition, 14YWT grains do not present as equiaxed shape, but their major axis is along the material flow direction.

Vickers microhardness mapping was used on the dissimilar materials FSW cross sections to investigate the FSW thermal – mechanical effects on both materials' mechanical properties, as well as to estimate the FSW temperature range since it is hard, if not impossible, to precisely measure stir zone temperature during FSW. Micro-hardness mapping and the corresponding cross section specimen are shown in Figure 5. From Figure 5, ODS material 14YWT, which is located on the upper left side, softened in the stir zone while modified 9Cr steel hardened in the stir zone. This matches the microstructure observations in Figure 4 of 14YWT grain growth and martensitic modified 9Cr in the stir zone. Furthermore, the current FSW temperature must have exceeded the modified 9Cr phase transformation temperature and could have affected nanoparticles in ODS material 14YWT.

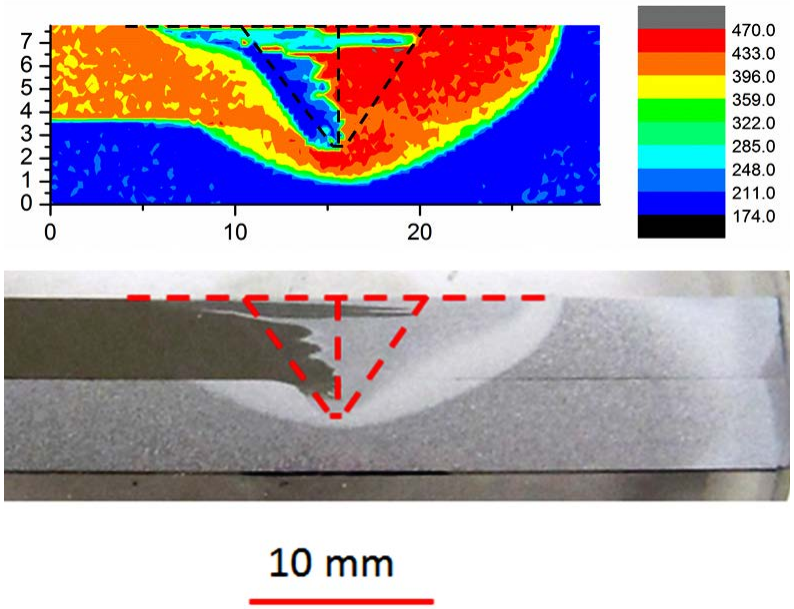

Figure 5. 14YWT & modified 9Cr FSW joint cross section and microhardness mapping

Atom probe tomography (APT) of 14YWT ODS alloy FSW

Atom probe tomography (APT) and electron backscatter diffraction (EBSD) analyses have been used on a 14YWT ODS steel/F82H steel FSW lap joint, mainly focused on the ODS material 14YWT. The APT measurements were carried out with datasets between 100 and >500 million atom collected for each condition, so that the overall distribution of nanocluster precipitates could be evaluated. Major findings are presented in Figures 6 to 9. Firstly, the average size of the grains in the stir zone was estimated to be 1.8 ± 0.4 μm compared with 1.1 ± 0.6 μm in the base metal. The mean radius of the nanoclusters increased from 1.9 ± 0.6 nm in the base condition to 2.7 ± 1.4 nm and 2.9 ± 1.4 nm, respectively in the stir and mixing zones. Secondly, the size increase is also reflected in the range of nanocluster precipitates sizes observed, i.e., the maximum precipitate increased from 4.3 nm in the base material to 18.0 and 11.0 nm, respectively in the stir and mixing zones, as well as the increases in the skewness and Kurtosis parameters. The average number densities of the nanocluster were estimated to be 5.2×10^{22}, 2.3×10^{22}, and 6.4×10^{22} m^{-3}, for the base metal, stir zone, and mixing zone, respectively. However, variations from 1.4×10^{21} m^{-3} to 5.2×10^{22} m^{-3} in the base metal (with an average of 1.4×10^{22} m^{-3}) and between 2.3×10^{22} and 7.1×10^{22} m^{-3} (with an average of 4.3×10^{22} m^{-3}) in the stir zone were observed in other datasets. These averaged are based on 144, 2072, and 696 precipitates, respectively for the base metal, stir zone and mixing zone, and a total of 2.5 billion atoms. Finally, post weld heat treatment didn't affect nanoclusters characteristics in the FSW joint.

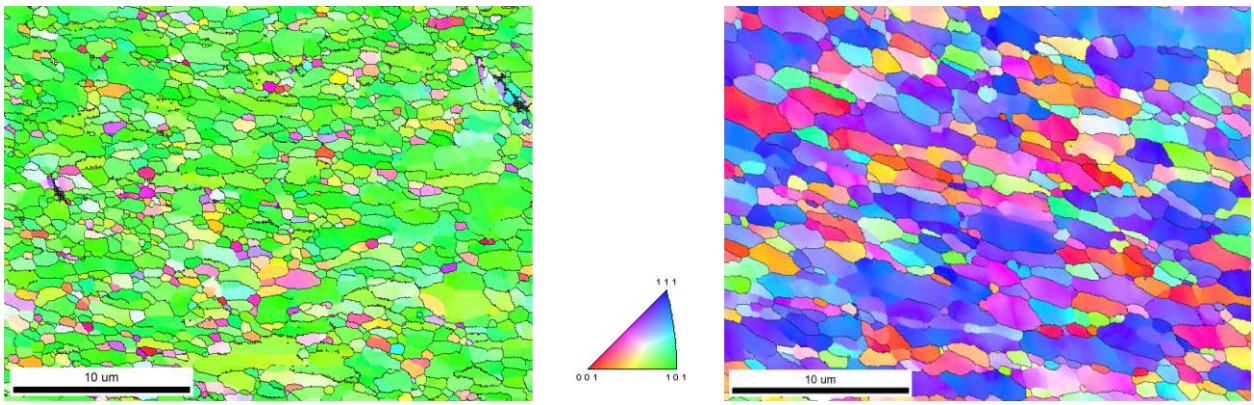

Figure 6. EBSD maps of (a) base metal (b) stir zone.

in nm	Base metal	Stir zone	TMAZ
Mean	1.91	2.69	2.94
Mode	1.56	1.63	1.58
Median	1.76	2.38	2.63
Minimum	0.90	0.71	0.92
Maximum	4.29	18.02	11.01
Skewness	1.18	3.26	1.87
Kurtosis	1.35	24.00	5.38

(a) As welded

in nm	Base metal	Stir zone	TMAZ zone (B)
Mean	1.6	2.0	2.3
Mode	1.0	0.83	1.94
Median	1.4	1.8	1.94
Minimum	0.5	0.55	0.52
Maximum	4.36	7.5	10.4
Skewness	1.07	1.42	1.85
Kurtosis	0.86	3.95	5.68

(b) Post weld heat treated

Figure 7. Nanoparticles atom probe characterization of ODS 14YWT base metal and FSW

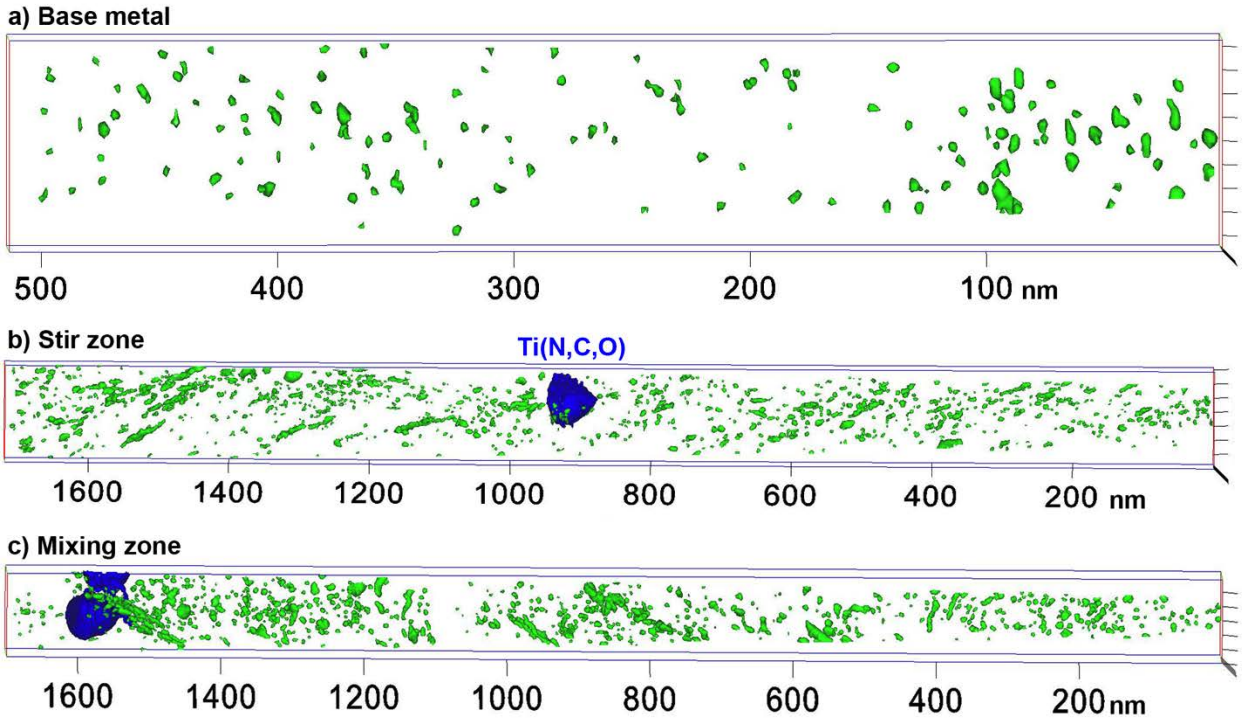

Figure 8. 5 at.% Ti isoconcentration surfaces of base metal, stir zone and mixing zone.

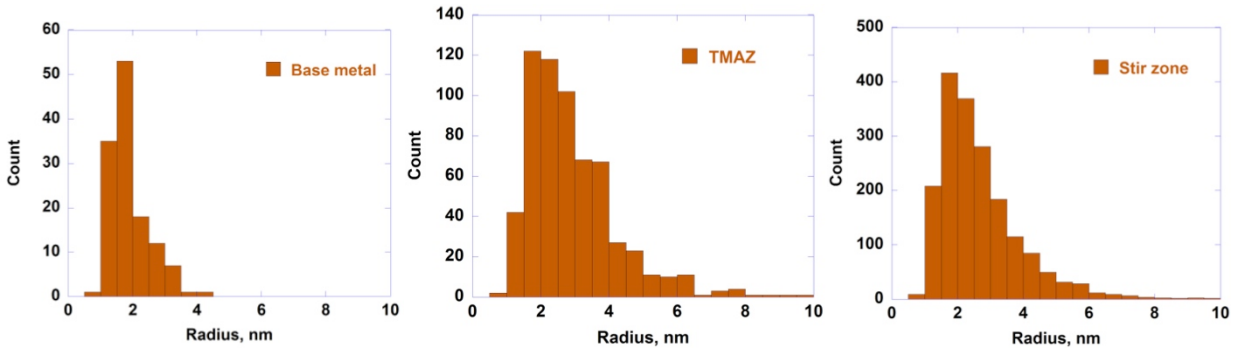

Figure 9. histograms of precipitates distribution in the base metal, TMAZ and stir zone.

Overall, the friction stir welding resulted in insignificant increase in average grain size and the radius of nanocluster precipitates, for the 14YWT/F82H lap joint FSW process conditions. Further investigation of the dissimilar materials FSW shown in Figure 1 will be carried out to reveal heat input effects on nanoparticles dimensions; however, consider the hardness drop of the ODS alloy after FSW shown in Figure 5, low heat input FSW is one of the keys to join ODS material without changing grain sizes and nanoparticle dimensions.

Friction-induced material behavior in FSW thermal-mechanical coupled computer modeling

The two fundamental key points regarding the thermal-mechanical conditions experienced by FSW are temperature and material deformation, which affect joints metallographic characterization and properties. However, it is extremely difficult or impossible to determine the thermal-mechanical fields accurately in FSW because they are coupled dynamic processes surrounded by solid metals. On the other hand, computational modeling, when appropriately constructed and performed, can simulate the complicated

processes and provide insights into the temperature and deformation during FSW, to guide FSW process development and optimization. To study the fundamental variables of FSW in joining ODS and RAFM steels, such as temperature, strain, strain rate and flow stress, 3D thermally and mechanically coupled numerical models were developed based on Computational Fluid Dynamics (CFD). In the model presented here, basic variables describing the heat flow and material flow in FSW are temperature and material velocity, which are obtained by solving governing equations in Eulerian formulation. The conservation equations of mass and momentum for incompressible single-phase flow are given by,

$$\nabla \cdot (\rho \vec{v}) = 0 \tag{1}$$

$$\nabla \cdot (\rho \vec{v} \vec{v}) = -\nabla p + \nabla \cdot \left(\mu (\nabla \vec{v} + \nabla \vec{v}^T)\right) \tag{2}$$

Where ρ is the density, μ is the viscosity, p is the pressure and $\vec{v}$ is the fluid velocity.

The energy conservation equation is given by,

$$\nabla \cdot (\vec{v} H) = \nabla \cdot (k \nabla T + S_V) \tag{3}$$

Where H is the enthalpy, T is the temperature, k is the thermal conductivity and S_V is a spatial source term regarding the heat generation due to plastic deformation.

Two tool pin configurations are chosen in the current modeling, with step spiral and without step spiral, which are shown in Figure 10.

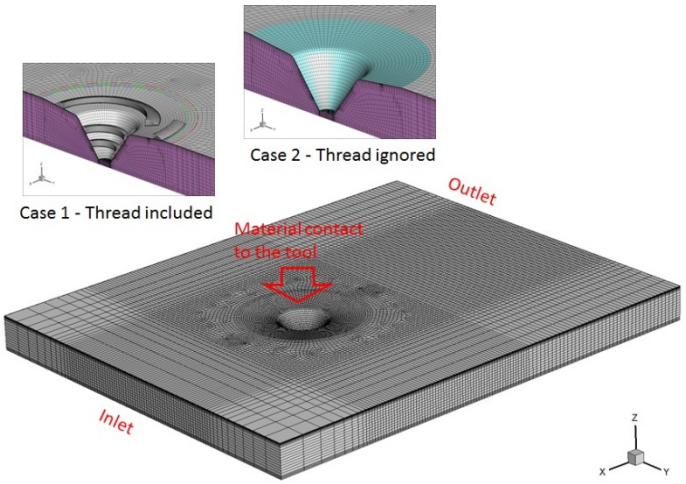

Figure 10. FSW process CFD computer model

A typical temperature field from FSW modeling is shown in Figure 11. From Figure 11, it is found that the predicted temperature field matches a typical FSW temperature distribution, where a localized high temperature area exists in the vicinity of the FSW tool and the temperature gradient is steeper in front of the tool than at back of the tool. The predicted peak temperature, 1326°C, was located close to the shoulder. This predicted stir zone temperature, which is higher than the modified 9Cr steel phase transformation temperature and 14YWT base metal heat treatment temperature, quenched the modified 9Cr and enlarged 14YWT grain sizes in the stir zone, and resulted in modified 9Cr hardening as well as 14YWT softening in the same metallurgical zone. Moreover, the step spiral pin tool caused more material deformation and resulted in higher welding temperature in FSW than the smooth pin tool, see Figure 12.

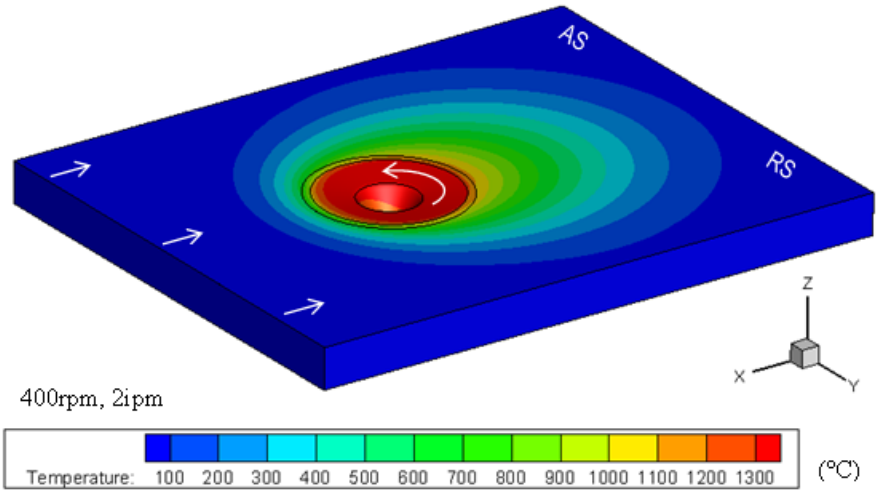

Figure 11. FSW temperature field from computer modeling

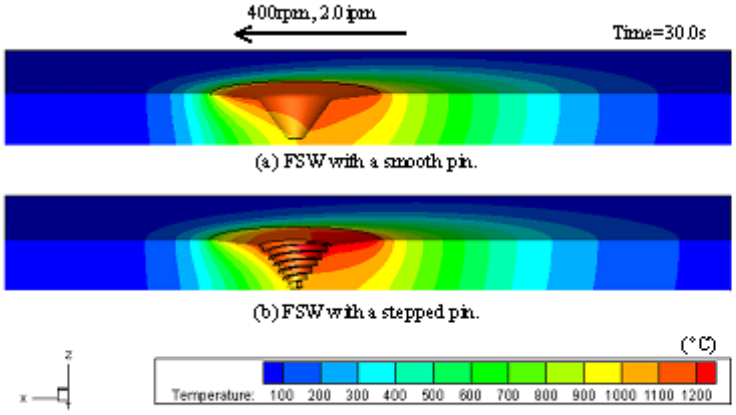

Figure 12. FSW Temperature fields established with and without pin step spirals

Material flow patterns are visualized by flow paths as shown in Figure 13. In order to capture the influence of tool on material flow, marker materials were released at different heights through the workpiece thickness, i.e., 1 mm (Figure 13(a)), 3 mm (Figure 13(b)), and 6 mm (Figure 13(c)) underneath the workpiece and tool shoulder interface, respectively. From Figure 13(a), it is clear that material on the advancing side flows up and towards the retreating side, while material on the retreating side flows down and towards the advancing side. Similar patterns show in Figure 13(b) but with less mixing, and Figure 13(c) showed the least deviation from their original flow path. Overall, flow paths predicted by the computer modeling in Figure 13 matches the FSW joint cross section materials flow pattern observations in Figure 3 and Figure 4, i.e., the modified 9Cr, which was located on the retreating side of the joint, rotated with the tool and moved up towards the plate top, while 14YWT, which was located on the advancing side of the joint, rotated and moved down to the plate bottom.

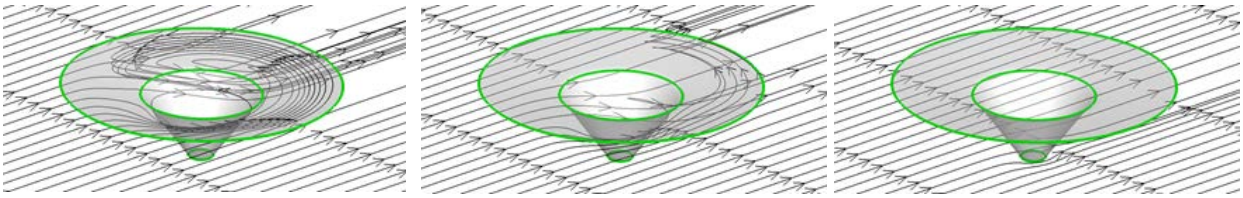

(a) 1 mm underneath shoulder (b) 3 mm underneath shoulder (c) 6 mm underneath shoulder

Figure 13. Flow pattern predictions by CFD computer modeling (Advancing side on the right and retreating side on the left)

FSW flow fields from the modeling indicate that step spiral pin tool caused more flow and a wider flow zone than smooth pin tool, see Figure 14 for details. Moreover, heavier flow close to the tool shoulder shown in Figure 14 explains more changes on microstructure characterization and microhardness distribution at the same region than areas close to the plate bottom from the experimental results.

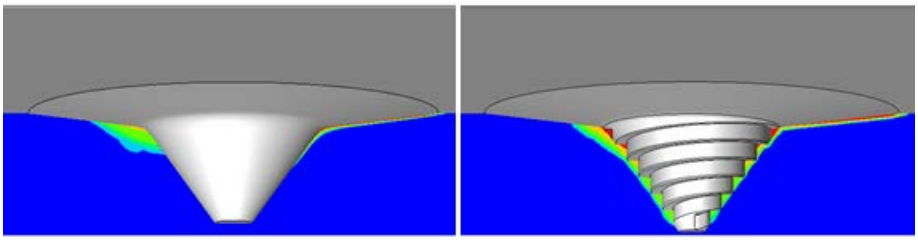

(a) Smooth pin (b) Step Spiral pin

Figure 14. FSW flow fields established with and without pin step spirals

Future Work

The following major activities are planned for the next 6 months:

- Produce additional RAFM steel FSW joints for high temperature creep tests.
- Preparing necessary plans and schedules for high temperature creep test with in-situ local deformation measurement to reveal high temperature creep resistance capabilities of materials at various metallurgical zones in a FSW joint.
- Further APT characterization of nano particles/clusters in the dissimilar FSW of 14YWT ODS alloy and the modified 9Cr steel to further understand FSW heat input effects to nanoclusters and ODS materials properties.
- Further computer modeling to reveal point by point thermal – mechanical history in FSW process for further understanding FSW fundamentals.

References

[1] D.T. Hoelzer, K.A. Unocic, M.A. Sokolov, and Z. Feng, "Joining of 14ywt and F82h by Friction Stir Welding," J. Nucl. Mater., 442 (1–3, Supplement 1) (2013) S529-S534.
[2] Z. Yu, Z. Feng, D.T. Hoelzer, L. Tan, M.A. Sokolov, “Friction Stir Welding of ODS Steels and Advanced Ferritic Structural Steels,” ICFRM16, Oct 20-26, 2013, Beijing, China.
[3] D.T. Hoelzer, K.A. Unocic, M.A. Sokolov, and Z. Feng, "Joining of 14ywt and F82h by Friction Stir Welding," ICFRM-15 15th (International Conference on Fusion Reactor Materials), 442, (2013), S529-S534.
[4] Z. Yu, Z. Feng, D.T. Hoelzer, L. Tan, M.A. Sokolov, “Similar and Dissimilar Friction Stir Welding of ODS and RAFM Steels,” TMS Annual Meeting, Feb 16-20, 2014, San Diego, CA.

[5] X. Chen, Z. Yu, and Z. Feng, "FSW of Reduced Activations Steels with PWHT," 10th International Friction Stir Welding Symposium, May 20-22, 2014, Beijing, China.
[6] X. Yu, B. Mazumder, M. K. Miller, S. A. David, and Z. Feng, "Stability of Y–Ti–O Precipitates in Friction Stir Welded Nanostructured Ferritic Alloys", Science and Technology of Welding and Joining, Accepted.

2.7 SOLID-STATE MIXING OF ODS 14YWT AND 9Cr F/M STEEL ALONG BUTT JOINT BY FRICTION STIR WELDING - D.T. Hoelzer, L. Tan, W. Tang and Z. Feng (Oak Ridge National Laboratory)

OBJECTIVE

The objective of this task is to characterize the solid-state mixing behavior between dissimilar metal joining of the advanced oxide dispersion strengthened (ODS) 14YWT ferritic alloy and reduced-activation 9Cr ferritic/martensitic steel (FMS) along a varying angle butt joint produced by friction stir welding (FSW). The study focuses on understanding the stability of the dispersion-strengthened phases and grain structure in the weld zone and ultimately the quality of the joint between dissimilar metals as a function of FSW process conditions.

SUMMARY

Plates of 5 mm thickness were fabricated from the ODS 14YWT ferritic alloy and 9Cr ferritic/martensitic steel (FMS) and joined by FSW along an effective angle of 9.6º relative to the butt joint between the two plates. Three cross section samples were cut from the joined plates representing solid-state mixtures of ~80%/20%, ~50%/50% and ~20%/80% by volume fraction of 14YWT and 9Cr FMS, respectively and prepared by metallographic procedures. The microstructural analysis of the stir zone observed by Secondary Electron Microscopy (SEM) in the 3 samples showed that very high temperatures from frictional heat caused grain size and oxide particle size increases for 14YWT and decreases in prior austenite grain size and martensite lath size with dissolution of carbides for 9Cr FMS. Complete solid-state mixing occurred in stir zone of the ~50%/50% sample, but only occurred in the region near the pin tool shoulder of the ~80%/20% and ~20%/80% samples.

PROGRESS AND STATUS

Introduction

Friction stir welding (FSW) was previously investigated for joining 14YWT (similar metal) and 14YWT to F82H (dissimilar metal) [1]. In the initial study, the 14YWT specimens were joined along a butt joint while specimens of 14YWT and F82H were joined along a plunge joint. In joining technology, the plunge joint is not as technologically important as is the butt joint. For example, the joining of two pipes is done using a butt joint. However, there have been few studies on the butt joining of dissimilar alloys, especially high strength steels and ferritic alloys, by FSW. This project addresses this deficiency in joining technology and will greatly add to the understanding of solid state mixing of dispersion strengthened dissimilar alloys, such as 14YWT and 9Cr FMS, along a butt joint by FSW. The results of this study will be important for advancing dispersion strengthened ferritic alloys for fusion energy reactors.

Experimental Procedure

Plate samples of 14YWT (SM13 heat) and 9Cr FMS were prepared for the FSW experiment. The SM13 heat of 14YWT was produced and fabricated into 1.06 cm thick plate by cross rolling in the Fuel Cycle Research and Development (FCRD), Nuclear Energy (NE) program. For the FSW experiment, the 1.06 cm thick plate of 14YWT was cross-rolled an addition 53% reduction in thickness at 1000ºC, or 0.5 cm thickness. The dimension of the 14YWT plate was 13.9 cm x 7.5 cm x 0.5 cm thick. The 9Cr FMS was supplied in the final thermo-mechanical treatment (TMT) condition as a 1 cm thick plate, which was mechanically cut along the mid-section of the thickness to 0.5 cm thickness. The final dimension of the plate was 12.7 cm x 5.6 cm x 0.5 cm thick. The plates of 14YWT and 9Cr FMS were cut into two sections with an angle of 7.4º parallel to the longest length. The 7.4º taper angle was based on a pin tool design that ultimately was not used in this experiment. A digital image showing the two plates of 14YWT and 9Cr FMS butted together along the 7.4º angle is shown in Figure 1.

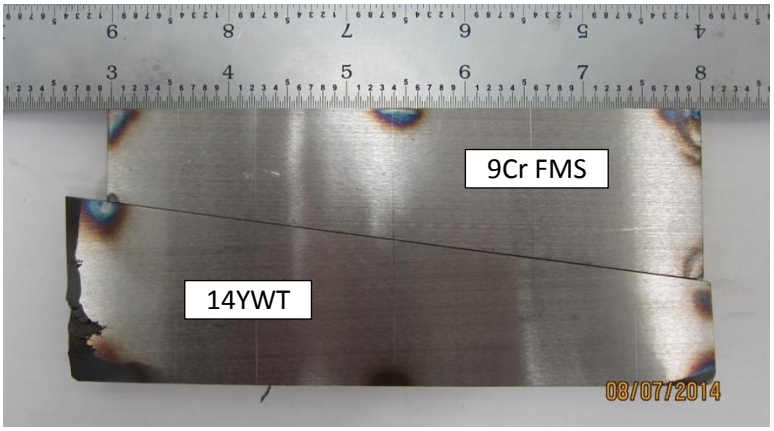

Figure 1. Digital image showing the plates of 14YWT and 9Cr FMS fitted together along the varying angle butt joint.

Figure 2 shows the experimental procedure for joining plates of 14YWT and 9Cr FMS along the varying angle butt joint. The FSW experiment was performed by having the pin tool travel along the center of the two adjacent plates resulting in varying volume fractions of the adjacent dissimilar alloys along the butt joint. Near the beginning, the pin tool will lie mostly in the 14YWT plate and overlap slightly with the 9Cr F/M steel plate to produce ~80%/20% mixture of the 14YWT and 9Cr F/M steel, respectively at the joint. At the mid-point, the pin tool will have roughly the same amount of each plate in the mixture, or 50% 14YWT and 50% 9Cr F/M steel occupying the butt joint. Finally, near the end of the FSW experiment, the pin tool reverses the mixture of the butt joint so that it will include ~20% 14YWT and 80% 9Cr F/M steel

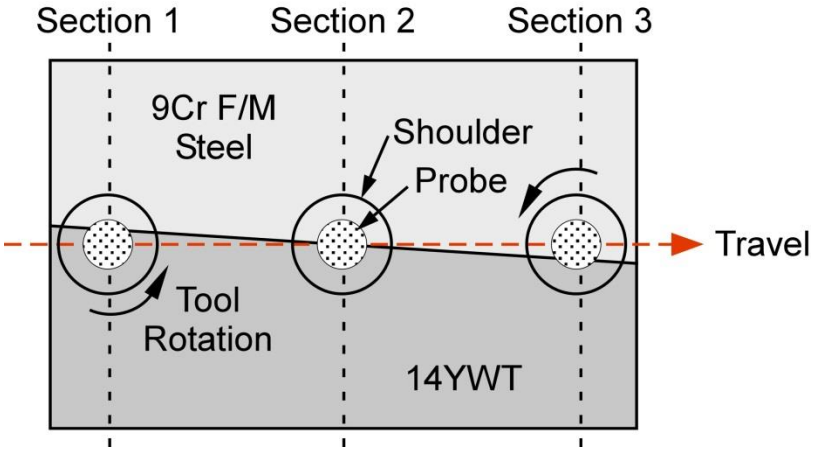

Figure 2. Illustration of the FSW experiment for joining plates of 14YWT and 9Cr FMS along the varying angle butt joint.

The FSW experiment was performed using a Polycrystalline Cubic Boron Nitride (PCBN) pin tool that was 6.5 mm long and tapered from 10 mm dia. at the base of the 25 mm dia. shoulder to 3.5 mm dia. at the tip. Because the dimensions of this pin tool were different from the one used in determining the 7.4º taper angle on the two plates, the path that the pin tool made was increased by 2.2º relative to the taper angle, which meant that the effective angle that the pin tool traveled was 9.6º. This modification was done in order to ensure that the pin tool started completely in the 14YWT plate and ended completely in the 9Cr FMS plate. The FSW run was performed with tool rotation speed of 250 rpm and translation welding speed of 7.62 cm per minute. Cross section samples for microstructural characterization were extracted from three sections of the joined plates illustrated in Figure 2 and were mounted and polished by

metallographic procedures. The final polishing step was conducted using colloidal silica. The microstructural analysis of the FSW samples was investigated using the JEOL 6500 FEG (Field Emission Gun) Scanning Electron Microscope (SEM).

Results and Discussion

Friction Stir Welding Run

The parameters used in the FSW run resulted in the successful joining of the 14YWT and 9Cr FMS plates as shown in Figure 3. The counter-clockwise rotating pin tool first entered the 14YWT plate on the left side of the image and traveled to the right side forming the varying angle butt joint where it exited (concentric rings) from the 9Cr FMS plate. The ascending side of the joined plates mainly contained the 14YWT plate (bottom) while the descending side mainly contained the 9Cr FMS plate (top). The cross section samples prepared for microstructural characterization were cut from the three sections marked with dashed lines and labelled (1A, 2A and 3A) shown in Figure 3.

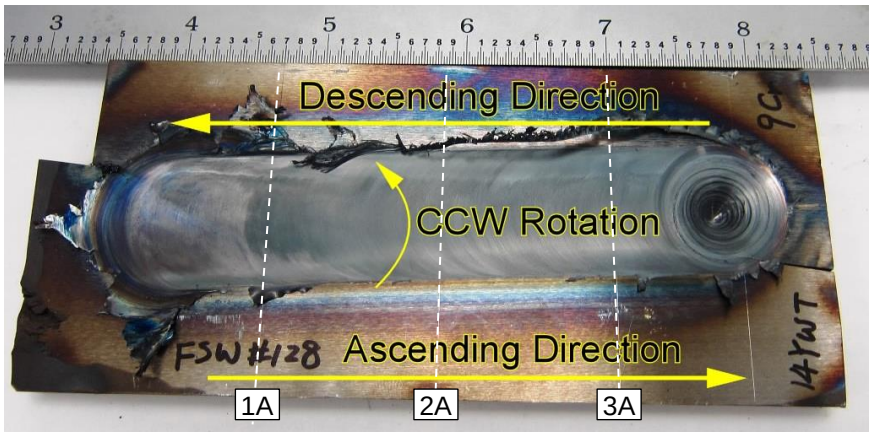

Figure 3. Digital image showing the successfully joined plates of 14YWT and 9Cr F/M steel by FSW along the varying angle joint. The ascending, descending and rotation directions of the pin tool are shown. The ruler shown at the top is in decimal inches.

Microstructural Characterization

The general microstructural features observed with backscattered electron (BSE) imaging for the 3 sample locations on the ascending and descending sides of the joined 14YWT and 9Cr FMS plates are shown in Figures 4 and 5, respectively. All of the BSE micrographs show the microstructure near the joint between the stir zone (SZ), thermomechanically affected zone (TMAZ) and the bottom supporting 9Cr FMS plate.

On the ascending side, the SZ at the 1A and 2 A locations (Fig.'s 4a and 4b) consisted of 14YWT with multiple protrusions extending downward into the supporting 9Cr FMS plate and a clear demarcation in contrast along the interface between the SZ and TMAZ of 14YWT. The finger-like pattern associated with the multiple protrusions of 14YWT into the 9Cr FMS result from the time elapsed behavior of solid-state mixing that occurs as the pin tool travels along the varying angle butt joint. The finger-like pattern suggests that large volume sections of 14YWT and 9Cr FMS must detach and then flow in spiral motion and are then forged in alternating sections as the pin tool progresses in travel. At the 3A location (Fig. 4c) on the ascending side, the SZ consisted of 9Cr FMS with little contrast variation along the interface between the SZ and TMAZ. The vertical crack demarcates the gap between the butted plates of 14WYT and 9Cr FMS that were not joined by the pin tool during the FSW run.

On the descending side, the SZ at the 1A location (Fig. 5a) consists of 14YWT and the interface separating the SZ and TMAZ is barely discernable based on contrast. In addition, the vertical crack observed in this figure defines the gap between the butted plates of 14YWT and 9Cr FMS that were not joined together during the FSW run and the horizontal gap separating 14YWT and 9Cr FMS defines the extent of the TMAZ for 14YWT. Material associated with the horizontal gap region does not experience

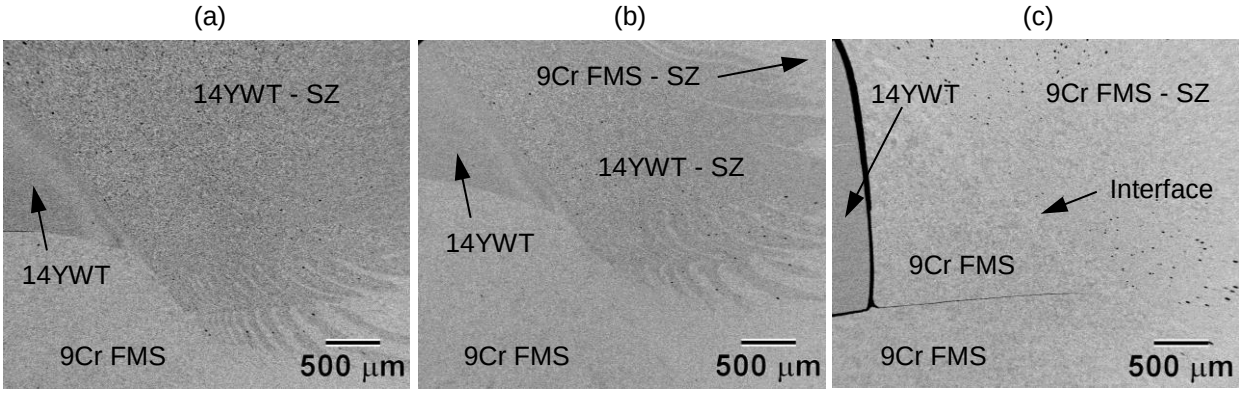

Figure 4. BSE micrographs at very low magnification showing the microstructure on the ascending side of joined plates between 14YWT and 9Cr FMS near the (a) start at 1A, (b) middle at 2A and (c) end at 3A).

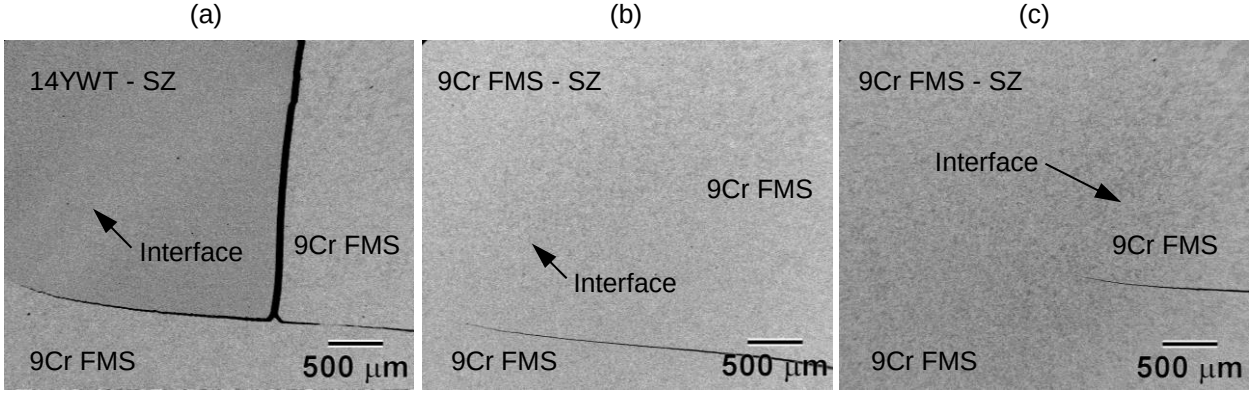

Figure 5. BSE micrographs at very low magnification showing the microstructure on the descending side of joined plates between 14YWT and 9Cr FMS near the (a) start at 1A, (b) middle at 2A and (c) end at 3A).

high enough temperatures during FSW to cause plastic flow. At the 2A and 3A locations (Fig.'s 5b and 5c), the SZ consists of 9Cr FMS with no discernable contrast along the interface between the SZ and TMAZ. However, the extent of the TMAZ can be determined from the end of the horizontal cracks that are due to the gap between the top and bottom plates of 9Cr FMS.

From these results, it was concluded that the microstructure of the SZ at the 2A location (Fig. 4b and 5b) consisted of a mixture of 14YWT and 9Cr FMS. However, due to the location of the 1A and 3A samples relative to the varying angle of the butt joint, little mixing occurred between 14YWT and 9Cr FMS since the microstructure of the SZ consisted almost entirely of 14YWT at the 1A location (Fig.'s 4a and 5a) and mostly of 9Cr FMS at the 3A location (Fig.'s 4c and 5c).

Near the top surface of the joined 14YWT and 9Cr FMS plates, the solid-state mixing behavior in the SZ was influenced by additional heat generated from the rotating shoulder of the pin tool. The microstructure observed with BSE on the ascending and descending sides of sample 1A are shown in Figure 6. On the

ascending side (Fig. 6a), variations in contrast are observed for 14YWT along the interface separating the SZ and TMAZ as well as for different regions of 14YWT in the SZ. The reason for these contrast variations will be shown in following figures. A small section of 9Cr FMS is observed at the top of the sample, which indicated that extensive plastic flow occurred due to the rotating shoulder of the pin tool. This section of 9Cr FMS is also observed at the top of sample 1A on the descending side (Fig. 6b). This result is ascertained by the contrast differences along the interface between the SZ of 14YWT and 9Cr FMS. However, the interface between the SZ and TMAZ of 9Cr FMS is not clearly observed.

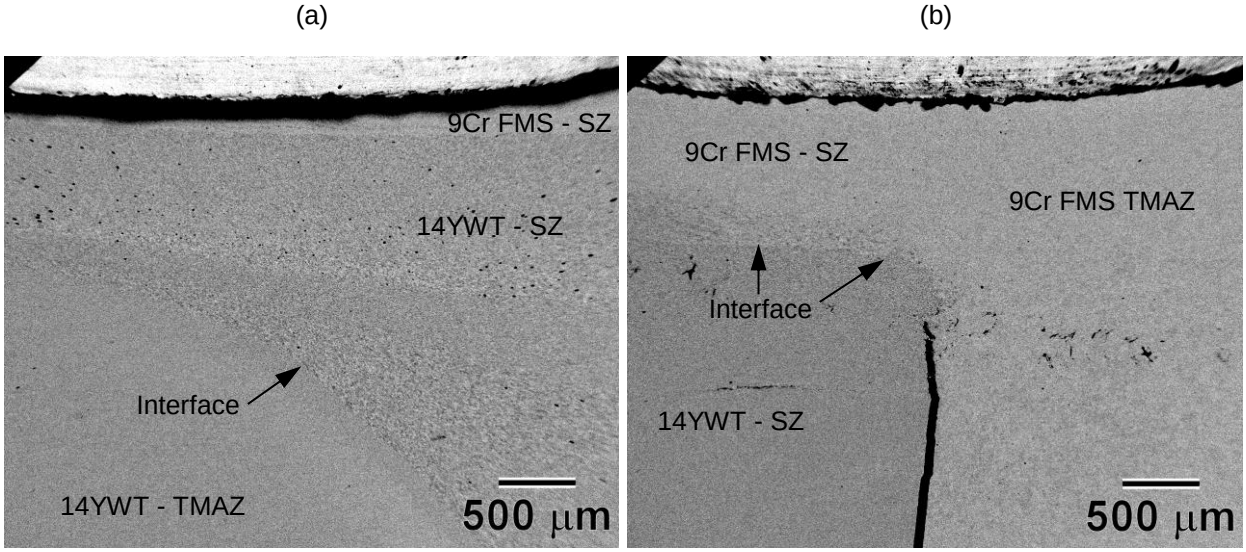

Figure 6. BSE micrographs showing the microstructure observed near the top of sample 1A on: (a) the ascending side and (b) the descending side.

To understand the reasons for the contrast variations observed between different regions of the joint between 14YWT and 9Cr FMS, it is necessary to become familiar with the microstructure observed in the base sections of the 14YWT and 9Cr FMS plates. Figure 7 shows BSE micrographs of the microstructure observed for 9Cr FMS in the unaffected region of the plate, away from the SZ, TMAZ and HAZ. The microstructure consisted of large prior austenite grains containing martensite laths laying in several crystallographic orientations (Fig. 7a) with visible carbides decorating the lath boundaries (Fig. 7b). The carbides show bright contrast relative to the laths indicating that they are composed of elements with high atomic number (Z). The contrast variations observed within the laths are most likely due to backscattered electron channeling variations due to overlapping laths. The typical dimension of the laths are ~1 to 2 μm wide and up to ~10 to 12 μm long. Figure 8 shows BSE micrographs of the microstructure observed for 14YWT in the unaffected region. The microstructure observed at low magnification (Fig. 8a) is noisy due to insufficient resolution for observing the grains. With improved resolution at higher magnification (Fig. 8b), ultra-small grains are observed that are elongated in the horizontal direction, which is parallel to the extrusion direction. Qualitative estimates indicate that the grain size in the unaffected zone is less than ~0.5 μm normal to the extrusion direction and up to ~2-3 μm parallel to the extrusion direction. The enhanced grain aspect ratio observed for 14YWT was caused by cross rolling the plate to 50% reduction-in-thickness, which compressed the grains in the thickness direction. Also observed at higher resolution are numerous sub-micron size particles and a few sub-micron size pores that show dark contrast in the BSE micrograph compared to surrounding grains. Previous characterization studies of 14YWT revealed that particles larger than ~20 nm were consistent with Ti(C,N) [2], which would account for the dark contrast observed in the BSE micrograph.

The interface region observed between the SZ and TMAZ of 9Cr FMS on the ascending and descending sides of sample 3A is shown in Figure 9. In both micrographs, the microstructure in the SZ appears featureless at low magnifications, while the TMAZ shows contrast variations associated with martensite laths. Numerous sub-micron size spots with dark contrast are distributed in the SZ on the ascending side (Fig. 9a) but are not so prevalent on the descending side (Fig. 9b).

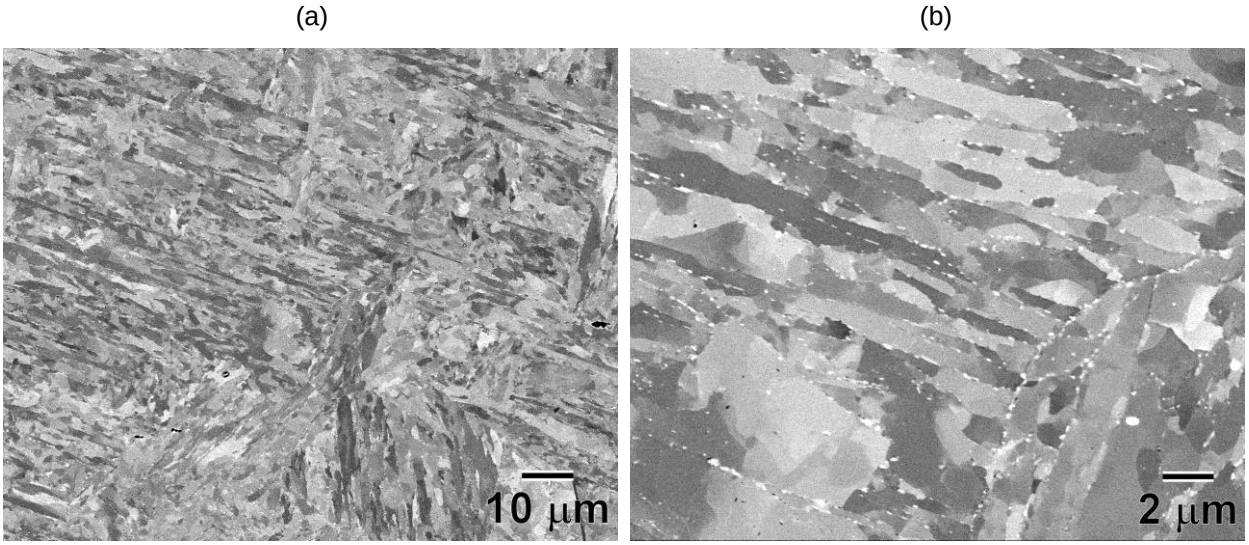

Figure 7. The microstructure observed in the base 9Cr FMS plate away from the SZ, TMAZ and HAZ in sample 3A. (a) BSE micrograph at low magnification and (b) BSE micrograph at higher magnification.

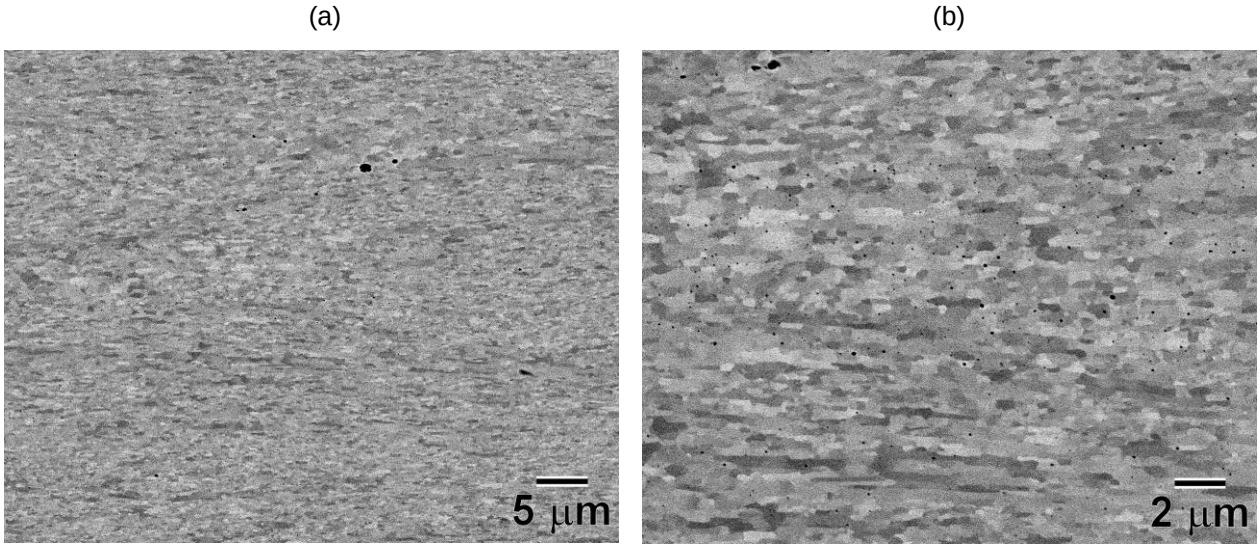

Figure 8. The microstructure observed in the base 14YWT plate away from the SZ, TMAZ and HAZ in sample 1A. (a) BSE micrograph at low magnification and (b) BSE micrograph at higher magnification.

Figure 10 shows BSE and SE (secondary electron) micrographs of the SZ of 9Cr FMS on the ascending side of sample 3A at higher magnification. The results indicated that considerable refinement occurred in the prior austenite grains containing martensite laths (observed in the unaffected zone) in the SZ. The austenite grain boundaries and lath structure are not discernable and no carbide particles are visible. However, there is a one-to-one correlation between the small dark contrast spots observed in the BSE micrograph (Fig. 10a) and the small dark contrast spots observed in the SE micrograph (Fig. 10b). Since

secondary electrons are generated from a depth less than ~10 nm from the surface of the specimen, the contrast, or emission yield, depends mainly on the specimen tilt angle and topography of the specimen surface. Therefore, the white contrast associated with the dark spots observed in the SE micrograph (Fig. 10b) is caused by curvature in the surface topography near the spots, which indicates that most of the dark spots observed on the ascending side of 9Cr FMS are pores.

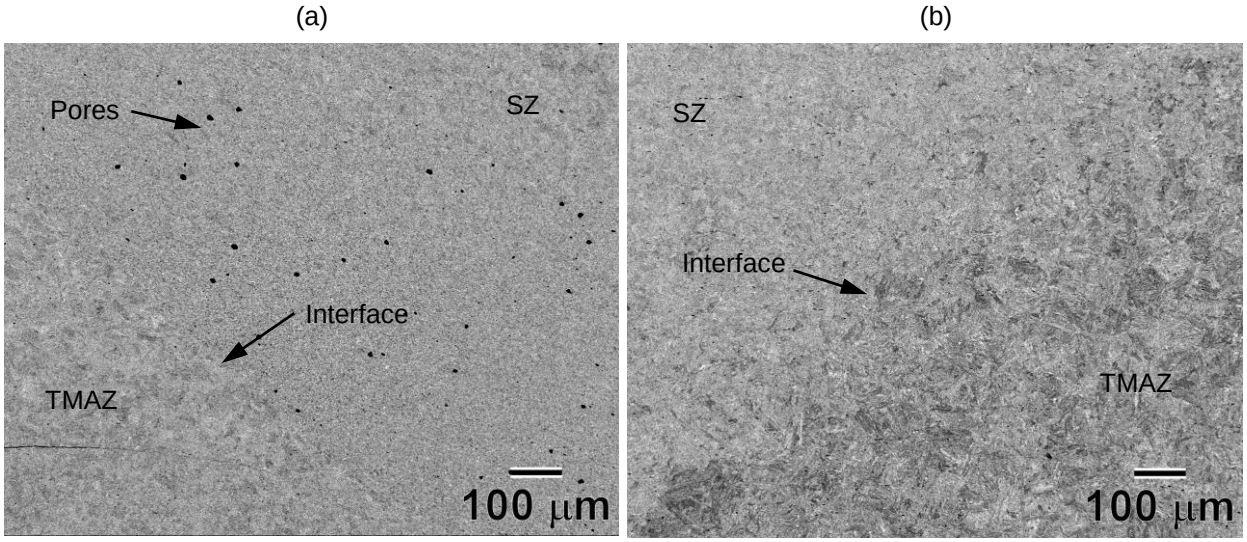

Figure 9. BSE micrographs showing the interface between the SZ and TMAZ of 9Cr FMS in sample 3A on (a) the ascending side and (b) the descending side.

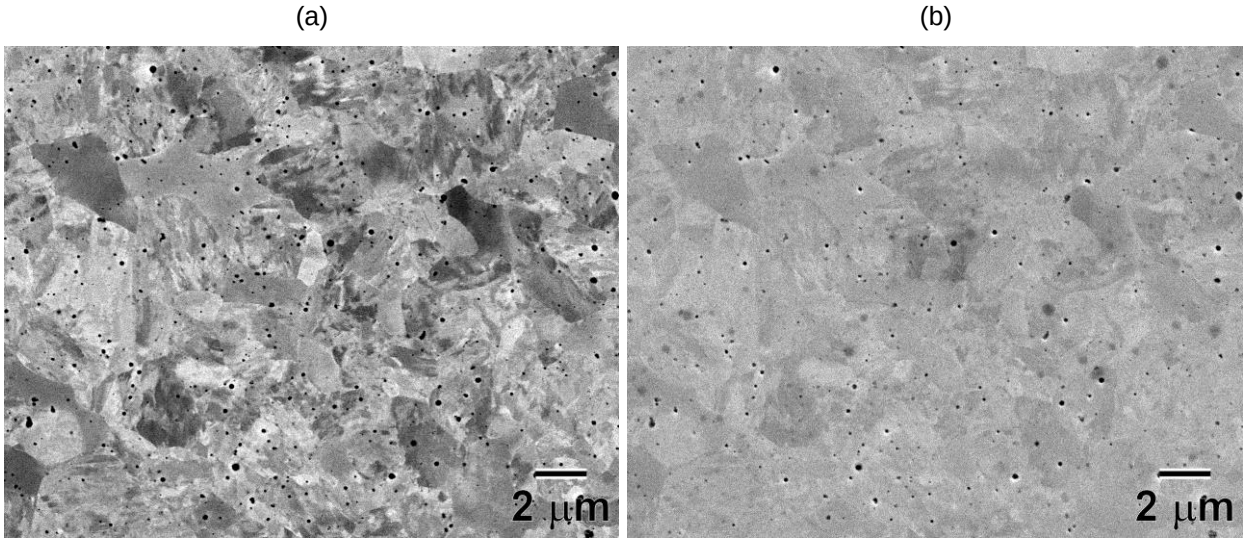

Figure 10. The microstructure observed in the SZ of 9Cr FMS in sample 3A on the ascending side. (a) BSE micrograph and (b) SE micrograph.

The microstructure observed at higher magnification in the SZ of 9Cr FMS on the descending side of sample 3A is shown in Figure 11. Similar to that observed on the ascending side, the austenite grain boundaries and lath structure are not well defined and no carbide particles are visible. A lower population of pores is distributed in the microstructure on the descending side (Fig. 11b) that appear smaller in size compared to those observed on the ascending side (Fig. 10a).

Figure 12 shows the microstructure that was observed at higher magnification in the TMAZ of 9Cr FMS on the ascending and descending sides in sample 3A. On both sides, grain boundaries associated with austenite grains containing martensitic laths showing distinct crystallographic orientations are observed. However, both the austenite grain size and martensite laths have been refined in size compared to the unaffected zone (Fig. 7). A few small particles showing bright contrast can be observed in the TMAZ on

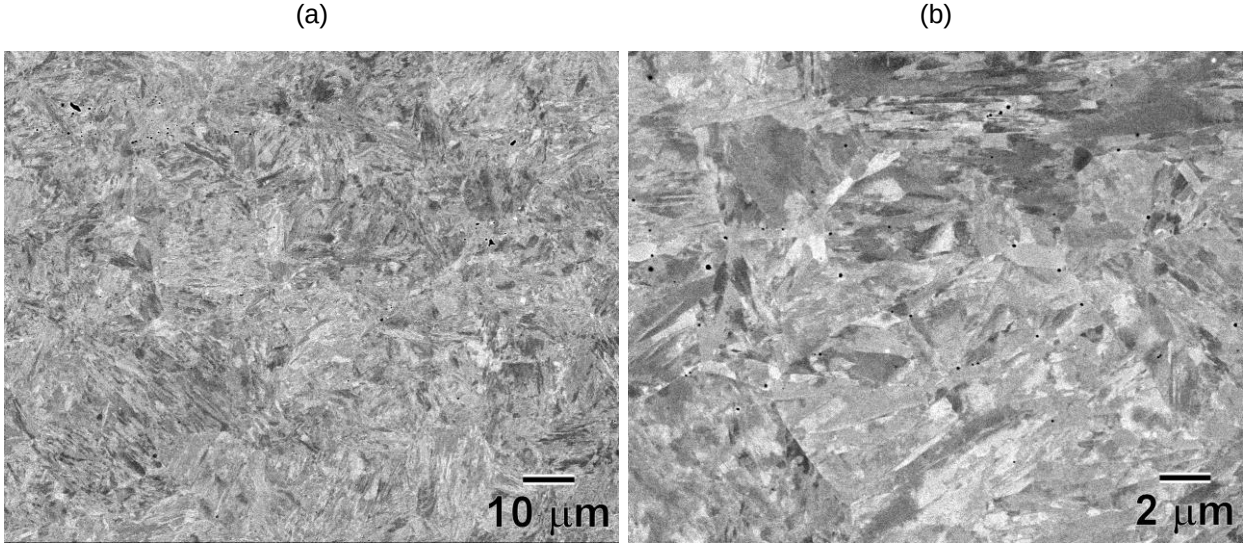

Figure 11. BSE micrographs showing the microstructure observed in the SZ of 9Cr FMS in sample 3A on the descending side. (a) Low magnification and (b) high magnification.

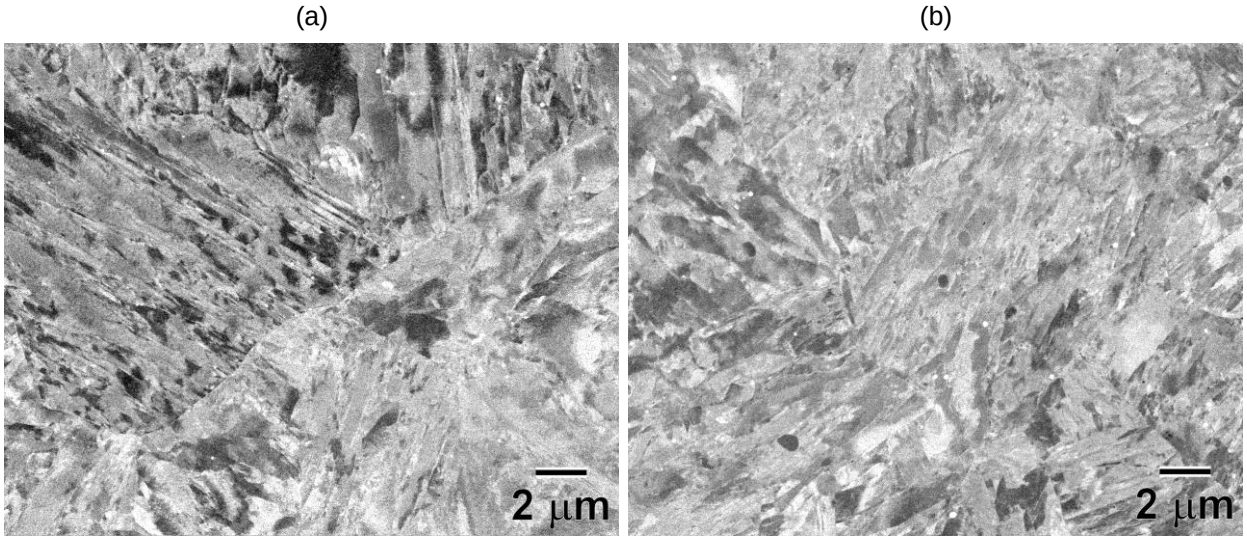

Figure 12. BSE micrographs showing the microstructure observed in the TMAZ of 9Cr FMS in sample 3A on (a) the ascending side and (b) the descending side.

the descending side (Fig. 12b). These observations suggest that the microstructure in the TMAZ reached temperatures far exceeding ~850ºC in order to cause complete austenization and dissolution of carbides in the microstructure followed by formation of martensite laths and precipitation of carbides upon cooling after passage of the rotating pin tool.

The interface region observed between the SZ and TMAZ of 14YWT on the ascending and descending sides of sample 1A is shown in Figure 13. The microstructure on the ascending side (Fig. 13a) experienced significant grain size coarsening in the SZ compared to that observed in the adjacent TMAZ. Most of the grains are larger than 5 μm in size, which represents an increase by a factor of up to 5-10X compared to the grain size observed in the unaffected zone (Fig. 8). The grain size also increased on the descending side of the SZ (Fig. 13b), but the increase was much less.

Figure 14 shows the microstructure of 14YWT that was observed at high magnification in the TMAZ and SZ of sample 1A. In the TMAZ (Fig. 14a), the size and morphology of the grains have been altered compared to the unaffected zone (Fig. 8b). Compared to the elongated grain morphology observed lying parallel to the extrusion direction, the grains in the TMAZ are nearly equiaxed with an increase in size to ~1 μm. The grains observed in the SZ (Fig. 14b) are also nearly equiaxed, but have undergone extensive coarsening. In addition, a relatively high number density of particles showing dark contrast relative to surrounding grains is observed in the large grains. The particle size resolved in the BSE micrographs is within the range from ~50 nm to ~350 nm. The preliminary composition analysis obtained by X-ray Energy Dispersive Spectroscopy (XEDS) showed that many of the dark contrast particles contained Ti and Y, but further analysis is still in progress. These results indicate that very high temperatures were reached in the SZ during passage of the rotating pin tool since significant increases in grain size and Y-, Ti-, O-enriched nanoclusters occurred in a relatively short period of time. The mechanism accounting for these rapid increases in size more likely was dynamic recrystallization.

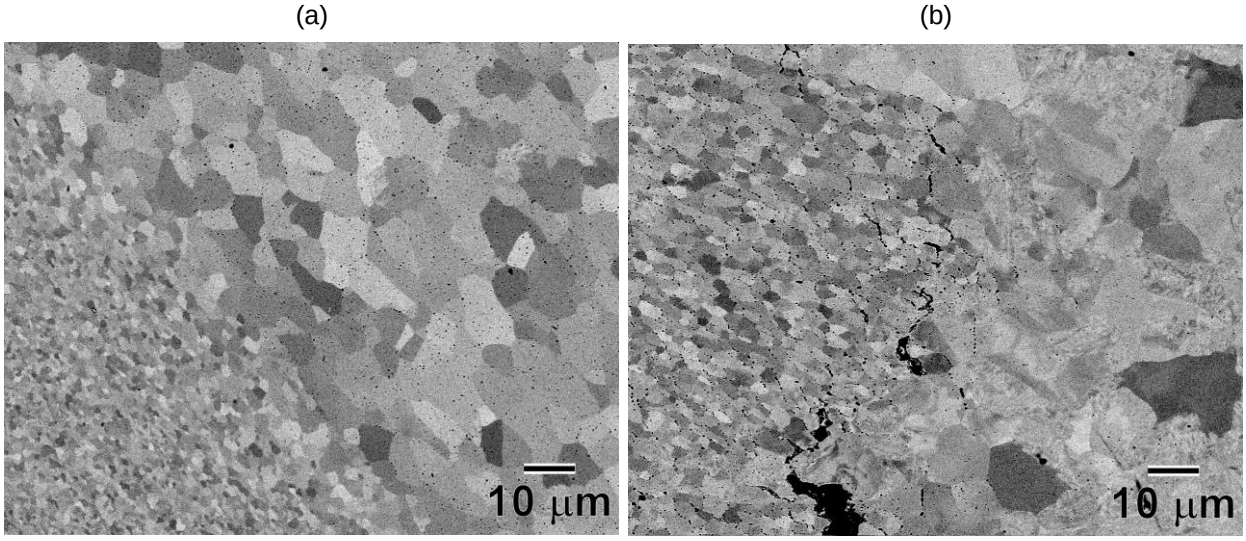

Figure 13. BSE micrographs showing the interface region observed between the SZ and TMAZ of 14YWT in sample 1A on (a) the ascending side and (b) the descending side.

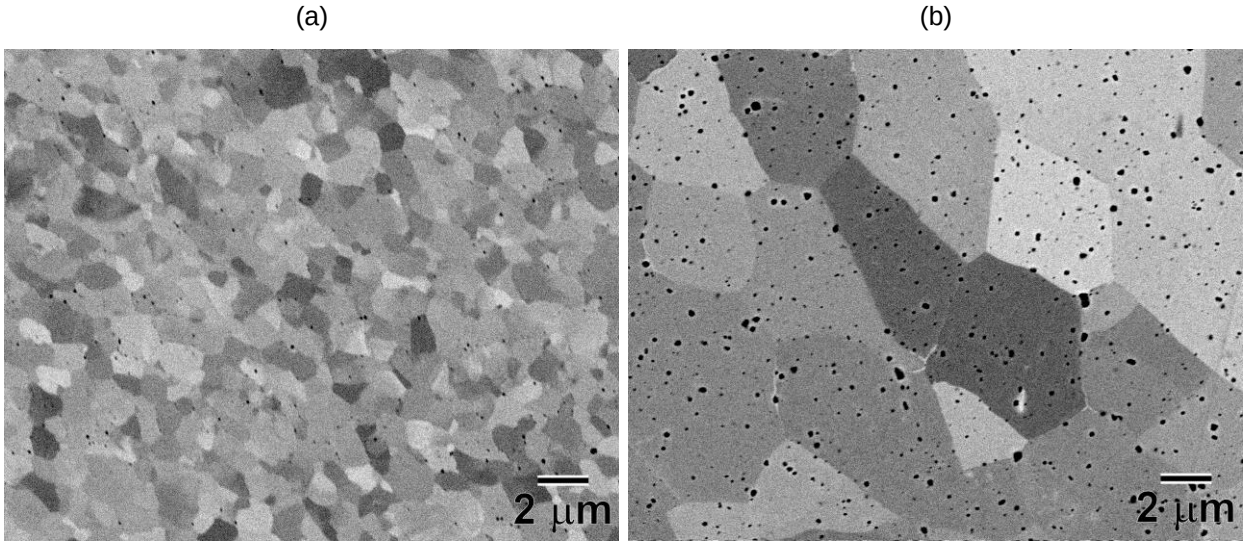

Figure 14. BSE micrographs showing the grain structure of 14YWT observed on the ascending side of sample 1A at high magnification in the (a) TMAZ and (b) SZ.

Conclusion

Friction stir welding was used to form a butt joint along an effective angle of 9.6º between 5 mm thick plates of ODS 14YWT and 9Cr FMS. Three cross section samples were cut from the joined plates representing solid-state mixtures of ~80%/20%, ~50%/50% and ~20%/80% by volume fraction of 14YWT and 9Cr FMS, respectively and prepared by metallographic procedures. The microstructural analysis of the SZ of the 3 samples by SEM showed no macro-scale pores formed. Only the ~50%/50% sample showed complete mixing between 14YWT and 9Cr FMS. The other two samples prepared from each end of the joined plates showed mixing between the two alloys only occurred near the top surface region of the joined plates where additional heating was caused by the shoulder of the rotating pin tool. The results indicated that very high temperatures from frictional heat occurred in the SZ that caused significant increases (up to 10X factor) in grain size and oxide particle size for 14YWT and decreases in prior austenite grain size and martensite lath size with dissolution of carbides for 9Cr FMS.

Future Work

Additional FSW experiments are planned that will focus on modifying the parameters (pressure, pin tool rotation rate and travel speed) in order to reduce the peak temperature reached in the SZ caused by frictional heating from the rotating pin tool. In addition, two additional samples will be extracted from the joined plates of 14YWT and 9Cr FMS from the initial FSW run in locations at are closer to the 2A (center) to obtain an more optimum mixture in volume fraction of 14YWT and 9Cr FMS. These samples will be prepared using metallographic procedures and investigated with SEM.

References

[1] D.T. Hoelzer, K.A. Unocic, M.A. Sokolov and Z. Feng, Journal of Nuclear Materials, Vol. 442, (2013), pp. 529-534.
[2] N.J. Cunningham, Y. Wu, G.R. Odette, D.T. Hoelzer and S.A. Maloy, Fusion Reactor Materials Program, DOE/ER-0313/54-Volume 54, (2013), p. 15-26.

3.1 DEVELOPMENT OF SiC JOINING TECHNOLOGIES FOR FUSION: TEST METHOD DEVELOPMENT - T. Koyanagi, J.O. Kiggans, J.M. Pryor, and Y. Katoh (Oak Ridge National Laboratory)

OBJECTIVE

This report presents a test method study on shear strength for ceramic joints toward development of a new ASTM C28 Test standard for the torsional shear strength of adhesive bonds for advanced ceramics. The effect of specimen dimensions on the apparent torsional shear strength was investigated utilizing brittle ceramic joints.

SUMMARY

Three different sizes of SiC to SiC brittle joint specimens were prepared for torsional shear tests; the machined hourglass test specimens have necks of 5, 10, or 15 mm diameter at the bonding plane. Uniformity of the bond quality was confirmed by acoustic scanning microscope prior to machining. Pure shear failure was observed for all the specimens, meaning that there was no obvious size effect on the fracture appearance. The size effect on the strength was apparently not clear due to the large scatter in strength values. The causes of the deviations and the possible methods to improve the testing are discussed.

PROGRESS AND STATUS

Introduction

The use of a reliable test for evaluation of bonding strength is a key to development of robust joining and integration technologies for ceramics materials. The lack of adequate standardized testing methods to evaluate the mechanical properties of ceramic joints is the motivation for the test method development in this work. Previous studies on evaluation of shear strength of ceramics joints revealed the usefulness of torsional testing to obtain pure shear strength, due to uniform stress state in bonding layer during testing [1]. For this reason, torsional tests were used in a post-irradiation experiment with various SiC joints, which provided understanding of irradiation tolerance of the SiC joints [2]. Because small-scale specimens are used in irradiation stability studies, specimen size effects on mechanical testing is an important consideration. There is limited space in a material test reactor, and the radiation exposure to personnel in post-irradiation testing needs to be minimized, making it a necessity to scale down the size of test specimens.

In this study, size effects on torsional shear strength of SiC to SiC brittle joints was investigated. The finding in this study will contribute to the test standard development for shear strength of ceramic joints in ASTM C28 on Advanced Ceramics.

Experimental Procedure

Plates of chemically vapor-deposited (CVD) SiC (99.9995 % pure, Dow Chemical, Marlborough, MA) were machined into 21 mm (w) × 31 mm (l) × 6 or 3 mm (t) blocks. The joining surface was perpendicular to the CVD growth direction. Commercial bonding slurry (Starfire AD-478, Starfire Systems Inc., Schenectady, NY) was used to fabricate SiC joints. The Starfire material is an adhesive in the form of a slurry. The composition is a proprietary mixture of SiC powder and polycarbosilane based SiC forming polymer (StarPCS^{TM}, Starfire Systems Inc., Schenectady, NY). A thin uniform layer of the adhesive was applied on each bonding surface of CVD SiC plates by spin coating with rotation speed of 4000 rpm, and then the plates were put together. The bonding layer was formed by hot pressing, according to the processing guidelines provided by the vender, except for use of vacuum as the furnace atmosphere.

The bonded plates were inspected by acoustic scanning microscopy with 10 or 15 MHz focused transducer, prior to machining into torsion specimens. The resolution limit of the images was 50 μm.

Figure 2 shows machined hourglass test specimens with a neck of 5, 10, or 15 mm diameter at the bonding plane. The specimen drawings and the IDs are shown in Fig. 1.

Figure 3 shows the setup for the torsion tests. Samples are mounted in a TestResources, Inc 160GT-125Nm torsion system with flexible couplers and sample grips. The flexible couplers were used to keep the alignment during testing. Aluminum tabs were installed at the square grip sections to obtain uniform stress distributions there. The rotation speed was ~0.10 deg/min. Nominal shear strength values (τ) in this work are given by following equation,

$$\tau = 16T/\pi d^3$$

where T is the applied torque and d is the specimen diameter of the neck. Further description of details of the test method can be found elsewhere [3]. All the torsion tests will be conducted at room temperature. The details of the fracture behavior will be investigated using a digital optical microscope (KEYENCE, VHX-1000).

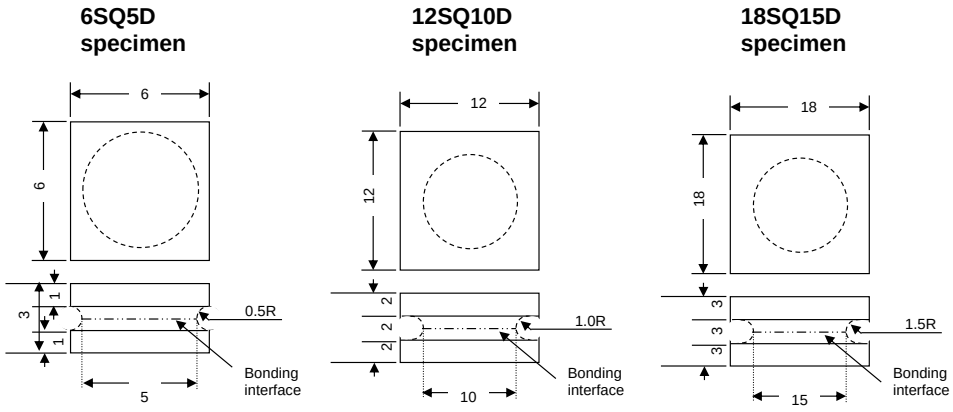

Figure 1. Drawings of three types of torsional shear specimens. Dimensions in mm.

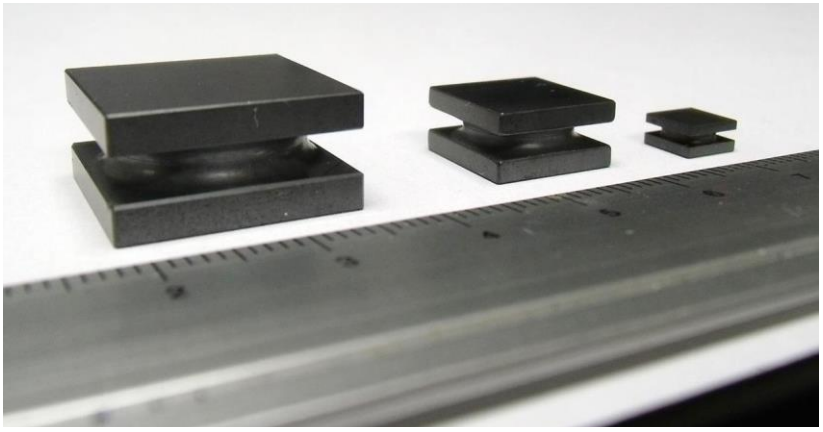

Figure 2. Three types of torsional test specimens. Scale is marked in mm and cm.

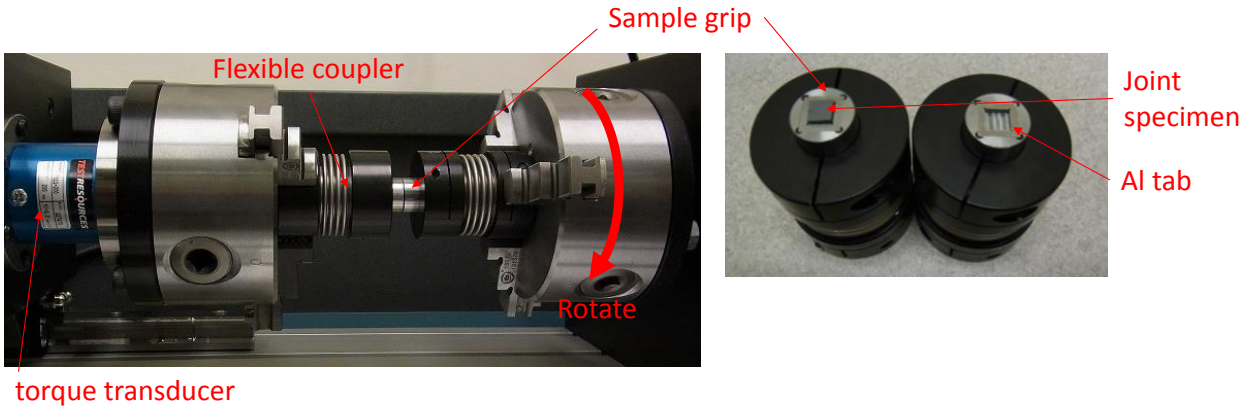

Figure 3. Appearance of torsional test system used to evaluate shear strength of joint specimens.

Results and Discussions

Images of the bonding plane taken using an acoustic scanning microscope are shown in Fig. 4. The image contrast shows amplitude change in the signal's gated area which is used to graphically display differences in the part's structure. Depending on the scan setup and type, this can show signal phase changes (an indicator of extreme acoustic impedance change) and/or reflectors showing the presence of defects such as pores and cracks. The left image shows significant contrast across the area, meaning that the bonding quality is non-uniform. On the other hand, contrast of the right image is uniform, showing absence of significant processing defects or non-uniformity in adhesion at this magnification. Only bonded plates with adequate uniformity confirmed by the ultrasonic imaging were machined into the torsional hourglass specimens used in this study.

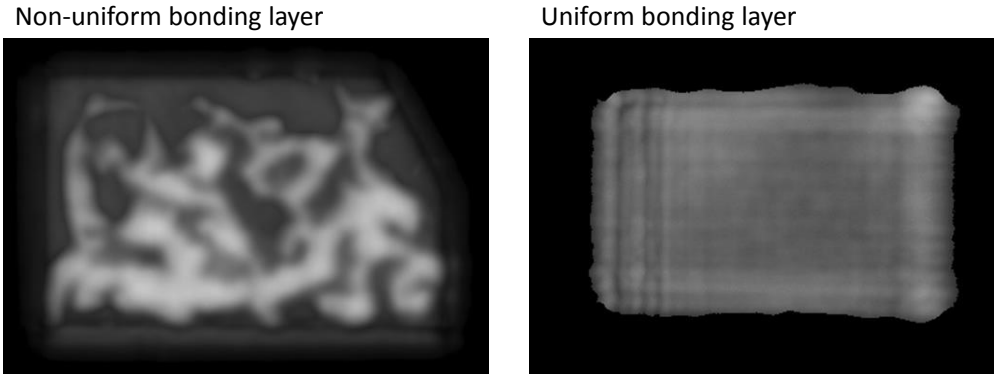

Figure 4. Acoustic images of SiC bonding plates with non-uniform and uniform qualities. The plate size was ~20 mm × ~30 mm.

Figure 5 shows a typical secondary electron image of the polished cross-section of the joint. The typical thickness of the bonding layer was ~10 μm. No processing defects such as cracks were observed in the CVD SiC substrates. Comparison of polished surface and the surface of the torsional test specimen for this SiC joint is shown in Fig. 6. No obvious pore larger than 100 μm was found in the polished surface. However, large pores were clearly found on the surface of the torsion specimen. The bonding layer and the CVD SiC substrate near the joint interface was locally damaged, likely during machining of the torsion specimen.

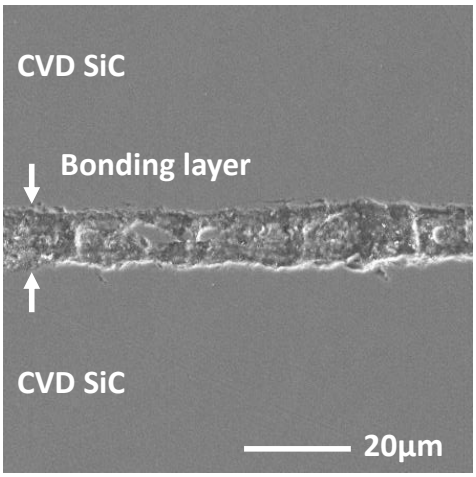

Figure 5. Cross-sectional secondary electron image of the SiC joint.

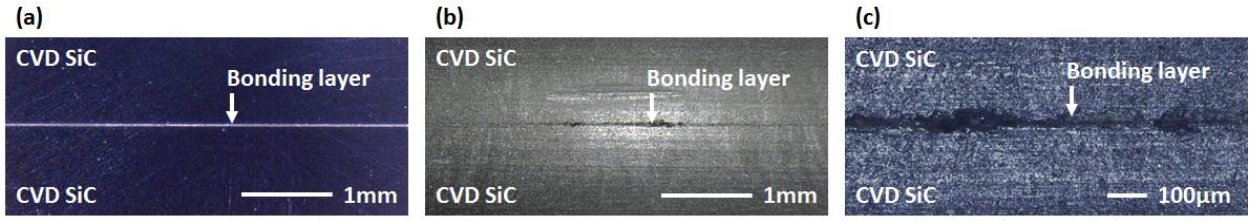

Figure 6. Optical micrographs of the SiC joint: polished surface (a), and surface of the torsion specimen (b) and (c).

Results of torsional shear tests are shown in Fig. 7. The graph shows both average strengths and individual data for each specimen tested. The error bars indicate ± one standard deviation. Similar average shear strengths of ~10 MPa were obtained for the three different size specimens. The scatter in shear strength appeared to be very significant, e.g., more than 30% of the average strength for all cases, making detailed discussion of size effect on the strength difficult. Optical micrographs of torsional tested specimens are shown in Fig. 8. It is important to note that all the tested specimens exhibited shear failure at the bonding plane as shown in the images, showing the lack of specimen size effect on the fracture behavior of the joints.

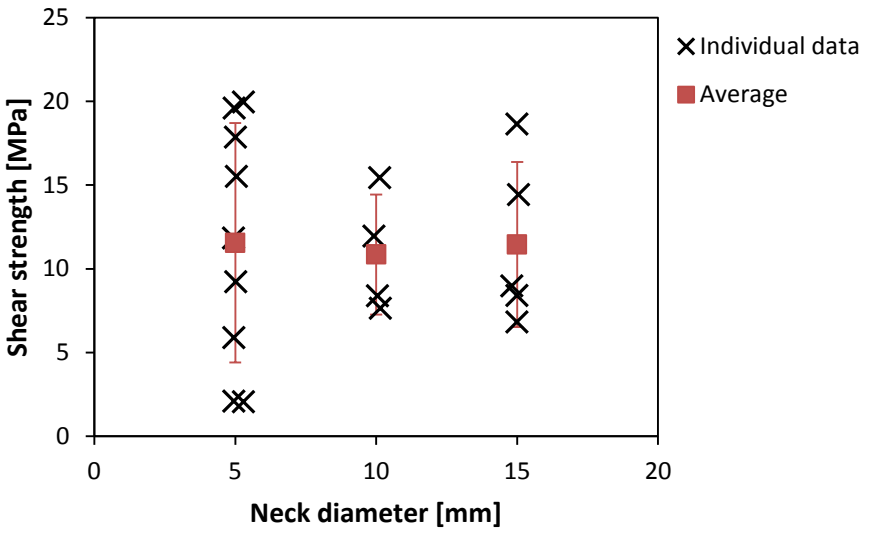

Figure 7. Torsional shear strength of SiC joints with different specimen sizes.

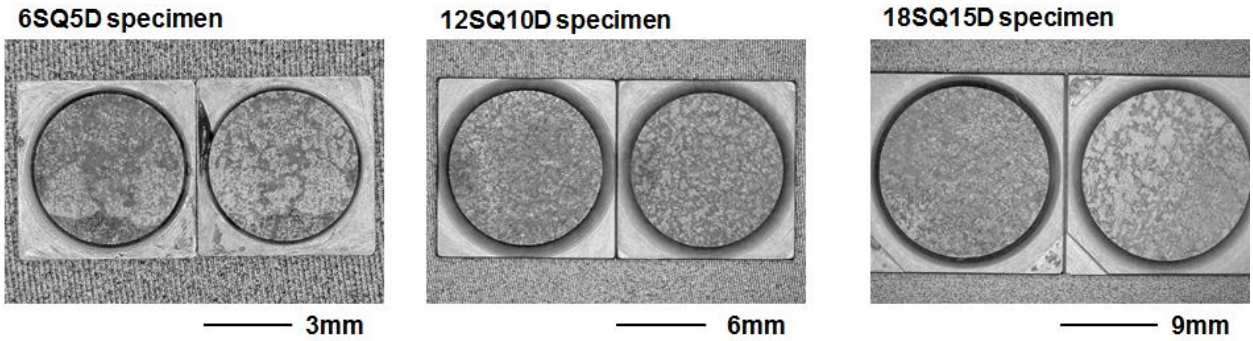

Figure 8. Typical fracture appearances of torsional tested specimens. The specimen IDs are shown in Fig. 1, and scale marks under each photo indicate sizes for the tested specimens.

Again, the large scatter in the torsional shear strength make detailed discussion on the specimen size effect a challenge. Such scatter, particularly for small specimen dimensions, may be at least partially attributed to the damage within bonding layer during machining in the torsion specimen surface, as shown in Fig. 6. The maximum shear stress is applied at the circumference of the bonding layer during the testing in the case that the joint is ideally uniform and the bonding layer has similar mechanical properties to the SiC substrate, according to the stress analysis [3]. Ferraris et al. also reported large data scatter in the torsional tests due to the surface defects [4].

In previous works [1, 2, 4, 5], two types of joint specimens were used. One was the specimen bonded prior to machining (Type A), which is same procedure as used to prepare the specimens in this work. The other was for the specimens bonded following machining (Type B). Ideally, machining defects on the surface of bonding layer can be avoidable by use of the specimen Type B. The one standard deviation for torsional shear strengths for the specimen Type A varied from 2 to 43% of the average strength [2], likely depending on the surface conditions and material uniformity. In the Type B specimens, unexpected up to 28% of large deviations of the strength were also observed [1, 2, 4, 5]. Based on the current knowledge, use of the specimen Type B might not significantly reduce the data scatter in the torsion test. Investigation of the size effect based on fracture statistics is one possible solution.

References

[1] M. Ferraris, M. Salvo, V. Casalegno, A. Ventrella, M. Avalle, Int. J. Appl. Ceram. Technol. 9 (2012) 795–807.
[2] Y. Katoh, L.L. Snead, T. Cheng, C. Shih, W.D. Lewis, T. Koyanagi, T. Hinoki, C.H. Henager Jr., M. Ferraris, J. Nucl. Mater., 448 (2014) 497-511.
[3] H.C. Jung, T. Hinoki, Y. Katoh, A. Kohyama, J. Nucl. Mater., 417 (2011) 383-386.
[4] M. Ferraris, A. Ventrella, M. Salvo, M. Avalle, F. Pavia, E. Martin, Composites: Part B 41 (2010) 182-191.
[5] M. Ferraris, M. Salvo, V. Casalegno, A. Ventrella, Int. J. Appl. Ceram. Technol., 9 [4] (2012) 795–807.

3.2 LOW ACTIVATION JOINING OF SiC/SiC COMPOSITES FOR FUSION APPLICATIONS: MODELING MINIATURE TORSION TESTS WITH ELASTIC AND ELASTIC-PLASTIC MODELS – C.H. Henager, Jr., B.N. Nguyen, R.J. Kurtz, T. Roosendaal, and B. Borlaug; (Pacific Northwest National Laboratory[1], Richland, WA, USA); M. Ferraris, (Politecnico di Torino, Torino, Italy); A. Ventrella[2], and Y. Katoh, (Oak Ridge National Laboratory)

OBJECTIVE

Mechanics damage models that have been modified to better match torsion experiments involving elastic and elastic-plastic materials are presented to help formulate a path forward with joint testing and analysis for SiC materials in nuclear environments. This report extends the analysis from the last reporting cycle.

SUMMARY

The use of SiC and SiC-composites in fission or fusion environments requires joining methods for assembling systems. The international fusion community designed miniature torsion specimens for joint testing and irradiation in test reactors with limited irradiation volumes. These torsion specimens fail out-of-plane when joints are strong and when elastic moduli are within a certain range compared to SiC, which causes difficulties in determining shear strengths for joints or for comparing unirradiated and irradiated joints. A finite element damage model was developed that indicates fracture is likely to occur within the joined pieces to cause out-of-plane failures for miniature torsion specimens when a certain modulus and strength ratio between the joint material and the joined material exists. The model was extended to treat elastic-plastic joints such as SiC/epoxy and steel/epoxy joints tested as validation of the specimen design.

PROGRESS AND STATUS

Introduction

The international fusion materials community is currently irradiating several joint types and compositions in the HFIR reactor at ORNL [1]. PNNL is working with Politecnico di Torino and ORNL using miniature torsion specimens (hourglass samples) that have been specifically designed for pre- and post-irradiation joint shear strength testing [2]. Many of the joints fail out-of-plane, or in the base CVD-SiC material, during torsion testing, but some do not. To elucidate how and where cracks can initiate and propagate in the torsion joint specimens, finite element analyses of these specimens subjected to torsion were performed using a continuum damage mechanics (CDM) model previously developed at PNNL for elastic materials for which any nonlinearity in stress/strain response is due solely to damage and not to other irreversible processes such as plasticity [3]. The CDM model was implemented in the ABAQUS® finite element code via user subroutines. Comparative analyses of the torsion joints using ABAQUS® and the damage model were conducted considering typical mechanical properties of CVD-SiC and different mechanical behaviors of the joint material manifested through the assumed stress/strain responses up to failure. Additionally, since SiC/epoxy and steel/epoxy joints were used to validate the miniature torsion specimen design, a CDM elastic-plastic model was added to this analysis and those results are presented.

Model Formulation

Approach

This section summarizes the damage model and method for predicting crack initiation and propagation [3-5] in the joined CVD-SiC or steel material together with a thin joint region consisting of either Ti_3SiC_2/SiC of varying modulus and strength or a hypothetical brittle epoxy and an elastic-plastic epoxy. Considering damage in an elastic and damageable material, for which any nonlinearity in stress/strain response is due solely to damage and not to other irreversible processes, can be described by a scalar variable, D, that can be related to the microcrack density or microcrack volume fraction, or simply a parameter to

[1] PNNL is operated for the U.S. Department of Energy by Battelle Memorial Institute under Contract DE-AC06-76RLO 1830.

phenomenologically quantify the level of damage accumulation in the material [4]. Damage affects the material stiffness according to a stiffness reduction law. Using the concepts of thermodynamics of continuous media [4, 6], a thermodynamic potential is defined to derive the constitutive relations and the thermodynamic force associated with the damage variable. This damage model uses the density of the elastic deformation energy as the thermodynamic potential that provides a coupling between damage and elasticity. A damage criterion dependent on a damage threshold function is defined and the damage evolution law is obtained. Damage evolves with the deformation according to the damage evolution law until a critical (saturation) state at which $D=D_{\mathrm{cr}}$ $(0<D_{\mathrm{cr}}<1)$ and failure occurs. D_{cr} is small for brittle materials, and this is the case for ceramic materials studied in this work. In this work, failure at damage saturation ($D=D_{\mathrm{cr}}$) leading to crack initiation and propagation is modeled by a vanishing finite element technique [7] that reduces the stiffness and stresses of the failed element to zero [3, 8].

As discussed in Refs. [9, 10] miniature torsion joints were made use Araldite AV119 epoxy between CVD-SiC and a 316-grade stainless steel. AV119 was used to bond these materials after acetone and ultrasonically cleaned surfaces were prepared. The epoxy was cured for 1 h at 130°C [9]. The torsion tests for these samples were performed in the same manner as all the other torsion testing. In addition, simple compressions tests were performed [10] on cylinders of cured AV119 epoxy to establish the mechanical properties of this toughened adhesive material [11, 12]. Materials such as 316SS and AV119 epoxy exhibit pronounced nonlinear behaviors controlled by plasticity and damage. Therefore, an elastic-plastic damage description is used in this work to model the nonlinear responses of these materials to monotonic loading up to failure. Specifically, the model used here is from a model used by Nguyen and Kunc [13] that describes the elastic-plastic damage behavior of a thermoplastic matrix in a long-fiber thermoplastic composite. In this model, the modified Ramberg-Osgood relation captures the material nonlinear stress-strain response:

$$\bar{\varepsilon} = \frac{\bar{\sigma}}{E\,(1-D)} + \frac{\sigma_0}{E}\left(\frac{\bar{\sigma}}{\sigma_0(1-D)}\right)^n = \frac{\tilde{\bar{\sigma}}}{E} + h\,\tilde{\bar{\sigma}}^n \tag{1}$$

where *D* is the isotropic damage variable, $\bar{\sigma}$ and σ_0 are the equivalent and reference stresses, respectively. The hardening *h* is given by $h=\sigma_0^{1-n}/E$ where *E* and *n* are the elastic modulus and power-law exponent. The "tilde" symbol denotes an effective quantity based on the principle of strain equivalence [14]. The equivalent stress can be expressed in terms of the equivalent plastic strain as:

$$\bar{\sigma} = (1-D)\,k\,(\bar{\varepsilon}^{\mathrm{p}})^{1/n} \tag{2}$$

where $k=(1/h)^{1/n}$ is the hardening coefficient. Using the deformation theory of plasticity and assuming proportional loading, an evolution law for *D* is sought in terms of stress and plastic strain quantities. To this end, we use the Lemaitre-Chaboche three-dimensional damage model in deformation for isotropic hardening materials [15] that expresses the damage variable increment in terms of the equivalent plastic strain increment as:

$$dD = \frac{D_{\mathrm{c}}}{\bar{\varepsilon}_{\mathrm{p}}^{\mathrm{R}} - \bar{\varepsilon}_{\mathrm{p}}^{\mathrm{D}}}\left(\left[\frac{2}{3}(1+\nu) + 3(1-2\nu)\left(\frac{\sigma^{\mathrm{h}}}{\bar{\sigma}}\right)^2\right] d\bar{\varepsilon}^{\mathrm{p}}\right) \tag{3}$$

where $\bar{e}_{\mathrm{p}}^{\mathrm{D}}$ and $\bar{e}_{\mathrm{p}}^{\mathrm{R}}$ are the equivalent plastic strains at damage initiation and at rupture, respectively, and D_{c} is the value of *D* at rupture. n is Poisson's ratio, and σ^{h} the hydrostatic stress.

This elastic-plastic damage model was implemented in ABAQUS via user subroutines to describe the constitutive behaviors of the AV119 joint [12] and of the joined 316SS material [16] in the ABAQUS analyses of torsion specimens. Figs. 1b and 1c show the uniaxial stress/strain curves of 316SS and AV119 that are well captured by this elastic-plastic damage model.

Results

Model Results

The damage models are implemented in ABAQUS® as a finite element analysis of the miniature torsion joint specimen. In order to investigate specimen failure for different types of joints, different material properties of the joints were considered and are reflected through the assumed stress/strain responses up to failure in the damage models. In addition, typical mechanical properties of CVD-SiC and nominal steel (316SS) as the joined halves in the experimentally observed range were assumed. Figure 1 and Table 1 present the mechanical properties assumed in this parametric study. There are 5 different behaviors (denoted by case study numbers 1 through 5) considered for the Ti_3SiC_2/SiC composite joint differentiated by their calculated modulus and assumed failure strength. In addition, a similar analysis was performed for two epoxy joined CVD-SiC and steel specimens. The damage variable value at saturation was taken to be 0.2 for all the ceramics while it was considered to be 0.4 for the brittle epoxy (case 6) leading to an epoxy strength of 120 MPa and failure strain of 0.02 and 0.48 for an elastic-plastic epoxy (AV119, case 7) with a strength of 80 MPa at 0.05 failure strain [9, 10, 12].

Damage analyses were conducted for all the torsion joint specimens made of the simulated materials listed in Table 1, which are based on the calculated modulus values for the various joints with differing amounts of porosity. The predicted failure patterns for all the studied cases are gathered in Figure 2. Cases 1 and 5 for the Ti_3SiC_2/SiC joint represent the extreme cases for the most dense joint in Case 1 and the least dense joint in Case 5. The failure location changes from within the CVD-SiC joined materials (Case 1) to within the joint plane (Case 5). Cases 2 and 3 represent Ti_3SiC_2/SiC joints made at 30 MPa and 20 MPa, respectively, which are increasingly less stiff than the joined CVD SiC. For both of these cases, failure is predicted to initiate in the joint but then develop into the SiC sample resulting in out-of-plan failure. Case 4 for the 10 MPa Ti_3SiC_2/SiC joint is now only about 1/3 as stiff as the CDV-SiC and the simulation indicates a mixture of failure within the joint and within the sample. Experimentally, these 10 MPa joints sometimes fail within the joint and sometimes within the CVD-SiC. Case 5 is predicted to fail within the joint and experiments confirm this failure mode. The brittle epoxy joint (Case 6) also always exhibits in-plane failure.

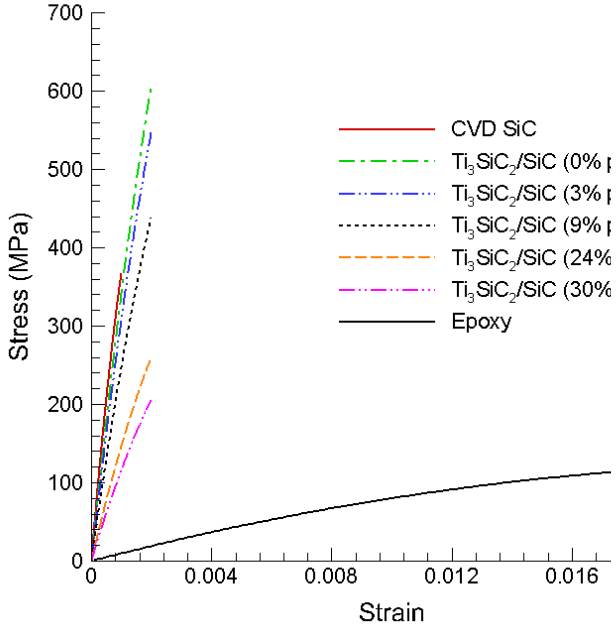

(a)

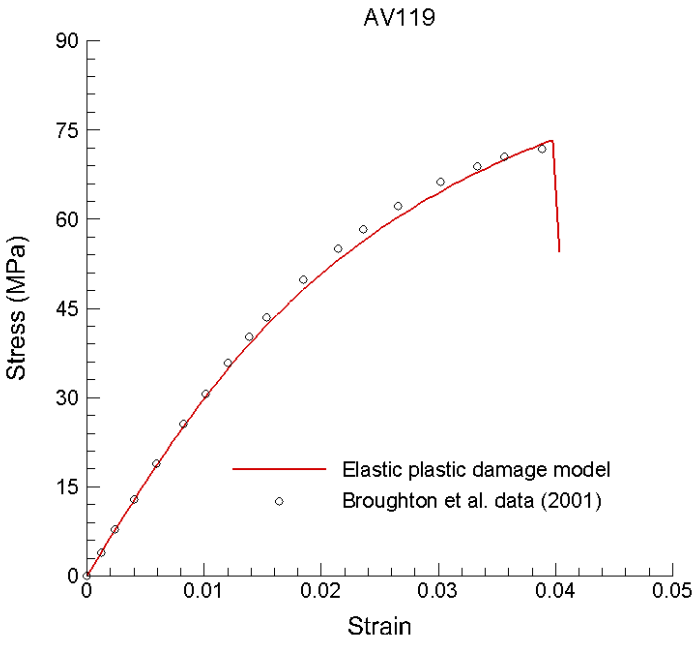

(c)

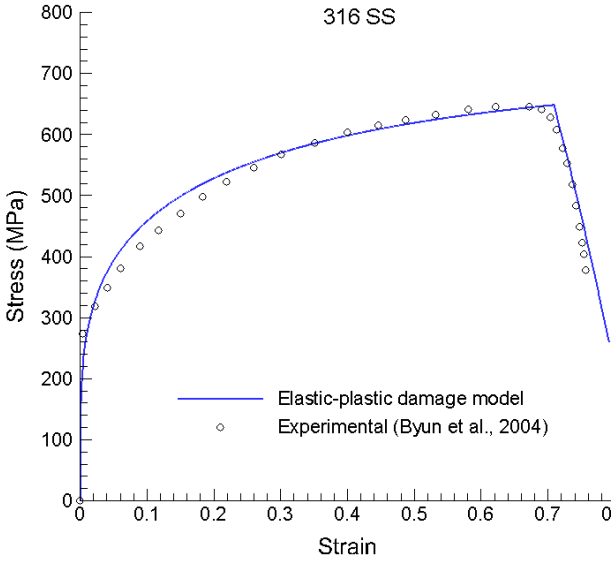

(b)

Figure 1. Uniaxial stress/strain responses considered for (a) an elastic damage model for CVD-SiC and different types of joint material, including a brittle epoxy, (b) an elastic-plastic damage model for 316SS [16] and (c) an elastic-plastic damage model for AV119 epoxy [12]. See Tables 1 and 2 for model parameters.

Table 1. Mechanical properties of the CVD-SiC and joint material assumed for the analysis.

Material	Case Study No.	Elastic Modulus (GPa)	Poisson Ratio	Strength (MPa)	Failure Strain	Damage Variable Critical Value
CVD-SiC	–	460	0.2	368	0.001	0.2
316SS	–	193	0.3	645	0.62	0.7
Ti_3SiC_2/SiC (0% porosity)	1	380	0.2	608	0.002	0.2
Ti_3SiC_2/SiC (3% porosity)	2	343	0.2	548	0.002	0.2
Ti_3SiC_2/SiC (9% porosity)	3	275	0.2	440	0.002	0.2
Ti_3SiC_2/SiC (24% porosity)	4	163	0.2	260	0.002	0.2
Ti_3SiC_2/SiC (30% porosity)	5	129	0.2	206	0.002	0.2
Epoxy (Brittle)	6	10	0.3	120	0.02	0.4
Epoxy 2 (AV119)	7					

Table 2. Parameters of the elastic-plastic models identified for 316SS and AV119.

Materials	E (MPa)	s_0 (MPa)	v	n	$\bar{\varepsilon}_p^D$	$\bar{\varepsilon}_p^R$	D_c
316SS	193000	150	0.3	4.3	0.02	0.42	0.7
AV119	3200	110	0.34	3	0	0.01	0.45

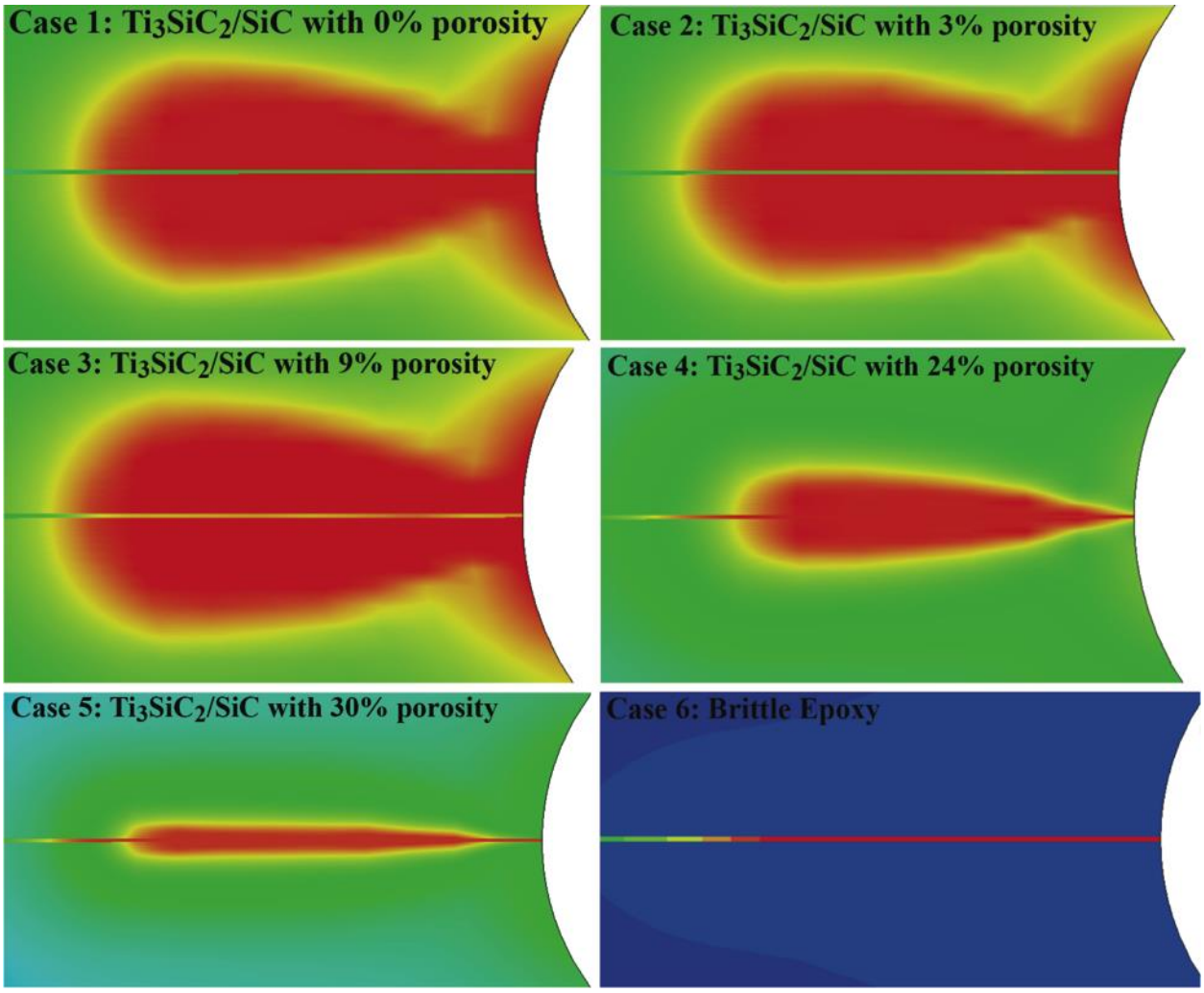

Figure 2. Predicted fracture patterns (red regions) using an elastic damage model for the torsion joint specimens made of different joint materials with mechanical properties listed in Table 1. Cases 1, 2, and 3 fail within the CVD-SiC base material (out-of-plane), while case 4 sometimes fails within the joint . Case 5 always fails in the joint region. Case 6 shows results from the brittle epoxy simulation, which also fails within the joint without exception.

As recognized by Ferraris et al. [10] the toughened adhesive epoxy AV119 is not a brittle material but behaves as an elastic-plastic material and, therefore, must be treated accordingly. Figure 1 and Table 2 together with the elastic-plastic damage model provide the necessary tools to address this issue. In addition to using an elastic-plastic response, the joint thickness in the model was modified to more closely simulate the work performed in Torino. Figure 3 shows the predicted failure locations for a 50-μm thick AV119 joint between CVD-SiC and 316SS. The CVD-SiC is treated elastically as before but in this case the AV119 and 316SS are treated using the elastic-plastic model developed here. The model results validate what the torsion testing observed, namely, that the torsion specimens fracture in the plane of the joint when bonded using AV119 adhesive epoxy regardless of the specimen material.

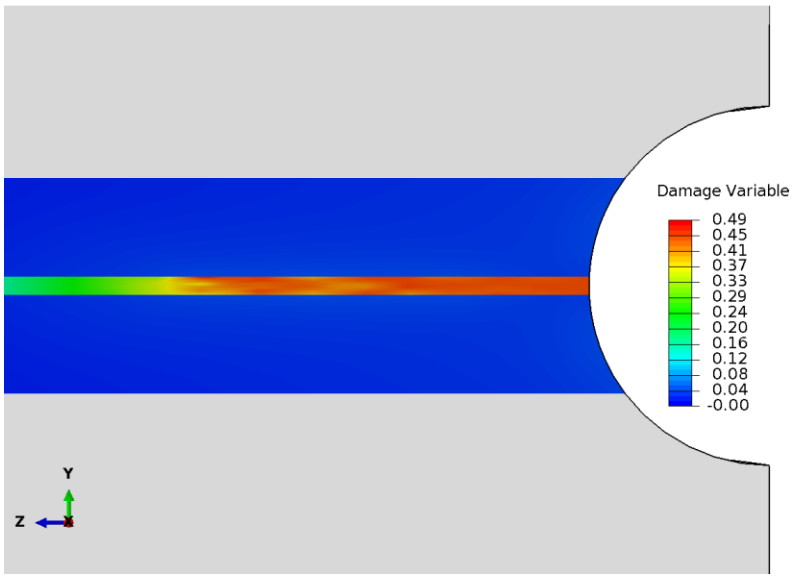

(a)

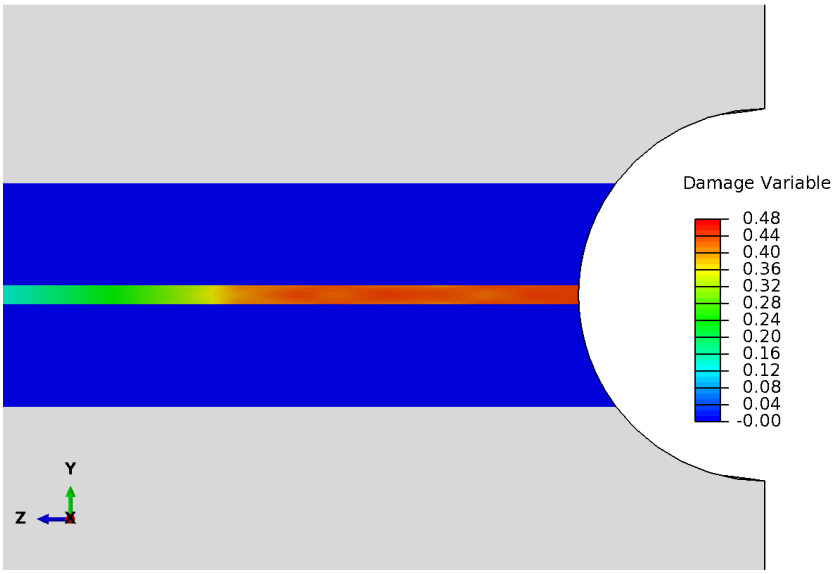

(b)

Figure 3. Predicted fracture patterns using an elastic-plastic damage model for the AV119 adhesive epoxy and for 316SS. Shown in (a) is the predicted fracture for CVD-SiC joined with AV119 where the epoxy is elastic-plastic and the SiC is elastic. Shown in (b) is the case for both materials obeying the elastic-plastic damage model for 316SS joined with AV119 epoxy. In all cases the failure occurs within the epoxy joint.

Discussion

Model Predictions and Comparisons

The damage models were created to help understand the fracture results from the torsion specimens that exhibited non-planar fracture that was not truly reflective of joint properties. Rather, the literature refers to this data as “torsional shear resistance” [1, 2, 17-20] when the torsion specimen fails in the base material, or out-of-plane. The damage model must be able to simulate the stress-strain curves for the constitutive materials; otherwise the model would not be reasonable. The curves shown in Fig. 1 using the data in

Tables 1 and 2 capture the material elastic constants as well as the failure strengths and are very reasonable assumptions. The accuracy of the damage modeling is predicated on the accuracy of the stress-strain data and, even though this model data is not completely precise, the expected results from carefully applying the model are expected to show the correct trends.

The models, both the elastic and elastic-plastic methods, capture the key observation, namely that there is a transition from planar to non-planar fracture over a range of elastic moduli and strength values. High strength and high moduli materials are predicted to fail out-of-plane and within the base material, whereas much lower modulus and lower strength epoxy (compared to CVD-SiC and 316SS) fails in plane. Intuitively, it is anticipated that low modulus epoxy will behave differently compared to high modulus Ti_3SiC_2/SiC in terms of load sharing with the CVD-SiC base material. In fact, one thought (gedanken) experiment is to imagine the entire miniature torsion specimen machined from a single piece of CVD-SiC and then to try to predict where it will fail. Probabilistic brittle fracture mechanics predicts that it will fail somewhere in the specimen that contains a combination of the largest flaw and the highest tensile/shear stresses, which will not necessarily coincide with the central plane of the torsion specimen. Thus, a high strength, high modulus joint may not fail in the plane of the joint either. As shown in Fig. 2 load sharing with the CVD-SiC forces a majority of the damage to occur within the base CVD-SiC material and failure is predicted to occur out-of-plane of the joint.

However, this load sharing is a function of the modulus difference between the joint and base material. The model predicts a high degree of load sharing and CVD-SiC damage for a joint modulus greater than about 200 GPa and a minimal amount of load sharing with highly localized (planar) fracture for moduli 100 GPa and lower (Fig. 2). This is in good agreement with the observed experimental data for the joints tested at Torino. In addition, the predicted failure strengths in shear match quite well with measurements from ORNL and Torino [1, 17]. The ORNL data for the unirradiated Ti_3SiC_2/SiC joints indicated a torsional shear resistance value of 117 GPa ± 10 GPa, which agrees well with the model data of 104 GPa [1]. Note that this predicted strength value follows from the CVD-SiC damage model that is determined from the assumed CVD-SiC mechanical properties. Thus, the model predicts that the torsion shear test will fail in the CVD-SiC material and that the torsional shear resistance of the sample will be 104 GPa because that is the predicted shear strength of the CVD-SiC simulated here. This failure stress could be increased if stronger base material was provided. Note that the NITE materials tested in Ref. [1] fail at much higher shear strengths compared to the CVD-SiC and this is attributed to the higher strength of the NITE SiC. However, the main point is that for certain joint material combinations that the torsion test will fail at the shear strength limit of the base material and will not provide information regarding the shear strength of the joint material. This is observed in the torsion testing and is predicted by the elastic-damage model.

The epoxy joined data from Politecnico di Torino is more complex. Results indicate a shear fracture strength of 36 MPa, which agrees well with the model prediction of about 38 GPa[2] for the brittle epoxy material (Case 6 and Fig. 4). In this case, where the epoxy modulus is only a fraction of the CVD-SiC or 316SS the fracture path is in the plane of the joint in the epoxy material. Thus, this test will measure a true shear stress value. However, since AV119 toughened adhesive epoxy is not a linear elastic brittle material, the elastic damage model is not appropriate and an elastic-plastic model was developed based on mechanical property data for AV119 and 316SS as discussed. This model predicts a shear failure strength of 28 MPa for a 50-µm thick joint region of AV119 (Figs. 3 and 4), which is less than the calculated value of 36 MPa[1]. However, Ferraris et al. also report a value of 66 MPa ± 10 MPa for AV119-joined CVD-SiC specimens where the shear strength is calculated using Eq. 2, which is inappropriate as discussed in Ref. [10]; rather it is suggested that this value be reduced by 25 to 30% and a value of 45 MPa is suggested as a more accurate value to report. However, this seems to be an arbitrary choice and the results here suggest that a value less than 30 MPa is more accurate. The elastic-plastic damage model provides that prediction based solely on the accuracy of the assumed mechanical properties of AV119 adhesive epoxy taken from Ref. [12]. Since the strength of AV119 depends on the curing time and temperature, etc., the values determined by the elastic-plastic model might differ from other shear strength datasets. However, as can be seen in Fig. 4b the predicted shear stress curves are nonlinear

[2] Personal Communication from Prof. M. Ferraris of Politecnico di Torino. They used AV119 Epoxy with an elastic modulus of 2.8 GPa and Poisson ratio of 0.4. They obtained in-plane shear failures for all tests and calculated a shear strength of 36 MPa ± 8 MPa.

and the use of linear models cannot accurately capture this behavior [10]. Thus, the approach developed here is a much-improved methodology for analyzing miniature torsion test results in the future.

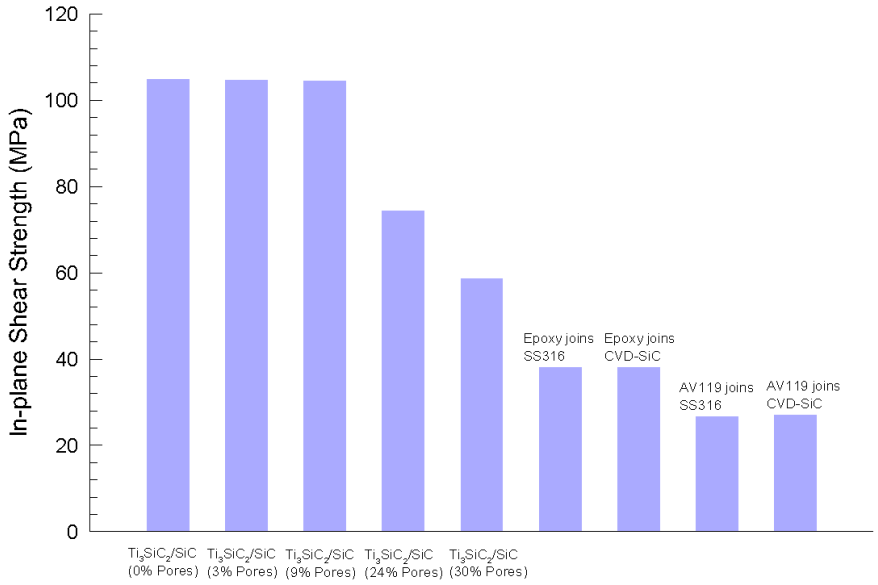

(a)

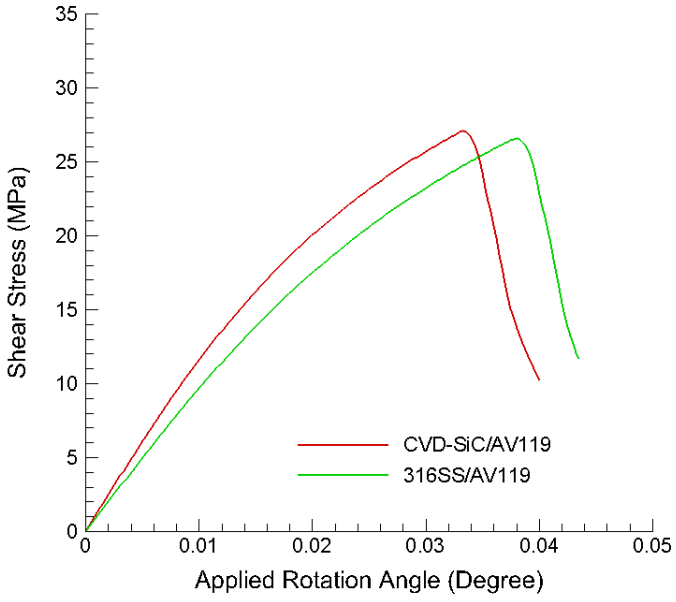

(b)

Figure 4. Graph showing the predicted maximum shear stresses at fracture in (a) for all damage model simulations. Shown in (b) is the predicted evolution of the maximum in-plane shear stresses with applied rotation angle for the elastic-plastic AV119 cases from Fig. 3.

Data Interpretation and Torsion Test Future

Miniature torsion specimens often fail within the joint body or out of the joint plane when the torsion sample base material is a ceramic, such as CVD-SiC, and the joint is strong. This study developed elastic and elastic-plastic damage models that demonstrated that for a wide range of joint moduli and strengths that out-of-plane failure is observed (and predicted) until the joint modulus falls below about 1/3 of the CVD-SiC modulus. The model indicates that out-of-plane fracture is due to load sharing between the joint material and the CVD-SiC causing high shear stresses to develop within the neck region of the torsion sample CVD-SiC (or other ceramic) that surpass the shear strength of the joined material. Since these fractures are probabilistic in nature, there is no guarantee that failures will occur within the plane of a joint for strong, stiff ceramic or glass-ceramic joints. In fact, since the highly stressed volume of the base material is much greater than the volume of the joint material this almost guarantees that for strong, stiff joints failure will occur within the joined ceramic. This finding is documented by many such tests with Ti_3SiC_2/SiC joints that are stronger and almost as stiff as CVD-SiC. Without exception, out-of-plane failure modes were observed for these joints tested in torsion. Joints with intentionally introduced porosity also failed out-of-plane until the joint modulus, which is reduced by the porosity, became less than about 1/3 of the CVD-SiC modulus. At that point in-plane shear failures were observed. However, these results notwithstanding, miniature torsion specimens can still be useful for identifying joint degradation following in-reactor radiation damage by observing either fracture mode changes or observable microstructural changes. The use of these specimens for true joint shear strength measurements is problematic, however. The elastic and elastic-plastic damage models appear to be useful methods that can provide valuable insights into the fracture behavior of the miniature torsion samples.

Future Work

The in-reactor miniature torsion sample irradiation results from ORNL display a failure mechanism that is not included in the model yet, namely, the failure of the joint/CVD-SiC interface. The model assumes a strongly bonded interface between the joint and CVD-SiC and no evolution of that bond is allowed. Future model implementations will treat the interface as a separate material region with an identifiable strength.

Acknowledgements

This research was supported by Office of Fusion Energy Sciences, U.S. Department of Energy (DOE) under Contract DE-AC05-76RL01830.

References

[1] Katoh, Y., L.L. Snead, T. Cheng, C. Shih, W.D. Lewis, T. Koyanagi, T. Hinoki, C.H. Henager Jr, and M. Ferraris, J. Nucl. Mater., 2014, 448(1-3), 497-511.
[2] Jung, H.-C., T. Hinoki, Y. Katoh, and A. Kohyama, J. Nucl. Mater., 2011, 417(1-3), 383-386.
[3] Nguyen, B.N., B.J. Koeppel, S. Ahzi, M.A. Khaleel, and P. Singh, J. Am. Ceram. Soc., 2006, 89(4), 1358-1368.
[4] Lemaitre, J. and J.L. Chaboche, Journal de Mecanique Appliquee, 1978, 2(3), 317-65.
[5] C. H. Henager, J., B.N. Nguyen, R.J. Kurtz, T. Roosendaal, B. Borlaug, M. Ferraris, A. Ventrella, and Y. Katoh, in Fusion Reactor Materials Program Semiannual Progress Reports, Vol. 56, F. Wiffen, R. Godfrey, and B. Waddell, Editors, 2014, ORNL: Oak Ridge, TN, p. 79-93.
[6] Maugin, G.A., The Thermomechanics of Plasticity and Fracture. 1992, Cambridge, UK: Cambridge University Press.
[7] Tvergaard, V., Int. J. Fract., 1986, 31(3), 183-209.
[8] Nguyen, B.N., V. Kunc, J.H. Phelps, C.L. Tucker III, and S.K. Bapanapalli, in 23rd Technical Conference of the American Society for Composites 2008, September 9, 2008 - September 11, 2008, 2008, Memphis, TN, United states: DEStech Publications Inc.
[9] Ferraris, M., M. Salvo, V. Casalegno, M. Avalle, and A. Ventrella, Int. J. Appl. Ceram. Technol., 2012, 9(4), 795-807.
[10] Ferraris, M., A. Ventrella, M. Salvo, and D. Gross, Int. J. Appl. Ceram. Technol., 2014, 11(2), 394-401.

[11] Xu, B., "Fracture Mechanisms and Failure Criteria of Adhesive Joints and Toughened Epoxy Adhesives," in School of Engineering and Materials Science. 2010, Queen Mary, University of London: University of London, p. 225.
[12] Broughton, W.R., L.E. Crocker, and J.M. Urquhart, "Strength of Adhesive Joints: A Parametric Study," 2001, T. National Physical Laboratory, Middlesex, TW11 0LW, UK, NPL Materials Centre, National Physical Laboratory, Teddington, Middlesex, TW11 0LW, UK, p. 41.
[13] Nguyen, B.N. and V. Kunc, Int. J. Damage Mech., 2010, 19(6), 691-725.
[14] Lemaitre, J., in Continuum Damage Mechanics of Materials and Structures O. Allix and F. Hild, Editors, 2002, Elsevier Science Ltd: Oxford, UK, p. 235-258.
[15] Lemaître, J. and J.-L. Chaboche, Mécanique des Matériaux Solides. 1985, Paris, France: Dunod.
[16] Byun, T.S., N. Hashimoto, and K. Farrell, Acta Mater., 2004, 52(13), 3889-3899.
[17] Ferraris, M., A. Ventrella, M. Salvo, Y. Katoh, and D. Gross, Int. J. Appl. Ceram. Technol., 2014, in press.
[18] Hinoki, T., Y. Katoh, L.L. Snead, H.-C. Jung, K. Ozawa, H. Katsui, Z.-H. Zhong, S. Kondo, Y.-H. Park, C. Shih, C.M. Parish, R.A. Meisner, and A. Hasegawa, Mater. Trans., 2013, 54(4), 472-476.
[19] Ferraris, M., M. Salvo, S. Rizzo, V. Casalegno, S. Han, A. Ventrella, T. Hinoki, and Y. Katoh, Int. J. Appl. Ceram. Technol., 2012, 9(4), 786-794.
[20] Ferraris, M., M. Salvo, V. Casalegno, S. Han, Y. Katoh, H.C. Jung, T. Hinoki, and A. Kohyama, J. Nucl. Mater., 2011, 417(1-3), 379-82.

3.3 MAGNESIUM PRECIPITATION AND DIFUSSION IN Mg^+ ION IMPLANTED SILICON CARBIDE —

W. Jiang, H. J. Jung, L. Kovarik, Z. Wang, T. J. Roosendaal, Z. Zhu, D. J. Edwards, S. Y. Hu, C. H. Henager, Jr., R. J. Kurtz (Pacific Northwest National Laboratory[1]), and Y. Wang (Los Alamos National Laboratory)

This extended abstract reports on some of the major results in a paper recently published in the *Journal of Nuclear Materials* [1].

Abstract

As a candidate material for fusion reactor applications, silicon carbide (SiC) undergoes transmutation reactions under high-energy neutron irradiation with magnesium as the major metallic transmutant; the others include aluminum, beryllium and phosphorus in addition to helium and hydrogen gaseous species. Calculations by Sawan *et al.* [2] predict that at a dose of ~100 dpa (displacements per atom), there is ~0.5 at.% Mg generated in SiC. The impact of these transmutants on SiC structural stability is currently unknown. This study uses ion implantation to introduce Mg into SiC. Multiaxial ion-channeling analysis of the as-produced damage state indicates a lower dechanneling yield observed along the <100> axis. The microstructure of the annealed sample was examined using high-resolution scanning transmission electron microscopy. The results show a high concentration of likely non-faulted tetrahedral voids and possible stacking fault tetrahedra near the damage peak. In addition to lattice distortion, dislocations and intrinsic and extrinsic stacking faults are also observed. Magnesium in 3C–SiC prefers to substitute for Si and it forms precipitates of cubic Mg_2Si and tetragonal MgC_2. The diffusion coefficient of Mg in 3C–SiC single crystal at 1573 K has been determined to be $3.8 \pm 0.4 \times 10^{-19}$ m^2/s.

Highlights

Figure 1a shows the inverse fast Fourier transformation (IFFT) of a high-angle annular dark field (HAADF) STEM image for 3C-SiC implanted at 673 K to 9.6×10^{16} ions/cm^2 and annealed at 1573 K for 12 h in Ar. The dark triangles are likely to be tetrahedral voids with 4 non-faulted sides on {111} planes and 6 dislocation-free edges along <110> directions. Similar spatially oriented non-faulted tetrahedral voids have been observed [3] in neutron irradiated 3C-SiC at 1733 K. In addition, the brighter triangles in Figure 1a resemble those observed for energetically favored stacking fault tetrahedra (SFTs) in low stacking fault energy face centered cubic (fcc) metals and alloys. Figure 1b is the fast Fourier transformation (FFT) of Figure 1a, which shows 6 dark spots besides the expected pattern of brighter spots from 3C-SiC. The 6 spots belong to two separate groups of patterns that are labeled with circles and squares and their d-spacing values are determined to be 0.3623 and 0.5070 nm, respectively. The best d-spacing matches suggest that the circled spots are from cubic Mg_2Si with (111) d-spacing of 0.36685 nm and the squared spots from tetragonal MgC_2 with (001) d-spacing of 0.502 nm. Comparison with the known electron diffraction patterns of fcc crystals suggests that Mg_2Si is (110)-oriented, or Mg_2Si (110)//3C-SiC(110). Figure 1b shows only 2 diffraction spots from MgC_2 {001}. In principle, the MgC_2 orientation can be <100> or <hk0> with h and k being equal to or greater than 1. Because strong {110} diffractions from <100>-oriented MgC_2 are not visible off the center line and high indices are not probable, the MgC_2

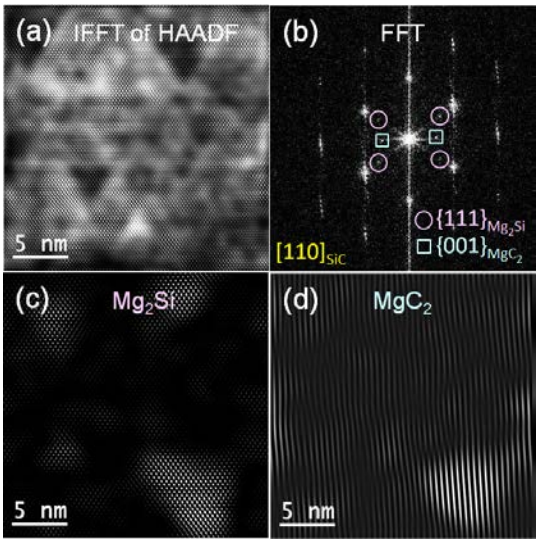

Figure 1. (a) IFFT of HAADF STEM micrograph for cross-sectional view of 3C-SiC irradiated with 200 keV Mg^+ to 9.6×10^{16} ions/cm^2 at 673 K and post annealed at 1573 K for 12 hours in Ar. (b) FFT of the micrograph in (a). (c) and (d) IFFT of precipitates Mg_2Si and MgC_2, respectively [1].

[1] PNNL is operated for the U.S. Department of Energy by Battelle Memorial Institute under Contract DE-AC06-76RLO 1830.

orientation is likely to be <110>, or MgC_2 (110)//3C-SiC(110). Determination of the complete orientation relationships of Mg_2Si and MgC_2 with 3C-SiC requires further studies. Based on the PDF-4+ database, the minimum lattice mismatch for the lowest possible indices suggests Mg_2Si (1 $\bar{1}$0) //3C-SiC(001) and MgC_2(1 $\bar{1}$2)//3C-SiC(001) with mismatches of 2.9% and 3.3%, respectively. Figures 1c and 1d show the images from IFFT operations for the precipitates filtered from specific spots in the FFT pattern (Figure 1b). The bright areas show where the precipitates are in the microstructure. The two large second-phase precipitates (~5 nm in size) are overlapping in the images and are likely located at different depths in the TEM specimen.

Figure 2 shows an Arrhenius plot for the relative peak width square of the ToF-SIMS Mg depth profiles in 3C-SiC implanted with 200 keV Mg^+ ions to 9.6×10^{16} ions/cm^2 at 673 K and isothermally annealed at 1573 K for a cumulative time of 180 and 720 min in Ar, respectively. Mg diffusion is observed at 180 min, below which it is not noticeable. There is significant Mg diffusion into the bulk at 720 min. For a Gaussian distribution $C(x,t) = K[\pi Dt]^{-1/2}\exp(-x^2/4Dt)$ in the dilute limit, the solution to Fick's equation leads to

$$[W(t)]^2 = 4Dt\ln 2 + [W(0)]^2,$$

where $W(t)$ is the FWHM of the peak at time t. The diffusion coefficient D can be determined through a linear fit to the data in the Arrhenius plot. While experimental profiles are not exactly Gaussian, the Mg peaks are assumed to consist of two independent Gaussian portions for the convenience of data analysis. The side towards the surface has implantation damage and the other side towards the bulk is largely a pristine crystal. Linear fits to the data lead to the diffusion coefficients of Mg in 3C-SiC at 1573 K:

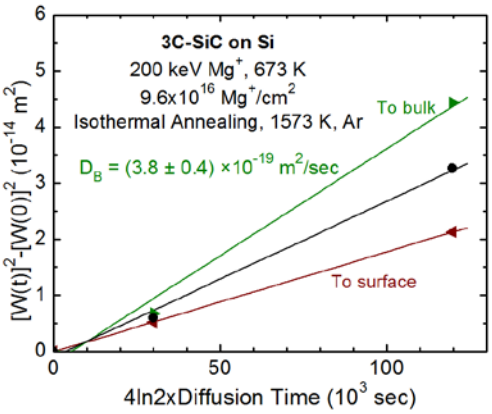

Figure 2. Arrhenius plot for the isothermal annealing data at 1573 K. Two separate diffusion regions (towards the surface and bulk) are considered, along with the FWHM broadening in black [1].

$D_S = (1.8 \pm 0.1) \times10^{-19}$ m^2/sec (towards surface),
$D_B = (3.8 \pm 0.4) \times10^{-19}$ m^2/sec (towards bulk), and
$D_A = (2.8 \pm 0.2) \times10^{-19}$ m^2/sec (average).

D_S and D_B are obtained through doubling the half FWHM on the corresponding side of the peak, while D_A is obtained from the FWHM of the peak. They have the same order of magnitude, but D_B may be most representative for Mg diffusion in unirradiated 3C-SiC bulk.

Acknowledgements

This work was supported by Office of Fusion Energy Sciences, U.S. Department of Energy (DOE) under Contract DE-AC05-76RL01830. A portion of the research was performed using EMSL, a national scientific user facility sponsored by the DOE's Office of Biological and Environmental Research and located at PNNL. Ion implantation was conducted at Ion Beam Materials Laboratory through a partial support from Center for Integrated Nanotechnologies (CINT), a DOE nanoscience user facility jointly operated by Los Alamos and Sandia National Laboratories.

References

[1] W. Jiang, H. J. Jung, L. Kovarik, Z. Wang, T. J. Roosendaal, Z. Zhu, D. J. Edwards, S. Y. Hu, C. H. Henager, Jr., R. J. Kurtz, and Y. Wang, J. Nucl. Mater. 458 (2015) 146.
[2] M. E. Sawan, Y. Katoh, L. L. Snead, J. Nucl. Mater. 442 (2013) S370.
[3] S. Kondo, Y. Katoh, L. L. Snead, Appl. Phys. Lett. 93 (2008) 163110.

3.4 HIGH DOSE IRRADIATION STUDY OF NEWER GENERATION NUCLEAR GRADE SiC COMPOSITES: IRRADIATION EXPERIMENTS - T. Koyanagi, N.O. Cetiner, Y. Katoh (Oak Ridge National Laboratory), T. Nozawa and K. Ozawa (Japan Atomic Energy Agency)

OBJECTIVE

This report describes the technical planning and progress of high dose irradiation experiment on newer generation nuclear grade SiC composites for fusion structural applications.

SUMMARY

A study of high dose neutron irradiation effects on newer generation nuclear grade SiC fiber reinforced SiC matrix composites has started, employing a series of new rabbit capsules. The activity is part of the JAEA-USDOE collaboration, with an irradiation matrix designed to achieve a maximum neutron fluence beyond 100 dpa-SiC for a range of irradiation temperature from ~300 to ~1000°C. Twelve capsules containing three types of SiC composites and high-purity monolithic SiC were prepared. Irradiations for all the rabbit capsules will start in Cycle 457 or 458 at the High Flux Isotope Reactor. Properties to be evaluated include dimensional stability, mechanical, thermal, and electrical properties, and microstructures.

PROGRESS AND STATUS

Introduction

Excellent irradiation stability up to ~40 dpa has been proven for early nuclear grade high-crystalline and near-stoichiometric Hi-Nicalon Type S SiC fiber reinforced SiC composite (SiC/SiC) with SiC-pyrolytic carbon (PyC) multilayer interphase in previous ORNL-JAEA collaborations on fusion materials; no obvious change was observed after the saturation of changes in properties such as swelling, thermal conductivity, and elastic modulus at low neutron fluence [1]. The recent work in this collaboration has accomplished neutron irradiations to greater than 70 dpa in HFIR, and provided an extended understanding of effects of high does neutron irradiation on thermomechanical properties of this SiC/SiC. One of the important findings was irradiation-temperature dependent degradation of ultimate flexural strength of this composite following irradiation to ~70 dpa, which was attributed primarily to fiber damage [2, 3]. In addition, damage to the multilayer interphase was also indicated at low irradiation temperatures.

Based on these results, additional high dose irradiation experiments on newer generation nuclear grade SiC/SiC with different SiC fibers and the same interphase is planned to seek SiC/SiC irradiation tolerant beyond 100 dpa. The SiC/SiC with high-crystallinity and near-stoichiometric Tyranno SA3 SiC fiber is expected to be more irradiation tolerant compared to Hi-Nicalon Type S SiC/SiC due to the difference of grain size and impurity phases, based on a high dose ion-irradiation experiment [4].

This report presents capsule design, the current status of HFIR irradiation, and plans for the post-irradiation evaluations.

Experimental Procedure

Materials

Three types of SiC/SiC were prepared for this irradiation study. All the matrices were fabricated through chemical vapor infiltration (CVI) methods by Rolls-Royce High Temperature Composites Inc. (Customer P.O. Number: 4000124452, Rolls-Royce HTC, Inc Job Number: 13C-529). The first type was a composite with two-dimensional (2D) satin-weave Hi-Nicalon Type S fiber reinforcement in a 0°/90° stacking configuration. The second was a composite with 2D satin-weave Tyranno SA3 fiber reinforcement in a 0°/90° stacking configuration. The third was a composite with 0°/90° cross-ply laminated Ultra SCS fiber reinforcement. The fiber/matrix interphase was PyC for all composites. The nominal PyC thickness was 125 nm for the SiC/SiC with Type S and SA3 fibers, and 400 nm for the SiC/SiC with SCS fiber. The nominal porosities for all the SiC/SiC were less than 15%. Note that

fiber/matrix interphase used in this work was different from that used for the previous series of high dose irradiation experiments so that discussion of effect of the interphase type on the high dose irradiation stability will be possible using two types of Type S SiC/SiC. The SiC/SiC plates were machined to bar specimens with dimensions 25×2.8×1 mm^3. The appearances of the bar specimens are shown in Figs. 1 and 2. The SiC fibers were typically exposed on the surfaces of all the composites.

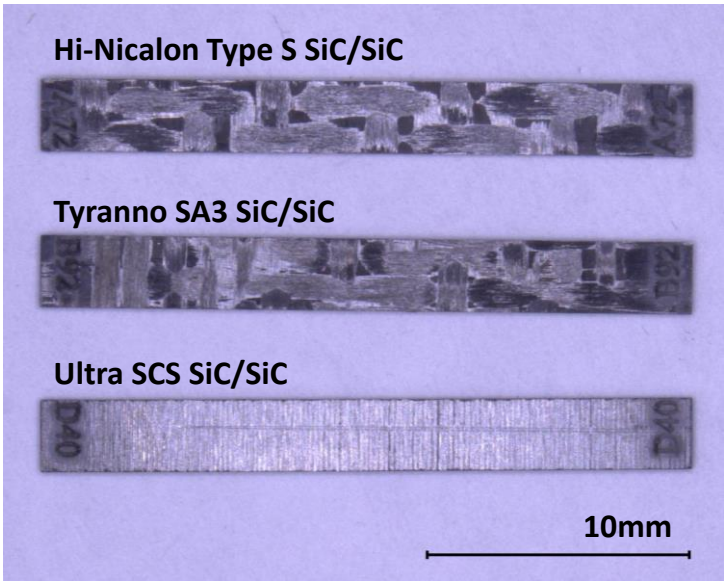

Figure 1. Appearance of SiC/SiC bend bar specimens used for this irradiation study.

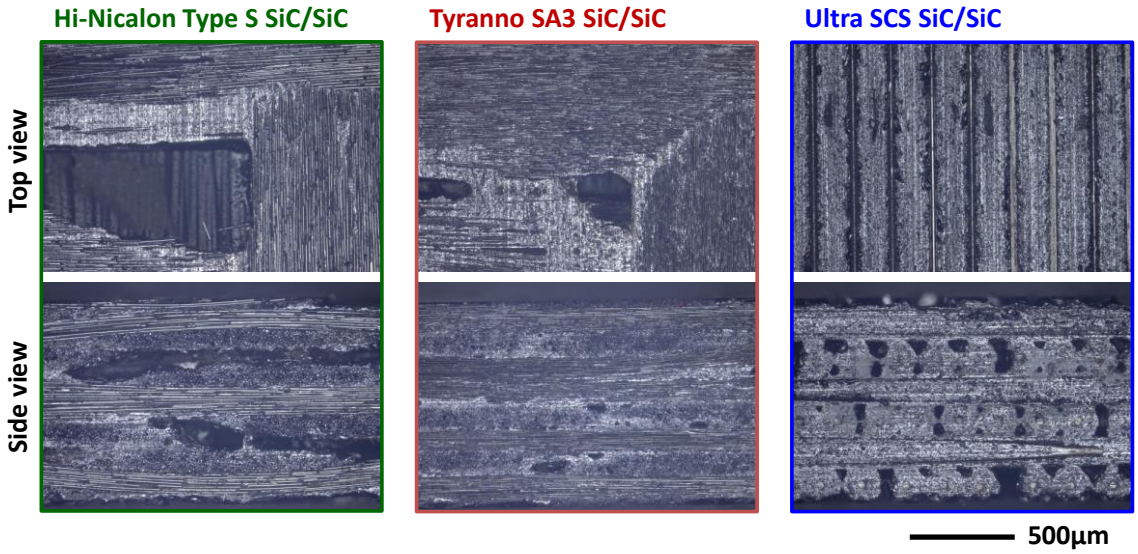

Figure 2. Top and side views of SiC/SiC bend bar specimens.

Irradiation Capsules

Schematic image of a capsule housing configuration is shown in Fig. 3. The specimen holders were made of V-4Cr-4Ti alloy or molybdenum. Each capsule contains 20 composite bar specimens (6 Type S,

7 SA3, and 7 SCS specimens), and 4 monolithic chemical vapor deposited (CVD) SiC (The Dow Chemical Company, High Resistivity Grade) specimens. Additional CVD SiC materials were located between SiC/SiC specimens and the holder to prevent any contamination of the specimens from the metallic holder during the irradiation. Springs made of CVD SiC are also used to maintain physical contact between the holder and internal SiC materials to control irradiation temperature.

Irradiation capsules were designed to control the specimen temperatures using three-dimensional thermal analysis with ANSYS software. The simulation results are shown in Fig. 4. The expected temperatures gradients in the SiC/SiC and CVD SiC specimens are less than 10% of target temperature for all irradiations. For irradiation at the target temperature of 950°C, the temperature of the SiC/SiC and CVD SiC specimens is expected to gradually decrease, depending on the dimensional change (swelling) of the molybdenum holder during irradiation [5]. The average irradiation temperature in the specimens will be ~900°C during the late stage of high does irradiation.

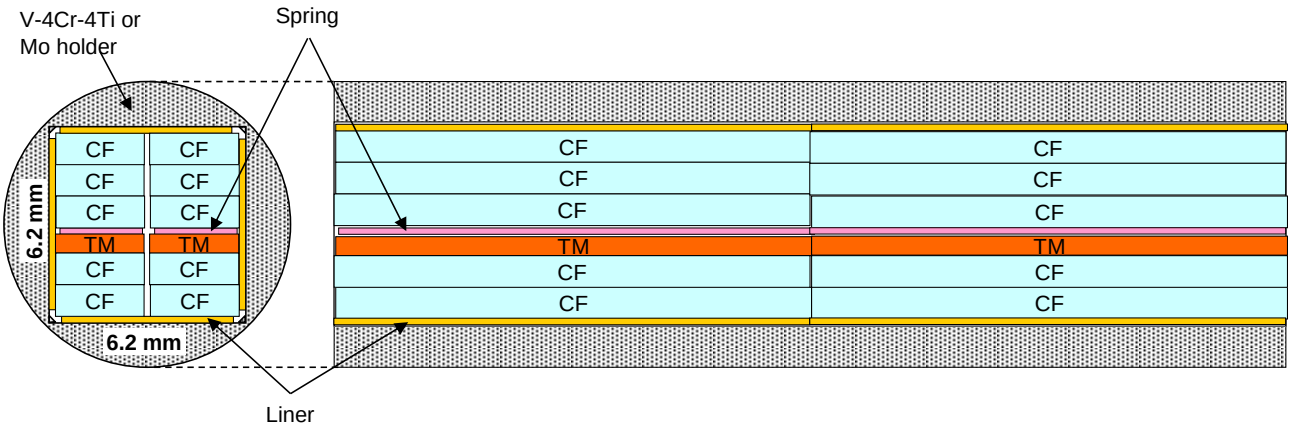

Type ID	Material	Dimensions[mm]	Qty	Main Purpose
CF	SiC/SiC	25x2.8x1	20	Flexure
TM	SiC	25x2.8x0.40	4	Thermometry
Spring	SiC	24 x 2.5 x 0.15	4	Spring
Liner	SiC	50x5.4x0.2	4	Separator

Figure 3. Schematic illustration of SiC/SiC specimens and SiC internal components in a metallic holder.

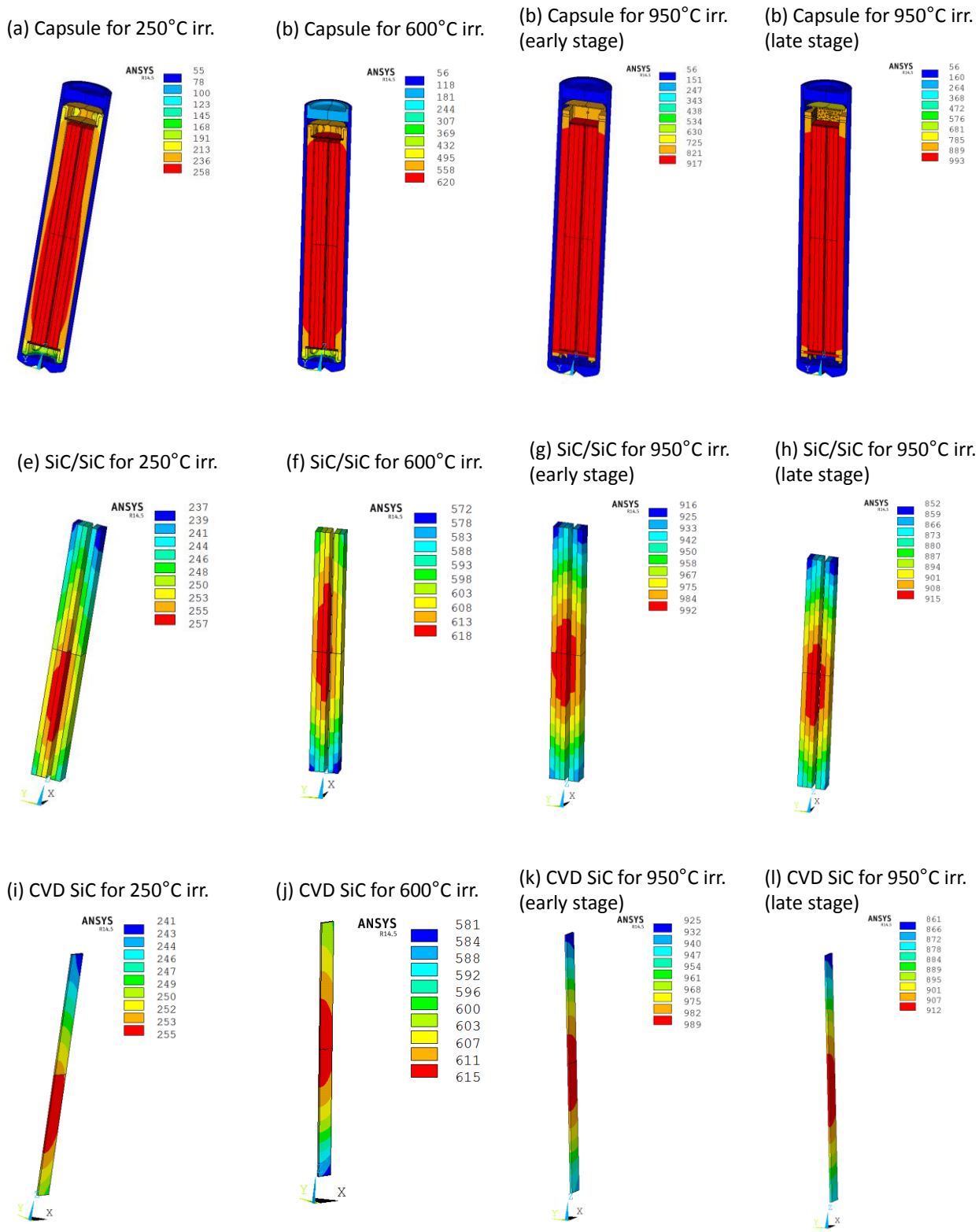

Figure 4. Simulation of temperatures in rabbit capsules, SiC/SiC specimens, and monolithic CVD SiC specimens designed for irradiation at ~250°C (a, e, f), ~600°C (b, f, j), ~950°C in the earlier stage (c, g, k), and ~950°C in the late stage (d, h, l).

Irradiation Matrix and the Schedule

This series of high dose irradiation experiments consists of irradiation of 12 rabbit capsules. All rabbits had the same capsule design, shown in Fig. 3. The planned target fluences are up to ~200 dpa , assuming the equivalence of 1 dpa with 1 x 10^{25} n/m^2 (E > 0.1 MeV). The target irradiation temperatures are 250, 600, and 950°C. The specimens are irradiated under inert gas atmospheres such as helium for 250°C irradiation, neon for 600°C, and argon for 950°C. The V-4Cr-4Ti holder is used for irradiation at 250 and 600°C. The molybdenum holder is used at 950°C. The irradiation matrix is summarized in Table 1.

The SCF1-9 rabbits will be irradiated starting in HFIR Cycle 457 (11/18/2014~), and the irradiations for SCF10-12 rabbits will start in Cycle 458 (1/13/2015~) [6].

Table 1. Irradiation conditions planned for high dose irradiation experiments.

RABBIT ID	TARGET TEMP. (°C)	HFIR POSITION		FAST FLUX (n/cm^2 s)	# OF CYCLES	FAST FLUENCE PER CYCLE (n/cm^2)	TOTAL FLUENCE (n/cm^2)	TARGET DPA
SCF1	~250	TRRH	6	9.50E+14	1	1.97E+21	1.97E+21	2
SCF2	~250	TRRH	6	9.50E+14	6	1.97E+21	1.18E+22	10
SCF3	~250	TRRH	5	1.04E+15	14	2.16E+21	3.02E+22	30
SCF4	~250	TRRH	4	1.08E+15	45	2.24E+21	1.01E+23	100
SCF5	~250	TRRH	4	1.08E+15	90	2.24E+21	2.02E+23	200
SCF6	~600	TRRH	6	9.50E+14	6	1.97E+21	1.18E+22	10
SCF7	~600	TRRH	5	1.04E+15	14	2.16E+21	3.02E+22	30
SCF8	~600	TRRH	4	1.08E+15	45	2.24E+21	1.01E+23	100
SCF9	~600	TRRH	4	1.08E+15	90	2.24E+21	2.02E+23	200
SCF10	~950	TRRH	5	1.04E+15	5	2.16E+21	1.08E+22	10
SCF11	~950	TRRH	5	1.04E+15	14	2.16E+21	3.02E+22	30
SCF12	~950	TRRH	4	1.08E+15	45	2.24E+21	1.01E+23	100

Plan of Post-Irradiation Experiments

The post-irradiation examination is planned to include evaluation of flexural strength, Young's modulus, swelling, thermal diffusivity at room temperature, electrical conductivity up to the irradiation temperature for the composite specimens, and microstructures. The flexural tests will be conducted in accordance with the guideline of ASTM standard C1341-13. Dynamic Young's modulus will be investigated by impulse excitation of vibration according to ASTM C1259-14. Swelling will be determined by apparent density measurement before and after irradiation. Thermal diffusivity will be measured using a flash diffusivity technique, per ASTM E1461-13. Electrical conductivity will be measured in a four-probe configuration for the in-plane orientation and in a two-probe configuration for the through-thickness orientation [7]. The microstructures will be investigated using optical and electrical microscopes. Properties of the monolithic CVD SiC TM specimens in Fig. 3 will be also investigated to understand the irradiation stabilities of the matrix of CVI SiC/SiC. The swelling will be evaluated by the density-gradient technique based on ASTEM D1505-10. Room temperature thermal diffusivity will be also measured. The actual irradiation temperatures will be determined by the post-irradiation annealing of the CVD SiC specimens [8].

References

[1] Y. Katoh, T. Nozawa, L.L. Snead, K. Ozawa, H. Tanigawa, J. Nucl. Mater., 417 (2011) 400-405.
[2] A.G. Perez-Bergquist, T. Nozawa, C. Shih, K.J. Leonard, L.L. Snead, Y. Katoh, J. Nucl. Mater. (2014), doi:10.1016/j.jnucmat.2014.06.038
[3] Y. Katoh, T. Nozawa, C. Shih, K. Ozawa, T. Koyanagi, W. Porter, L. L. Snead, "High Dose Neutron Irradiation of Hi-Nicalon Type S Silicon Carbide Composites, Part 2: Mechanical and Physical Properties", submitted to Journal of Nuclear Materials.
[4] S. Kondo, T. Hinoki, M. Nonaka, K. Ozawa, Acta Materialia, 83 (2015) 1-9.
[5] B.V. Cockeram, R.W. Smith, N. Hashimoto, L.L. Snead, J. Nucl. Mater., 418 (2011) 121-136.
[6] http://neutrons.ornl.gov/facilities/HFIR/pdf/OperatingForecast.pdf
[7] Y. Katoh, S. Kondo, L.L. Snead, DC Electrical Conductivity of Silicon Carbide Ceramics and Composites for Flow Channel Insert Applications, J. Nucl. Mater., 386-388 (2009) 639-642.
[8] L.L. Snead, A.M. Williams, A.L. Qualls, Revisiting the Use of SiC as a Post Irradiation Temperature Monitor, in: M.L. Grossbeck, T.D. Allen, R.G. Lot, A.S. Kumar (Eds.) The Effects of Radiation on Materials: 21st International Symposium, ASTM STP 1447, ASTM International, West Conshohocken, PA, 2003.

4.1 RECENT PROGRESS IN THE DEVELOPMENT OF DUCTILE-PHASE TOUGHENED TUNGSTEN FOR PLASMA-FACING MATERIALS: W-Ni-Fe COMPOSITES – C. H. Henager, Jr., R. J. Kurtz, T. J. Roosendaal, B. A. Borlaug, E. A. Nyberg, C. A. Lavender (Pacific Northwest National Laboratory[1]), G. R. Odette, K. H. Cunningham, and F. W. Zok (University of California, Santa Barbara)

OBJECTIVE

The objective of this study is to fabricate a lamellar W-Ni-Fe composite based on tungsten heavy metal alloys suitable for model material development for fusion reactor studies of ductile-phase toughening.

SUMMARY

A promising approach to increasing fracture toughness and decreasing the DBTT of a W-alloy is by ductile-phase toughening (DPT) [1-3]. In this method, a ductile phase is included in a brittle matrix to prevent fracture propagation by crack bridging. W-Ni-Fe alloys consisting of nearly spherical W-particles embedded within a Fe-Ni-W ductile matrix are being manipulated by hot-rolling to create lamellar W/Fe-Ni-W composites with anisotropic fracture properties.

PROGRESS AND STATUS

Background

Tungsten (W) and W-alloys are the solid materials of choice for plasma-facing components (PFCs) of future fusion reactors, such as the International Thermonuclear Experimental Reactor (ITER) and Demonstration Power Plant (DEMO), due to their high melting point, strength at high temperatures, high thermal conductivity, low coefficient of thermal expansion, and low sputtering yield [4-8]. However, W and most W-alloys exhibit low fracture toughness and a high ductile-brittle transition temperature (DBTT) that would render them as brittle materials during reactor operations [4, 6, 9]. The DBTT for unirradiated W-alloys typically ranges from 573K to 1273K (300 to 1000˚C) and in a reactor environment radiation hardening would further elevate this range [6, 10, 11]. W-alloys toughened by engineered reinforcement architectures, such as ductile-phase toughening (DPT), are strong candidates for PFCs. In DPT, a ductile phase is included in a brittle matrix to prevent fracture propagation. This is accomplished by the formation of an intact bridging zone behind the crack tip, which provides reinforcement, resulting in an increase in the remote load stress intensity for continued crack growth with increasing crack length [12, 13]. The principles of DPT are illustrated in Figure 1, which shows an actual and schematic illustration of ductile bridging ligaments stretching across an open crack in a brittle matrix material, such as W [12, 13]. For a brittle material containing a suitable volume fraction of a ductile phase, a highly effective resistance curve toughening mechanism develops as the crack extends. This reduces the crack tip stress intensity factor so that: $\boldsymbol{K_{Tip} < K_{Applied}}$. The crack opening (u) increases with increasing distance behind the crack-tip until the reinforcement breaks at a critical u*.

[1] PNNL is operated for the U.S. Department of Energy by Battelle Memorial Institute under Contract DE-AC06-76RLO 1830.

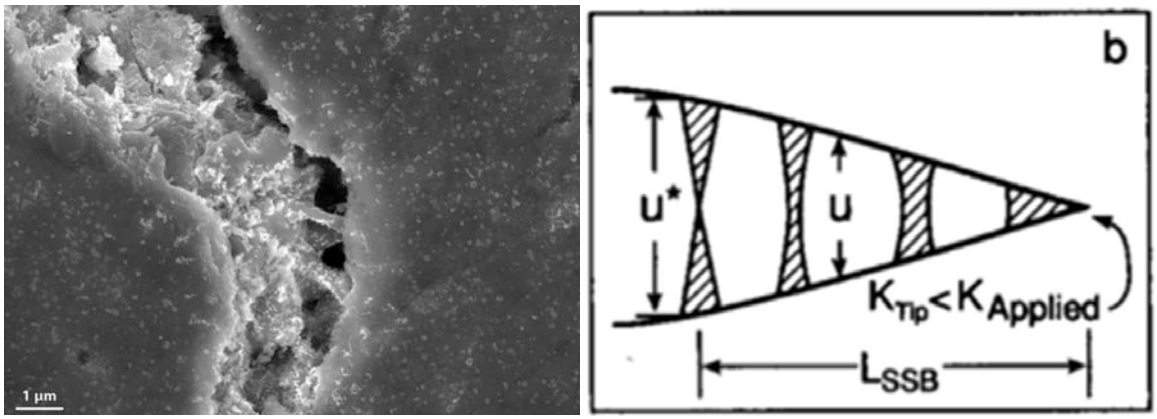

Figure 1. a) SEM image of W-Cu fracture where the ductile phase (Cu) is effectively bridging the crack. b) A steady-state bridging zone shown schematically in 2D [13].

Experimental

Fe-Ni-W alloys, purchased as green bodies consisting of W-7%Ni-3%Fe[2], are being prepared for testing using hot-rolling to provide a range of microstructures with anisotropic fracture behavior. The starting alloy shown in Figure 2 is formed using liquid phase sintering methods and exhibits an isotropic structure consisting of W-Ni-Fe spheres embedded in a Fe-Ni-W matrix. The W-spheres are 99.7% W, 0.2% Ni and 0.1% Fe by wt%. The matrix, which is basically a Ni-based superalloy, is 56.9% Ni, 29.3% W, and 13.8% Fe by wt%.

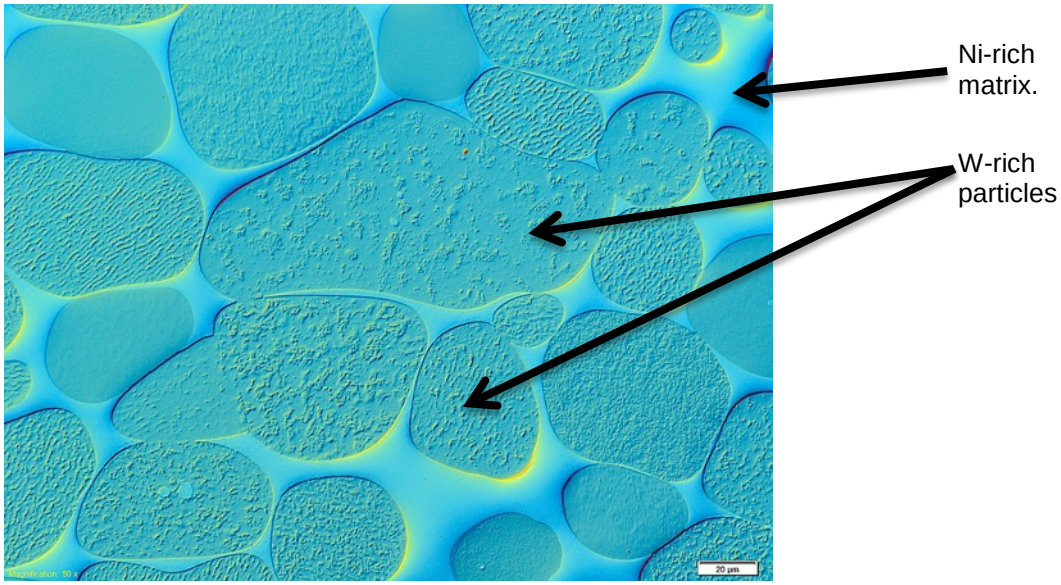

Figure 2. W-Ni-Fe alloy showing W-rich particles and Ni-rich ductile matrix.

These alloys are being successively hot-rolled at 1150˚C for two passes with 5% reduction per rolling pass after initial sintering. Then the alloys are rolled at 900˚C in 11% reduction passes to the final reductions (Fig. 3), noting that after three passes the materials are annealed at 900˚C for 1 hour in argon. Figure 3 shows optical images of the as-rolled materials at different reduction percentages. Samples continue to be rolled to higher reductions but are not yet available for imaging.

[2] Mi-Tech Metals, Indianapolis, IN, USA.

Discussion

The goal is to achieve a rolled W-Ni-Fe alloy that resembles a lamellar alloy consisting of W-rich lamellae separated by ductile-phase regions. Fig. 3c shows a microstructure of that type. The W-rich lamellae are strong but brittle, while the ductile-phase metallic regions now have a thin, plate-like morphology that should act as a ductile bridging region. Such a material would be oriented with the W-rich lamellae parallel to principal stresses so that surface cracking would be normal to the ductile-phase bridging regions.

Future Work

Additional amounts of reduction are planned so that reductions greater than 90% are achieved and thinner lamellar regions are produced to be able to more completely explore morphological effects on mechanical properties. Fracture toughness samples in the form of 4-point bend bars are being fabricated from these rolled alloys and will be tested at ambient and elevated temperatures. Exploration of alternative alloy compositions that reduce the amount of Ni in the alloy due to neutron activation concerns will follow successful fracture testing.

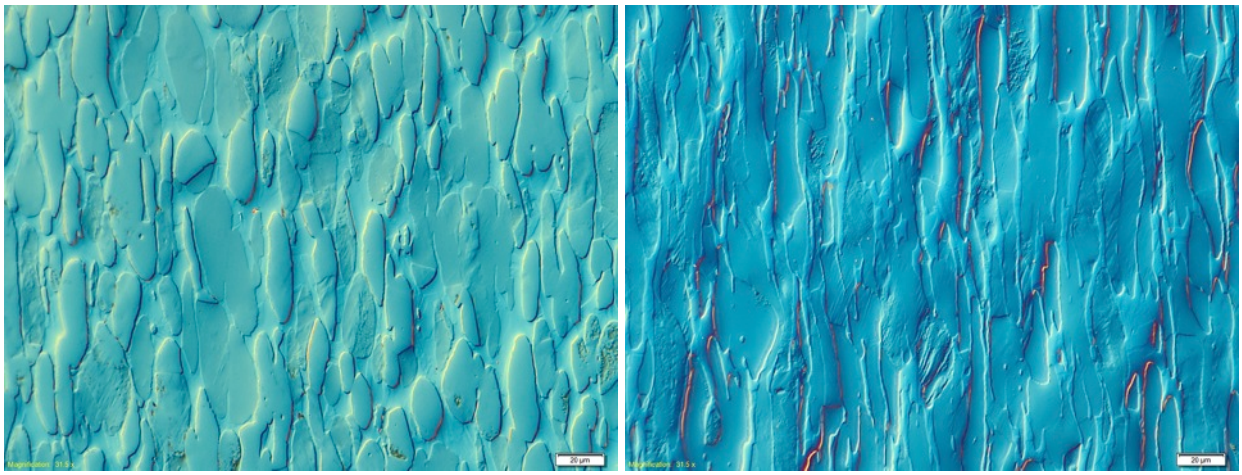

(a) 62% (b) 74%

(c) 88%

Figure 3. Optical images of hot-rolled W-Ni-Fe alloy with (a) 62%, (b) 74%, and (c) 88% reductions, respectively. A goal is to achieve a rolled reduction of 90% or greater to form a lamellar tungsten alloy with anisotropic fracture properties. These rolled materials will be tested with the specimens oriented so that crack growth was horizontal (right to left) in the image.

References

[1] Deve, H.E., A.G. Evans, G.R. Odette, R. Mehrabian, M.L. Emiliani, and R.J. Hecht, "Ductile reinforcement toughening of -TiAl: effects of debonding and ductility," Acta metallurgica et materialia, 1990, 38(8), 1491-502.

[2] Erdogan, F. and P.F. Joseph, "Toughening of ceramics through crack bridging by ductile particles," Journal of the American Ceramic Society, 1989, 72(2), 262-270.

[3] Sigl, L.S., P.A. Mataga, B.J. Dalgleish, R.M. McMeeking, and A.G. Evans, "On the Toughness of Brittle Materials Reinforced with a Ductile Phase," Acta Metallurgica, 1988, 36(4), 945-953.

[4] Rieth, M., J.L. Boutard, S.L. Dudarev, T. Ahlgren, S. Antusch, N. Baluc, M.F. Barthe, C.S. Becquart, L. Ciupinski, J.B. Correia, C. Domain, J. Fikar, E. Fortuna, C.C. Fu, E. Gaganidze, T.L. Galan, C. Garcia-Rosales, B. Gludovatz, H. Greuner, K. Heinola, N. Holstein, N. Juslin, F. Koch, W. Krauss, K.J. Kurzydlowski, J. Linke, C. Linsmeier, N. Luzginova, H. Maier, M.S. Martinez, J.M. Missiaen, M. Muhammed, A. Munoz, M. Muzyk, K. Nordlund, D. Nguyen-Manh, P. Norajitra, J. Opschoor, G. Pintsuk, R. Pippan, G. Ritz, L. Romaner, D. Rupp, R. Schaublin, J. Schlosser, I. Uytdenhouwen, J.G. Van Der Laan, L. Veleva, L. Ventelon, S. Wahlberg, F. Willaime, S. Wurster, and M.A. Yar, "Review on the EFDA programme on tungsten materials technology and science," Journal of Nuclear Materials, 2011, 417, 463-467.

[5] Pitts, R.A., A. Kukushkin, A. Loarte, A. Martin, M. Merola, C.E. Kessel, V. Komarov, and M. Shimada, "Status and physics basis of the ITER divertor," Physica Scripta Volume T, 2009, 2009(T138), 014001 (10 pp.).

[6] Mertens, P., T. Hirai, M. Knaup, O. Neubauer, V. Philipps, J. Rapp, V. Riccardo, S. Sadakov, B. Schweer, A. Terra, I. Uytdenhouwen, and U. Samm, "A bulk tungsten divertor row for the outer strike point in JET," Fusion Engineering and Design, 2009, 84(7-11), 1289-93.

[7] Gervash, A., R. Giniyatulin, T. Ihli, W. Krauss, A. Makhankov, I. Mazul, P. Norajitra, and N. Yablokov, "Fabrication of a He-cooled divertor module for DEMO reactor," Journal of Nuclear Materials, 2007, 367-370 B(SPEC. ISS.), 1472-1475.

[8] Merola, M., W. Danner, and M. Pick, "EU RD on divertor components," Fusion Engineering and Design, 2005, 75-79(SUPPL.), 325-331.

[9] Mertens, P., V. Philipps, G. Pintsuk, V. Riccardo, U. Samm, V. Thompson, and I. Uytdenhouwen, "Clamping of solid tungsten components for the bulk W divertor row in JET-precautionary design for a brittle material," Physica Scripta Volume T, 2009, 2009(T138), 014032 (5 pp.).

[10] Gludovatz, B., S. Wurster, A. Hoffmann, and R. Pippan, "Fracture toughness of polycrystalline tungsten alloys," International Journal of Refractory Metals and Hard Materials, 2010, 28(6), 674-8.

[11] Zinkle, S.J. and N.M. Ghoniem, "Operating temperature windows for fusion reactor structural materials," Fusion Engineering and Design, 2000, 51-52, 55-71.

[12] Venkateswara Rao, K.T., G.R. Odette, and R.O. Ritchie, "Ductile-reinforcement toughening in -TiAl intermetallic-matrix composites: effects on fracture toughness and fatigue-crack propagation resistance," Acta Metallurgica et Materialia, 1994, 42(3), 893-911.

[13] Odette, G.R., B.L. Chao, J.W. Sheckherd, and G.E. Lucas, "Ductile phase toughening mechanisms in a TiAl-TiNb laminate composite," Acta metallurgica et materialia, 1992, 40(9), 2381-9.

4.2 RECENT PROGRESS IN THE FABRICATION AND CHARACTERIZATION OF DUCTILE-PHASE-TOUGHENED TUNGSTEN LAMINATES FOR PLASMA-FACING MATERIALS—K. H. Cunningham, G. R. Odette, K. Fields, D. Gragg, T. Yamamoto, and F. W. Zok (University of California, Santa Barbara), C. H. Henager, Jr., R. J. Kurtz, T. J. Roosendaal, and B. A. Borlaug (Pacific Northwest National Laboratory)

OBJECTIVE

The objective of this study is to develop ductile-phase-toughened tungsten composites as candidates for plasma-facing components in future fusion reactors.

SUMMARY

A promising approach to increasing the fracture toughness of W-alloys is ductile-phase toughening (DPT). A ductile phase reinforcement in a brittle matrix increases toughness primarily by crack bridging. A W-Cu laminate was fabricated and the properties of the constituent metals were characterized along with those for the composite. Development of a design model for large-scale crack bridging continued.

PROGRESS AND STATUS

Introduction

Background information and previous progress have been discussed in earlier semi-annual reports [1-3].

Experimental Procedure

Brazed W-Cu Laminate

Diffusion bonding of W to Cu via hot pressing was found to be inconsistent, so brazing W plates with thin layers of Cu was explored. Lapped 0.85 x 50 x 50 mm W plates were stacked alternating with 75-μm Cu foils, and clamped with stainless steel wire. The layup was heated in an Ar-5%H_2 environment to 1113 °C at 15 °C/min and held for 6 s before cooling. Notched three-point bend bars were fabricated from both the as-received W plate and the W-Cu laminate. The dimensions of the W bars were 22 x 4.65 x 0.85 mm, and the W-Cu bars were 21 x 4.65 x 2.125 mm. The notch depth was nominally 0.93 mm. All specimens were identified with respect to the rolling direction of the W plate: the “L” and “T” labels indicate the crack propagation direction was parallel (L) or perpendicular (T) to the rolling direction. Laminate specimens were also separated into “edge” and “face” orientations, where the crack propagation direction was normal to the edge or face of W and Cu layers, respectively.

Characterization of the fracture toughness of the W plate in the L and T orientations is needed to establish a constituent baseline for comparison with the laminate fracture resistance. Notched W bend bars were compression pre-cracked by standing them upright in a load frame with the span along the fatigue loading direction as shown in Figure 1. The specimens were compression-compression fatigued at 20 Hz and the crack length was observed at intervals of 10,000 cycles until reaching a length of approximately a/W=0.3. The specimens were then tested in three-point bending and toughness values were calculated following ASTM E399-12. The pre-crack depth was measured by applying a dye penetrant to the sample prior to testing and subsequently observing the marked area.

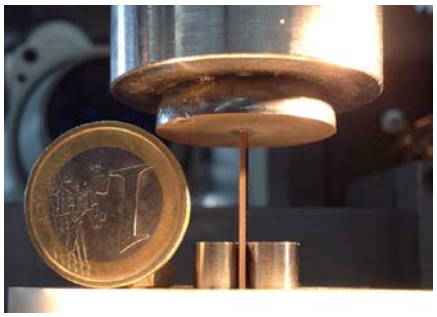

Figure 1. Photograph of end-on compression fatigue setup for W bend bars. A steel clip is used to help stand the specimen upright.

The W-Cu laminate bars were fatigued in three-point bending to attempt to develop a precrack, without success. The current test data from several specimens comes from bend bars with a rounded EDM-cut notch, with an average radius of 158 μm. Some precracking attemps resulted in the laminate specimens breaking to roughly a/W=0.9. This allowed investigation of the Cu bridging phase. Other specimens were tested in three-point flexure with a crosshead displacement rate of 0.1 mm/min.

Large-Scale Crack Bridging Code

In parallel with laminate fabrication efforts, we have been developing a code to predict resistance and load-displacement curves for ductile-phase-toughened composites for different geometries and composite architectures. The code is adapted from work by Odette and Chao [4, 5] on TiAl-TiNb laminates. The approach of the code is to calculate the shape of the crack from the applied load (opening) and the distributed bridging stresses along the crack face (closing) using Castigliano's Theorem and stress intensity solutions from Tada. An iterative calculation reaches a self-consistent solution by matching the stress-displacement function of the reinforcing phase with those calculated for the crack opening displacement profile. The code predicts both the fracture resistance and load-displacement curves. Note the p-Δ curves are equivalent to stress-strain curves in cracked bodies, hence they provide engineering measures of composite strength and ductility. A description of the algorithm sequence is shown below, and Figure 2 shows the model of a three-point bend specimen.

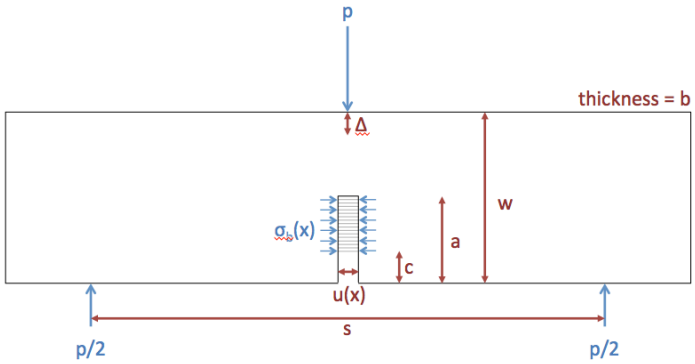

Figure 2. Schematic of the three-point bend specimen modeled in the bridging code. Note that the x-direction is the crack propagation direction with a range of 0 to a. Specimen dimensions are shown in red and stresses in blue.

- Input information
  - Specimen and crack dimensions
  - Matrix properties (K_m, E, v)
  - Reinforcement stress-displacement law $\sigma_b(u)$
- Iterative calculation of crack face displacements and stresses
  - Assume a bridge stress distribution $\sigma_b^*(x)$

- Calculate the stress intensity factor (K_I) for a specified crack length (a) and remote load (p)
- Calculate the stress intensity reduction at the crack tip due to the $\sigma_b^*(x)$ distribution
- Calculate the applied increased stress intensity needed to advance the crack at $K_{tip} = K_m$
- Calculate the net crack face displacement distribution $u^*(x)$ due to the applied K_I (opening) and the bridging zone traction stress distribution $\sigma_b^*(x)$ (closing)
- Estimate a new stress distribution using a specified ductile ligament stress-displacement function $\sigma_b(u)$ and the calculated $u^*(x)$ as described in the next two steps
- Compare the $\sigma_b^*(x)$ distribution used initially with $\sigma_b[u(x)]$ and compute the difference $\varepsilon(x)$
- Set $\sigma_b[u(x)]$ to a new $\sigma_b^*(x)$ and repeat the above calculations, iterating until $\sigma_b^*(x) = \sigma_b[u(x)]$ and thus $\varepsilon(x) \approx 0$ for all x.
- Use the expressions in Tada to calculate the corresponding load-point displacement (Δ)
- Increase the crack length a by a small increment (da) and repeat to calculate the resistance curve $K_I(a)$ and load-displacement curve $p(\Delta)$

Results

W Plates and Brazed W-Cu Laminate

Fracture toughness values of the W plate in both orientations are shown in Table 1. The average toughness values in the L and T directions are 13.06 and 20.90 MPa $m^{0.5}$, respectively. Bend testing on the W-Cu laminate did not show pseudo-ductile behavior, but crack bridging did occur. In Figure 3, the dye penetrant on the fracture surface of the broken specimen indicates that when the specimen was still intact with an a/W ≈ 0.9, the Cu the reinforcement was bridging the crack. An increase in load-bearing capacity and fracture resistance is not seen in these specimens because the applied stress intensity needed to grow a sharp crack from the blunt notch tip was greater than that needed to unstably propagate a sharp dynamic crack to a/w=0.9, since the corresponding crack opening profile does not activate a significant bridging traction. Using the compression precracking method on the W-Cu samples should allow for stable crack growth and characterization of the corresponding resistance curves.

Table 1. Measured fracture toughness values for pure W three-point bend specimens. Test dimensions are 20.5 x 4.65 x 0.85 mm.

Specimen	a/W	Load (N)	K_{IC} (MPa $m^{0.5}$)
L2	0.26	101.60	10.52
L5	0.28	98.96	10.74
L6	0.33	120.70	14.70
L7	0.27	129.73	13.60
L8	0.31	135.54	15.73
T2	0.27	195.29	20.46
T3	0.30	190.81	21.52
T6	0.27	199.55	20.85
T8	0.26	200.55	20.75

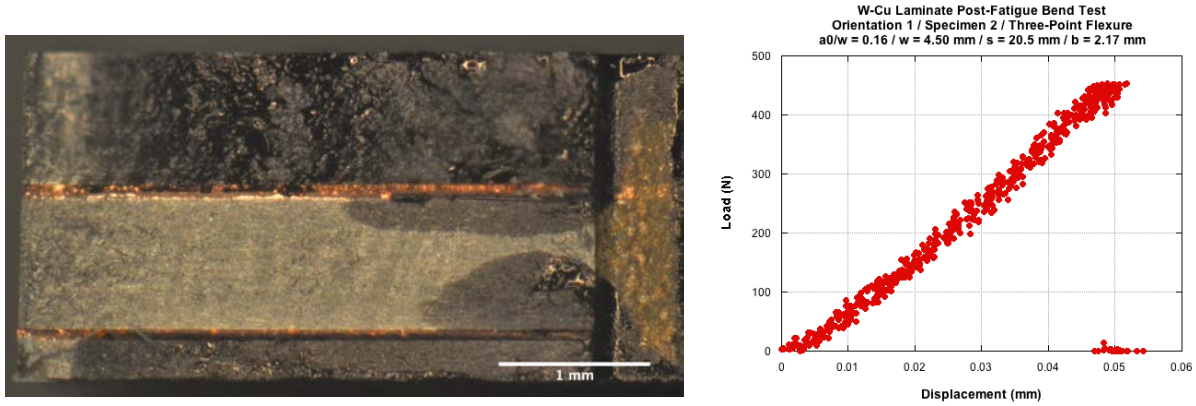

Figure 3. Left: a representative fracture surface of edge specimen 1 marked with dye penetrant. Notch is on the right side of image. Specimen was broken to a/W = 0.9, as marked by the dye. Lack of penetration through Cu layers indicates Cu was bridging the crack. Right: a representative load-displacement curve for edge specimen 2 indicates brittle failure.

Large-Scale Crack Bridging Code

The large-scale crack bridging code results were compared the previous work of Odette and Chao [4, 5], since that work was validated experimentally. Examples of the crack shape and accompanying stress distribution for an arbitrary reinforcement in W are shown in Figure 4. Figure 5 shows resistance curves and load-displacement curves calculated for three different bridging stress-displacement functions, indicated by color. The new resistance curve calculations (points) compare very well with the previous results (lines) but the p-Δ predictions are only consistent up to nearly the peak load. After the peak load, the load-point displacement is under-predicted with respect to the previous results. The calculation converges quickly when modeling specimens in the edge orientation because the reinforcement is continuous in the direction of crack propagation. The presence of discontinuities in the reinforcement phase with respect to the crack propagation direction results in convergence issues when modeling the face orientation.

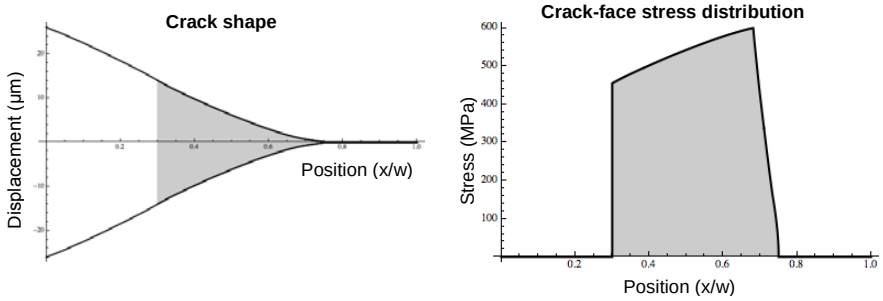

Figure 4. Example output from large-scale bridging code. Left: crack shape with bridging zone shaded. Right: crack-face stress distribution.

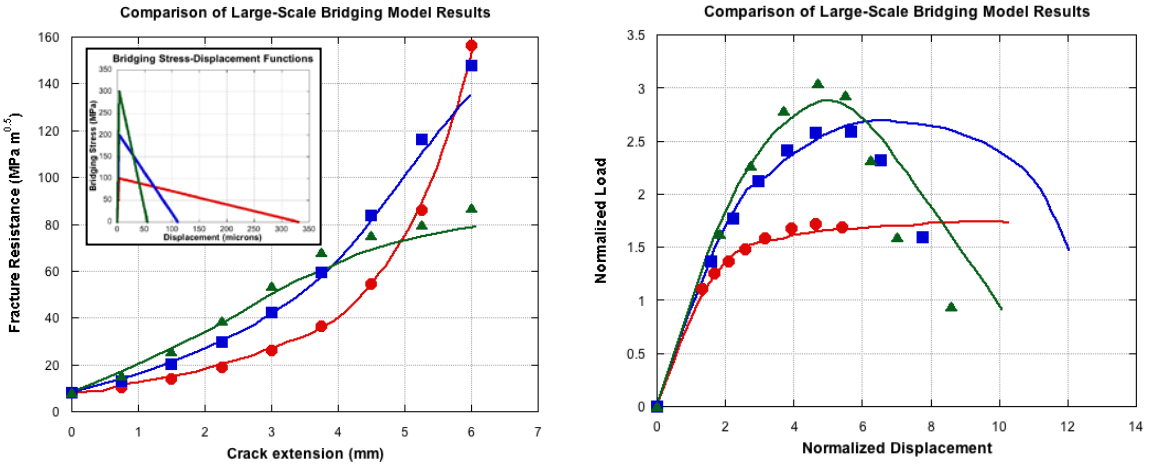

Figure 5. Experimentally-verified models (lines) [4] compared with current models (points) for identical initial conditions, modeling a TiAl-TiNb laminate. Left: comparison of resistance curves. Right: comparison of load-displacement curves. Values are normalized by the load capacity and displacement at fracture of a non- reinforced test specimen. Inset at left: bridging stress-displacement functions corresponding to the colors in each plot.

Ongoing and Future Work

Laminate testing and large scale bridging code development will continue. The laminate studies will include a variety of ductile reinforcement phases as alternatives to Cu. New methods will be developed to pre-crack the laminates and to utilize the data from the notched bars.

References

[1] K. H. Cunningham, K. Fields, D. Gragg, F. W. Zok, C. H. Henager, Jr, R. J. Kurtz, and T. Roosendaal, Recent Progress in the Development of Ductile-Phase Toughened Tungsten for Plasma-Facing Materials, in DOE/ER-0313/54 - Volume 54, Semiannual Progress Report, June 30, 2013. 2013, US DOE: ORNL, TN.

[2] C. H. Henager, Jr, R. J. Kurtz, T. J. Roosendaal, B. A. Borlaug, G. R. Odette, K. H. Cunningham, K. Fields, D. Gragg, and F. W. Zok, Recent Progress in the Development of Ductile-Phase Toughened Tungsten for Plasma-Facing Materials, in DOE/ER-0313/55 - Volume 55, Semiannual Progress Report, Dec. 31, 2013. 2013, US DOE: ORNL, TN.

[3] K. H. Cunningham, G. R. Odette, K. Fields, D. Gragg, F. W. Zok, C. H. Henager, Jr., R. J. Kurtz, T. J. Roosendaal, and B. A. Borlaug, Recent Progress in the Fabrication and Characterization of Ductile-Phase-Toughened Tungsten Composites For Plasma-Facing Materials, in DOE/ER-0313/56 - Volume 56, Semiannual Progress Report, Jun. 30, 2014. 2014, US DOE: ORNL, TN.

[4] G. R. Odette, B. L. Chao, J. W. Sheckherd, and G. E. Lucas. Acta Metall. Mater. 40-9 (1992) 2381-2389.

[5] G. R. Odette and B. L. Chao, unpublished notes.

4.3 PROCESS IMPROVEMENTS OF SPECIMEN PREPARATIONS FOR MECHANICAL TESTING AND HYDROGEN PERMEATION OF NANO-W -- C. Ren and Z. Zak Fang (University of Utah)

OBJECTIVE

The objective of this work is to improve specimen preparation method to minimize cracking during abrication and optimize sample quality. The prepared nano-W specimens will be used to evaluate mechanical properties and hydrogen permeation for fusion reactor material applications.

SUMMARY

During the last period, attempts have been made to make crack-free specimens for mechanical and hydrogen permeation evaluations of nano W. The ongoing work in this reporting period including: development of a new multi-step pelletizing and compaction process (MPC) for preparing crack-free specimens, and evaluation of the effect of Ti-based additives on the sintering behavior of nano-W materials.

PROGRESS AND STATUS

Introduction

High performance mechanical properties before and after irradiation is the most desired characteristic for fusion reactor material applications. Among various materials, tungsten alloys with grain size less than 100 nm (Nano-W) is one of the most promising candidates due to its superior mechanical and thermal properties [1-2]. In our previous work, a new process method for making nano W with grain size near 100 nm has been developed [3-4]. This process method uses a “two-step” sintering strategy which includes a low temperature hydrogen sintering and a high pressure rapid heating modified rapid omni-directional compaction (m-ROC).

To further develop this material, large sample for mechanical properties evaluation is required. However, the large samples experience laminate and radial cracking as a result of the compaction introduced non-uniform density distribution. During the last reporting period, systematic studies on the effect of heating rate of sintering, compaction pressure, pressuring method and amount of binder have been performed on nano W materials. The results showed reduced formation of cracks by lower the compaction pressure and also suggested that the cracks were more likely to occur at lower density region.

In this period, work to eliminate cracks in sintered samples has been continued. Based on the experience of previous work, the cracking problem may be solved via obtaining green parts with more homogenous density. Therefore, the new MPC process has been developed which minimizes the density inhomogeneity and successfully eliminates formation of cracks.

To further decrease the grain size and increase the relative density of sintered nano W materials, effects of Ti-based additives on the sintering behavior have also been studied in this period. The parameters of

additive type (Ti and TiC), composition and sintering temperature have been considered as the most sensitive factors and may significantly affect the sintering results.

Experimental Procedure

Powder preparation

Commercial tungsten powders with particle size of about 100 nm and titanium hydride powders with particle size of 45 μm were used as raw materials. The powders were milled using the high energy planetary mill machine (HEPM) in a mixture of heptane and ethanol. One mm diameter tungsten carbide balls were used as grinding media with ball to powder ratio of 4:1. The milled nano tungsten powders were dried in evaporating dishes.

Multi-steps pelletizing and compaction process

The new MPC process is a solution developed during this reporting period which solves the cracking problem by minimizing the frictions between particles. The dried tungsten powders were compacted, pelletized, and re-compacted.

Low temperature hydrogen sintering

A low temperature step was performed at 700ºC for 3 h to reduce the oxidized W powders and minimize its effect on sintering. The sintering steps were carried out in temperatures range of 1000 to 1300ºC under hydrogen atmosphere using a tube furnace.

Characterizations

After sintering, the densities of the samples were measured by Archimedes method. The fractured surface microstructures of sintered samples were examined by Scanning Electron Microscope (SEM). Vickers hardness was measured under a load of 2 kg and a dwell time of 15 s.

Results

Disc specimen fabrication

To examine the radiation damage resistance properties, 1” thin nano-W disc specimens are required for the tritium permeating experiments. During the previous period, extensive works have been performed focusing on minimizing the formation of cracks during sintering. This part of work follows the previous efforts and by applying the new developed MPC process, the cracking problem has been solved.

Figure 1 compares the sintered 1” thick nano-W discs with and without MPC process. As shown in Figure 1 (a), a clear crack can be observed at the right side of the disc. Experimental result indicates that the crack is caused by the non-uniform green density throughout the sample. This non-uniform green density is formed by the friction between particles during compaction which is inevitable during traditional high pressure compaction process.

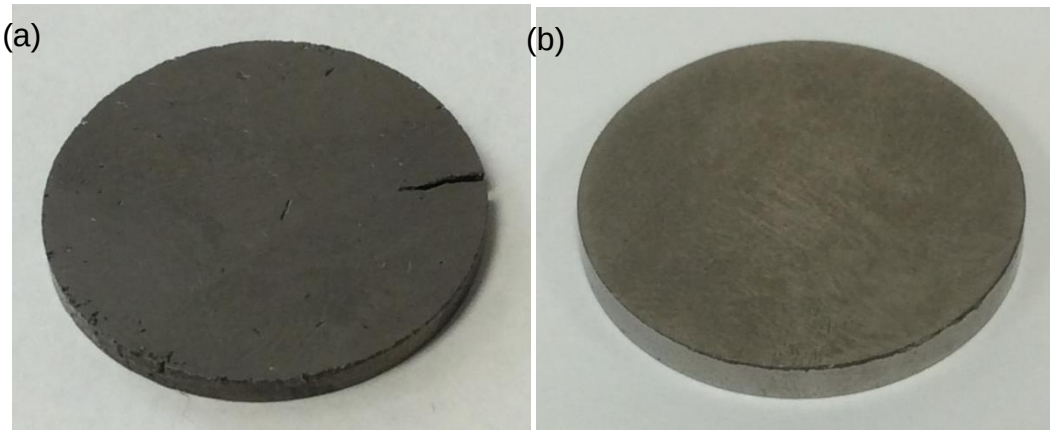

Figure 1. Nano W disc sintered at 1300 ºC for 1 hour. (a) Traditional compaction process. (b) MPC process.

The multi-step pelletizing and compaction process (MPC) offers a solution to achieve high green density while avoid causing high strain. During each compaction/re-pelletizing cycle, the long range macro strains are relieved by breaking the compact while high density are maintained inside each micro particles. Figure 1 (b) demonstrates a specimen prepared using the MPC process, no crack could be observed on the disc sample. The compacted sample has a relative green density of 34% which is comparable to the traditional method and could reach 97% relative density after low temperature hydrogen sintering.

Based on the results, the crack problem has been solved. Several high quality test specimens have been fabricated and one of them has been sent to our collaborator at Sandia National Laboratory (Dr. Buchenauer, Hydrogen & Metallurgy Science Department) for hydrogen permeation tests.

Effect of additive type, composition and sintering temperature

Two types of additive Ti and TiC have been selected for comparison. Figure 2 shows the relative density of W – x wt.% Ti/TiC (x = 0, 1, 2, 3.) samples. The samples were prepared by MPC process, then low temperature hydrogen sintered at 1050 ºC for 2 h and 1300ºC for 1 h. The pure W sample has the highest relative density of 98.1% and the relative density decreases as the composition of additive increases. Based on the previous research, Ti-based additives function as grain growth inhibitor during sintering of nano-W which keeps the grain size small and also decreases the relative density. Although small grain size is highly desired for fusion reactor applications, a very high relative density is required for structure materials. Based on Figure 2, at the same additive composition, nano-W with Ti additive has significant higher density than TiC additive. W with Ti additive also behaves less decrease in density as the additive composition increases. Based on this, Ti has been selected as better additive for further researches.

The effect of sintering temperature on relative density of nano-W has been studied by sintering a set of W – 1 wt.% Ti samples at 1000, 1100, 1200 and 1300 ºC for 1 h. As shown in Figure 3, a significant increase of relative density was achieved by increasing temperature to 1300 ºC. Relative density increases faster at

lower temperate and the rate becomes slower as the temperature higher. Relative density increased only 2% by increasing temperature from 1200 to 1300 ºC.

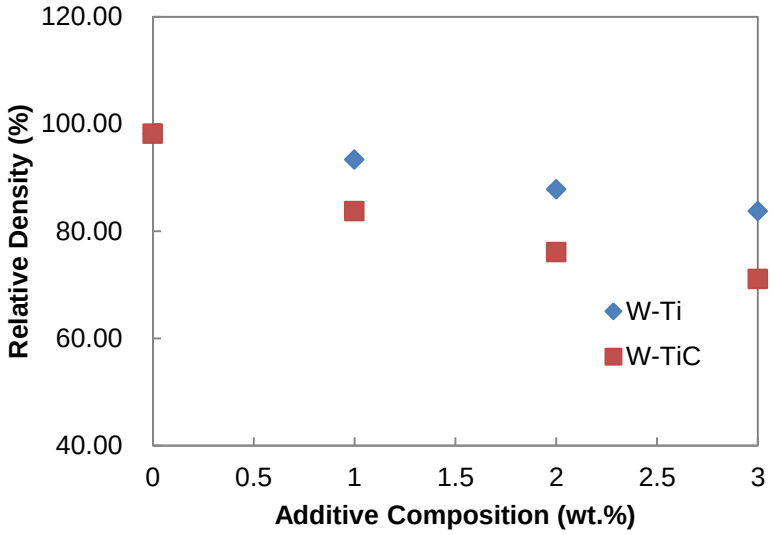

Figure 2. Effect of additive composition on densification of nano-W.

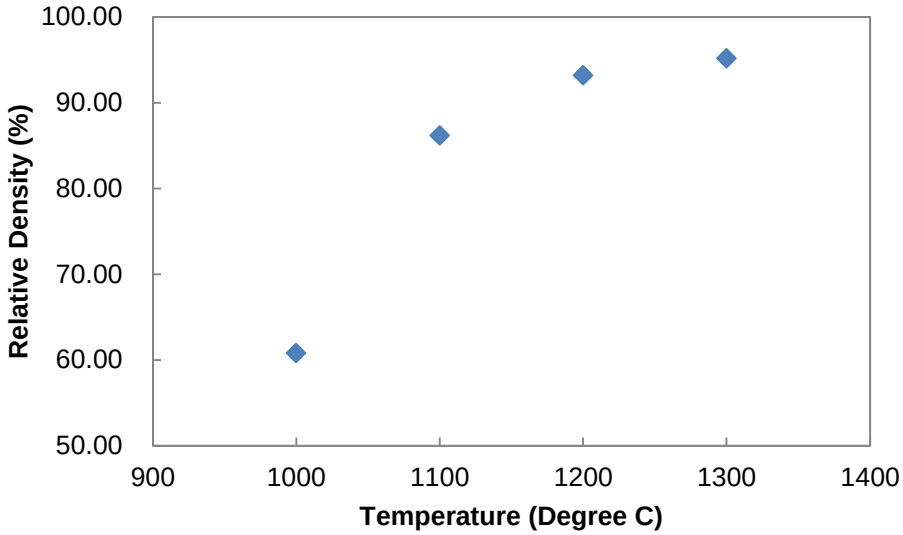

Figure 3. Effect of temperature on densification of nano W.

Samples of W – x wt.% Ti (x=0, 0.26, 1, 1.63, 2.7) have been prepared by sintering at 1100 ºC for 1h. The grain sizes are characterized using SEM on the fractured surface and the results are shown in Figure 4. As the Ti content increases, accompanied with decrease in relative density, a significant decrease is observed in the grain size of sintered samples. The hardness of the sample was determined using Vickers hardness test system. As shown in Figure 5, the HV value increases significantly as the Ti content increases and reaches a maximum of 1040 at the composition of W – 2.7 wt.% Ti.

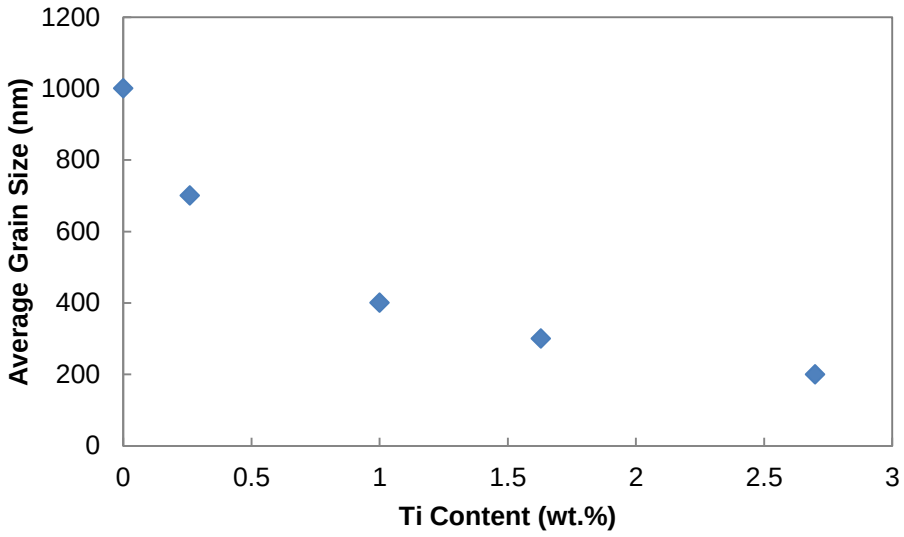

Figure 4. Effect of Ti content on grain size of sintered nano-W samples.

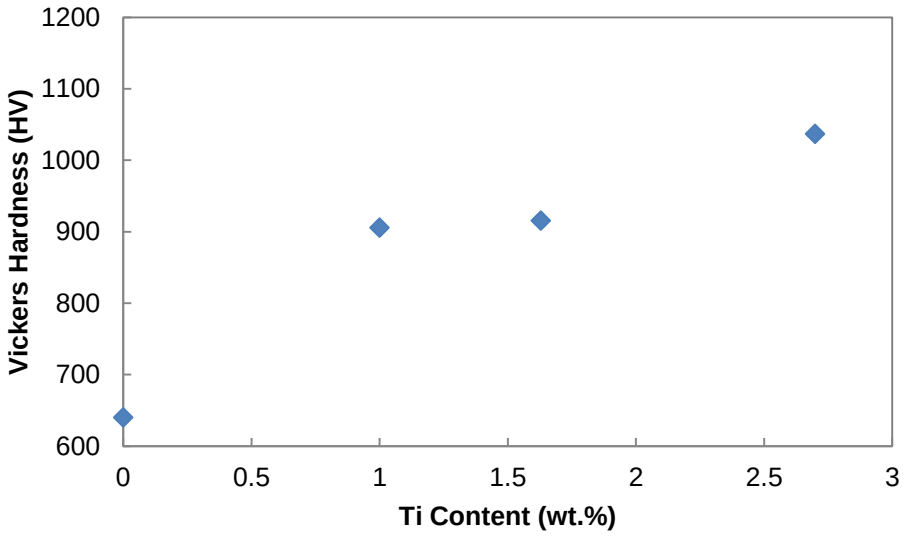

Figure 5. Effect of Ti content on hardness of nano W.

Mechanism of additive effect

To understand the mechanism of additive on nano-W's sintering behavior, SEM images had been taken on the W – 1 wt.% Ti 1300ºC sintered sample. Figure 6 shows one of the images taken at grain boundaries. EDS measurements have been performed on both phases which proved that the darker one is Ti and lighter one is W. Based on the image, a clearly tendency could be observed that Ti grains precipitates at the grain boundaries of nano-W which works as pin spots for grain boundary migration during sintering. This could explain the grain growth inhibitor effect of Ti-additives on sintering of nano-W.

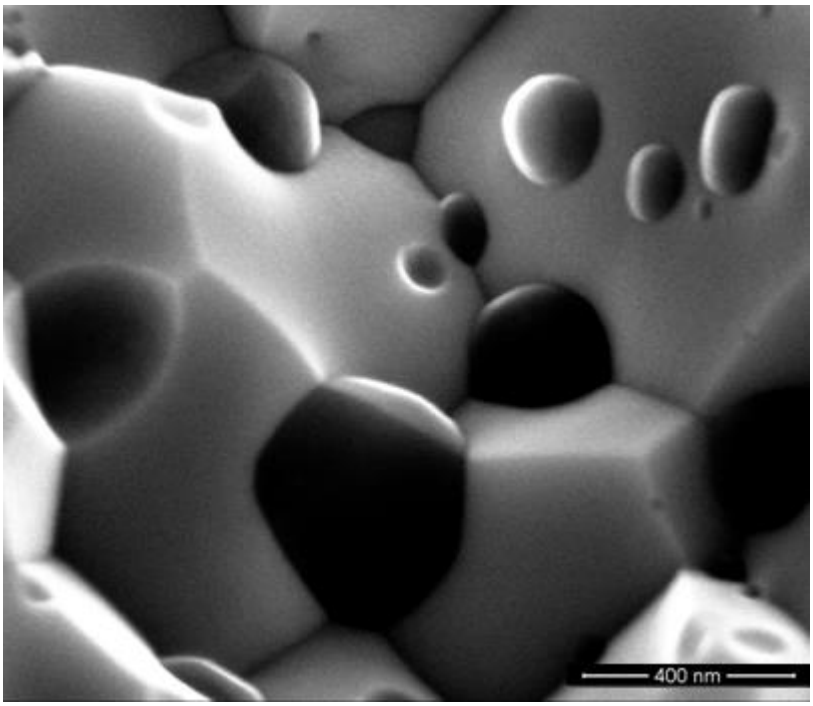

Figure 6. Microstructure of sintered W – 1 wt.% Ti sample at W grain boundary.

Future Work

The process will be further improved to obtain samples with optimized density and minimized grain size. Then the mechanical properties and hydrogen permeation behavior will be evaluated.

References

[1] M. Rieth, et al, J. Nucl. Mater. 432 (2011) 482-500.
[2] M. Jain, et al, Int. J. Powder Metall. 42 (2006) 53.
[3] X. Wang, Z. Fang. Fusion Materials Semiannual Report DOE/ER-0313/53 (2013) 40.
[4] X. Wang, Z. Fang. Fusion Materials Semiannual Report DOE/ER-0313/54 (2013) 108.

4.4 FABRICATION OF FUNCTIONALLY GRADED, TUNGSTEN STEEL LAMINATE - L.M. Garrison, E. Ohriner (Oak Ridge National Laboratory)

OBJECTIVE

The objective of this project is to create functionally graded tungsten to steel laminate composites for use in plasma facing components in fusion reactors.

SUMMARY

Tungsten foils in thicknesses 250, 100, and 25 µm and grade 92 steel foils in nominal thicknesses 250, 100, and 76 µm were obtained. The foils were alternately stacked within a stainless steel container and then hot rolled at 1000°C to approximately 80% reduction of the original height to induce bonding. A sample of the rolled composite material was polished for metallographic analysis. Metallographic analysis of the foils is ongoing. Samples of the foils and the rolled composite will be tensile tested.

PROGRESS AND STATUS

Introduction

Tungsten's thermal and plasma-interaction characteristics have made it the chosen material for plasma-facing components in fusion reactors. However, tungsten's low toughness and small thermal expansion compared to structural steels are remaining challenges for using tungsten in a reactor. Creating a tungsten-steel graded composite would simplify the joint between the two materials in a plasma-facing component and would reduce the stresses induced by their different thermal expansions.

Results

Foil metallography

Tungsten foils in thicknesses 250, 100, and 25 µm were purchased. Grade 92 steel foils in nominal thicknesses 250, 100, and 76 µm were fabricated by cold rolling. In the as-rolled state, the foils' surfaces had striations from the rolling, but individual grains could not be identified (Figure 1). To understand the foil properties, it is necessary to examine the grain structure and texture in the initial state. Because of the thin nature of the foils, attempts to mount them in resin in the traditional way for polishing were unsuccessful. Instead, foils were attached to resin discs with double sided tape and then polished to a 1 µm diamond paste and colloidal silica finish. For the steel foils (Figure 2a and 2b) this polish was successful in removing the surface texture from rolling. However, it appears individual particles of the polishing media were trapped in the sample surface, seen as the dark spots with trails in the figure. For the thicker tungsten samples, Figure 2c and 2d, the polishing appears to have removed the directional striations from the rolling, but a finer texture remains on the surface that obscures the grains. For the thinnest tungsten sample, Figure 2e, some of the rolling texture is still visible after polishing. Alternate ways of preparing samples to reveal the grains for crystallographic texture analysis are being explored.

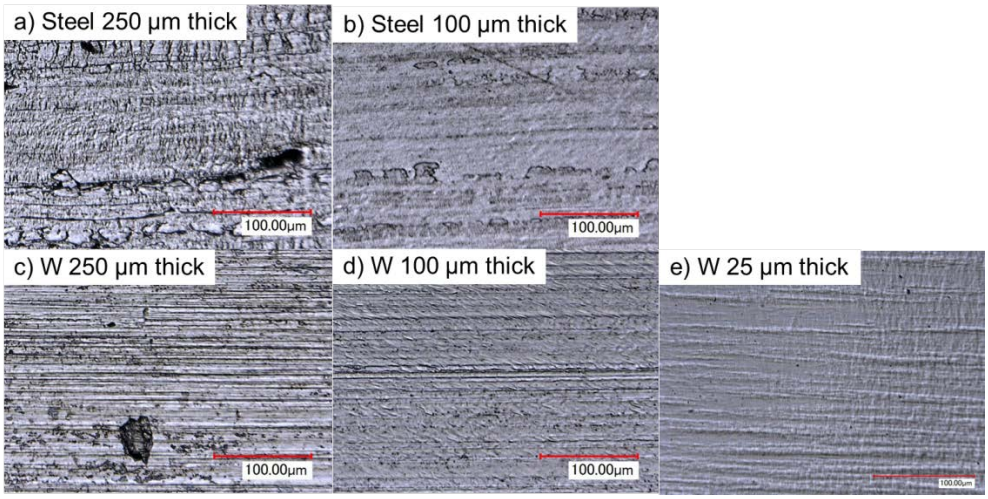

Figure 1. Surfaces of as-fabricated steel and tungsten foils imaged in a digital optical microscope using the HDR mode to enhance the texture.

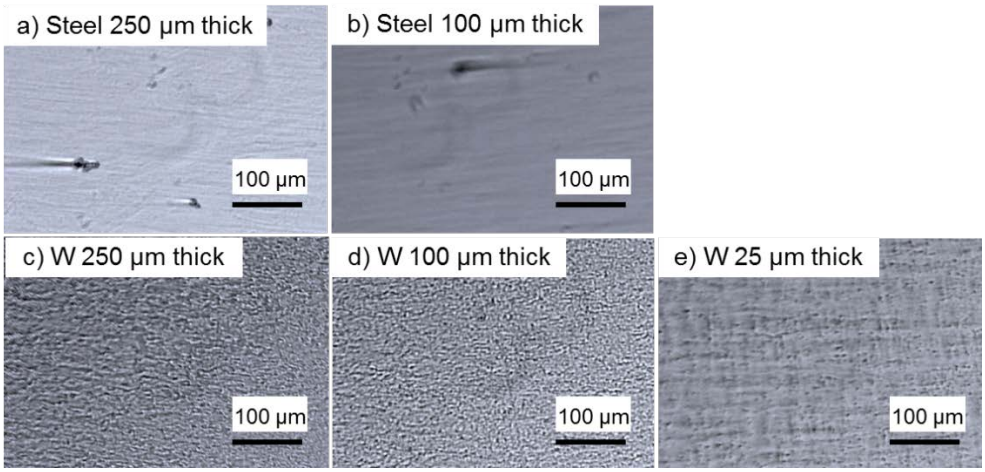

Figure 2. Surfaces of steel and tungsten foils after mechanical polishing, imaged in a digital optical microscope using the HDR mode to enhance the texture.

Rolled laminate composite

The foils were alternately stacked in a stainless steel box and then rolled at 1000°C to approximately 80% reduction. A sample of the resulting laminate composite was cut using electric discharge machining, mounted on its side, and polished to reveal the cross section of the layers (Figure 3). Layers that appear darker in the image are determined to be tungsten and those that are lighter are steel, based on the image contrast of the stainless steel outer layer and the nanohardness results (discussed below). In higher magnification images, contrast from other phases can be seen between the more evident tungsten and steel layers. Energy dispersive spectroscopy is planned to identify these phases.

Several numbered cracks are shown in Figure 3. All of the cracks that are visible are in the tungsten layers, and all of them are in Section 1 of the sample, which has the thickest tungsten pieces. Crack 1 is the widest of the cracks and is visible to the eye throughout the entire laminate material. At the left edge in Figure 3, Crack 1 is on the boundary between the tungsten and steel layer, but the crack moves to the interior of the tungsten layer for the remainder of the image. Cracks 2 and 4 are narrower, are in the

tungsten layer, and do not cross the whole sample. Crack 3 is located on the boundary between a steel and tungsten layer and traverses the whole section that was imaged. To avoid cracks in future laminate samples two strategies are proposed: reduce the processing temperature and increase the reduction per pass of rolling. Tungsten and steel have different coefficients of thermal expansion, so at a lower temperature the difference in expansion will be less, leading to less strain in the sample. An increased reduction per rolling pass also reduces the induced stress in the material. No cracks were observed in Section 2 or Section 3 that had initially thinner pieces of tungsten, so the thickest, 250 µm, tungsten foils may not be optimal for this project.

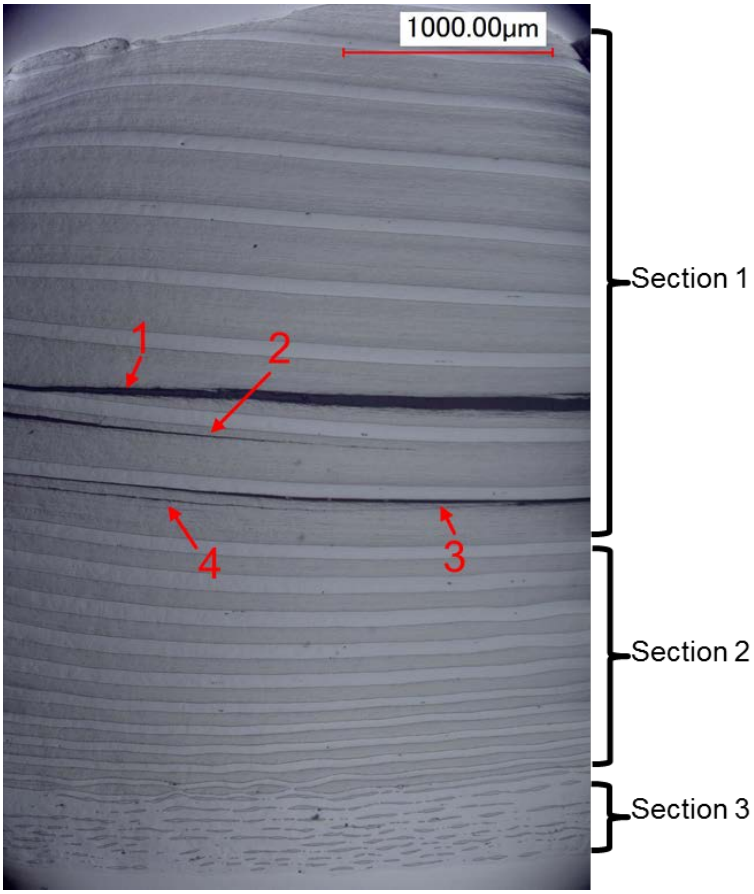

Figure 3. Cross section view of the rolled tungsten-steel laminate composite. The visible cracks are numbered. Layers with darker contrast are tungsten and those with lighter contrast are steel. Sections refer to different initial thicknesses of the foils. The rolling direction was horizontal in the image. Rounding at the edges of the image is an artifact of the optical microscope.

Figure 4 compares the initial thicknesses of the foils to the average thickness of the foils in the composite after rolling. The reduction of the tungsten and steel layers was essentially uniform in Section 1 with both materials experiencing approximately 34% reduction. The thickness of the layers In Section 2 after rolling varied from thicker layers closer to Section 1 and thinner layers closer to Section 3. In the pictured area in Figure 4c, the steel thickness was reduced by approximately 53% while the tungsten was reduced by approximately 44%. Within Section 2, but closer to the boundary with Section 3, the steel was more severely reduced than the tungsten; the maximum reduced layer of steel experienced about 78% reduction while the thinnest layer of tungsten in this section was only reduced by approximately 56%. The layers have a partially sinusoidal character to them, so there is a variation in the thickness of each layer throughout the sample. Because the steel and tungsten layers had different thickness reductions,

they also changed dimensions laterally by correspondingly different amounts to conserve volume, leading the composite to have a non-uniform outer boundary.

Section 3 was initially composed of the thickest steel foils and the thinnest tungsten foils. After rolling, the steel in this section experienced significantly more reduction, an average on the order of 83% reduction, than the steel in the other sections while the tungsten in Section 3 had approximately a 48% reduction (Figure 4d). The tungsten layers do not appear continuous, so the thickness and reduction estimates for the tungsten are taken from the centers of the visible tungsten islands. Because many cracks were found in Section 1, and the tungsten in Section 3 appears segmented, Section 2 appears to be the most successful.

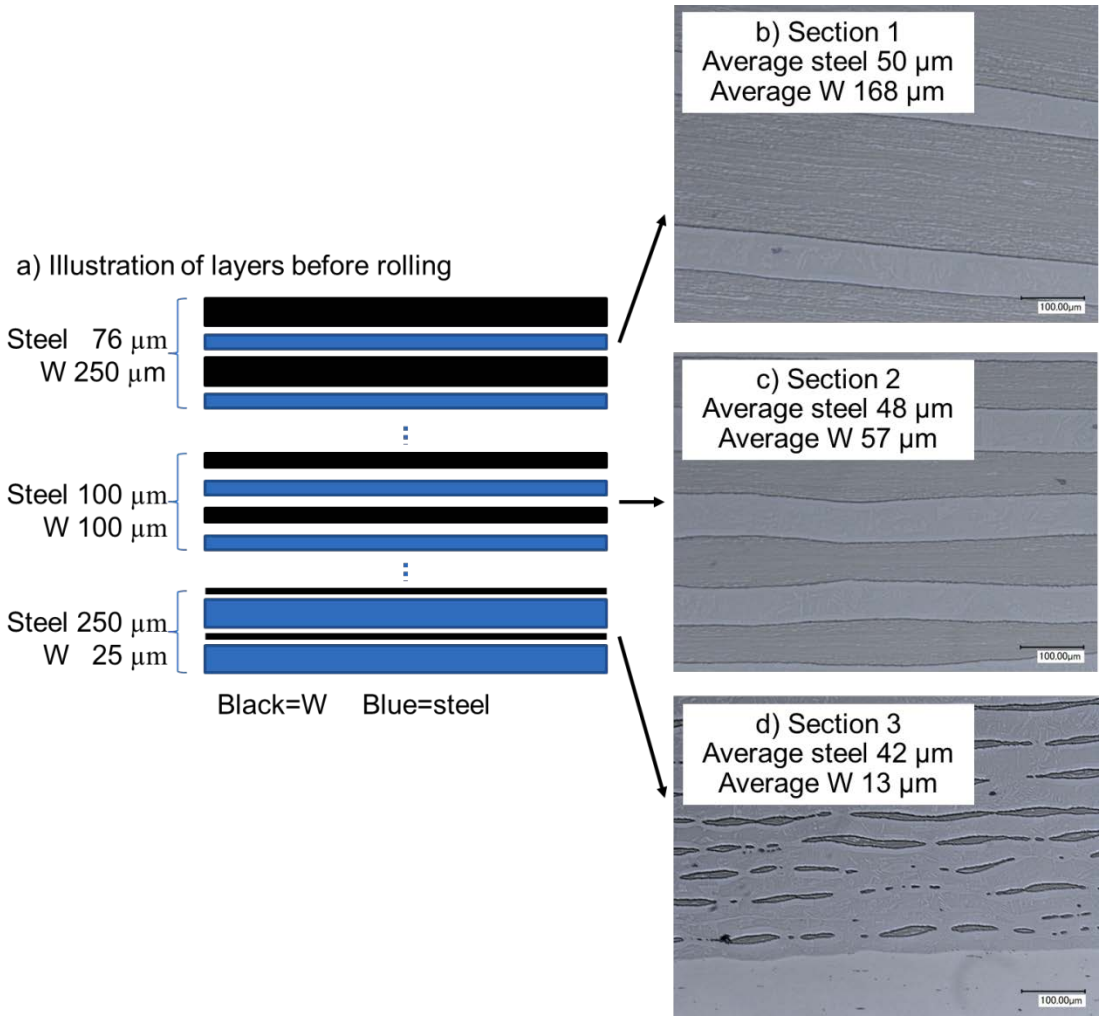

Figure 4. a) The stacking sequence of foils before rolling. Only four of the twenty layers of each of the three sections are illustrated. b), c), and d) are representative optical microscope images from each of the three different sections after rolling

Hardness

The as-received foil hardness measurements are shown in Figure 5; the measurements were taken on the 1 in. by 1 in. surface of the foils. Selected areas of the sample shown in Figure 3 were hardness tested and the results are presented in Figure 6. The hardness values in Figure 6 are of single measurements, and the corresponding indent images show that the indent size is comparable to the

thickness of the layers. Therefore the hardness values may be influenced by the surrounding layers and are only an initial estimate of the hardness. The general features revealed by the hardness tests are that the tungsten layers have higher hardness values than the steel layers, as was the case before roll-bonding the composite. A direct comparison between the hardness values in Figures 5 and 6 is difficult because the measurements were taken on different faces of the foils. It is expected that the foils have highly anisotropic grain dimensions, which may influence the hardness values on the top, as in Figure 5, versus on the cross section, as in Figure 6.

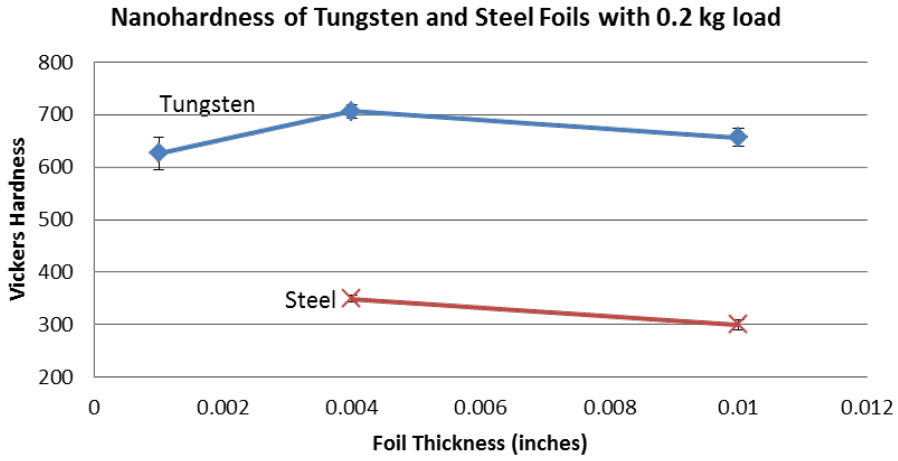

Figure 5. Hardness values for the tungsten and steel foils of various thicknesses.

Figure 6. Individual hardness measurements for selected layers on the rolled laminate-composite material.

4.5 RECENT PROGRESS OF CRACK BRIDGING MODELING OF DUCTILE-PHASE-TOUGHENED W-Cu COMPOSITES – W. Setyawan, C. H. Henager, Jr., K. B. Wagner, T. J. Roosendaal, B. A. Borlaug, and R. J. Kurtz (Pacific Northwest National Laboratory); G. R. Odette, K. H. Cunningham, and F. W. Zok (University of California, Santa Barbara)

OBJECTIVE

The objective of this study is to develop the materials science of ductile-phase W-composites for plasma-facing components in fusion reactors. Parametric study of a bridging model for W-Cu is discussed.

SUMMARY

A crack bridging model using calculated Cu stress-strain curves has been developed to study the toughening of W-Cu composites. A strengthening factor and necking parameters have been added to the model for the ductile-phase bridges to incorporate constraint effects at small bridge sizes. Parametric studies are performed to investigate the effect of these parameters. The calculated maximum applied stress intensity, a_{Kmax}, to induce a 1-mm stable crack is compared to the experimental stress intensity at peak load, K_{peak}. Without bridge necking, increasing the strengthening factor improves the agreement between a_{Kmax} and K_{peak} when plotted vs. logarithm of the displacement rate. Improvement can also be achieved by allowing necking with a larger failure strain. While the slope is better matched with this latter approach, the calculated value of a_{Kmax} is significantly larger than K_{peak}.

PROGRESS AND STATUS

Updated Results

In our previous report [1], the conversion of the displacement rate to strain rate was incorrect. In this report, we update the crack-bridging model using the corrected strain rate data. In addition, we include the effect of bridge necking. The 3-point bending specimen has a span L = 16.05 mm, a height w = 3.3 mm, and a thickness b = 1.67 mm. The experimental midpoint displacement rates, $\dot{\delta}$, were converted into a tensile strain rate, $\dot{\epsilon}$, using the following 3-point bending formula [2],

$$\dot{\epsilon} = \frac{2w(n+2)}{L^2}\dot{\delta} \quad (1)$$

where n is the stress exponent for creep (n = 1 for elastic bending). Note that n depends on $\dot{\epsilon}$ and does not correspond to the exponent appearing in the Dorn equation. The conversion is performed until the displacement rate converges to the experimental value within 1% relative error (see Table 1).

To compare model results to experimental data, an equivalent dataset was considered. The model begins by considering an initial applied K, a_{K0}, and a_0/w, where a_0 is the initial crack length. For the case treated here, a_0 was 0.7 mm and w was 3.3 mm. A bridge radius of 5 μm was assumed with a Cu volume fraction of 0.4 to match previous SEM data on Cu area fraction in polished cross-sections. The bridges are uniformly distributed according to the volume fraction with the first one at 0.02 mm from a_0. The Young's modulus for W at 293, 679, and 905 K is 410, 393, and 385 GPa, respectively, and for Cu is 130, 110, and 95, respectively. The Young's modulus of the composite was taken as the average value based on the volume fraction.

Table 1. Conversion of the midpoint displacement rate, $\dot{\delta}$, measured in experiments to the tensile strain rate, $\dot{\varepsilon}$, for the flow stress model of Cu [1].

T (K)	$\dot{\delta}$ (mm/min)	$\dot{\varepsilon}$ (1/s)	n	c_L	σ_y (MPa)	σ_{ulteng} (MPa)	ε_{ulteng}
293	2.0	1.178e-1	135.900	33.75	79.5	209.9	0.2612
	0.2	1.139e-2	131.300	34.37	78.2	206.2	0.2611
	0.02	1.100e-3	126.700	34.98	76.7	202.5	0.2612
	0.002	1.061e-4	122.100	35.60	75.1	198.7	0.2614
	0.0002	1.022e-5	117.460	36.23	73.3	194.8	0.2618
679	2.0	3.884e-2	43.198	36.47	74.9	175.4	0.2496
	0.2	3.497e-3	38.637	38.49	69.8	165.1	0.2507
	0.02	3.113e-4	34.101	40.56	63.6	154.4	0.2534
	0.002	2.697e-5	29.582	42.67	56.0	142.8	0.2581
	0.0002	2.294e-6	24.857	45.01	46.5	129.7	0.2658
905	2.0	2.349e-2	25.470	40.53	71.8	151.1	0.2375
	0.2	1.967e-3	20.997	44.33	62.4	135.3	0.2411
	0.02	1.596e-4	16.638	48.33	50.2	117.9	0.2500
	0.002	1.240e-5	12.393	52.98	35.0	98.1	0.2662
	0.0002	9.128e-7	8.688	59.74	19.3	76.7	0.2890

In the model, the crack growth was simulated under constant load. The criteria for crack growth was a_{Kcrit} = 8 MPa√m so that a crack will arrest when a_{Ktip} falls below 8 MPa√m. The maximum applied K (a_{Kmax}) was determined for each temperature and strain rate for which the crack was still bridged and stable after 1-mm of crack growth. Determining a_{Kmax} for which crack arrest will still occur is roughly equivalent to measuring the peak load stress intensity, K_{peak}, in the experiments, and allows for a direct comparison of datasets, one experimental and one simulated. In addition to recording a_{Kmax}, other calculated values were recorded as well: a_{Ktip} and the difference between a_{Kmax} and a_{Ktip}, denoted as ΔK, which represents the total closure force due to the bridges, or the net toughening due to the bridges.

A strengthening factor, *sfact*, is introduced into the model to account for bridge size effects and tri-axial constraint. This factor linearly scales the stress strain curve to account for these effects that can act to greatly increase the fracture strength of small, constrained bridges. In this approach, stress in the stress-strain curve is multiplied by *sfact* while the strain is unchanged. The value of *sfact* is determined as the strengthening factor needed to arrest a 1-mm crack at 905 K (*2/3*T_m) with a displacement rate of 0.0002 mm/min. We arbitrarily take the value obtained using the smallest applied load. The resulting *sfact* is 3.9. This value is then used for other temperatures and strain rates.

Using *sfact* = 3.9, the value of a_{Kmax} is then determined. The results are shown in Table 2. The value of a_{Kmax} is typically larger than K_{peak}. Note that within a 1-mm crack there are 40 bridges. From Table 2 we see that the number of bridges is less than 40. However, if we increase the applied K, the crack becomes unstable. Figure 1a plots a_{Kmax} and K_{peak} as a function of displacement rate. In Fig. 1a, a single-value shift has been applied to the a_{Kmax} data so that at 679 K (*1/2*T_m) and 0.0002 mm/min the value matches K_{peak}. In this case, the shift is 14.5-18.3 = -3.8 MPa√m. The shift allows for a more convenient comparison between model and experimental data. The best match is obtained at the intermediate temperature (*1/2*T_m). We varied *sfact* to explore its effects and with *sfact* = 8 (Fig. 1b) the match of room-temperature (*RT*) and *1/2*T_m curves are improved. However, the curve at *2/3*T_m is less sensitive to *sfact* changes.

Table 2. Model results showing computed values of critical parameters for stable bridged cracks with *sfact* = 3.9.

Temp (K)	Displ. Rate (mm/min)	Strain Rate (1/s)	# bridges	ΔK (MPa√m)	a_{Kmax} (MPa√m)	Exp. K_{peak} (MPa√m)
293	2	1.178e-1	23	15.1	22.9	23.5
293	0.2	1.139e-2	23	14.8	22.7	23.7
293	0.02	1.100e-3	23	14.5	22.4	21.3
293	0.002	1.061e-4	23	14.2	22.1	19.6
293	0.0002	1.022e-5	23	13.8	21.8	20.5
679	2	3.884e-2	22	12.1	20.0	17.6
679	0.2	3.497e-3	22	11.3	19.1	17.0
679	0.02	3.113e-4	23	11.2	19.2	15.2
679	0.002	2.697e-5	25	11.2	19.1	15.2
679	0.0002	2.294e-6	26	10.4	18.3	14.5
905	2	2.349e-2	21	10.2	18.2	13.5
905	0.2	1.967e-3	23	10.1	17.9	11.3
905	0.02	1.596e-4	25	9.4	17.3	9.4
905	0.002	1.240e-5	27	8.2	16.2	8.6
905	0.0002	9.128e-7	31	7.2	15.2	4.9

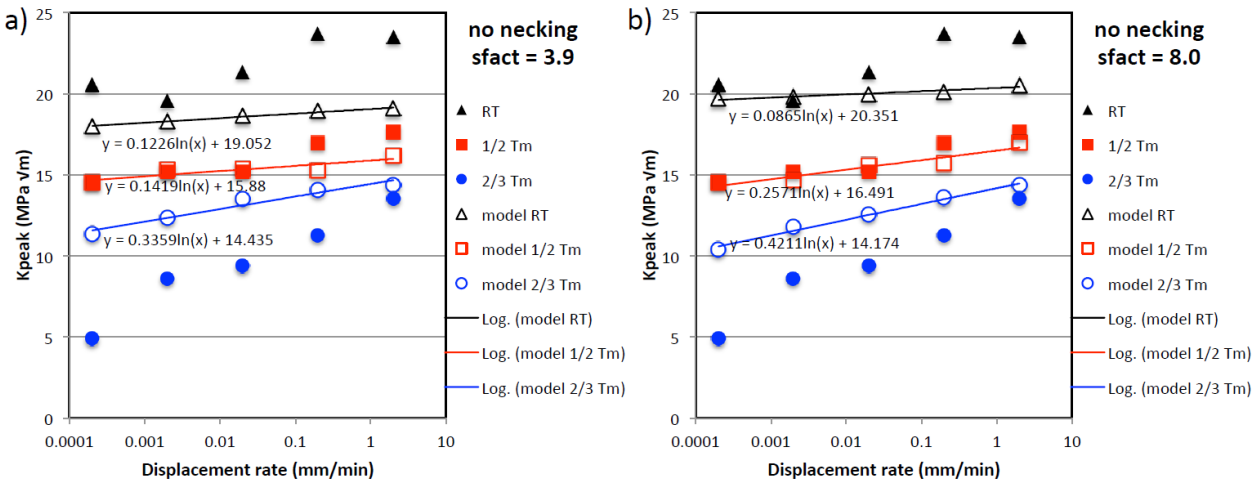

Figure 1. Experimental K_{peak} (filled symbols) and computed a_{Kmax} (open symbols) for W-Cu bridge model vs. displacement rate at room temperature (*RT*), 679 K (*1/2T$_m$*), and 905 K (*2/3T$_m$*). A shift of -3.8 and -9.8 MPa√m is applied to a_{Kmax} data in a) and b) respectively.

We have added a new capability in the crack bridging model to include necking of the bridges before failure. At this moment, we take the necking model from [3] as follows:

$$y(x) = \sqrt{x}\left[e^{(1-x^{(c+1)/2})}\right]^{1/(c+1)} \quad (2)$$

where $x = \varepsilon/\varepsilon_{ulteng}$ and $y = \sigma/\sigma_{ulteng}$. Necking is applied when $\varepsilon > \varepsilon_{ulteng}$. Figure 2 illustrates the necking curve for several values of *c*.

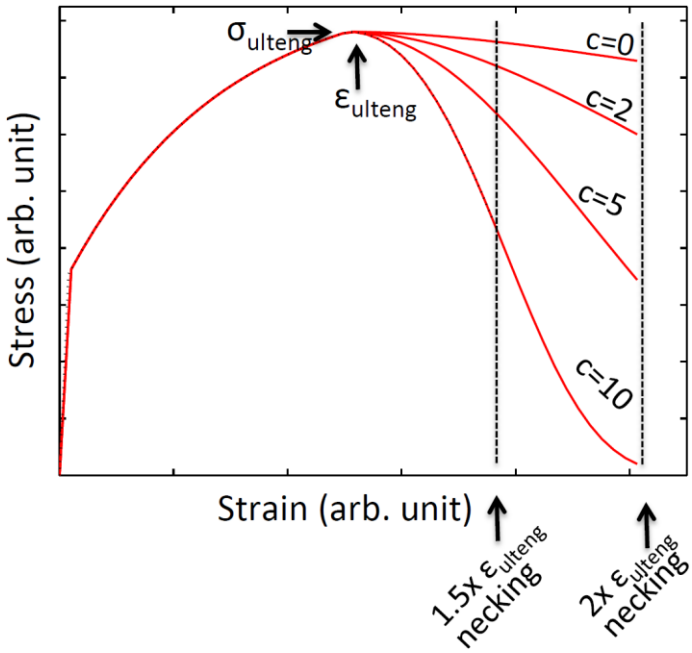

Figure 2. Illustration of the necking model for different values of *c*. Necking occurs when the strain is larger than the ultimate engineering strain, ε_{ulteng}.

To investigate the toughening behavior when necking is taken into account, we use *sfact* = 3.9 data and necking parameter c = 5 and vary the necking extension factor up to 2x. An extension factor of 2x necking denotes a failure strain of $\varepsilon_{fail} = 2\varepsilon_{ulteng}$. Table 3 summarizes the results for the 2x necking. Figure 3a shows the a_{kmax} plot with a shift of -6.3 MPa$\sqrt{m}$. Compared to Fig. 1a, necking improves the slope match of the *RT* and *1/2*T_m curves. Note that 1.5x necking (not shown) yields very similar curves as the 2x necking. Next, with *sfact* = 3.9 and 2x necking, we simulate with a necking parameter *c* of 0, 2, 5, and 10. The data with *c* = 2 is presented in Table 4 and is plotted in Fig. 3b with a shift of -8.5 MPa$\sqrt{m}$. Reducing the value of *c* from 5 to 2 appears to improve the slope match for the *2/3*T_m curve. Further improvement of the slope match at *2/3*T_m can be obtained with a lower value of *c*, e.g. *c* = 0 as shown in Figure 4. In Fig. 4, a shift of -12.5 MPa$\sqrt{m}$ has been applied to a_{Kmax}.

Table 3. Model results showing computed values of critical parameters for stable bridged cracks with *sfact* = 3.9 and necking condition of $\varepsilon_{fail} = 2\varepsilon_{ulteng}$ with *c* = 5. Maximum necking denotes the ratio of the maximum strain with ε_{ulteng} of the most stretched bridge.

Temp (K)	Displ. Rate (mm/min)	# bridges	# necking bridges	max. necking	ΔK (MPa√m)	a_{Kmax} (MPa√m)
293	2	26	6	1.25	17.9	25.8
293	0.2	26	6	1.25	17.5	25.5
293	0.02	27	7	1.49	18.1	25.7
293	0.002	27	7	1.72	17.8	25.7
293	0.0002	27	6	1.26	17.4	25.3
679	2	26	6	1.27	15.2	23.2
679	0.2	27	7	1.75	15.0	22.8
679	0.02	27	6	1.23	13.9	21.8
679	0.002	29	7	1.91	13.9	21.8
679	0.0002	30	6	1.25	13.0	20.8
905	2	26	7	1.60	13.3	21.2
905	0.2	27	7	1.26	12.4	20.4
905	0.02	29	7	1.22	11.6	19.5
905	0.002	32	7	1.25	10.7	18.7
905	0.0002	37	9	1.49	10.0	18.0

Table 4. Model results showing computed values of critical parameters for stable bridged cracks with *sfact* = 3.9 and necking condition of $\varepsilon_{fail} = 2\varepsilon_{ulteng}$ with *c* = 2. Maximum necking denotes the ratio of the maximum strain with ε_{ulteng} of the most stretched bridge.

Temp (K)	Displ. Rate (mm/min)	# bridges	# necking bridges	max. necking	ΔK (MPa√m)	a_{Kmax} (MPa√m)
293	2	28	10	1.69	19.9	27.9
293	0.2	28	10	1.66	19.6	27.6
293	0.02	29	11	2.00	20.0	27.9
293	0.002	29	11	1.73	19.6	27.5
293	0.0002	29	11	1.55	19.2	27.2
679	2	28	10	1.72	16.9	24.8
679	0.2	28	9	1.44	15.8	23.8
679	0.02	30	11	1.81	16.0	23.9
679	0.002	31	11	1.63	15.4	23.3
679	0.0002	33	13	1.89	15.0	23.0
905	2	28	11	1.73	14.7	22.6
905	0.2	28	8	1.32	13.1	21.0
905	0.02	31	11	1.58	12.8	20.7
905	0.002	34	11	1.48	11.8	19.8
905	0.0002	39	13	1.63	11.1	19.0

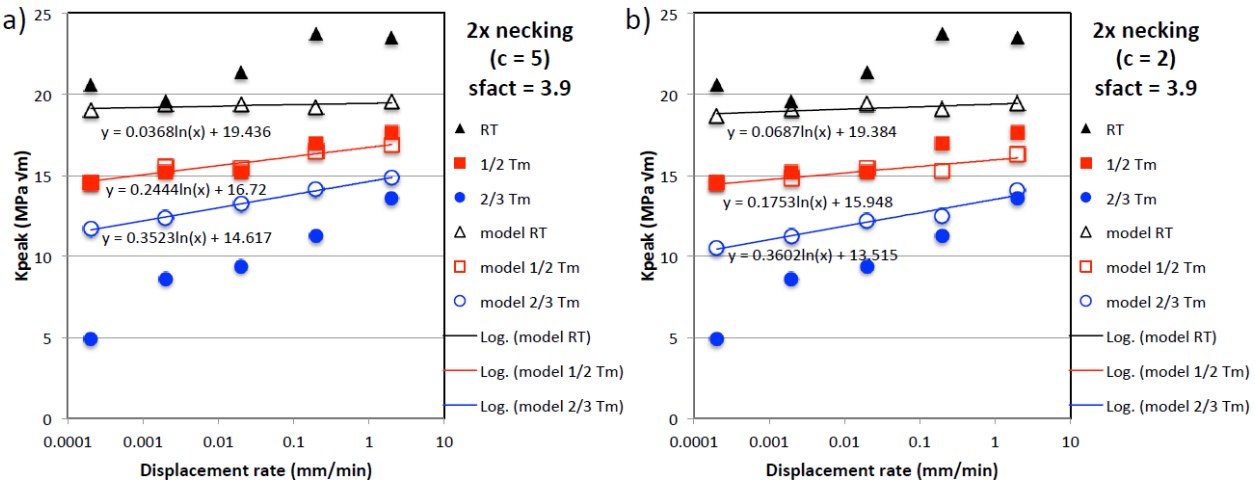

Figure 3. Experimental K_{peak} (filled symbols) and computed a_{Kmax} (open symbols) for W-Cu bridge model vs. displacement rate at room temperature (*RT*), 679 K (*1/2T$_m$*), and 905 K (*2/3T$_m$*). A shift of -6.3 and -8.5 MPa√m is applied to a_{Kmax} data in a) and b) respectively.

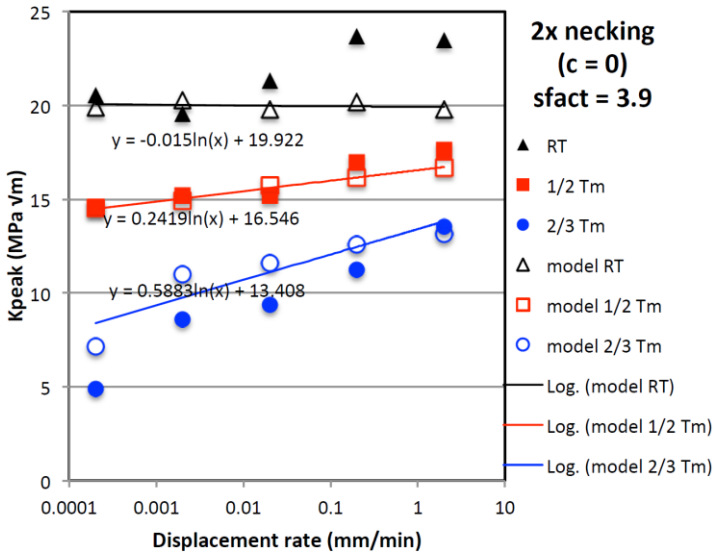

Figure 4. Experimental K_{peak} (filled symbols) and computed a_{Kmax} (open symbols) for W-Cu bridge model vs. displacement rate at room temperature (*RT*), 679 K (*1/2T$_m$*), and 905 K (*2/3T$_m$*). A shift of -12.5 MPa√m is applied to a_{Kmax}.

Discussion

The discrete bridging model described here has been improved to include a more complete treatment of a Cu-bridge in terms of plastic flow as a function of strain rate and temperature, strengthening due to size effects and constraints, and necking with complete control over how the bridges unload and fracture. However, this treatment has some problematic issues associated with it. One is that both strengthening effects and necking effects can be used as adjustable parameters and they appear to provide similar effects on toughening calculations. This makes for difficulties in model validation. Secondly, the comparison with peak load stress intensity, while necessary at this point and convenient, is not as strong a validation test as desired. A better test of the model will be to simulate the load displacement curves as a function of strain rate and temperature. This will also prove challenging given that the observed failure

mode is multiple cracking over a significant plastic zone that is not captured in the model of a single bridged crack. This research will continue to explore model validation and more informative fracture toughness testing, if possible.

References

[1] C. H. Henager, J., R.J. Kurtz, T.J. Roosendaal, B.A. Borlaug, G.R. Odette, K.H. Cunningham, K. Fields, D. Gragg, and F.W. Zok, "Recent Progress in the Development of Ductile-Phase Toughened Tungsten for Plasma-Facing Materials," in Fusion Reactor Materials Program June 30, 2014 DOE/ER-0313/56 – Volume 56, Vol. 56, F. Wiffen, R. Godfrey, and B. Waddell, Editors, 2014, US DOE: ORNL, TN, p. 117-125.

[2] Hollenberg, G.W., G.R. Terwilliger, and R.S. Gordon, "Calculation of stresses and strains in four-point bending creep tests," J. Am. Ceram. Soc., 1971, 54(4), 196-9.

[3] Cox, B.N., "Extrinsic factors in the mechanics of bridged cracks," Acta metallurgica et materialia, 1991, 39(6), 1189-1201.

4.6 ALLOYING AND NEUTRON IRRADIATION EFFECTS IN TUNGSTEN-RHENIUM - L.M. Garrison, L.L. Snead, E. Ohriner (Oak Ridge National Laboratory)

OBJECTIVE

The objective of this project is to gain a fundamental understanding of the changes to mechanical and thermal behavior of tungsten that are caused by neutron irradiation and rhenium additions.

SUMMARY

Five alloys of tungsten with different amounts of rhenium additions as well as one pure tungsten control material were fabricated by arc melting. After arc melting the samples were hot-rolled to approximately 80% reduction. Samples for mechanical testing, thermal testing, and neutron irradiation are being prepared from these alloys.

PROGRESS AND STATUS

Introduction

Rhenium additions to tungsten are known to change the thermal and mechanical properties. Because rhenium is produced by transmutation in neutron irradiated tungsten, any neutron irradiated sample of tungsten displays a combination of the irradiation induced structural changes as well as the changes caused by the rhenium. In order to separate and understand these two effects, samples of tungsten with varying amounts of rhenium were fabricated for thermal and mechanical testing before and after irradiation.

Results

The alloy compositions are listed in Table 1. After the initial arc-melting, the materials were brittle and had internal cracks and voids which made them difficult to machine. To improve the microstructure, the materials were hot-rolled at 1200°C to approximately 80% reduction. The rolling has been completed on all six alloys.

Table 1. W-Re alloy compositions.

Alloy number	Initial Re wt.%
Alloy 1	0.033
Alloy 2	0.165
Alloy 3	0.830
Alloy 4	3.440
Alloy 5	17.700
Alloy 6	0.000

Figure 1a shows the representative structure of the material after hot-rolling. After the rolling was completed, the materials' machinability had improved and samples were able to be cut and polished from the materials. Disk samples (Figure 1b) for neutron irradiation, thermal testing, and mechanical testing have been machined from Alloy 1 and Alloy 4. Alloys 2, 3, 5, and 6 are currently being prepared for machining.

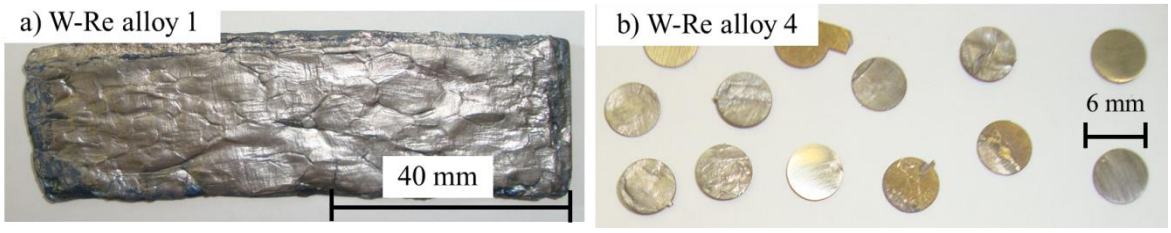

Figure 1. a) Tungsten-rhenium Alloy 1 (0.033 wt. % Re) after hot rolling. b) Alloy 4 (3.44 wt. % Re) disks cut from the rolled material in various stages of finish.

In the as-melted state, a sample of Alloy 4 was polished and examined in the SEM (Figure 2). It had large grains on the order of a few millimeters, and at some grain boundaries there was separation (Figure 2b). After rolling, a sample of W-Re Alloy 4 was mechanically polished down to a diamond paste and then finished with a colloidal silica solution (Figure 3). The texture visible in Figure 3 was apparent only after the silica polishing step, so may be the result of preferential chemical etching by the silica. Further metallographic analysis will be performed on the rolled alloys.

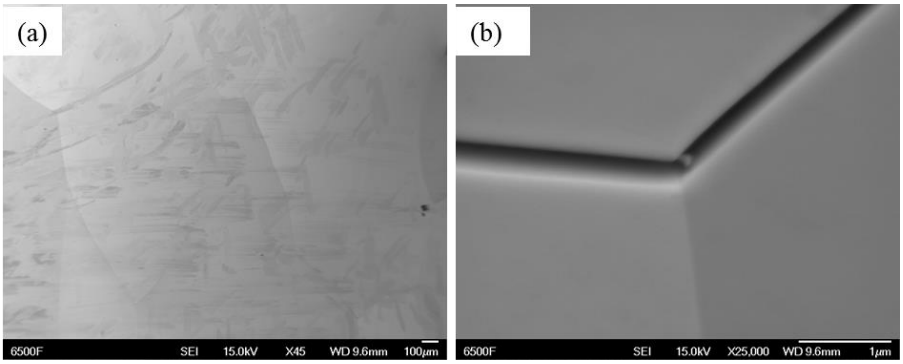

Figure 2. Tungsten Alloy 4 with ~3 wt. % rhenium in the as-melted state had (a) large grains on the order of ~0.5-2mm and (b) separation along some grain boundaries.

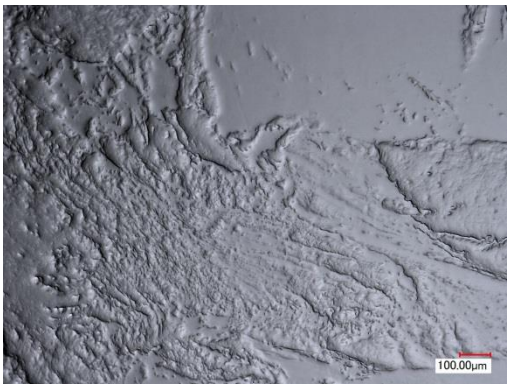

Figure 3. Alloy 4 after it was hot rolled and polished.

4.7 NEUTRON IRRADIATION EFFECTS IN TUNGSTEN - L.M. Garrison, L.L. Snead, X. Hu, T. Koyanagi, N.A.P. Kiran Kumar (Oak Ridge National Laboratory), M. Fukuda (Tohoku University, Japan) and K. Yabuuchi (Tohoku University, Japan)

OBJECTIVE

The objective of this work is to evaluate the effect of neutron irradiation on the mechanical properties of tungsten with selected microstructures to aid in developing plasma-facing materials for fusion reactors.

SUMMARY

A total of 440 samples were irradiated in HFIR at temperatures from 70 to 900°C and fast neutron fluences of 0.01 to 20 $\times 10^{25}$ n/m^2 at E>0.1 MeV. Types of tungsten irradiated in this study were [110] single crystal tungsten, [100] single crystal tungsten, wrought tungsten foils, annealed tungsten foils, and tungsten-copper laminates. Each rabbit irradiation capsule also contained silicon carbide (SiC) samples to be used as temperature monitors. The post-irradiation analysis of the SiC samples has been completed, and the estimated tungsten irradiation temperatures were determined. A subset of single crystal [110] samples was selected to study the effects of annealing on recovering mechanical properties and defects through positron annihilation spectroscopy (PAS) and hardness testing.

PROGRESS AND STATUS

PAS and Hardness Tests

Samples 1W05 and 1W25 were selected for PAS and hardness testing. The samples were tested after irradiation, and then the tests were repeated after 1 hour anneals at 400, 500, and 650°C. Comparing the unirradiated to the as-irradiated state of 1W05 (Figure 1 and Table 1) and 1W25 (Figure 2 and Table 2), showed that each sample experienced a large increase in the mean positron lifetime. After each subsequent annealing step, the lifetime has continued to increase for each sample up to 322 ps in 1W05 and 339 ps in 1W25 after the 650°C anneal. At all measured points, sample 1W25, irradiated to the higher fluence, had a longer mean lifetime than sample 1W05.

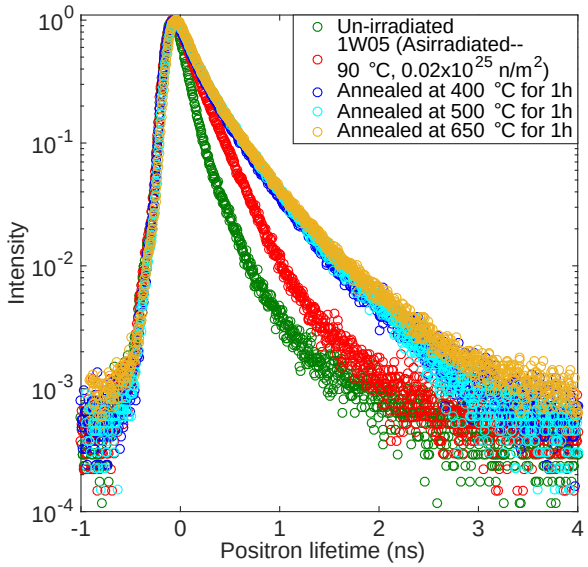

Figure 1. PAS results on 1W05 after irradiation and after three annealing stages.

Table 1. PAS data for sample 1W05.

Samples	τ_1 (ps)	τ_2 (ps)	τ_3 (ps)	I_1 (%)	I_2 (%)	I_3 (%)	Mean Lifetime (ps)
Unirradiated	91	184	489	70	23	7	140
1W05	124	231	516	26	69	5	218
Annealed at 400 °C	95	189	452	8	42	50	312
Annealed at 500 °C	108	269	510	20	46	34	318
Annealed at 650 °C	101	232	507	18	41	41	322

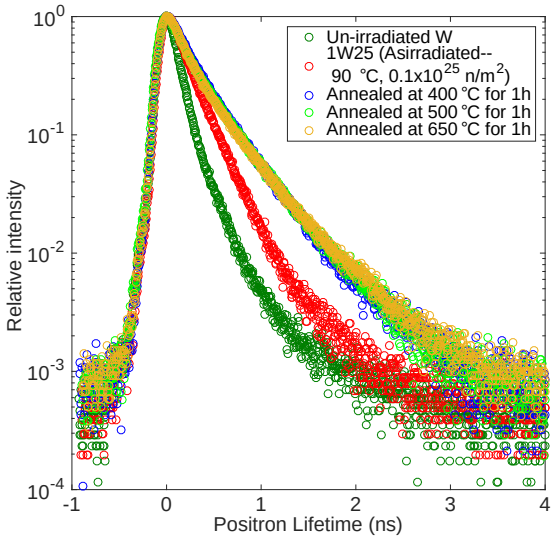

Figure 2. PAS results for sample 1W25.

Table 2. PAS data for sample 1W25.

Samples	τ_1 (ps)	τ_2 (ps)	τ_3 (ps)	I_1 (%)	I_2 (%)	I_3 (%)	Mean Lifetime (ps)
Unirradiated	91	184	489	70	23	7	140
1W25	125	220	525	15	78	7	228
Annealed at 400 °C	122	203	414	12	22	66	332
Annealed at 500 °C	118	314	574	18	56	26	345
Annealed at 650 °C	108	283	545	20	45	35	339

From the PAS data, information about the vacancy cluster size can be extracted (Figure 3). Five-component analysis is used, four of which have fixed lifetimes: 200, 260, 330, and 437 ps, equivalent to three-dimensional vacancy clusters of sizes of about 0.312 (1V), 0.49 (4V), 0.67 (10V) and >1.14 (50V) nm in diameter, respectively. For both samples, the vacancy clusters grew after each annealing step.

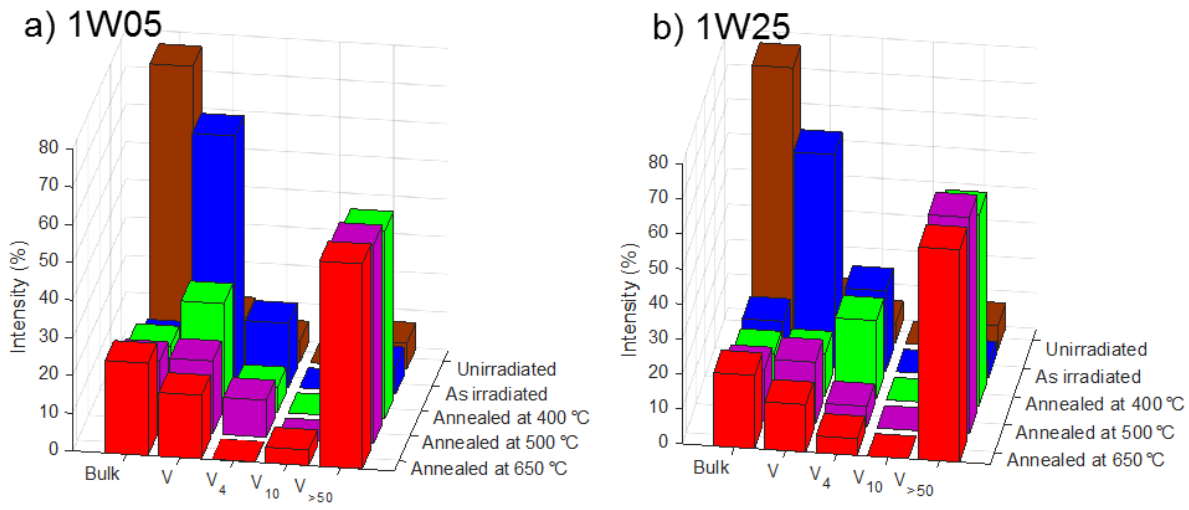

Figure 3. Vacancy cluster evolution in samples a) 1W05 and b) 1W25 after irradiation and annealing.

Hardness was measured on samples 1W05 and 1W25 after each annealing step (Figure 4). The hardness values increased after each annealing step. This is caused by the microstructural changes such as cluster growth in the materials during annealing. The experiment will continue with annealing at 800, 1000, and 1300°C. TEM analysis will also be conducted on the samples to aid in understanding the hardness changes.

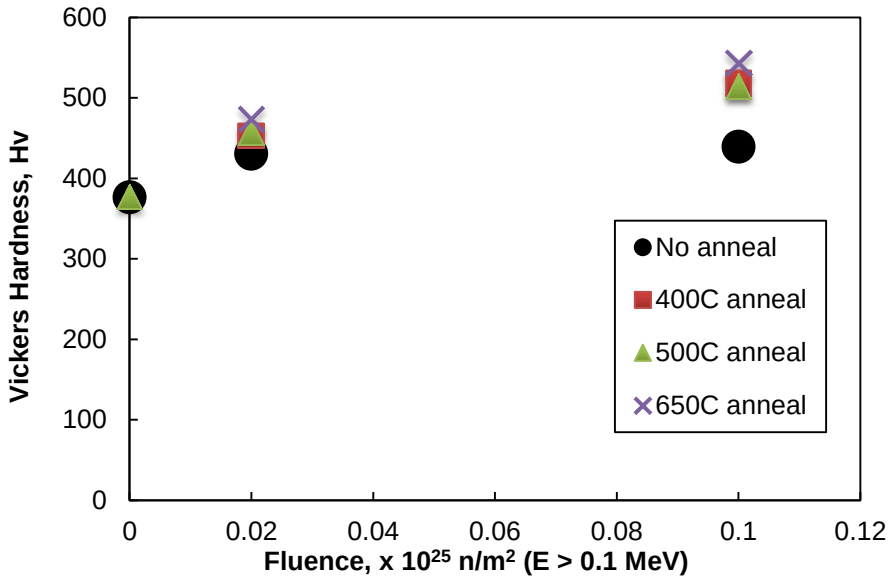

Figure 4. Hardness of 1W05 and 1W25 after annealing.

Sample Temperatures during Irradiation

The length changes of the SiC temperature monitors from each rabbit capsule were measured during heating and cooling. A program in the software R, written by Anne Campbell, was used to analyze the SiC data to extract the irradiation temperatures. The program allows the analysis of SiC data to be more repeatable and reduces the operator bias in analyzing the data. There is still an element of human

interpretation for the more difficult data sets, so the values obtained should be considered within an uncertainty on the order of 10°C. The version "TM_Analysis 20141017 new first guess.R" was used to analyze these data. The results of the SiC data fitting are reported in Table 3 under the heading "Values from curve fitting measured SiC data."

To relate the SiC irradiation temperatures to the W sample temperatures, an Ansys model by Nesrin Cetiner was used. In the Ansys model, the Top and Bottom sections of each rabbit are assumed to be identical, so are not independently modeled. To obtain the estimated W sample temperatures during irradiation, the difference between the SiC and W sample temperature in the Ansys model is added to the temperature obtained from the curve fitting of the SiC data. The final result is listed in the far right column in Table 3. All the W sample irradiation temperatures are higher than the target temperatures for which the capsules were designed.

Table 3. Measured and modeled temperature values for the irradiation capsules.

				Values from curve fitting measured SiC data			Values from Ansys thermal model			Result
	Rabbit Capsule	SiC sample ID	Target temp (°C)	Max (°C)	Median (°C)	Min (°C)	SiC (°C)	W (°C)	Dif. SiC to W (°C)	W sample temperature (°C)
Top	TB-300-1	658	300	333.8	318	NaN	268	320	52	370
	TB-300-2	675	300	427.9	409	393.4	268	320	52	461
	TB-300-3	686	300	343.1	311.4	291.4	268	320	52	363.4
	T9G-11	603	300	393	376.7	356.3	269	319	50	426.7
	TB-500-1	699	500	743.4	728.6	708.1	457	526	69	797.6
	TB-500-2	709	500	663.5	620	590.8	457	526	69	689
	TB-500-3	582	500	712.9	704.2	673.2	459	524	65	769.2
	T9C-14	644	500	668.2	638.6	615.1	458	524	66	704.6
	TB-650-1	646	650	746.7	724	697.6	585	695	110	834
	TB-650-2	723	650	703.9	686.9	646.6	585	695	110	796.9
Middle	TB-300-1	664	300	370	360.3	349.9	278	325	47	407.3
	TB-300-2	670	300	428.3	414.3	399.4	278	325	47	461.3
	TB-300-3	690	300	384.6	365	351.8	278	325	47	412
	T9G-11	601	300	422.2	393.5	373.7	279	325	46	439.5
	TB-500-1	695	500	776.6	737.7	720.9	472	533	61	798.7
	TB-500-2	712	500	744.4	722.3	715.3	472	533	61	783.3
	TB-500-3	581	500	741.1	733.8	710.6	473	530	57	790.8
	T9C-14	638	500	690.7	667.4	669.1	474	531	57	724.4
	TB-650-1	649	650	685.7	681.7	661.5	613	712	99	780.7
	TB-650-2	718	650	682.6	646.3	576.6	613	712	99	745.3

Continued

				Values from curve fitting measured SiC data			Values from Ansys thermal model			Result
	Rabbit Capsule	SiC sample ID	Target temp (°C)	Max (°C)	Median (°C)	Min (°C)	SiC (°C)	W (°C)	Dif. SiC to W (°C)	W sample temperature (°C)
Bottom	TB-300-1	665	300	382.7	362.1	345.7	268	320	52	414.1
	TB-300-2	679	300	412.4	396	377.4	268	320	52	448
	TB-300-3	682	300	386.2	368	347.6	268	320	52	420
	T9G-11	597	300	424.3	401.5	387.2	269	319	50	451.5
	TB-500-1	703	500	696.2	681.5	645.4	457	526	69	750.5
	TB-500-2	710	500	615.1	598.4	582.1	457	526	69	667.4
	TB-500-3	583	500	609.2	567.8	535.3	459	524	65	632.8
	T9C-14	642	500	659.2	640	613.7	458	524	66	706
	TB-650-1	656	650	692.9	666.1	637.4	585	695	110	776.1
	TB-650-2	588	650	670.1	649.4	627.8	585	695	110	759.4

4.8 HIGH-HEAT FLUX TESTING OF LOW-LEVEL IRRADIATED MATERIALS USING PLASMA ARC LAMPS - A.S. Sabau, L.L. Snead, Y. Katoh (Oak Ridge National Laboratory), Kazutoshi Tokunaga (Kyushu University, Japan)

OBJECTIVE

The objective of this work, part of the PHENIX collaboration with Japan, is testing of irradiated materials that are candidate divertor component materials and mock-up divertor components under high-heat flux using Plasma Arc Lamps (PAL).

SUMMARY

In this reporting period, high-heat flux testing of five specimens, supplied by the Japanese collaborators in the PHENIX program, was conducted at ORNL. Dr. Tokunaga was on assignment at ORNL for four weeks as part of the joint US/Japan PHENIX program, during which time this high-heat flux testing and evaluation of the clamping fixture and vacuum system was conducted.

PROGRESS AND STATUS

Effort was conducted in three main areas: (a) reducing the oxidation of the specimen during high-heat flux testing and implicitly enhancing the radiation safety during testing of irradiated specimens, (b) achieving a high thermal gradient through the specimen while enhancing the measurement accuracy of the specimen temperature, and (c) conducting high-heat flux testing with non-irradiated samples as part of the joint US/Japan PHENIX program.

Reduction in the oxidation and enhancing the radiation safety

The reduction in the oxidation during testing of irradiated specimens was accomplished by employing an additional high-vacuum test section embedded within the main test chamber (low-vacuum). The high-vacuum test section would enclose the cooling rod, holder, and irradiated sample (Fig 1a). The main test chamber will not be contaminated, lowering the maintenance and operational costs. Also, the limited amount of O_2 in the high-vacuum test section will severely limit formation of tungsten oxide on the irradiated sample. Specifically, the high-vacuum section is made by a quartz dome, whose circumference is shielded by a Cu plate in order to protect the O-ring seal from direct heating by the plasma-arc lamp (Fig. 1b).

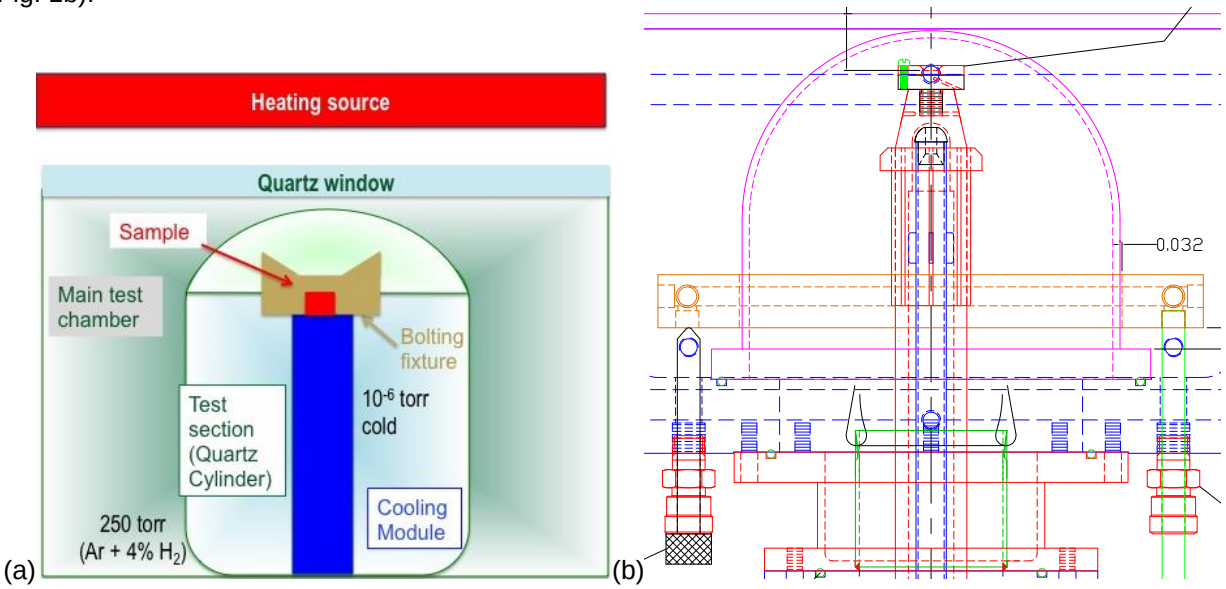

Figure 1. Schematic illustrating the use of two confinement enclosures in the test section.

High-thermal gradient during HHFT

In order to attain a high thermal gradient through the samples, new bolting holders were fabricated from a Ta10W alloy that exhibits high strength at high temperature. In the final design, as shown in Figure 2, the specimen was mounted directly onto a Cu cooling rod to attain the lowest temperature on the back surface of the specimen and thus enabling the highest thermal gradient in the specimen. Pictures of the actual setup are shown in Figure 3. The thermocouple wires were shielded by a Nb cone.

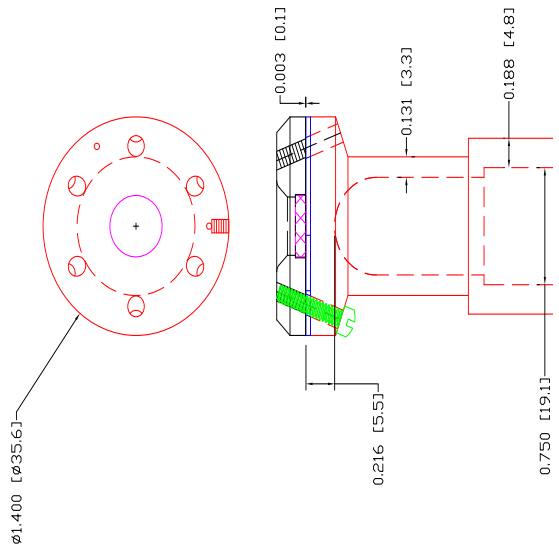

Figure 2. Drawing of the final design for the cooling rod and bolting fixture.

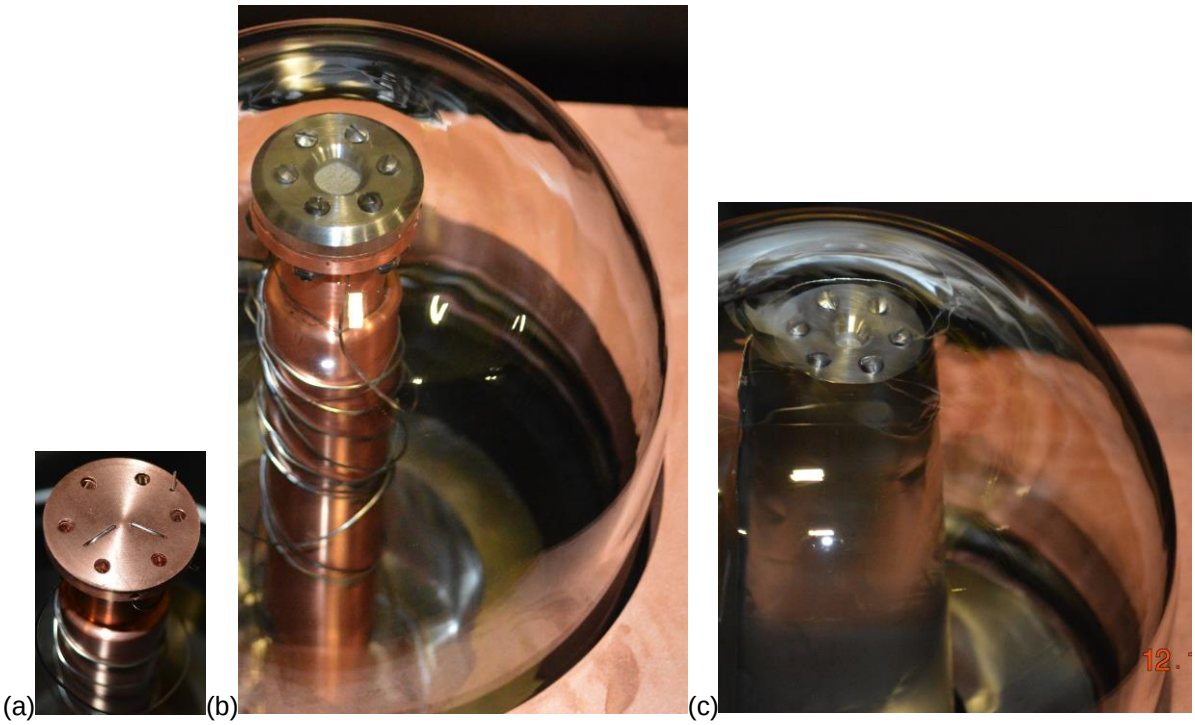

Figure 3. Thermocouples mounting: (a) top view of washer showing 2 thermocouples that will be sandwiched between Cu rod and specimen, (b) view of specimen 1 and bolting flange through quartz dome and unshielded thermocouple wires, (c) view of specimen 5, bolting flange, Nb cone (shielding the thermocouple wires) through quartz dome.

High-heat flux experiments

Several high-heat flux experiments were conducted during the December visit of Dr. Kazutoshi Tokunaga of Kyushu University as part of the joint US/Japan PHENIX program. Five W/F82H specimens, which were supplied by the Japanese collaborators in the PHENIX program, were exposed to high-heat fluxes at ORNL (Table 1). Thickness of W and F82H steel was 1 mm, each. Each specimen was exposed to corresponding high-heat fluxes such that the maximum temperature would attain the target temperature shown in Table 1. During high-heat flux testing, a non-uniform temperature is expected in the specimen. The specimen temperature was measured with thermocouples inserted between the back surface of the specimen and top surface of Cu rod, $T_{BS, Cu}$. The data for the high-vacuum pressure and $T_{BS, Cu}$ is next shown for selected cycles for specimens 1, 2 and 5.

Table 1. W/F82H specimens exposed to high-heat flux testing.

	Diameter [mm]	[1]Target Max. Temp. [^oC]	[2]No. of Cycles	[3]Cycle duration [s]	Max. Heat Flux [W/cm^2]	Comments
1	10	750	101	10-15	300	Delamination observed
2	10	500	164	7-10	210-278	No delamination observed (Visual)
3	10	550	214	4-5	300	No delamination observed (Visual)
4	6	450	110	10-16	300	No delamination observed (Visual)
5	6	550	42	10-15	300-323	[4]No delamination observed (Visual)

[1] The target temperature for the interface between the W and F82H.
[2] Number of cycles at heat flux.
[3] Thickness W and F82H steel was 1 mm each.
[4] Shielded thermocouples from the direct IR flux

In order to keep the vacuum pressure to acceptable levels, the heat flux was increased incrementally to its maximum value. Data acquired with a high-vacuum pressure transducer indicated that the absolute pressure increased during the HHFT (Figures 4a and 4c). The temperature is shown in Figures 4b and 4d for specimen 1 for cycles 84-85 and 132-134, respectively. For specimen 1, $T_{BS, Cu}$ temperatures higher than 600^{o}C were measured when the high-heat flux exposure was increased from 12 s to 15 s (cycles 132-134).

The pressure and temperature data is shown for specimen 2 in Figure 5. The maximum pressure was approximately 10^{-4} Torr, higher than that for specimen 1. This higher vacuum was maintain for all the subsequent specimens, indicating that the entire testing section was preconditioned during the HHFT of specimen 1 by slowly evolving most of the volatile species in the test section. The peak heat fluxes for specimen 2 were lower than those for specimen 1 in order to keep the measured temperature $T_{BS, Cu}$ below 500^{o}C.

The pressure and temperature data is shown for specimen 5 in Figure 6. The temperature data for specimens 1 and 2 (Figures 4b, 4d, and 5b) was obtained with unshielded thermocouples while the temperature data for specimen 5 (Figure 6b) was obtained with shielded thermocouples. The peak of the measured temperature $T_{BS, Cu}$ was approximately 240^{o}C. An analysis of this temperature data is being conducted to understand the effects of: (a) contact area between the thermocouple sheath with both back surface of specimen and cooling rod, and (b) shielding of the thermocouple wires in a region away from the thermocouple bead, the junction at which the temperature is actually measured. The temperatures at the top surface of the specimen are expected to be higher than measured temperature $T_{BS, Cu}$.

Profilometry measurements were conducted before and after HHFT. The specimens were flat before HHFT. The post-HHFT profilometry data indicated that the specimens bowed, raising the center of the W above its edge. The profilometry data was used to obtain the height of the center of the samples and it is shown in Table 2. The data showed that the 10 mm diameter specimens (i.e., specimens 1, 2, and 3) bowed more than 6 mm diameter specimens (i.e., specimens 4 and 5). The profilometry data is useful to

obtain the residual stresses in the specimens and further validate the maximum temperature conditions during HHFT.

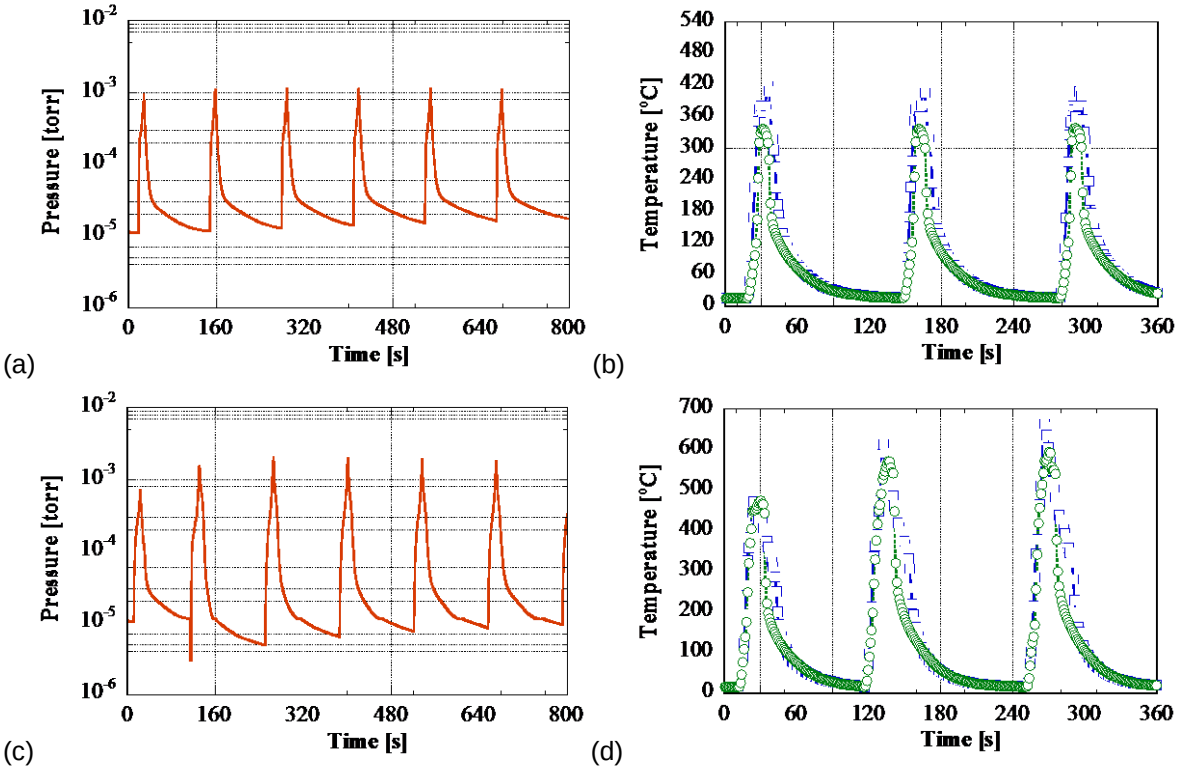

Figure 4. Representative data for specimen 1: (a) absolute pressure for cycles 84-89 (300 W/cm^2 for 10 s) and (b) measured temperature $T_{BS,\ Cu}$ for cycles 84-85 with un-shielded thermocouples, (a) absolute pressure for cycles 132-137 and (b) measured temperature $T_{BS,\ Cu}$ for cycles 132-134 (300 W/cm^2 for 12 s cycle 132 and 15 s for cycles 133-137).

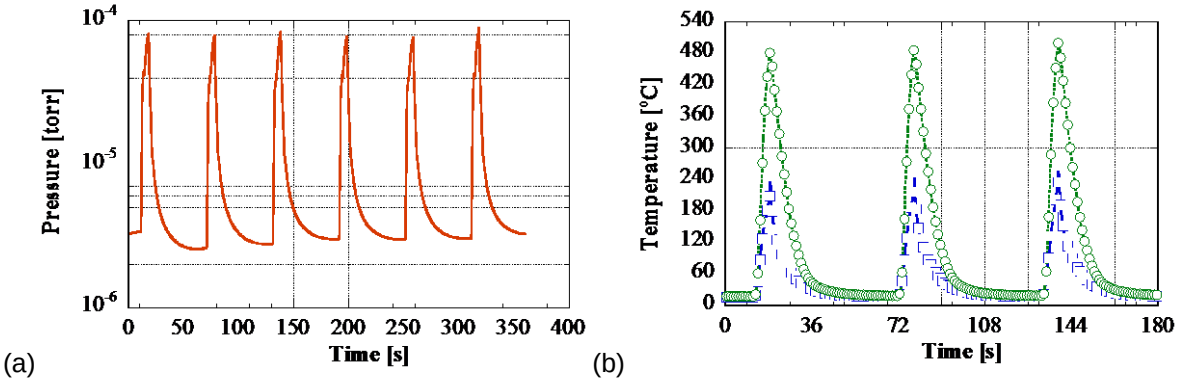

Figure 5. Representative data for specimen 2: (a) absolute pressure for cycles 114-119 and (b) measured temperature $T_{BS,\ Cu}$ for cycles 114, 115, and 116 with un-shielded thermocouples (each cycle: 278 W/cm^2 for 7 s).

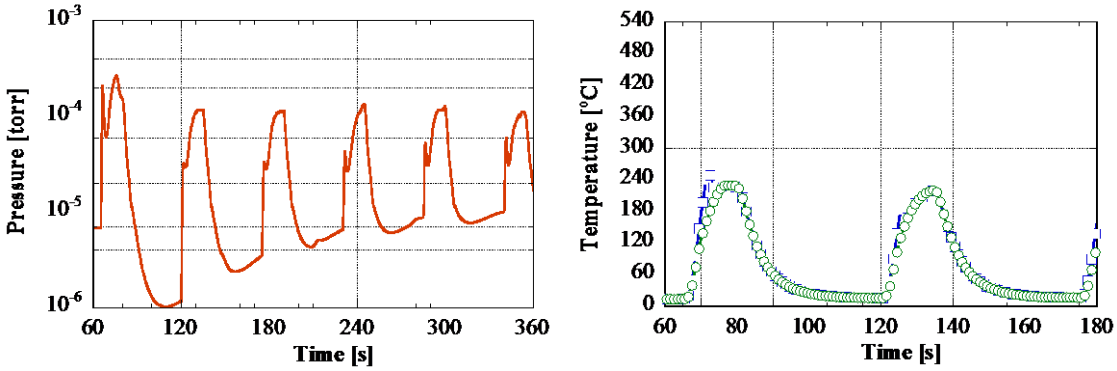

Figure 6. Representative data for specimen 5: (a) absolute pressure for cycles 37-42 and (b) measured temperature $T_{BS,\ Cu}$ for cycles 37 and 38 with shielded thermocouples (each cycle: 323 W/cm^2 for 15 s).

Table 2. Height of the center of the sample [μm] with respect to the edge of the specimen in two orthogonal directions.

Sample	X	Y
1	31.1	53.2
2	41.3	49.2
3	33.1	45.1
4	8.2	19.9
5	3.5	26.3

Acknowledgments

The authors would like to thank Evan Ohriner for material selection based on strength, oxidation, and fabrication considerations, Charles Ross (Chuck) Schaich for assisting with CAD design, fabrication specifications, and assembly; Jim Kiggans for design and fabrication of the Al enclosure, David Harper for operating the PAL, and John Henry Jr. for conducting profilometry measurements. We would also like to acknowledge the following Japanese collaborators from the joint US-Japan PHENIX program, Y. Ueda of Osaka University, Japan for numerous discussions related to clamping and T. Yokomine of Kyoto University, Japan for presentations made as part of the PHENIX program, discussing high-heat flux testing of He cooled tungsten.

6.1 LIQUID METAL COMPATIBILITY - S. J. Pawel (Oak Ridge National Laboratory, USA)

OBJECTIVE

The objective of this task is to identify potential structural materials having sufficient compatibility with flowing Pb-Li eutectic that the maximum metal temperature for operation can be increased to improve overall system efficiency.

SUMMARY

Operation of the first thermal convection loop (TCL) using dispersion strengthened FeCrAl (Kanthal APMT) tubing and specimens was completed in the previous reporting period. The working fluid in the TCL was eutectic Pb-17at%Li, and both the peak temperature (550˚C) and temperature gradient (116˚C) were maintained without interruption for 1000 h. When TCL operation was terminated, a problem with complete draining of the Pb-Li from the loop was encountered, which delayed retrieval of specimens and related examinations; however, post-exposure analysis of all specimens is now nearing completion.

PROGRESS AND STATUS

Introduction

Currently, the maximum allowable wall temperature for the dual coolant lead-lithium (DCLL) blanket concept is set at 475˚C based primarily on corrosion limitations of the structural containment materials. To increase overall system efficiency, potential structural materials are being sought with a combination of high strength and creep resistance with simultaneous resistance to dissolution in eutectic Pb-Li at temperatures > 500˚C. Preliminary research using static capsule exposures has indicated that dispersion strengthened FeCrAl (Kanthal APMT) may be resistant to dissolution in eutectic Pb-Li at temperatures in the range of 600-800˚C, at least in part due to the stability of an Al-rich oxide film. However, corrosion data in a flowing system must be generated to analyze the potential for issues associated with thermal gradient mass transfer – that is, relatively high dissolution in hotter portions of the flow system with concomitant deposition in the colder portions – which has been known to disrupt heat transfer and even plug flow paths completely in some temperature gradient/material combinations.

Thus, thermal convection flow loops (TCLs) are being incorporated as the follow-on step to capsule testing for evaluation of liquid metal compatibility. The initial testing associated with this effort utilized a mono-metallic TCL fabricated of Kanthal APMT tubing (26.7 mm OD, 3.1 mm wall) with a “chain” of APMT specimens (miniature tensile specimens termed “SS3s”) inserted within each of the hot leg and cold leg of the TCL for use in post-exposure evaluation. Examination and analysis of specimens exposed within the loop was advanced substantially in the reporting period.

Results

Figure 1 reports the weight change of the APMT specimens – after cleaning in a solution of 1:1:1 mixture of ethanol, hydrogen peroxide, and acetic acid – removed from the loop as a function of exposure temperature. The cleaning solution readily dissolves residual Pb-Li rendering weight change measurements more meaningful. Following exposure to the cleaning solution, the specimens were further cleaned ultrasonically in acetone followed by air drying. The approximate temperature of each specimen location was estimated by linear extrapolation as a function of position between thermowell locations at which the temperature was known.

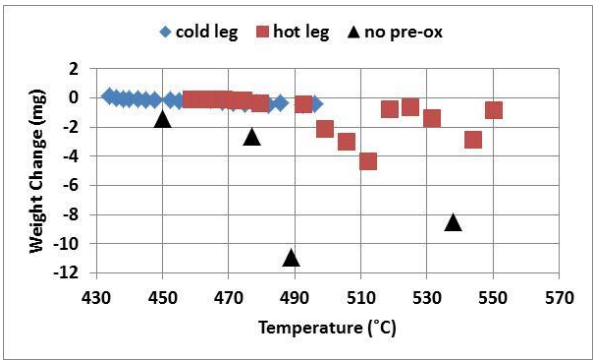

Figure 1. Weight change of specimens as a function of exposure temperature in the Pb-Li thermal convection loop. Black triangular data points correspond to specimens that were not given the pre-oxidation heat treatment.

The weight changes for most specimens are based on the original weight of the pre-oxidized specimen – that is, treated 8 h at 1050˚C in air to form a chromium oxide film rich in alumina prior to exposure – but data for a few specimens that did not receive the pre-oxidation treatment are included in Fig. 1. The data indicate the oxide film is at least partially protective of the substrate in Pb-Li because all four of the specimens exposed in the TCL without the oxide film – independent of exposure temperature – exhibit significantly greater weight loss than adjacent specimens that were pre-oxidized. However, with the exception of the specimen exposed at the lowest temperature within the loop (bottom of the cold leg), all specimens exposed within the TCL experienced at least some amount of weight loss suggesting that the oxide film is only partially stable in the Pb-Li environment, perhaps being converted to a lithium aluminate constituent and/or becoming somewhat soluble with extended time at temperature. Such a reaction seems more aggressive at higher temperature – specimen weight loss is at least sporadically greater at exposure temperatures above 500˚C in the hot leg – but visual assessments and metallographic cross sections of specimens reveal at least small regions that retain some of the original oxide film even at the highest exposure temperature. Using specimen density (~ 7.2 g/cm^3), specimen area (2.0 cm^2), and total exposure time (1000 h) to convert weight change to average uniform dissolution rate, note that even the highest weight loss among the pre-filmed specimens, approximately 4.4 mg, corresponds to only about 25 µm/y (1.0 mil/y) of annual wastage. While this is not a fixed rate, likely accelerating somewhat as more and more of the oxide film is removed, it is threatening primarily from the perspective of potential deposition at cold spots (plugging flow or disrupting heat transfer) as opposed to gross structural thinning considerations. Metallographic cross-sections revealed only very modest surface roughening in locations where the oxide film was removed, and element mapping revealed no chemical gradients in the base metal at exposed (no oxide film) locations, suggesting general dissolution as opposed to selective leaching in Pb-Li. Further, the element maps indicated no surface deposits on any specimens, suggesting all dissolution products are relatively soluble for the total extent of mass loss in this experiment.

Figure 2 presents the yield strength as a function of TCL exposure temperature for each APMT specimen. For comparison, data are also included for APMT specimens that did not receive the pre-oxidation heat treatment (8 h in air at 1050˚C) but were placed at a few positions around the loop for comparison exposure. While there appears to be some distinction between hot leg and cold leg specimens, it is clear that the yield strength of APMT increased substantially as a result of exposure at the relatively lower temperatures around the TCL. Note that the specimens with the largest weight loss – those not receiving the pre-oxidation treatment – did not deviate from the pattern of yield strength established by the pre-oxidized specimens. The most dramatic increase in yield strength results for specimens exposed below about 475-500˚C, although the temperature at which the strength increase occurs appears to modestly depend on whether specimens were exposed within the cold leg or hot leg (in which there is larger potential for dissolution rather than deposition). Interestingly, the yield strength of as-received APMT specimens (mill-annealed), pre-oxidized specimens, and pre-oxidized specimens heat treated for 1000 h

at 550˚C in argon was consistently 647 ± 10 MPa for all conditions. These observations suggest that precipitation reactions within the APMT structure, rather than interaction with the Pb-Li eutectic, are responsible for the change in yield strength. It seems likely that a precipitation reaction similar to that termed "475˚C embrittlement" is responsible for the observed increase in yield strength. In this reaction, an embrittling phase rich in chromium – often termed α-prime in many susceptible stainless alloys – forms on grain boundaries and within the bulk alloy to cause a significant increase in strength and concomitant loss of ductility. Advanced techniques, such as transmission electron microscopy and/or focused ion-bean studies, are necessary to confirm the occurrence of 475˚C embrittlement, and such work will be initiated soon. It is important to note that the data for the ultimate tensile strength (UTS) of the APMT specimens followed the same pattern as that for the yield strength, with nominal UTS values near 862 MPa increasing to about 1207 MPa as the exposure temperature was decreased.

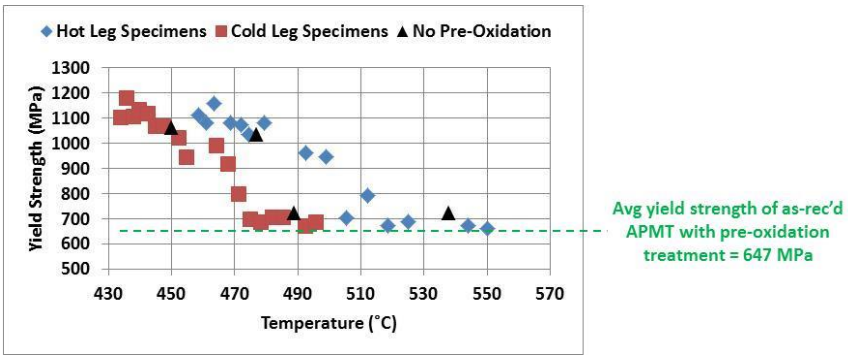

Figure 2. Room temperature yield strength of APMT specimens exposed to flowing Pb-Li eutectic for 1000 h at the indicated temperature. Black triangles represent data for specimens that did not receive the pre-oxidation heat treatment.

More scatter was observed in the relative ductility data, which is represented by total plastic elongation plotted in Fig. 3. Note that the lowest ductility values occurred at temperatures consistent with the concomitant increase in strength, but it is also apparent that very large variations in ductility were observed for adjacent specimens within the TCL (at an exposure temperature difference of only ~ 2˚C). Again, the elongation of as-received APMT specimens (mill annealed), pre-oxidized specimens, and pre-oxidized specimens heat treated for 1000 h at 550˚C in argon was consistently 23 ± 2% for all conditions. It is not clear that 23% elongation for sheet material can be expected for all forms and heats of material, because the as-received tubing used to fabricate the TCL was relatively brittle when strained at room temperature (order of 2% elongation or less, but not analytically assessed in specimens of the same size/shape as those exposed within the TCL).

Consistent with the above observations of wide variations in ductility even for similar exposure temperature, Fig. 4 shows representative views of the fracture surface of post exposure tensile specimens from the TCL hot leg. In this case, the specimen exposed at lower temperature exhibited increased yield strength and a largely planar fracture surface, indicating a predominantly cleavage-style fracture with some amount of cracking evident. In contrast, the specimen exposed at a temperature almost 50˚C higher generated a nominal yield strength and a very ductile fracture surface indicative of micro-void coalescence.

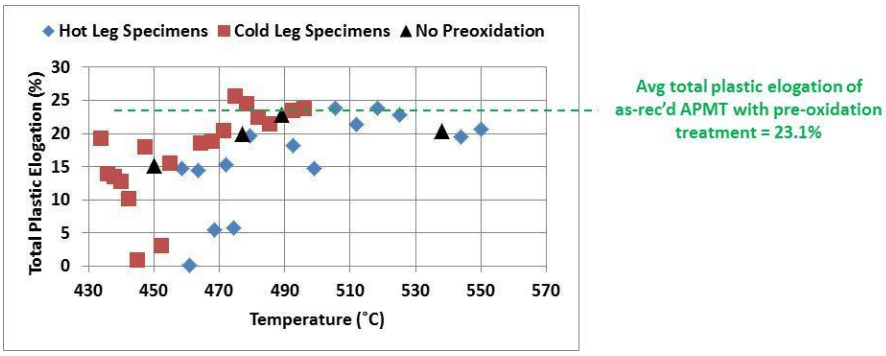

Figure 3. Room temperature ductility data (represented by total plastic elongation) of APMT specimens exposed to flowing Pb-Li eutectic for 1000 h at the indicated temperature. Black triangles represent data for specimens that did not receive the pre-oxidation heat treatment.

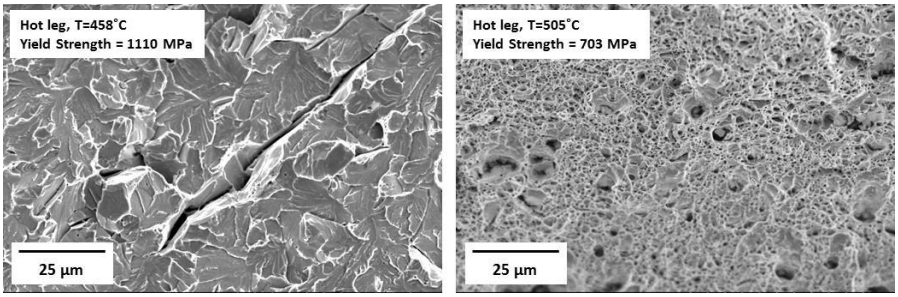

Figure 4. Post-exposure fracture surface of APMT miniature tensile specimens. The specimen exposed at relatively lower temperature (at left) reveals a high yield strength and a brittle fracture while the specimen exposed at relatively higher temperature (at right) reveals a lower strength and is much more ductile.

Future plans include continued analysis of specimens removed from the TCL (primarily, to confirm the strengthening mechanism observed at relatively low exposure temperatures) and initiation of the fabrication process for two additional APMT thermal convection loops with attendant specimens and components.

7.1 THE ORIGIN OF STRAIN AVALANCHES IN SUBMICRON PLASTICITY IN fcc METALS - T. Crosby, G. Po, C. Erel, N.M. Ghoniem (University of California, Los Angeles)

EXTENDED ABSTRACT *- paper accepted with revisions in Acta Materialia (2014).*

In small-scale plasticity, single crystals experience a stress-strain relation that has at least three distinct characteristics: the flow stress is higher than in bulk materials, its magnitude is stochastic, and the post-yielding behavior is jagged rather than uniform. The flow stress is stochastic because at these length scales the individual behavior of dislocation lines (rather than the collective behavior in case of bulk crystals) leads to dramatic differences in the stress-strain relation, making the flow stress very sensitive to the initial distribution and initial density of dislocations in the material. This apparent stochasticity is not just present in the initial flow strength, but have also been reported in the later stages past the yield point (1, 2). The exact mechanisms behind size effect and the observed jerky stress past the yield point have been the subject of some controversy. In general, one may divide the factors influencing strength and hardening in nano- and micro-pillars into two main groups: extrinsic and intrinsic effects. In this work, we propose a different explanation for the observed jerky flow in stress-strain curves that is based on the dynamics of dislocation dipolar-loops, which act as debris inside the material.

Multiple three-dimensional discrete dislocation dynamics (3D-DDD) simulations, with different initial dislocation densities and distributions, were performed. In each, compression of a Nickel nano-pillar, Fig. 1, with a diameter of 250 nm and 3:1 aspect ratio, oriented with the loading axis is in the [111] direction, was carried out by applying a displacement on the top surface while fixing the bottom. Typical results at the end of simulations are shown in Fig. 2. The stress-strain curves showed both a stochastic flow stress and a jerky stress past the initial yielding point. Fig. 3 shows snap shots of the pillar microstructure.

The jerky behavior of the stress is intrinsic and a property of small-scale systems, and not the result of some external fluctuations or randomness. We suggest, based on the simulation results, that this is attributed to the nonlinear dynamics of formation and destruction of dislocation debris, which are dipolar-loops formed by cross-slip. The debris-mechanism for intermittent plasticity appears to be fundamental to the understanding of plastic flow in confined, submicron plasticity. An analysis for the evolution of dislocation densities that correspond to different dislocation families, confirms the role dipolar-loops play in dictating the onset of strain avalanches. The analysis suggests that the continuous shift in the peaks and valleys of the glissile and dipolar-loops densities correspond to the continuous space-time shifts of sources inside the material.

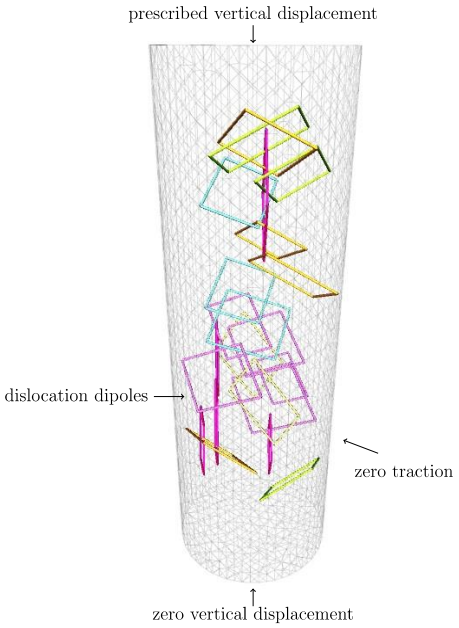

Figure 1. Nano-pillar considered in our DD simulations.

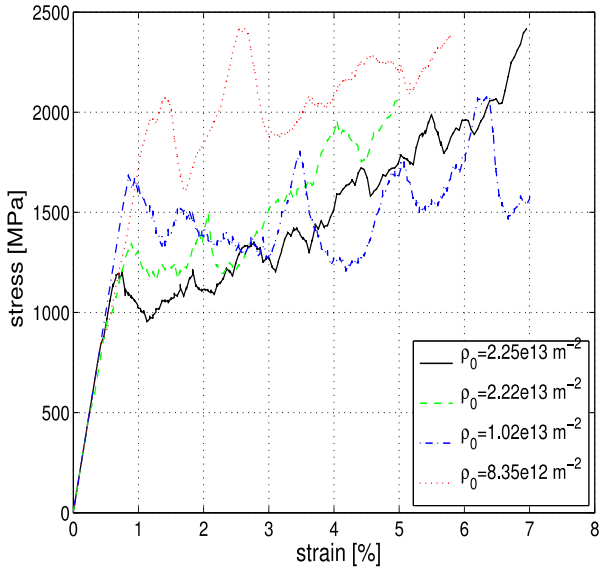

Figure 2. Stress-Strain curves for a D=250nm pillar under compression.

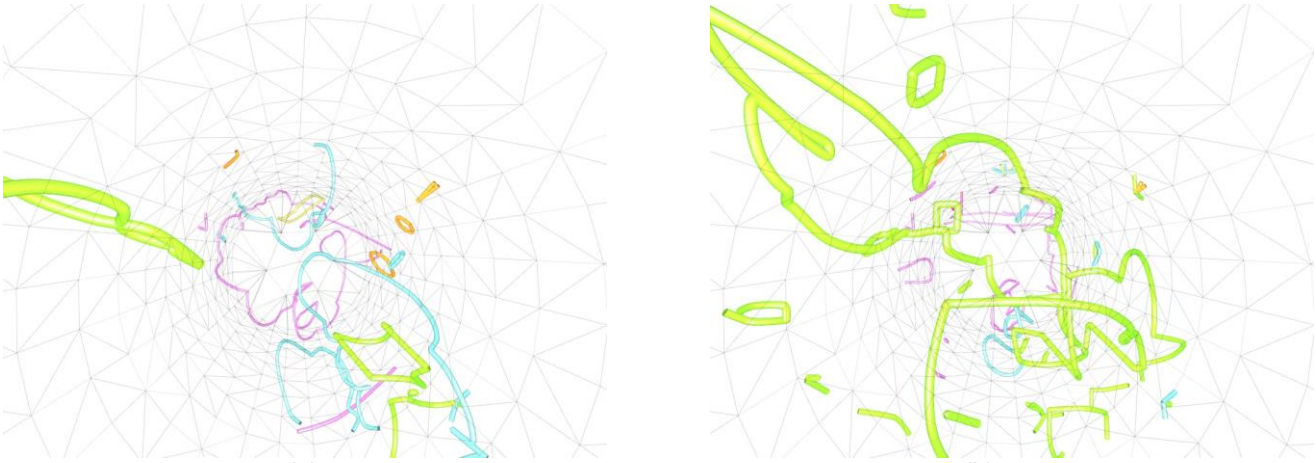

(a) (b)

Figure 3. Snap shots (top-view of the pillar) showing the evolution of dislocation microstructure inside the pillar. (a) Nearly starved (ε=0.08%), (b) Full (ε=1.95%).

References

[1] S. -W. Lee, S. M. Han, W. D. Nix, Uniaxial compression of fcc Au nanopillars on an MgO substrate: The effects of prestraining and annealing, Acta Materialia 57 (15) (2009) 4404–4415.
[2] A. T. Jennings, J. Li, J. R. Greer, Emergence of strain-rate sensitivity in Cu nanopillars: Transition from dislocation multiplication to dislocation nucleation, Acta Materialia 59 (14) (2011) 5627–5637.

7.2 NUDGED ELASTIC BAND SIMULATIONS OF KINK PAIRS IN TUNGSTEN -- David Cereceda and Jaime Marian (Lawrence Livermore National Laboratory and University of California at Los Angeles)

OBJECTIVE

The objective of this work is to calculate properties of tungsten at the atomistic level that are key to predicting the yield stress and flow stress of the material.

SUMMARY

Atomistic techniques have been used to calculate energy barriers for dislocation motion that control the strength (yield stress and flow stress) of the material. In particular, the calculations focus on the change in enthalpy as a straight dislocation moves through the crystal lattice (the Peierls barrier) and kink pair formation enthalpy that controls the thermally activated double-kink mechanism important at low to moderate stresses. A novel means of assessing kink widths within atomistic simulations is introduced.

PROGRESS AND STATUS

Introduction

The movement of dislocations can be considered as a set of successive processes that define a pathway through the potential energy landscape. Each of these processes happens between two configurations of atoms that are local minima corresponding to straight dislocations in equilibrium, providing information about the activation energy of the process and what intermediate equilibrium configurations may exist along the transition.

The nucleation and propagation of kink pairs between these local minima appears to be one of the underlying mechanisms that explain some of the characteristics of the motion of dislocations.

Below, we describe the general ideas on how these processes are studied by the 'nudged elastic band' (NEB) method discussed in more detail by Henkelman et al. [1] and by Tadmor and Miller in section 6.3.1 of the book *Modeling Materials* [2].

In the NEB method, a replica of a system with N atoms is defined by a N × 3 matrix that contains the positions of all the atoms in the system, $\mathbf{P} = (\mathbf{r}^1, \mathbf{r}^2, ..., \mathbf{r}^N)$. Given a total number of *R* replicas to study the movement of a dislocation between two consecutive Peierls valleys, the first and last replicas, P^1 and P^R, are at local energy minima in the energy landscape. All the other intermediate replicas can be characterized in different ways, but they are not in equilibrium, exhibiting a force on the atoms of each replica *i* that comes from the non-zero gradient of the potential energy

$$\mathbf{F}^i_{pot} = -\nabla_P V(\mathbf{P}^i) = \{-\nabla_{r^1} V|_{P^i}, ..., -\nabla_{r^N} V|_{P^i}\} \qquad (1)$$

The minimization of these forces would displace each intermediate replica to one of the local minima. In the NEB method, replicas 1 and R are fixed, and each intermediate replica is connected to the previous and next replica by a spring of constant k. These springs introduce a new force $\mathrm{F}^i_{\mathrm{spring}}$ that depends on the value of the spring constant. If k is small, the spring forces will not affect the minimization and the replicas will fall to one of the local minima. If k is big, the replicas are more rigid, and the spring forces will define a higher-energy path.

Considering the combined action of these two types of forces, the 3N-dimensional force on replica *i*, F^i, is defined as

$$\mathbf{F}^i = \mathbf{F}^i_{pot}|_\perp + \mathbf{F}^i_{spring}|_\parallel, \qquad (2)$$

where

$$\mathbf{F}^i_{pot}|_\perp = \mathbf{F}^i_{pot} - (\mathbf{F}^i_{pot} \cdot \mathbf{t}^i)\mathbf{t}^i, \qquad \mathbf{F}^i_{spring}|_\parallel = k(\|\mathbf{P}^{i+1} - \mathbf{P}^i\| - \|\mathbf{P}^i - \mathbf{P}^{i-1}\|)\mathbf{t}^i,$$

t^i is the 3N-dimensional tangent to the path at replica *i*, $\mathbf{F}^i_{pot}|_\perp$ is the component of the forces derived from the potential energy that is perpendicular to the path and $\mathbf{F}^i_{spring}|_\parallel$ is the component of the spring forces acting parallel to the path. In this distribution of forces, $\mathbf{F}^i_{pot}|_\perp$ will attempt to move each replica vertically to the minima and $\mathbf{F}^i_{spring}|_\parallel$ will attempt to move it along the reaction coordinate. The minimum energy path (MEP) between Peierls valleys can now be obtained by running an algorithm that moves the atomistic configurations of all the replicas until the global force defined in Eq.2 is reduced to zero.

Computational details

The principal axes x, y, and z, of the simulation box were oriented along the $\frac{1}{2}[111]$, $[\bar{1}2\bar{1}]$, and $[\bar{1}01]$ directions, corresponding to the line, glide and normal directions, respectively, of the screw dislocation. The dimensions of the simulation box were chosen to maximize the physical fidelity of the results while keeping the computational cost manageable. According to these criteria the dimensions are: L_x = 27.2 nm (100 b), L_y =10.8 nm, and L_z = 10.7 nm, with a total number of 208300 atoms.

Two screw dislocations with Burgers vector **b** = $\frac{1}{2}[111]$ are generated by using the isotropic elastic displacement solution [3] in two independent simulation boxes (one dislocation per box) with the orientation and dimensions described before. The first dislocation d_1 is generated at the center of the box. The second dislocation d_2 is generated at a distance[1] of $\frac{\sqrt{6}}{3}a_0$ from the center of the simulation box along the glide direction $[\bar{1}2\bar{1}]$, which corresponds to the distance between two consecutive Peierls valleys in that direction.

Prior to the NEB simulations, dislocations d_1 and d_2 are relaxed using the conjugate gradient algorithm implemented in LAMMPS [4]. Periodic boundary conditions are applied in the x direction while non-periodic and shrink-wrapped boundary conditions are applied in the y and z directions.

A stress range from zero to the Peierls stress of the potential is studied by applying shear stress σ_{xz}. To reproduce the effect of this applied stress, a external force f_x is added to the atoms in the top and bottom surfaces along the normal direction $[\bar{1}01]$.

[1] a_0 is the lattice parameter of the interatomic potential used in the simulations.

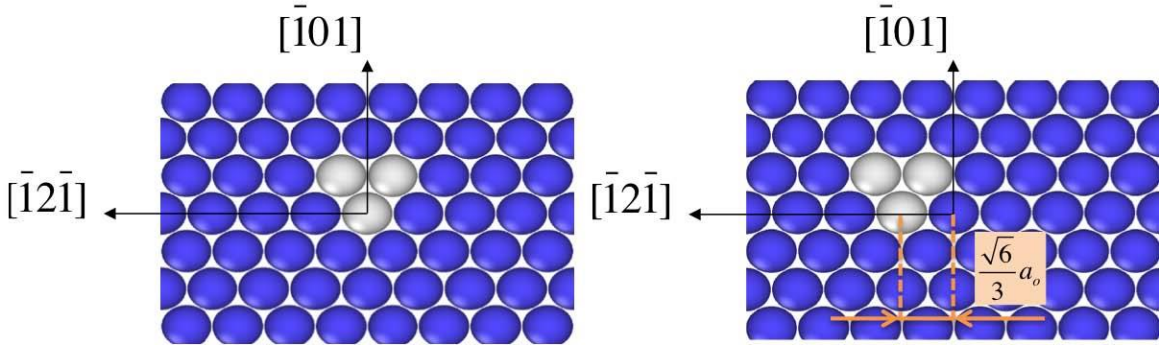

(a) dislocation d_1 (b) dislocation d_2

Figure 1. Position of the first d1 and second d2 dislocation with (1 0 1) plane.

The external force per atom satisfies $f_x = \frac{\sigma L_x L_y}{N_s}$, where σ is the desired stress and N_s is the number of atoms in each surface.

The MEP is obtained using the NEB method described before [1, 4, 5, 6, 7]. In this work we present two different types of NEB simulations depending on the intermediate configurations: straight dislocations or kink-pairs. Both of them use a total of 31 replicas, a spring constant of 1 eV $Å^{-1}$ and set relaxed dislocations d_1 and d_2 as the initial (1) and final (R) configurations respectively.

In this work we have used two different interatomic potential parameterized for tungsten: an embedded-atom method (EAM) potential [8] and a modified embedded-atom method (MEAM) potential [9]. Both of them predict the correct symmetric core structure at 0 K. They predict a Peierls stress of 2.03 and 3.2 GPa, respectively.

Results

Enthalpy and Energy Barriers

Straight dislocations

For the study of a straight dislocation moving between two consecutive Peierls valleys along the glide direction, the initial coordinates of all the atoms in the intermediate replica i, P^i_0, are set to values linearly interpolated between the corresponding atoms in replicas 1 and R.

$$\mathbf{P}_0^i = \mathbf{P}^1 + \frac{i-1}{R-1}\left(\mathbf{P}^R - \mathbf{P}^1\right), \qquad (3)$$

where i=2 . . . R-1.Therefore, the initial path of the NEB simulation contains a single dislocation for every replica.

The dimension along the dislocation line is reduced to L_x = 1.36 nm (5 b). In contrast with the study of kink-pairs where a value of L_x = 27.2 nm (100 b) is required for the nucleation of the kinks, this reduced size of the box is big enough for the straight dislocation to reproduce the physical fidelity of the results while decreasing the computational cost of the simulations.

For a given replica *i*, its enthalpy, H_i, includes the contribution of the internal energy and the mechanical work generated by the applied stress

$$H_i = U_i - \sigma \cdot b \cdot L_x \cdot \theta_r, \qquad (4)$$

where U_i is the internal energy of the replica, σ is the applied stress and θ_r is the reaction coordinate along the MEP. The enthalpy barrier per unit length is represented in Fig.2 as the difference between the enthalpy of each replica and the enthalpy of the initial configuration of the NEB simulation. One can notice that the increase in the applied stress increases the negative slope of the enthalpy barrier and decreases the maximum value achieved.

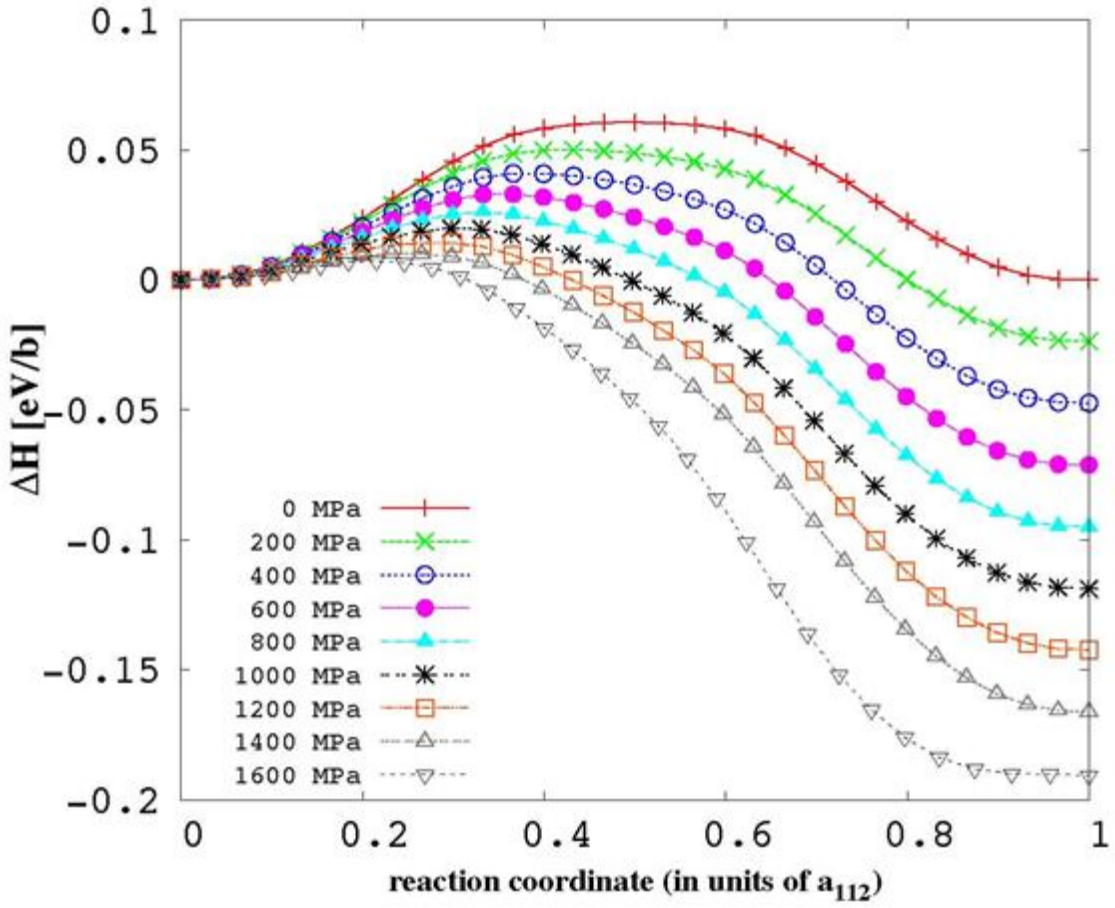

Figure 2. Enthalpy barrier per Burgers vector for a straight screw dislocation with normal plane $[\bar{1}01]$, computed with the NEB method using the EAM potential under the full range of applied stress.

According to Eq.4, the energy barrier is obtained by adding the mechanical work to the enthalpy. Similar to the enthalpy barrier, the energy barrier per unit length is represented in Fig.3.a as the difference between the energy of each replica and the energy of the initial configuration of the NEB simulation. In Fig.3.b, energies and reaction coordinates were shifted to overlap the potential minima for the different applied stresses [10].

In addition to the study of the $\frac{1}{2}<111>\{110\}$ screw dislocation, the Peierls potential for the $\frac{1}{2}<111>\{112\}$ screw dislocation was also studied. In this case the directions $\frac{1}{2}[111]$, $[\bar{1}01]$, and $[\bar{1}2\bar{1}]$ correspond to the line, glide and normal directions of the simulation box, respectively. The second dislocation d_2 is generated at a distance of $\sqrt{2}a_0$ from the center of the simulation box along the new glide direction $[\bar{1}01]$. For this orientation of the system Fig4.b shows a MEP with two barriers to move the straight dislocation between two consecutive Peierls valleys along the (1 2 1) plane. These results, in addition to the results of Fig.5.a, where the energy barriers along the $(10\bar{1})$ and $(\bar{1}2\bar{1})$ planes are plotted together at 0 MPa, suggest that the MEP along the $(\bar{1}2\bar{1})$ plane can be explained as two partial MEP along the x plane. Therefore the study of the kink-pair enthalpy has been completed only for the $\frac{1}{2}<111>\{110\}$ system.

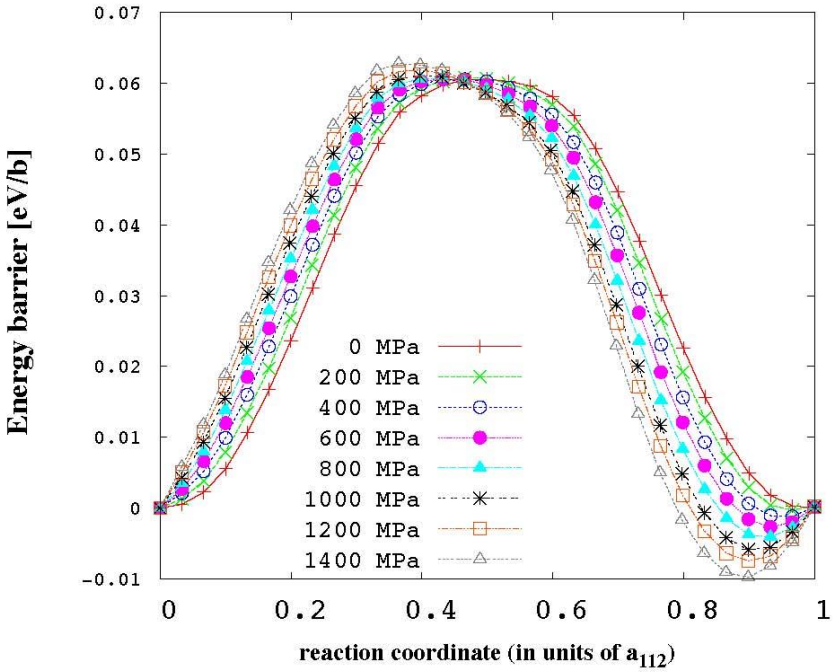

(a)

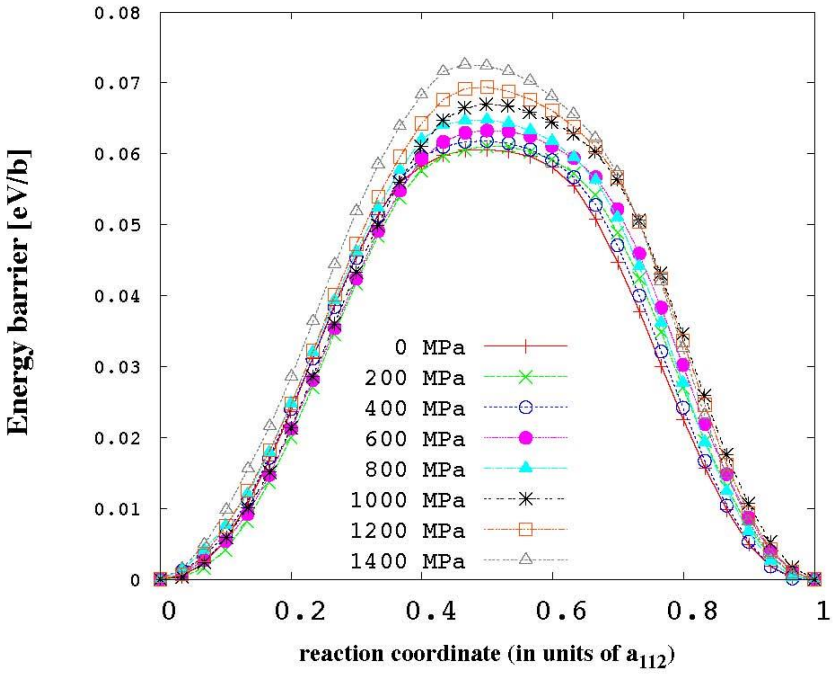

(b)

Figure 3. Energy barrier per Burgers vector for a straight screw dislocation with normal plane $(10\bar{1})$ and EAM potential.

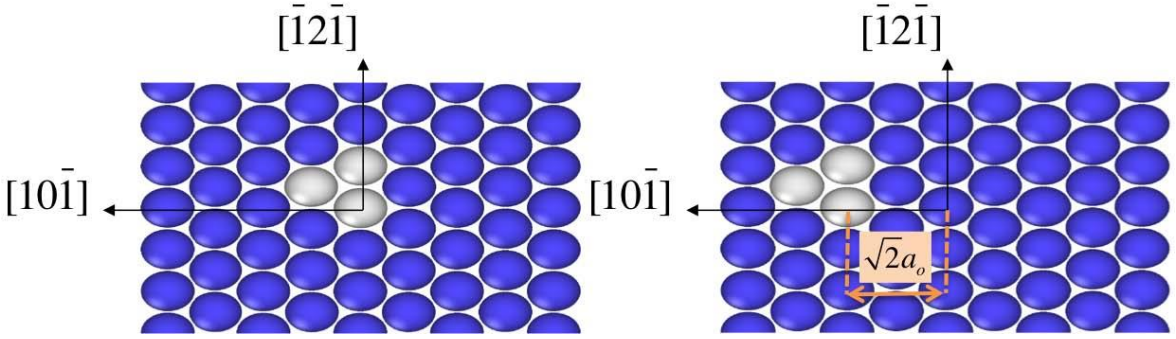

(a)

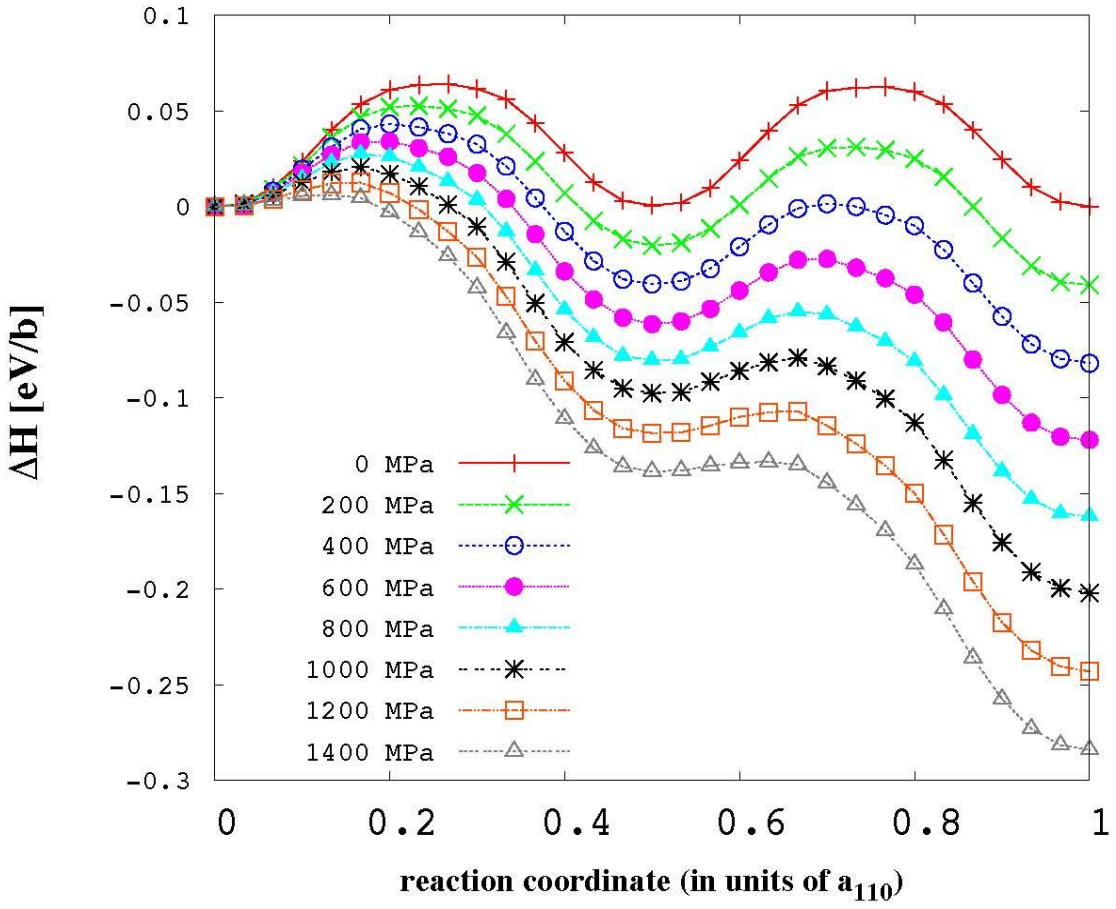

(b)

Figure 4. (a) Position of dislocations d_1 and d_2 when the screw is oriented with $(\bar{1}2\bar{1})$ as the normal plane. (b) Enthalpy barrier per Burgers vector for a straight screw dislocation with normal plane $(\bar{1}2\bar{1})$, computed with the NEB method using the EAM potential.

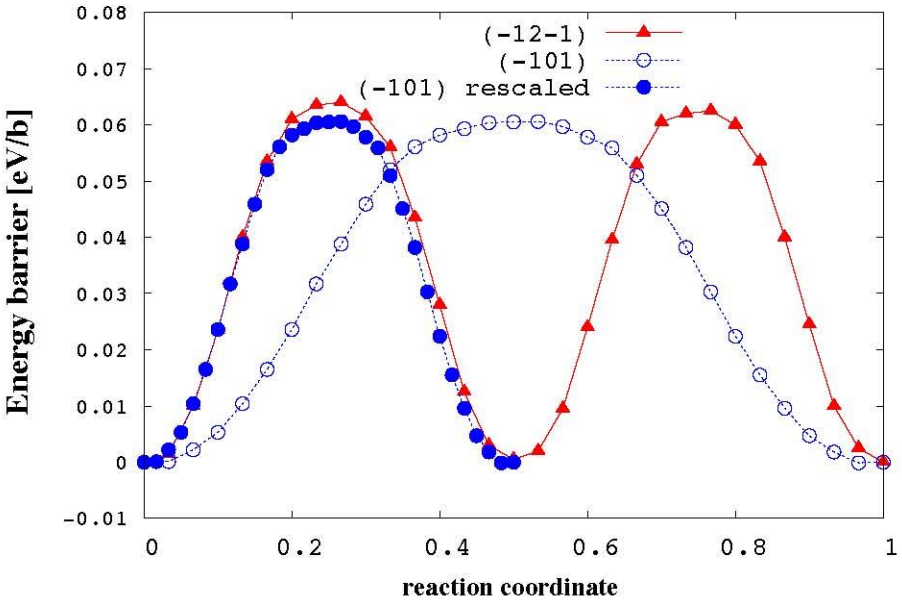

(a) EAM potential

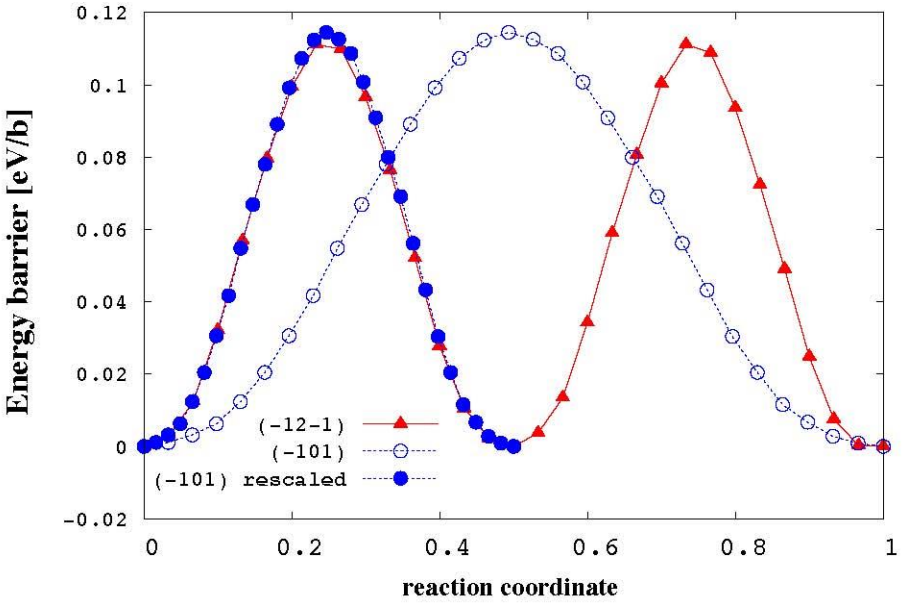

(b) MEAM potential

Figure 5. Energy barrier at 0 MPa for the $(10\bar{1})$ and $(\bar{1}2\bar{1})$ planes versus the reaction coordinate in units of the glide direction, $[\bar{1}2\bar{1}]$ and $[10\bar{1}]$ respectively.

The enthalpy and energy barriers have also been computed for more accurate and more expensive [11] MEAM potential. The results of Fig.6.b and the comparison between Fig.5.a and Fig.5.b reflect a more sinusoidal behavior of the MEAM potential, in agreement with the results of all the bcc transition metals [12].

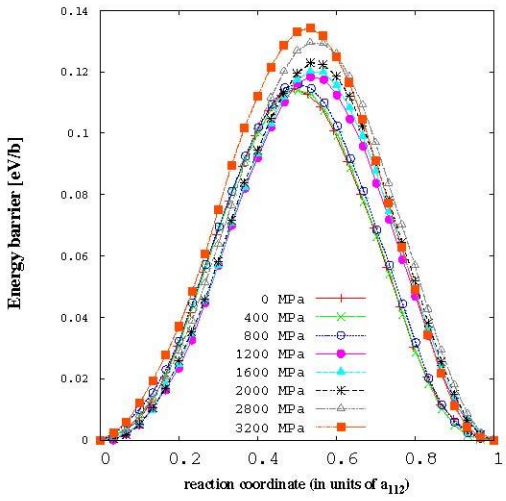

(c) Energy barrier (shifted)

Figure 6. Enthalpy and energy barriers versus the reaction coordinate in units of the glide direction, $[\bar{1}2\bar{1}]$, for the MEAM potential.

Kink-pairs

For the study of the enthalpy and energy barriers in kink-pairs, the initial configurations of the intermediate replicas 2, 3, …, R-1 contain a kink pair in the simulation box. The width of the kink pair *w* depends on the number of the replica *i* as follows

$$w_i = 0.5\left(1 + \frac{i-2}{R-2}\right) L_x, \qquad (5)$$

where *i*=2 . . . R-1. The initial coordinates of the atoms in the intermediate replicas correspond to the initial configuration except for a region of width w_i around the YZ central plane where atomic positions are taken from the final configuration [13].

In this case, the initial path of the NEB simulation contains a single dislocation for the initial and final replica, and a kink pair for the intermediate replicas 2 . . . R-1.

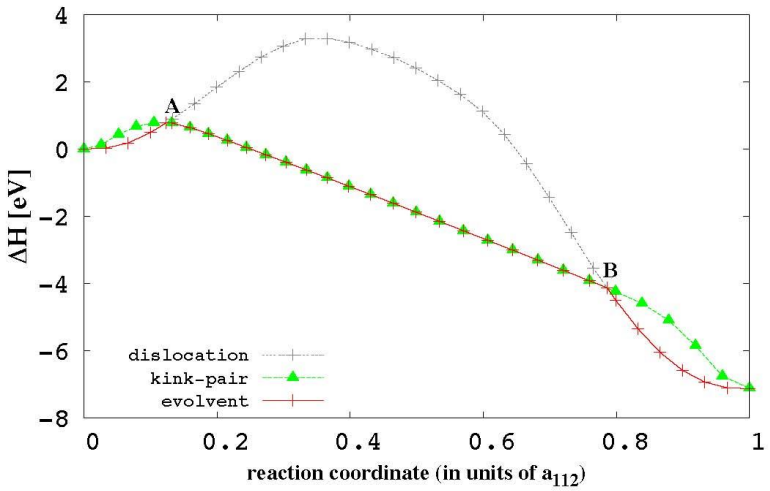

Figure 7. Enthalpy barrier when the initial configurations of the intermediate replicas are straight dislocations, kink-pairs, and the resultant envelope of minimum enthalpy of this two cases for the EAM potential at 600 MPa.

For each value of applied stress, the real pathway between two consecutive Peierls valleys is defined by the envelope of minimum enthalpy when overlapping the enthalpy barriers of the straight dislocation and the kink-pair.

$$H_{MEP}(i) = \begin{cases} H_{disloc}(i) & \text{if } H_{disloc}(i) \leq H_{kp}(i) \\ H_{kp}(i) & \text{if } H_{disloc}(i) < H_{kp}(i) \end{cases}, \qquad (6)$$

where $H_{MEP}(i)$ is the enthalpy of the replica *i* defined by the MEP, $H_{disloc}(i)$ is the enthalpy of the replica *i* at the end of the NEB simulation when the initial configurations of the intermediate replicas are straight dislocations and $H_{kp}(i)$ is the enthalpy of the replica *i* at the end of the NEB simulation when the initial configurations of the intermediate replicas are kink-pairs.

The point *A* in Fig.7 where the enthalpy barriers of the straight dislocation and the kink-pair intersect represents the state where the kink-pair is nucleated, and it defines, for a specific applied stress, the enthalpy and width of the kink-pair. The point *B* where the enthalpy barriers of the straight dislocation and the kink-pair also intersect, but in this case with a negative slope, represents the state where the kink-pair is totally expanded and becomes a straight dislocation situated in the next Peierls valley. All the replicas in the segment *AB* contain a kink-pair with an increased width.

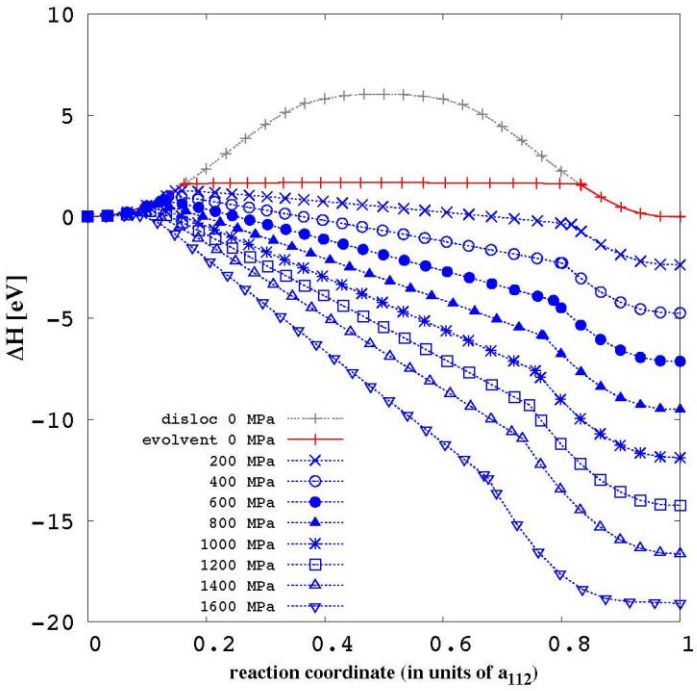

Figure 8. Enthalpy barrier of the straight dislocation at 0 MPa and the envelope of minimum enthalpy for the full range of applied stress 0 -1600 MPa and EAM potential.

Kink-Pair Enthalpy

The interest of obtaining the kink-pair enthalpy as a function of the stress comes from the important role that this variable plays when defining the nucleation rate of a kink-pair, j_{kp}. This nucleation rate can be defined as:

$$j_{kp} = \nu_0 exp\left\{-\frac{\Delta F_{kp}}{2kT}\right\} \qquad (7)$$

where ν_0 is an attempt frequency, k is Boltzmann's constant, T is the temperature and ΔF_{kp} is the (Gibbs) free energy difference resulting from the nucleation of an embryonic kink pair, i.e. one with the minimum lattice separation. The 1/2 factor arises from the fact that it is only necessary to take the dislocation to the activated state (saddle point) to achieve a transition. This is only appropriate for cases where the free energy landscape is symmetric about the midpoint of the reaction coordinate. Since figures 3.b and 6.c are mostly symmetric and bcc metals reflect a sinusoidal behavior [12], our case of study satisfies the conditions to use the 1/2 factor.

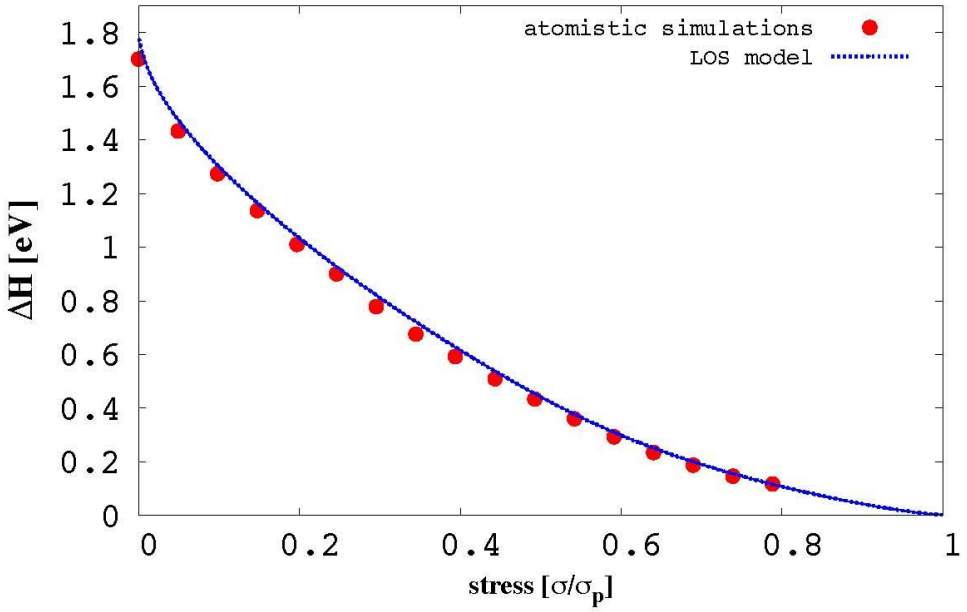

Figure 9. Kink-pair formation enthalpy comparing atomistic simulations using EAM potential and the LOS model fitted with the same potential.

The free energy can be defined as:

$$\Delta F_{kp} = \Delta H - T\Delta S$$

where ΔH is the enthalpy and ΔS the entropy. Assuming that the entropy can be taken as ΔS ~ 3k, the enthalpy is the missing variable to compute the nucleation rate of the kink-pair.

The atomistic data in Fig. 9 shows the dependence of the kink-pair enthalpy as a function of the applied stress. It results from obtaining, for each value of applied stress, the enthalpy of the point of intersection *A* in Fig. 7. As we expected, the value of the kink-pair enthalpy tends to zero when the applied stress is close to the Peierls stress.

To obtain the kink-pair enthalpy at 0 MPa the procedure developed by Ventelon et al. [14] was used, where 'the formation energy of a single kink is calculated as the difference between the energy of a kinked screw-dislocation and the energy normalized to the same number of atoms of a straight dislocation lying in a single Peierls valley'. The formation enthalpy (equivalent to the energy since there is no mechanical work at 0 MPa) of the kink-pair at 0 MPa is obtained as the sum of the formation enthalpies for the left and right kink. Fig.10 shows the convergence of the formation enthalpies with the number of atoms per plane perpendicular to the Burgers vector, obtaining a value of 1.701 eV for the EAM potential. Experimentally, Brunner [15] has obtained a value of 1.75 eV from the temperature dependence of flow stress measurements in W, in very good agreement with the calculated value.

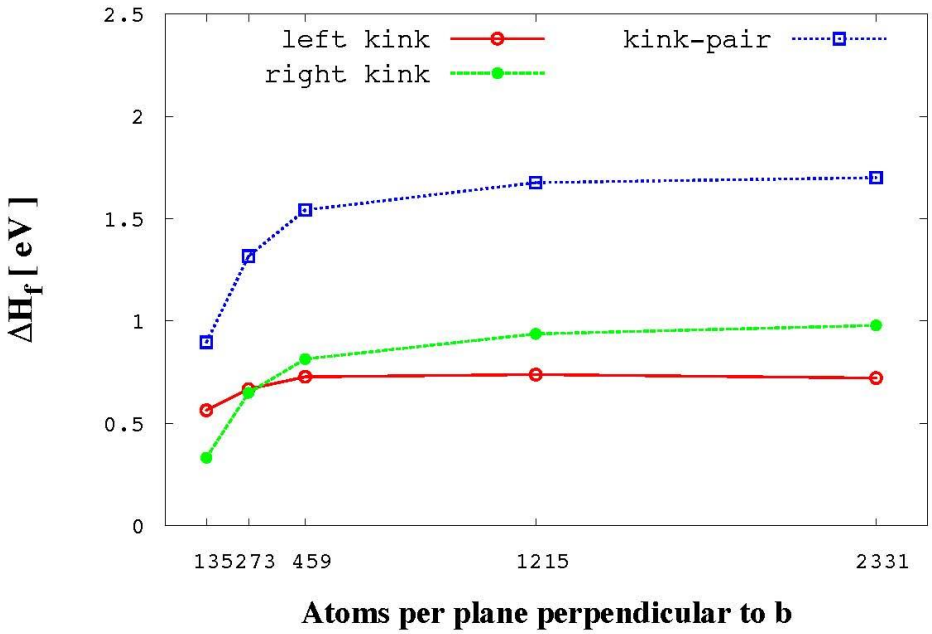

Figure 10. Kink formation enthalpies as a function of the number of atoms per Burgers vector.

Kink-Pair Width

As it was described in section 3.1, the study of the enthalpy barrier in kink-pairs requires that the initial path of the NEB simulation contains a single dislocation for the initial and final replica, while the intermediate replicas (2 . . . R-1) contain a kink pair of a specific width. The initial and final replicas maintain their dislocation shape after the NEB simulation. Some of the intermediate replicas achieve the minimum along the path in the form of a dislocation while some others keep the kink pair shape with a different width from the one that was imposed when defining the initial configurations of the intermediate replicas.

The envelope of minimum enthalpy represented in Fig. 7 gives an idea of when to expect the change of shape between dislocation and kink pair: intermediate replicas in regions 0-A and B-1 have a dislocation shape, whereas, intermediate replicas in region A-B have a kink pair shape. This can also be probed by visualizing the relaxed replicas via Ovito [16]. Figure 11 shows the results of this visualization, where the atoms defining the dislocation and the kink pair have been highlighted using the common neighbor analysis (CNA) technique [17, 18, 19].

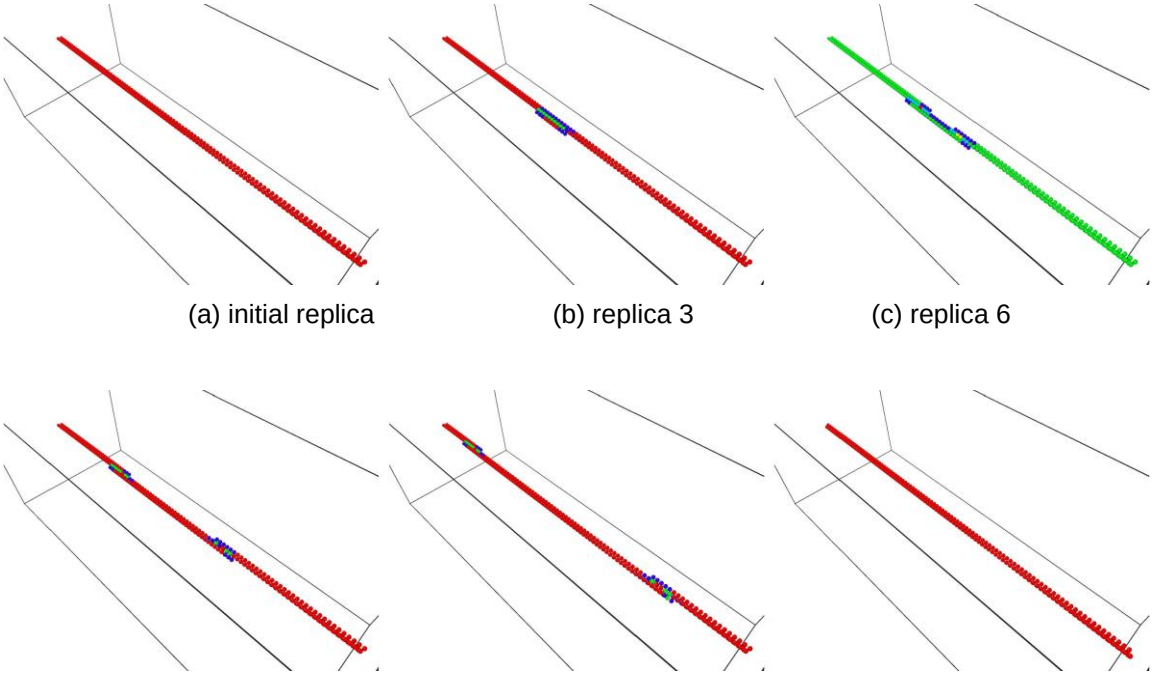

Figure 11. Atomistic visualization obtained via Ovito [16] of different replicas along the final pathway of the NEB simulation at 1200 MPa.

Atomistic visualizations of Fig. 11 using the CNA technique present kink pairs with a sharp shape and do not reproduce the details of their profile, required to determine the width. In order to obtain the details on the shape of the replicas, we suggest an analytical methodology that takes into account the coordinates of all the atoms in the simulation box and the displacement field associated with the dislocation.

The steps to obtain the shape of each replica with this analytical method suggested are:

- **i.** The simulation box is divided into slices along the dislocation line direction *x*. Each slice has a width of **b**/3 and contains the atoms of one single plane of the ABC stacking sequence of {111} planes in bcc metals.
- **ii.** For each slice, a grid of nodes that are candidates to host the centroid of the dislocation is created. The grid spacing would determine the efficiency of the method in terms of the precision of the results and the computational cost. The purpose is to identify between all the possible nodes in the grid, the node that is closer to the real position of the centroid of the dislocation.
- **iii.** Given a perfect bcc lattice oriented with *x*, *y* and *z* axes corresponding to the line, glide and normal directions respectively, inserting a screw dislocation in the box requires that every atom *i* is displaced according to the following field [3]:

$$u_x^i = \frac{b}{2\pi}\theta = \frac{b}{2\pi} tan^{-1}\left(\frac{R_z^i - c_z}{R_y^i - c_y}\right) \qquad (8)$$

$$u_y^i = y_z^i = 0$$

where R_x^i, R_y^i, R_z^i are the coordinates of an atom i in the perfect lattice and c_x, c_y, c_z are the coordinates of the centroid of the dislocation. Applying the previous displacement field to all the atoms in the box guaranties that the centroid of the dislocation is at $C(c_x, c_y, c_z)$.

If we want to obtain the centroid of a dislocation already inserted in a simulation box the previous process needs to be applied in reverse. Denoting r_x^i, r_y^i, r_z^i as the coordinates of an atom *i* in the distorted configuration with the screw dislocation, the centroid of the dislocation must satisfy the following condition for all the atoms *i* present in the slice:

$$r_x^i - R_x^i - \frac{b}{2\pi} tan^{-1}\left(\frac{R_z^i - c_z}{R_y^i - c_y}\right) = 0 \qquad (9)$$

We then use as a measure error to locate the centroid. The displacement error on atom *i* when the centroid of the dislocation corresponds to node *n* is defined as:

$$\epsilon_n^i = r_x^i - R_x^i - \frac{b}{2\pi} tan^{-1}\left(\frac{R_z^i - R_z^n}{R_y^i - R_y^n}\right), \qquad (10)$$

where R_x^n, R_y^n, R_z^n are the coordinates of the node *n*. Node *n* is considered the centroid of the dislocation for this slice if it minimizes, compared with all the other candidate nodes of the grid, the following sum:

$$\sum_{i=1}^{N_{at}} \epsilon_n^i \qquad (11)$$

where N_{at} is the number of atoms in this slice.

iv. We repeat step (iii) for all slices and obtain the kink pair shape shown in Fig. 12.

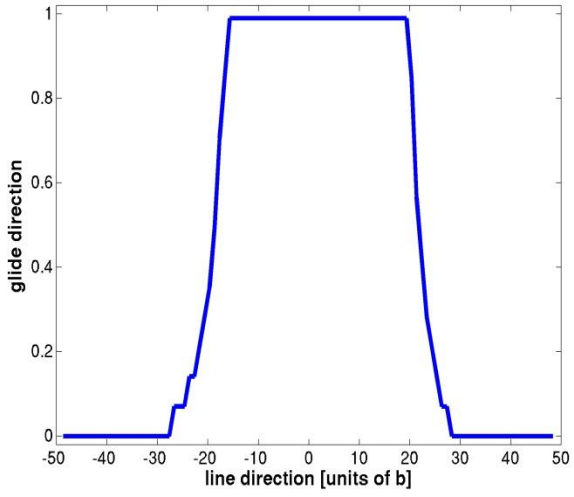

Figure 12. Shape of kink pair for replica number 14 of the reaction pathway at 1200 MPa.

It is important to consider that the positions of the centroid represented in Fig. 12 correspond only to the slices taken three by three, since the stacking sequence of {111} planes in bcc metals has three planes. The comparison between Fig. 11 and Fig. 12 reveals that the analytical method suggested provides the shape of the dislocation line with more detail than the atomistic visualizations.

Results from Fig. 13 shows that the initial and final replicas (1 and 31 respectively) maintain their dislocation shape, some of the intermediate replicas achieve the minimum along the path in the form of a dislocation (replicas number 4, 28) and some others keep the kink pair shape (replica numbers 5, 6, 7, 14, 21).

The enthalpy of the point of intersection *A* in Fig. 7 determines the kink pair enthalpy for each value of applied stress in Fig. 9. Therefore, ideally, the width of the kink pair should be computed at the same point *A*. However, replicas are spread along the reaction pathway in a linear way so it cannot be guaranteed that there is a replica that corresponds exactly with *A*. Consequently, the kink pair width is going to be computed from the first replica that exhibits a kink pair behavior with a fraction of the dislocation line totally positioned on the next valley.

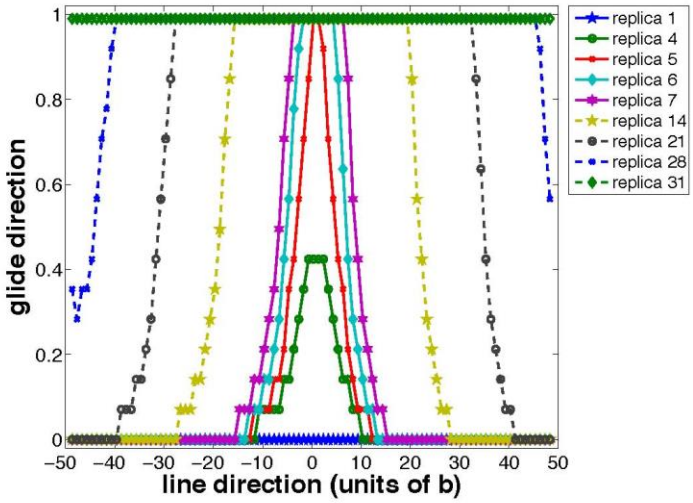

Figure 13. Shape of several replicas from the final pathway of the NEB simulation when applying 1200 MPa.

Once the replica with the first kink pair behavior is selected, the kink pair width is measured between the inflection points of the two legs of the kink pair. When repeating this process for all the values of applied stress, Fig. 14 is obtained.

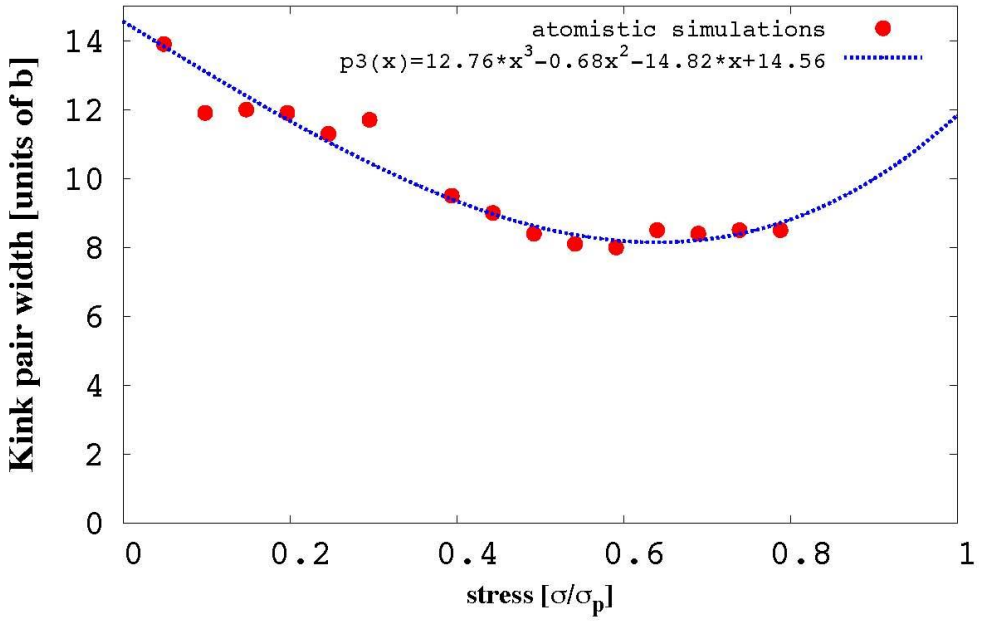

Figure 14. Kink pair width as a function of the applied stress.

Acknowledgments

This work was performed in part under the auspices of the U.S. Department of Energy by Lawrence Livermore National Laboratory under Contract DE-AC52-07NA27344. Document number LLNL-TR-666244.

References

[1] *Methods for Finding Saddle Points and Minimum Energy Paths*. G. Henkelman, G. Jöhannesson, and H. Jönsson. Kluwer Academic Publishers, 2000.
[2] Ellad B. Tadmor and Ronald E. Miller. *Modeling Materials, Atomistic and Multiscale Techniques*. Cambridge University Press, 2011.
[3] D. Hull and D. J. Bacon. *Introduction to Dislocations*. Butterworth-Heinemann, Oxford, 2001.
[4] S. Plimpton. *Fast Parallel Algorithms for Short-Range Molecular-Dynamics*. http://lammps.sandia.gov. Journal Of Computational Physics, 117(1):1-19, 1995.
[5] G. Henkelman, B.P. Uberuaga, and H. Jonsson. A climbing image nudged elastic band method for finding saddle points and minimum energy paths. *Journal of Chemical Physics*, 113(22):9901-9904, 2000.
[6] G. Henkelman and H. Jonsson. Improved tangent estimate in the nudged elastic band method for finding minimum energy paths and saddle points. *Journal of Chemical Physics*, 113(22):9978-9985, 2000.
[7] Aiichiro Nakano. A space-time-ensemble parallel nudged elastic band algorithm for molecular kinetics simulation. *Computer Physics Communications*, 178(4):280-289, 2008.
[8] Mihai-Cosmin Marinica et al. Interatomic potentials for modelling radiation defects and dislocations in tungsten. *Journal of Physics: Condensed Matter*, 25, 395502, 2013.
[9] Hyoungki Park, Michael R. Fellinger, Thomas J. Lenosky, William W. Tipton, Dallas R. Trinkle, Sven P. Rudin, Christopher Woodward, John W. Wilkins, and Richard G. Hennig. Ab initio based empirical potential used to study the mechanical properties of molybdenum. *Phys. Rev. B*, 85:214121, 2012.
[10] L. Proville, L. Ventelon, and D. Rodney. Prediction of the kink-pair formation enthalpy on screw dislocations in α-iron by a line tension model parametrized on empirical potentials and first-principles calculations. *Physical Review B*, 87(14):144106, 2013.

[11] D. Cereceda, A. Stukowski, M. R. Gilbert, S. Queyreau, Lisa Ventelon, M-C Marinica, J. M. Perlado, and J. Marian. Assessment of interatomic potentials for atomistic analysis of static and dynamic properties of screw dislocations in W. *Journal of Physics-Condensed Matter*, 25(8):085702, 2013.
[12] Christopher R. Weinberger, Garritt J. Tucker, and Stephen M. Foiles. Peierls potential of screw dislocations in bcc transition metals: Predictions from density functional theory. *Physical Review B*, 87(5):054114, 2013.
[13] David Rodney and Laurent Proville. Stress-dependent Peierls potential: Influence on kink-pair activation. *Physical Review B*, 79(9):194108, 2009.
[14] L. Ventelon, F. Willaime, and P. Leyronnas. Atomistic simulation of single kinks of screw dislocations in α-fe. *Journal of Nuclear Materials*, 386-388(C):26-29, 2009.
[15] D Brunner. Comparison of ow-stress measurements on high-purity tungsten single crystals with the kink-pair theory. *Materials Transactions JIM*, 41(1):152-160, 2000.
[16] Alexander Stukowski. Visualization and analysis of atomistic simulation data with OVITO-the Open Visualization Tool. *Modelling and Simulation in Materials Science And Engineering*, 18(1), JAN 2010.
[17] J. Dana. Honeycutt and Hans C. Andersen. Molecular dynamics study of melting and freezing of small Lennard-Jones clusters. *The Journal of Physical Chemistry*, 91(19):4950-4963, 1987.
[18] Daniel Faken and Hannes Jnsson. Systematic analysis of local atomic structure combined with 3d computer graphics. *Computational Materials Science*, 2(2):279-286, 1994.
[19] Helio Tsuzuki, Paulo S. Branicio, and Jos P. Rino. Structural characterization of deformed crystals by analysis of common atomic neighborhood. *Computer Physics Communications*, 177(6):518-523, 2007.

8.1 MOLECULAR DYNAMICS OF CASCADES OVERLAP IN TUNGSTEN WITH 20-keV PRIMARY KNOCK-ON ATOMS - W. Setyawan, G. Nandipati, K. J. Roche, R.J. Kurtz (Pacific Northwest National Laboratory[1]); B. D. Wirth (University of Tennessee)

OBJECTIVE

The objective of this research is to investigate how existing vacancies and interstitial atoms influence the defect production of the next cascade and vice versa.

SUMMARY

Molecular dynamics simulations are performed to investigate the mutual influence of two subsequent cascades in tungsten. The influence is studied using 20-keV primary knock-on atoms, to induce one cascade after another separated by 15 ps, in a lattice temperature of 1025 K (i.e. 0.25 of the melting temperature of the interatomic potential). The center of mass of the vacancies at the peak damage during the cascade is taken as the location of the cascade. The distance between this location to that of the next cascade is taken as the overlap parameter. Empirical fits describing the number of surviving vacancies and interstitial atoms as a function of overlap are presented.

PROGRESS AND STATUS

Introduction

Displacement cascade damage accumulation simulations are typically performed with object kinetic Monte Carlo (OKMC) method in which surviving defects (cascade debris) obtained from molecular dynamics (MD) are added into the simulation domain. This methodology assumes that existing defects do not affect the collision process of the next cascade. If the overlap process is ignored, introducing the same cascade debris exactly on top of each other (perfect overlap) would result in doubling the size of the defect objects. However this is likely to be inaccurate in a real life because the existing vacancies may be completely erased by the next cascade's core during the peak damage. In this research, we investigate the effect of the overlap process on the number of defects.

Simulation Details

Molecular dynamics (MD) technique as implemented in LAMMPS [1] is employed to simulate displacement cascades. The interatomic potential developed by Juslin et al. [2] is used. An important feature of this potential for radiation damage is that it gives the correct order of stability among dumbbells: <111>, <110>, and <100> with the <111> configuration being the most stable.

From our previous experience of cascade simulation in tungsten, a 20-keV primary knock-on atom (PKA), without electronic loss, results in average 15.5 surviving Frenkel pairs, N_F = 15.5. This number is sufficient to produce observable overlap effect. Therefore, this energy is chosen for this study. A cubic box of side equals 64 lattice units (203.75 Å) is used with periodic boundaries in all axes. The total number of atoms is 524,288. The coordinate of the atoms is shifted by a vector = (0.1, 0.3, 0.5) Å. This shift effectively results in a velocity vector with high Miller indices for any atom directed towards the box's center. Before the displacement cascade, the system is equilibrated at 1025 K at zero pressure. Subsequently, for the cascade simulation, the volume is fixed and a border region as thick as two atomic layers is defined in all sides. A Nosé-Hoover thermostat at 1025 K with a time constant of 100 fs is applied to the border atoms to model heat extraction during cascade. The rest of the atoms are evolved within the microcanonical (*NVE)* ensemble. Every cascade is followed up to 15 ps.[1]

The center of mass of vacancies at the peak damage is taken as the location of the cascade. To estimate the distance between the initial position of the PKA to the cascade location, λ_{peak}, 25 separate simulations are performed. In these simulations, a PKA is chosen from near the center of the box and given a velocity with a random direction. We obtain an average of λ_{peak} = 34.3 Å. These simulations are then discarded.

[1] PNNL is operated for the U.S. Department of Energy by Battelle Memorial Institute under Contract DE-AC06-76RLO 1830.

For all cascades, a PKA will be chosen from a pool of atoms within a spherical shell of 34.3 ± 0.2 Å from the box's center, and given a velocity directed towards the box's center. There are approximately 367 atoms within such a shell.

Results

Two hundred cascades are generated which constitute the first set of the cascade, cascade-1. From this set, we obtain N_F = 15.4 ± 0.3, λ_{peak} = 35.7 ± 0.7 Å, and λ_{end} = 31.8 ± 0.7 Å (λ_{end} is the distance between the PKA's initial position to the center of mass of the surviving vacancies). Figure 1 shows the variation of λ_{peak} and λ_{end} among simulation runs. It is interesting to note that $\lambda_{end} < \lambda_{peak}$ as if there is a collective restoring momentum back towards where the PKA originates after the peak damage phase.

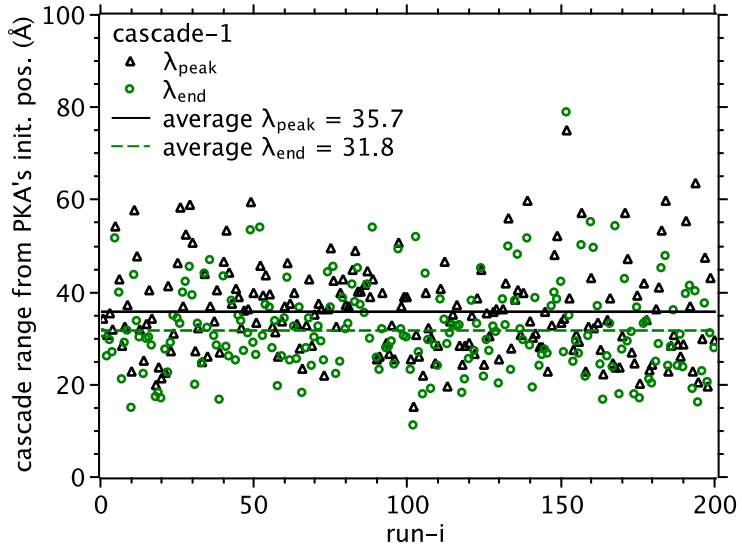

Figure 1. Variation of the distance from the PKA's initial position to the center of mass of vacancies at peak damage λ_{peak} (triangles) and to the center of mass of the surviving vacancies λ_{end} (circles) among simulation runs.

Cascades in cascade-1 are followed up to 15 ps. Afterwards, in each of these cascades, another PKA is chosen with the same procedure as described before to initiate a subsequent cascade. These subsequent cascades are again followed for 15 ps and constitute the second set of the cascades, cascade-2. The peak-to-peak damage distance between the first and the second cascade is taken as the overlap parameter, R_{pp}. Figure 2 shows the number of surviving vacancies at the end of cascade-2 as a function of R_{pp}. We fit the data to

$$N_{Vac,cascade-2} = N_\infty - \Delta \exp\left(-\left(R_{pp}/\alpha\right)^j\right)$$

where N_∞ is the number of vacancies when $R_{pp} = \infty$, therefore $N_\infty = 2 \times 15.4 = 30.8$. Parameters Δ and α are fitted for various integer values of j. The best fit is obtained with j = 2 and the fitted equation is

$$N_{Vac,cascade-2} = 30.8 - 10.6 \exp\left(-\left(R_{pp}/43.1\right)^2\right)$$

This result indicates that on average the net number of defects from the second cascade is smaller than the number of defects from the first cascade. At perfect overlap condition, the net value is (30.8-10.6)-15.4 = 4.8, i.e. the second cascade adds only 4.8 vacancies compared to 15.4 if the overlap process is ignored. We note that in 18 out of 200 runs, the net value is in fact < 0. Figure 2 also shows that the effect of the overlap is monotonic as a function of R_{pp}. This behavior will not be obtained in OKMC simulations which disregard the overlap process. In such OKMC simulations, most inter-cascade recombination

occurs at a certain overlap distance where the interstitials of the first cascade overlap with the vacancies of the second cascade and vice versa.

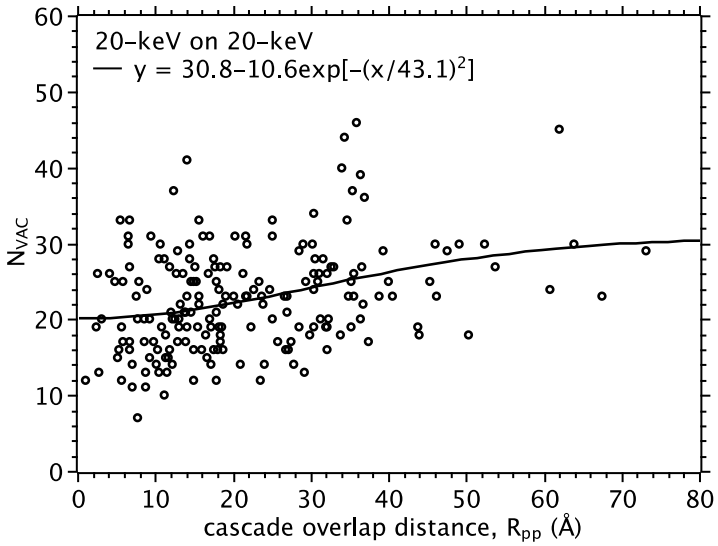

Figure 2. The number of surviving vacancies after the second cascade as a function of the distance between the center of mass of vacancies at the peak damage of the first and the second cascade, R_{pp}. The average number of surviving vacancies from the first cascades is 30.8/2 = 15.4.

If the time scale between subsequent cascades is much longer than that of SIAs diffusing away from the cascade region, practically only vacancies from the preceding cascade are left. To investigate the overlap effect for this situation, we construct another set of cascade overlap as follows. From run-1 to run-100 of cascade-1 set, another set is created by removing the existing SIAs and is denoted as cascade-1b. Cascade-2b is obtained after performing the second cascade on cascade-1b. The number of surviving vacancies and SIAs in cascade-2b is shown in Figure 3. The data points are fitted with a constraint of N_{∞}equals 30.8 and 15.4 for N_{Vac} and $N_{SIA,}$ respectively. The fit curves are

$$N_{Vac,cascade-2b} = 30.8 - 7.0\exp\left(-\left(R_{pp}/23.9\right)^2\right)$$
$$N_{SIA,cascade-2b} = 15.4 - 6.7\exp\left(-\left(R_{pp}/21.4\right)^2\right)$$

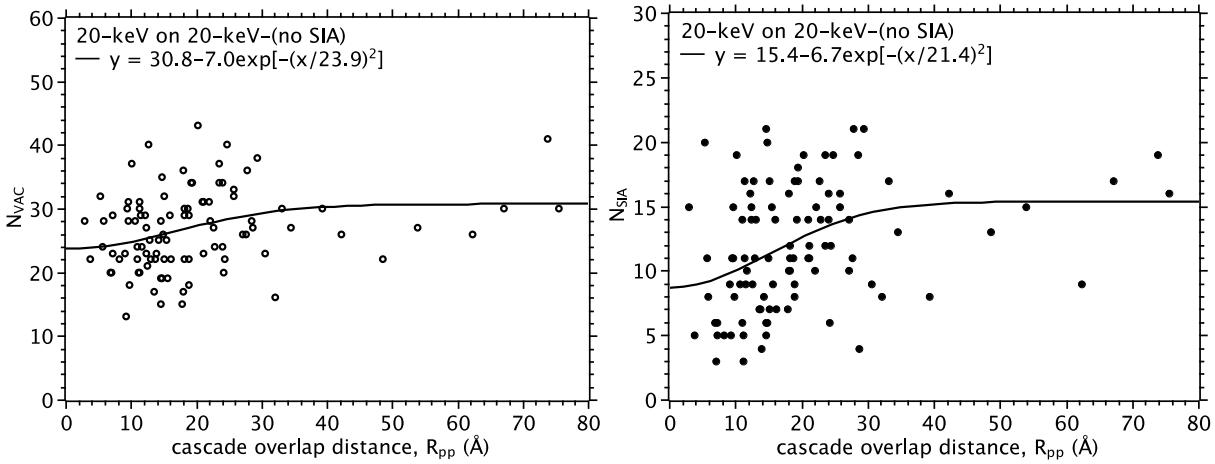

Figure 3. The number of surviving vacancies and SIAs after the second cascade with SIAs from the first cascade removed.

For a complete cascade overlap, the number of vacancies is 30.8-7.0. In other words, there is a reduction of 7 vacancies (or 7/30.8 = 23%) as compared to if a proper overlap simulation is not accounted for. Compared to cascade-2, the overlap effect in cascade-2b is smaller. In addition, the overlap region of influence parameter α is much shorter (23.9 Å) compared to that in cascade-2 (43.1 Å).

In the future, we will define another overlap parameter ϕ as follows. The vacancies from the first cascade are assigned type = 1 and are denoted as V_A. During the second cascade, any vacancies not occupying V_A are assigned type = 2 and denoted as V_B. If a V_A migrates during the second cascade to a location not occupied by any other V_A, then it becomes V_B. A V_A is flagged as overlapped if it has been a part of a V_AV_B cluster anytime during the second cascade. Consequently, a V_A that becomes a V_B will not be flagged as overlapped as long as it forms only a V_B cluster. The fraction of overlapped V_A to the initial number of V_A is taken as ϕ. Hence, ϕ has a value between 0 and 1 with 1 denoting a complete overlap. We will compare the merit as well as disadvantage between R_{pp} and ϕ as the overlap parameter.

References

[1] S. Plimpton, J. Comp. Phys. 117 (1995) 1.
[2] N. Juslin and B.D. Wirth, J. of Nuc. Mat. 432 (2013) 61.

8.2 OBJECT KINETIC MONTE CARLO SIMULATIONS OF RADIATION DAMAGE IN TUNGSTEN—
G. Nandipati, W. Setyawan, H. L. Heinisch, K. J. Roche, R. J. Kurtz (Pacific Northwest National Laboratory) and B. D. Wirth (University of Tennessee)

OBJECTIVE

The objective of this work is to study the radiation damage created by primary knock-on atoms (PKAs) of various energies, at various temperatures in bulk tungsten using the object kinetic Monte Carlo (OKMC) method.

SUMMARY

We used our recently developed lattice-based object kinetic Monte Carlo code; *KSOME* [1] to carryout simulations of radiation damage in bulk tungsten at temperatures of 300, and 2050 K for various dose rates. Displacement cascades generated from molecular dynamics (MD) simulations for PKA energies at 60, 75 and 100 keV provided residual point defect distributions. It was found that the number density of vacancies in the simulation box does not change with dose rate while the number density of vacancy clusters slightly decreases with dose rate indicating that bigger clusters are formed at larger dose rates. At 300 K, although the average vacancy cluster size increases slightly, the vast majority of vacancies exist as mono-vacancies. At 2050 K no accumulation of defects was observed during irradiation over a wide range of dose rates for all PKA energies studied in this work.

PROGRESS AND STATUS

Introduction

Tungsten is considered as the primary solid material choice for divertor components in future fusion reactors due to its high melting point, low sputtering coefficient, high thermal conductivity, low transmutation probability, low tritium retention and good mechanical strength. Bulk tungsten will be exposed to energetic neutrons escaping the plasma. The deuterium-tritium fusion reaction produces neutrons with a characteristic kinetic energy of 14.1 MeV. Collisions of 14.1 MeV neutrons with tungsten atoms produce tungsten primary-knock-on atoms with various recoil energies. PKA atoms then lose the acquired energy to a large extent by displacing other atoms, in a sequence known as a displacement cascade. This process creates defect clusters such as vacancy and self-interstitial atom (SIA) clusters. Creation of point defects and clusters of these defects, subsequent migration, additional clustering and dissolution of clusters results in dramatic microstructural changes during neutron irradiation.

Simulation Details

Simulations were performed on a non-cubic block of tungsten atoms with dimensions 95.1 x 110.95 x 126.8 nm^3, with each axis parallel to a <100> direction of the crystal. Each defect is allowed to hop to one of eight body-centered cubic nearest neighbor lattice sites at *a*/2 (111), where *a* is the lattice constant. Finite periodic boundary conditions were adopted in all three directions i.e. periodic boundary conditions are applied but whenever a mobile object has moved a distance larger than the average grain size, it is removed from the simulation and it is no longer tracked. This approach is physically meaningful because SIA clusters diffuse very fast and reach the grain boundaries very quickly. In the present simulation we used an average grain size of 1 m was used. In these simulations no other traps were considered.

The values of the binding energies of defects used in the present annealing simulations were taken from the *ab initio* calculations of Becquart *et al*. [3] while the migration barriers were taken from MD simulations [4] using an EAM potential for W [5]. In the present simulations SIA clusters larger than size five were constrained to diffuse in 1D along one of four <111> directions. SIA clusters up to size five were allowed to change their direction of 1D motion via rotation and thereby performing mixed 1D/3D motion. The activation barrier for changing direction from one <111> direction to another is 0.38 eV [6]. Since the MD simulations of cascade damage do not provide information on the orientation of SIA diffusion, the direction of 1D motion was assigned randomly to the SIAs at the start of a simulation. Also there is no

information available on the infrequently occurring immobile SIA clusters in these cascades therefore we assumed that all interstitial clusters are glissile (mobile). Their migration/diffusion rates decrease with increasing cluster size (n) according to $\square_o n^{\square 1}$ ($\square_o$ = 6 x 10^{12} s^{-1}) while the migration barrier is independent of cluster size.

For a single vacancy, the activation barrier for diffusion is taken as 1.30 eV [4], and vacancy clusters larger than five are assumed to be immobile. But vacancy clusters of all sizes are allowed to emit mono-vacancies. All mobile vacancy clusters migrate in 3D, and their diffusion rates decrease with cluster size (n) according to $\square_o(q^{-1})^{n-1}$ ($\square_o$ = 6 x 10^{12} s^{-1}, q = 1000) [3]. The vacancy (SIA) dissociation rate is given by $\square_d = \square_d \exp((E_m + E_d)/k_B T)$, where E_d is the binding energy of a vacancy (SIA) to a vacancy (SIA) cluster, and E_m is the migration energy of a single vacancy (SIA). We have assumed that defect clusters of all sizes and types are spherical objects and their capture radii were obtained from Reference [3].

Cascades are randomly selected the database of cascades and inserted into the simulation box at random positions based on the cascade production rate, which depends on the dose rate. In addition, to introduce more variability the coordinates of defects in a cascade are rotated by same amount in random directions around the point of insertion. The production rate of cascades, which is number of cascades produced in the simulation cell per second, and the accumulated dpa (displacements per atom) are calculated based on the NRT displacements per cascade ($\square_{NRT}$) [7], the total number of atoms in the simulation cell of size (N_{atoms}) and the dose rate (dpa/s)

$$\upsilon_{NRT} = 0.8 \frac{E_{MD}}{2E_D} \qquad (1)$$

Where E_{MD} is the damage energy, i.e the fraction of kinetic energy of the PKA that is not absorbed by electronic excitation, equivalent to the cascade energy in the corresponding MD simulation, and E_D is the displacement threshold energy, which is 128 eV for tungsten [5]. Using the above expression one can calculate dpa per cascade (dpc) as

$$dpc = \frac{\upsilon_{NRT}}{N_{atoms}} \qquad (2)$$

Table 1 shows the NRT displacements per cascade and the dpa per cascade in tungsten at various PKA energies, which is calculated based on the number of atoms in the simulation cell. Total number of atoms in the simulation cell used in the present set of simulations is 84 x 10^6 atoms.

Table 1. NRT displacements per cascade and dpa per cascade in tungsten at various PKA energies

PKA energy (KeV)	**10**	**20**	**30**	**40**	**50**	**60**	**75**	**100**
$\square_{NRT}$	31.25	62.50	93.75	125.0	156.25	187.50	234.38	312.50
dpc (x 10^{-6})	0.372	0.744	1.12	1.49	1.86	2.23	2.79	3.72

Results

A database of 15,15 and 20 cascades at PKA energies of 60, 75 and100 keV respectively, created using MD simulations, was used to carry out these irradiation simulations. The simulations at 300 and 2050 K at dose rates of 10^{-5}, 10^{-6}, 10^{-7} and 10^{-8} dpa s^{-1} and using equations (1) and (2) cascade production rates with 100 keV cascades are 2.7, 0.27, 0.027, 0.0027 cascades per second respectively. To understand the

annealing of single cascades in tungsten we have also collected runtime information like number densities of defects, reaction events (recombination, coalescence, emission, transformation), average cluster sizes and their size distributions, and number densities of defects escaping the box for all the types (in this only SIAs and vacancies) as a function of time. Since this is ongoing work (simulations are still in progress) and simulations at various dose rates are at different levels of defect accumulation, we chose to show the latest information available for a particular dose rate and PKA energy. As mentioned in the introduction, interstitial clusters diffuse very fast and are absorbed by grain boundaries very quickly, leaving only vacancy clusters in the simulation box. Therefore we will only show the vacancy cluster distribution is displayed here.

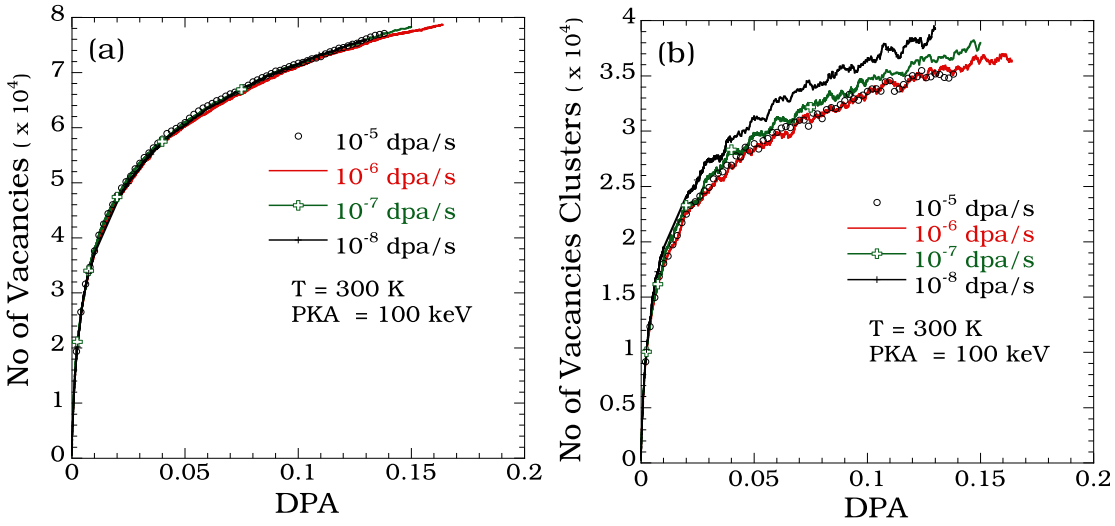

Figure 1. Comparison of damage accumulation at different dose rates using 100 keV cascades at 300 K. (a) Number density of vacancies (b) Number density of vacancy clusters.

Figure 1 shows the plot of the total number of vacancies and vacancy clusters as function of dose at a temperature of 300 K for 100 keV cascades at different dose rates. One can see that there is no noticeable difference in the number density of vacancies but the number density of vacancy clusters decreases with dose rate. Although not shown, the behavior of the number density of vacancies and vacancy clusters at various dose rates is similar for 60 and 75 keV cascades at 300 K.

Figure 2 shows snap shots of the vacancy distributions in the simulation box at various dose rates at 300 K for 100 keV cascades. The radius of each sphere in a snap shot is scaled by the vacancy cluster size as (cluster size)$^{1/3}$. To aid the visualization of the snap shots this radius for each sphere is further increased by 5 times. The coloring scheme for each sphere is based on this new increased radius. It can be seen from Figure 2 that the scale goes from 5 to 26.3882, which corresponds to vacancy cluster sizes from ranging from 1 to 147 vacancies. From Figure 2 it can be seen that at 300 K for 100 keV cascades, most of the vacancies exist as mono-vacancies and are randomly distributed in the simulation cell. Since mono-vacancies are immobile at 300 K most of the large clusters seen in the snap shots are created during cascade production. Again the behavior is very similar for 60 and 75 keV cascades at 300 K (not shown).

At 2050 K for all PKA energies shown in this article, it was found that there was no defect accumulation. At 2050 K, both mono-vacancy diffusion and dissociation of vacancy clusters is active. Therefore all vacancy clusters eventually dissociate into mono-vacancies and diffuse out to the grain boundary before the next cascade is produced. This process is further enhanced by the minimal vacancy clustering in the cascades produced at 2050 K, resulting in no defect accumulation over a wide range of dose rates ranging from 10^{-2} to 10^{-8} dpa s^{-1}. It is likely that this would be true even for other PKA energies not shown in this report.

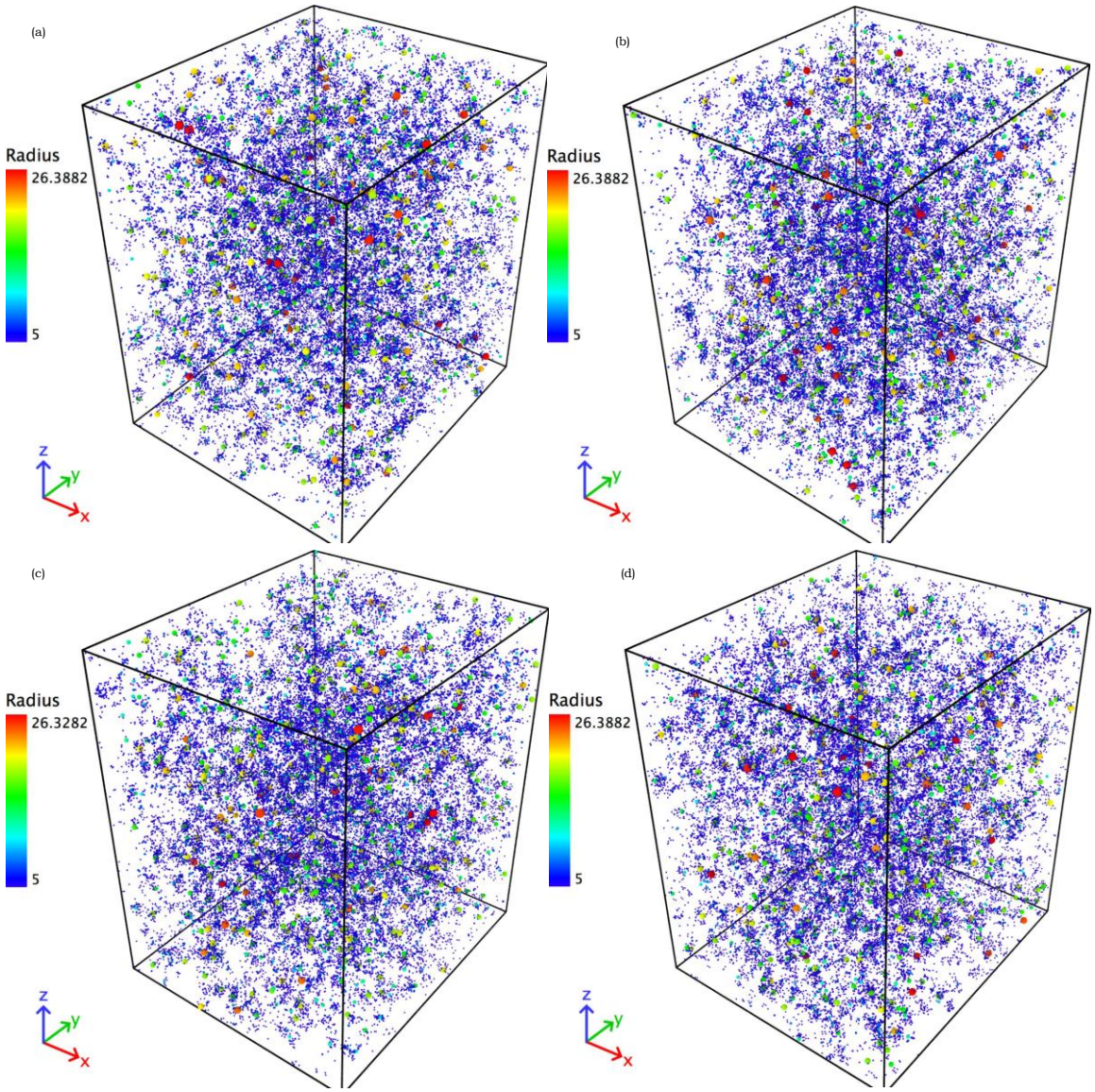

Figure 2. Snap shots of vacancy clusters in the simulation box (a) 10^{-5} dpa/s, 0.138 dpa (b) 10^{-6} dpa/s, 0.173 dpa (c) 10^{-7} dpa/s, 0.15 dpa (d) 10^{-8} dpa/s 0.130 dpa. (Vacancy Cluster Size = $(\text{Radius}/5)^3$).

Figure 3 (a), (b) and (c) shows plots of total number of vacancies, total number of vacancy clusters and average vacancy clusters size as a function of dose for 60, 75 and 100 keV cascades at 300 K for a dose rate of 10^{-6} dpa s^{-1}. As expected, the number density of vacancies increases with PKA energy due to increased defect production with PKA energy, Figure 3a. Larger clusters form at higher PKA energies resulting in a similar dose dependency of the number of vacancy clusters, Figure 3b. Figure 3(d) shows the fraction of surviving vacancies, which is a ratio of total number of vacancies present in the simulation cell and the total number of vacancies created, as a function of dose. It should be noted that the surviving fraction of vacancies for three PKA energies collapses into a single curve. This suggests that the rate of defect accumulation is independent of PKA energy of the cascade and depends primarily on the dose, at least for the PKA energies and doses shown in this report.

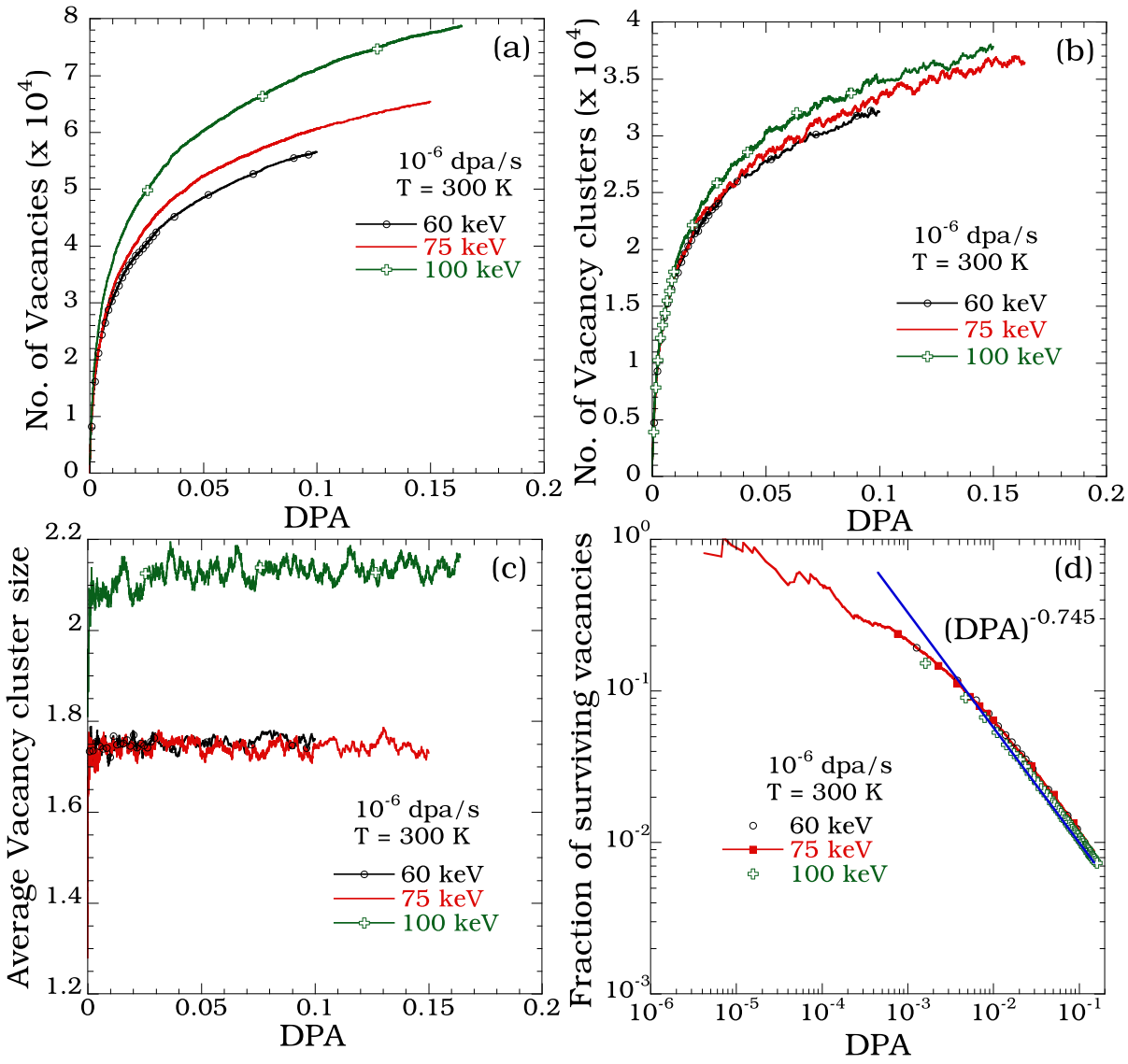

Figure 3. Comparison of damage accumulation at 10^{-6} dpa s^{-1} for 60, 75 and 100 keV cascades at 300 K as a function of dose (a) Number density of vacancies (b) Number density of vacancy clusters (c) average vacancy cluster size (d) fraction of surviving vacancies.

Future Work

Further simulations will be carried out to understand defect accumulation at various dose rates, PKA energies, temperatures, simulation cell and grain size, and also for different PKA spectra. In addition we sensitivity studies will be carried out to understand the effects of kinetic parameters and, in-cascade SIA and vacancy clustering.

Acknowledgement

All computations were performed on CARVER at National Energy Research Scientific Computing Center (NERSC) and Argonne National Lab, MCS Workstations

References

[1] G. Nandipati *et al* Semiannual Progress Report DOE/ER-0313/54, June 2013, 179-183
[2] W. Setyawan *et al* Semiannual Progress Report DOE/ER-0313/54, June 2013, 200-204
[3] C. S. Becquart *et al.* J. Nucl. Mater. 403 (2010) 75
[4] T.Faney, N.Juslin, B.D.Wirth,(*private communication)*.
[5] N.Juslin, B.D.Wirth, J. Nucl. Mater. 432(2013)61.
[6] D. A. Trentyev, L. Malerba, M. Hou, Phys. Rev. B 75 (2007) 104108.
[7] M.J. Norgett, M.T. Robinson, I.M. Torrens, Nucl. Eng. Des. 33 (1975) 50.

8.3 SINGULARITY-FREE DISLOCATION DYNAMICS WITH STRAIN GRADIENT ELASTICITY - G. Po, M. Lazar, D. Seif, N.M. Ghoniem (University of California, Los Angeles)

EXTENDED ABSTRACT *- paper published in JMPS 68 (2014) 161-178.*

The discrete Dislocation Dynamics (DD) method is one of the fundamental tools for the numerical investigation of the mechanical properties of defects in irradiated materials. For example, massive atomistically-informed DD simulations have been performed to study the phenomenon of plastic shear localization and formation of defect-free channels in irradiated materials [1]. Based on the classical theory of elasticity, the method allows to compute the elastic interaction between dislocations and other defects and to predict the evolution of the defect microstructure. However, because the classical theory of elasticity predicts singular elastic fields of dislocations, the DD method suffers both theoretical limitations and practical complications when computations are performed in the proximity of dislocation cores. One way to avoid singularities is to assume that the strain energy density of a certain material depends not only on strains but also on their gradients. This assumption, which models a weak non-locality of the energy density, allows to obtain a physically-based regularization of the singularities in the elastic fields of defects, and in particular of dislocations. In fact, in gradient elasticity, the issue of singularity is removed at the outset and smooth elastic fields of dislocations are available.

In this work [2] we consider theoretical and numerical aspects of the non-singular theory of discrete dislocation loops in gradient elasticity of Helmholtz type, a particular version of Mindlin's gradient elasticity with only one characteristic length scale parameter. Emphasis is focused on the application of the theory to three-dimensional DD simulations. The gradient solution is developed and compared to its singular counterpart in classical elasticity using the unified framework of eigenstrain theory. The fundamental equations of curved dislocation theory are given as non-singular line integrals suitable for numerical implementation using fast one-dimensional quadrature. These include expressions for the interaction energy between two dislocation loops and the line integral form of the generalized solid angle associated with dislocations having a spread core. The single characteristic length scale of Helmholtz elasticity is determined from independent molecular statics (MS) calculations (Fig 1). The gradient solution is implemented numerically within our variational formulation of DD, with several examples illustrating the viability of the non-singular solution. The displacement field around a dislocation loop is shown to be smooth (Fig 2), and the loop self-energy non-divergent, as expected from atomic configurations of crystalline materials. The loop nucleation energy barrier and its dependence on the applied shear stress are computed and shown to be in good agreement with atomistic calculations (Fig 3). DD simulations of Lomer–Cottrell junctions in Al show that the strength of the junction and its configuration are easily obtained, without ad-hoc regularization of the singular fields (Fig 4). Numerical convergence studies related to the implementation of the non-singular theory in DD are presented.

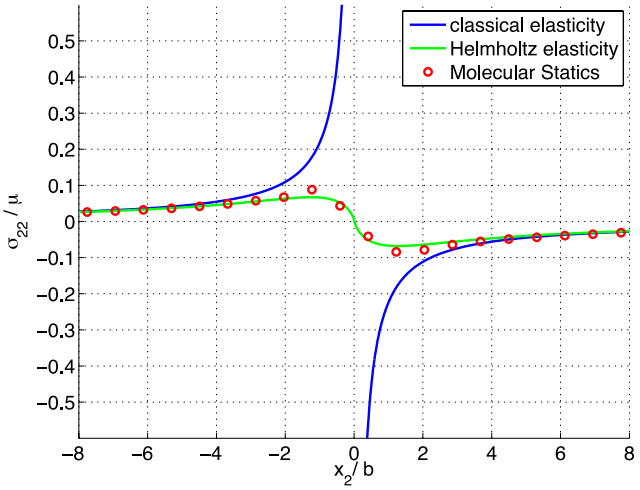

Figure 1. Comparison between virial stress and Cauchy stress (singular and non-singular). The gradient parameter L of the non-singular theory was chosen as a fitting parameter.

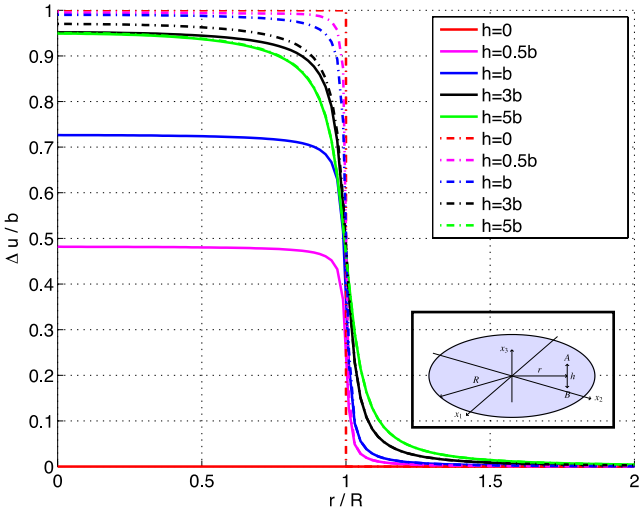

Figure 2. The displacement field of a dislocation loop suffers no jump discontinuity when crossing the loop plane, as a consequence of the regularized solid angle in the non-singular theory.

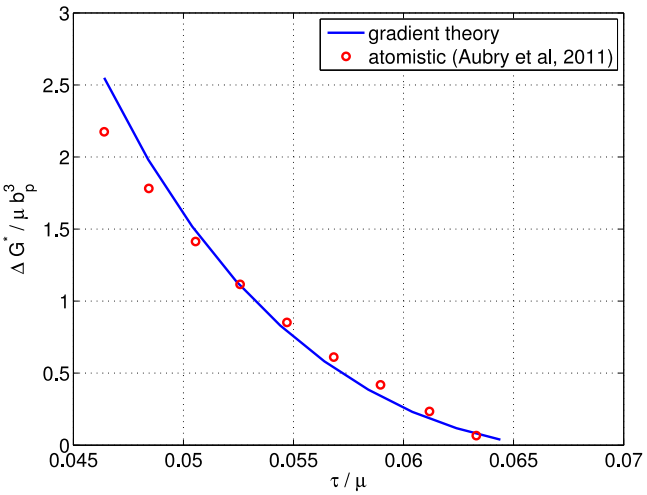

Figure 3. Nucleation enthalpy for a dislocation loop under an applied shear stress τ, according to the non-singular theory. Results compare well with existing atomistic simulations.

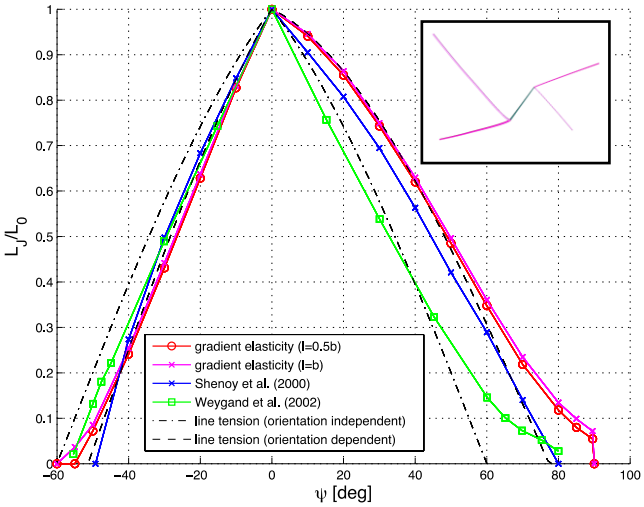

Figure 4. Verification of the strength of a Lomer-Cottrell junction (in insert) in Cu. The choice of the gradient parameter L influences only weak junctions (those with high incident angle ψ).

References

[1] de La Rubia TD, Zbib HM, Khraishi TA, Wirth BD, Victoria M, Caturla MJ. Multiscale modeling of plastic flow localization in irradiated materials. Nature 406 (2000) 871-874.
[2] Po G, Lazar M, Seif D, Ghoniem NM. Singularity-free dislocation dynamics with strain gradient elasticity. JMPS 68 (2014) 161-178.

8.4 ATOMIC-SCALE MECHANISMS OF HELIUM BUBBLE HARDENING IN IRON - Yuri N. Osetsky and Roger E. Stoller (Oak Ridge National Laboratory)

OBJECTIVE

The purpose of this research is to understand atomic level hardening mechanisms in materials with barriers such as voids, helium bubbles and rigid precipitates found in ODS alloys. This report covers effects of helium bubbles.

SUMMARY

Generation of helium in (n,α) transmutations changes the response of structural materials to neutron irradiation. The whole process of radiation damage evolution is affected by He accumulation and leads to significant changes in the material properties. A population of nanometer-size He-filled bubbles affects mechanical properties and the impact can be quite significant at high bubble density. Understanding how these basic mechanisms affect mechanical properties is necessary for predicting radiation effects. We completed an extensive study of the interactions between a moving edge dislocation and bubbles using atomic-scale modeling, focused on the effect of bubble size and He concentration in bubbles. The ability of bubbles to act as obstacles to dislocation motion is close to that of voids when the He-to-vacancy ratio is in the range 0 to 1. A few simulations at higher He contents demonstrated that the interaction mechanism is changed for over-pressurized bubbles and they become weaker obstacles. The results are discussed in light of post-irradiation materials testing.

Introduction

Generation of helium in materials under neutron irradiation occurs due to (n,α) transmutation reactions [1]. This phenomenon significantly changes the whole microstructure evolution for the commercially interesting temperatures above 600K and is a particular concern for future fusion applications due to elevated temperatures and high He-generation rates [2-3]. The need to develop predictive models for He effects has led to extended research programs worldwide (see e.g. [4].) According to the issues considered, studies of He effects can be generally considered in two categories.

One aspect is the prediction of He effects on microstructure evolution. This includes understanding the state of the He in the material and in bubbles, the interactions between mobile defects (vacancies, interstitial atoms) with He atoms and He-filled bubbles, and their impact within the appropriate models for microstructure evolution. There have been numerous studies of how helium generation influences cavity and other microstructural evolution using a range of simulation methods [5-8]. Recently we employed molecular dynamics simulations to study the behavior of He inside bubbles in an Fe matrix and its dependence on bubble size and temperature; this work led to the development of a modified equation of state for helium in bubbles [9]. In particular, it was found that the equilibrium He-to-vacancy (He/Vac) ratio obtained for bubbles 2 to 5 nm in diameter is about 0.4-0.7 at room temperature and weakly decreases with increasing temperature. This is quite consistent with recent experiments where the He/Vac ratio for small bubbles in ferritic-martensitic steels was determined using electron energy loss spectroscopy [10,11]. For example, helium density results for a 1.3 nm bubble lead to a He/vacancy ratio of 0.6 [10]. For bubbles from 2 to 5 nm, the He/vacancy ratio was in the range of 0.25–0.85 [11]. It is clear that He/Vac ratio depends on the irradiation temperature, rates of atomic displacements and He generation. However these numbers are an estimation of the He/Vac ratios to be considered.

The second aspect is the study of He as an impurity and in bubbles on mechanical properties. Although the first related modeling studies were reported quite a long time ago [12], this issue is much less explored for it demands quite a large-scale computing effort to receive robust results. The series of publications by Hafez Haghighat and Schaublin [13-16] is the most comprehensive research to date related to He bubble hardening in iron. The following conclusions can be formulated on the basis of results presented in [13-16]: 1) He-filled bubbles are strong obstacles consistent with corresponding size voids at He/Vac ≤ 2 and stronger than voids at He/Vac > 2; 2) bubble strength decreases at higher temperatures; and 3) there are certain quantitative but not qualitative effects on the bubble obstacle

strength at different He/Vac and temperatures when different Fe-matrix potentials [17-19] were used together with either the Wilson-Johnson [20] or Juslin-Nordlund [21] pair potentials for He-Fe interactions.

There are several aspects of this previous modeling work that should be mentioned. First, relatively small model crystals were used; as a result, the maximum dislocation length was 17 nm and the distance between dislocations in the periodic array was 25 nm even for large 7 nm diameter obstacles. Second, the quite high strain rate applied (the slowest reported is equal to $3x10^8$ s^{-1}) resulted in a dislocation velocity equal to 60 m/s. Third, very high He/Vac ratios of 1 to 5 were modeled. The mechanical stability of such bubbles was not investigated or reported.

Based on these observations, we conclude that many important aspects of dislocation interactions with helium bubbles require further attention to clarify the mechanisms involved. Among the most obvious issues are the following:

- Determining the obstacle strength of bubbles in the experimentally reasonable range of He content, i.e. He/Vac ratios ≤ 1,
- Understanding the sensitivity of the modeling results to the applied modeling parameters such as crystal size, strain rate and temperature,
- The atomic scale details of dislocation-bubble interaction mechanisms, and
- The stability and structure of over-pressurized bubbles with high He/Vac ratios and their temperature dependence.

Some of these issues were studied in the present research. However, we focus on one temperature, T=300K, because the majority of experimental mechanical testing has been performed at room temperature. We modeled bubbles with a relatively low He content, mainly He/Vac≤1, which is relevant to the experimental conditions. We report only a few cases with He/Vac=2 to demonstrate the dramatic change in the interaction mechanism due to over-pressurized conditions. Special attention was paid to the choice of modeling conditions and estimating the accuracy of the modeling results.

Atomic scale model

The atomic scale model we have used to study the ½<111> (110) edge dislocation interaction with He-filled bubbles is based on the molecular dynamics (MD) model described in [22]. This model describes a periodic array of dislocations and obstacles. The dislocation length, or equivalently, the distance between obstacles along the dislocation <112> line, is one of the most important modelling parameters. It should be long enough to permit the dislocation to adopt the necessary curvature at the critical state, i.e. before it is released from the obstacle. When interacting with strong obstacles, an edge dislocation usually adopts an "Orowan-like" configuration with an extended screw dislocation dipole formed in the obstacle's vicinity. This configuration may be called "Orowan-like" because it is similar to the dipole configuration that occurs for the true Orowan mechanism which involves impenetrable obstacles. It is important here that the interactions of screw segments belonging to the dipole are much stronger the interactions through the periodic boundaries along the dislocation line. In other words, the simulated dislocation segment length, L, should be much longer than the largest simulated obstacle diameter, D_O. In the present research we have used the constant L = 42 nm for the obstacle size up to D_O = 6 nm. Another important parameter is the crystal size along the $\boldsymbol{b}$ = ½<111> Burgers vector, $L_{\boldsymbol{b}}$. The importance of this parameter also arises because of the "Orowan-like" interaction mechanism; the length of the screw dislocation dipole at the critical state should be much smaller than $L_{\boldsymbol{b}}$ to minimize the contribution from the through-boundary interaction along the Burgers vector. In the present research the $L_{\boldsymbol{b}}$ value was chosen depending on the obstacle size and varied from ~30 nm to ~90 nm for obstacles from 1 nm to 6 nm in diameter. The crystal height, the measurement in the <110> normal direction to the dislocation slip plane, was chosen to be constant, H = 20 nm, for all the obstacles according to estimations described in [22]. The total number of lattice sites in the mobile crystals simulated was therefore varied from 2,074,024 to 6,236,064 depending on the obstacle size. The constant value of L allows direct comparison of the strength of all the obstacles. To generate force to move the dislocation, we have applied the strain rate loading described in [22]. We have used the constant strain rate value, $\dot{\varepsilon}$ = $5x10^6$ s^{-1}. The dislocation velocity depends on the applied strain rate and dislocation density and in the applied model can be estimated as: $v_D = \dot{\varepsilon}\, L_{\boldsymbol{b}} H / \boldsymbol{b}$ and varied from ~16 m/s to ~49 m/s in the smallest and largest crystals, respectively. The applied strain generates a

shear deformation of the modeled crystal which in turn generates shear stress (see [22] for how to calculate the shear stress value) which forces a dislocation to move. In MD modeling the instantaneous stress fluctuates depending on the temperature and dislocation velocity (i.e. applied strain rate.) Fig. 1 shows the variation of the instantaneous shear strain,τ, calculated every 100 time steps (the time step for motion equation integration is equal to 2fs) during the steady state motion of a ½<111>{110} edge dislocation under $5x10^6 s^{-1}$ applied strain rate modeled at 300K over 2.5 ns. One can see that its value fluctuates from <-20 MPa to almost 40 MPa. Statistical treatment resulted in the mean value $\bar{\tau}$=3.53 MPa (solid line in Fig. 1) and a standard deviation σ=9.8 MPa (the values of ($\bar{\tau} \pm \sigma$) are indicated by point-dash lines in Fig. 1). Here we accepted the standard deviation as providing the most accurate estimate of the uncertainty in the mean shear stress. However, in the case of dislocation-obstacle interactions the uncertainty in the shear stress estimate should be higher because this process is far from the case of equilibrium steady state dislocation motion considered in Fig. 1. It is difficult to estimate this uncertainty for it depends on the temperature and applied strain rate. We cannot estimate the mean shear stress by a simple time average as in Fig. 1 for the interaction process is limited in time. More important is the obstacle release stress that exists over a limited and rather short time depending on the strain rate applied. As an example we illustrate the typical stress-strain, τ(ε), dependence obtained when modeling the interaction between a moving dislocation and a 2 nm bubble with He/Vac=0.5. The grey line presents the instantaneous shear stress calculated every 100 time steps. One can see that stress fluctuations are rather big and quite similar to that in Fig. 1 for the steady-state dislocation motion. To extract a reasonably averaged instantaneous value of τ we used adjacent average (AA) processing of the instantaneous data. The AA processing data with 5, 10 and 20 neighboring points (AA5, AA10 and AA20) are shown by green, black and red lines in Fig. 2. Data for AA20 show reasonably smooth behavior. We used this treatment to produce all of the results reported here, assuming as well that the uncertainty in estimating the shear stress values is the same as for the steady state dislocation motion at the same temperature where its lower limit is >10 MPa. Note that processing parameters (the number of neighboring points) and the shear stress uncertainty (standard deviation of the mean stress) depend upon the model strain rate and temperature; both values decrease at low temperature and $\dot{\varepsilon}$ and increase at higher temperatures and $\dot{\varepsilon}$. The maximum on the processed τ(ε) curve indicates the critical resolved shear stress (CRSS) which is the measure of the obstacle strength for a given interaction geometry. As shown in [22], if the dislocation segment, *L*, is long enough then CRSS ∝ 1/*L* for a given obstacle.

The atomic-scale interaction mechanisms were assessed using an on-the-fly visualization during simulation. For the dislocation line visualization we have used two techniques, either analyzing the common neighbors or the atomic disregistry in the dislocation core. The details can be found in [22].

To complete the description of the model accuracy, we consider one more issue related to the equilibration and annealing of simulated gas-filled bubbles: Any defect created in atomic-scale modeling requires a certain period of annealing to reach the equilibrium state. The He-filled bubble is an example that needs a long time to reach equilibrium depending on the size and He/Vac ratio as was reported recently in [9]. The need for a long equilibration time s demonstrated in [9], ~1-2 ns, to accurately estimate the value of He pressure inside small bubbles with low He/Vac ratios. For larger bubbles with higher He/Vac ratios, equilibration can be reached faster. The dynamics of temperature and pressure equilibration for He atoms inside a 4 nm bubble with He/Vac=0.4 is shown in Fig. 3. In this case the bubble reaches its equilibrium state sometime between 50 and 100 ps. In this study we annealed each crystal with the dislocation and bubble over this time before strain was applied.

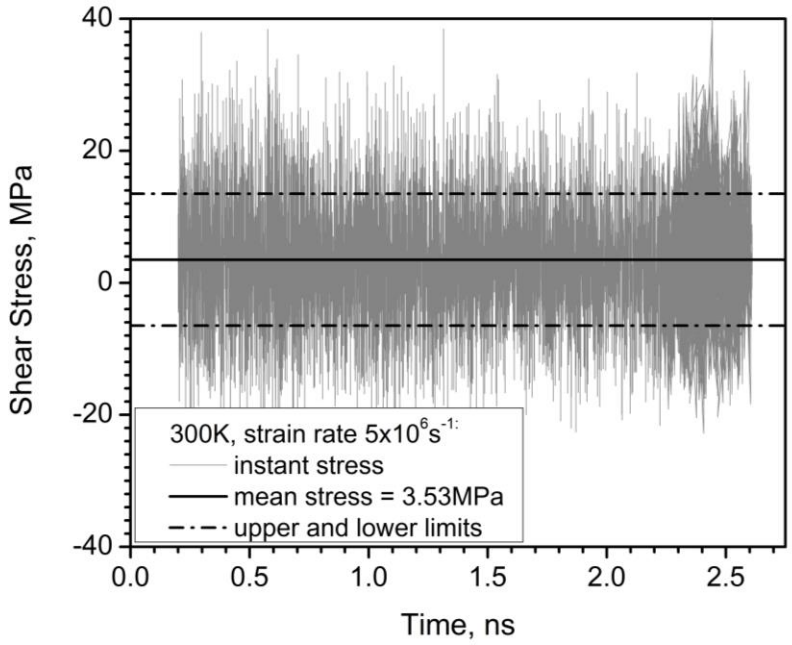

Figure 1. Modeling of steady state motion of ½<111>{110} dislocation at a strain rate of $5x10^6s^{-1}$ at 300K: grey line - instantaneous shear stress calculated every 100 time steps ; solid black line - mean value, 3.8MPa, estimated over 2.5ns, point-dash lines – mean stress plus/minus standard deviation value, σ = 9.8MPa.

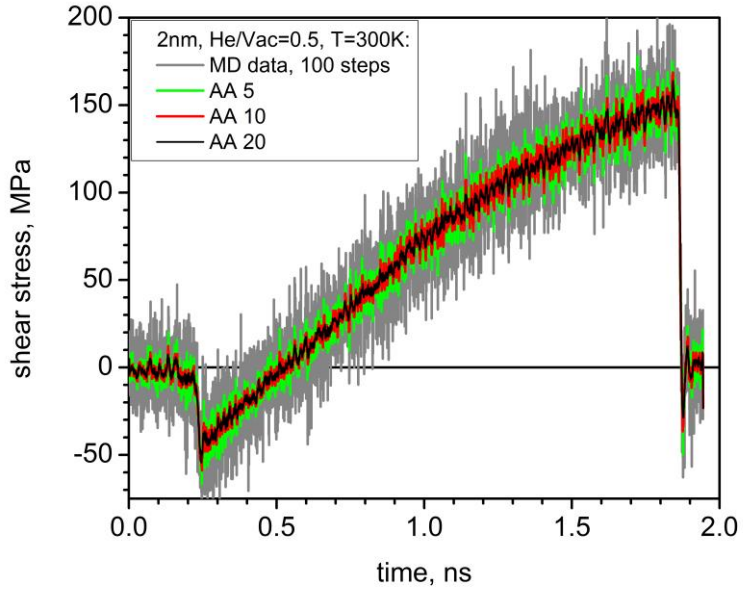

Figure 2. Stress-strain curve observed during dislocation interaction with 2 nm bubble with He/Vac=0.5: grey line - instantaneous shear stress calculated every 100 time steps; green, red and black lines – processes by adjacent average over 5, 10 and 20 neighbor points respectively.

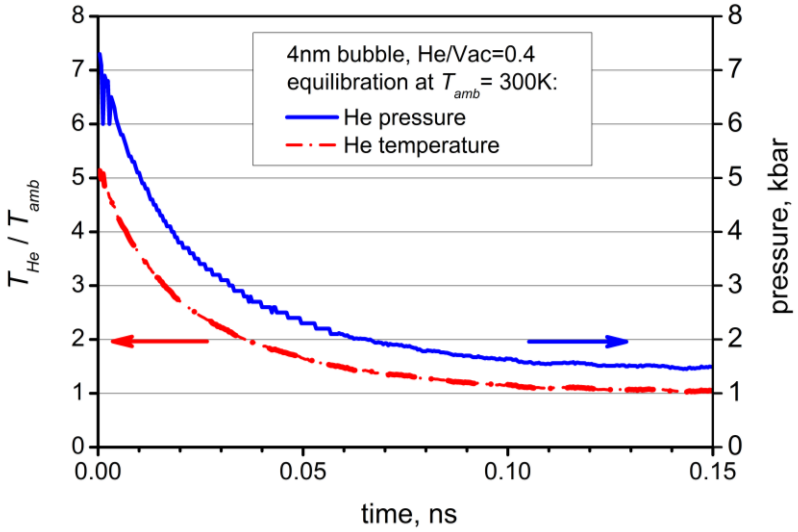

Figure 3. Evolution of He-atoms temperature and pressure inside the 4 nm bubble with He/Vac=1 during bubble equilibration.

For all simulations in this research we have used the following set of interatomic potentials: the embedded atom model potential for Fe from [17], the three-body potential for Fe-He interaction from [23, 24] and the pair potential for He-He interaction from [24]. The three-body He-Fe potential was fitted to a wide set of first principles data with the main emphasis on the properties of He-vacancy clusters [25]. This set of potentials was successfully applied in extensive studies of He-vacancy clusters, He-bubble nucleation, growth and stability and He transport in bcc Fe [9, 24, 25-28].

In this paper we report data for 1, 2, 4 and 6 nm diameter bubbles that contain up to 9640 vacancies and the corresponding number of He-atoms when the He/Vac ratio is varied from 0 to 1. The He/Vac ratio was extended up to 2 in the case of 2 nm bubbles to demonstrate when the interaction mechanism changes.

Results and discussion

The results for 1, 2, 4 and 6 nm bubbles are summarized in Fig. 4 which show the dependence of the CRSS on the He/Vac ratio. The size dependence is strong and follows that observed for voids. Moreover, within the presented values of He/Vac, the dislocation-bubble interaction mechanism is the same and very close to that of voids. To demonstrate this, we present a set of dislocation line configurations at some characteristic stages during its interaction with a 4 nm bubble with He/Vac=1 in Fig. 5. These states are fully compatible with similar states for the void described in [13]. In Fig. 5, State 1 is related to dislocation motion through the crystal before it comes into contact with the bubble. This is equivalent to the initial stage of τ(ε) curve shown in Fig. 2 when the shear stress is eventually constant. State 2 occurs when the dislocation is attracted by the bubble and comes into contact. This state is characterized by a strong attractive force and is accompanied with the sudden drop of shear stress to the negative value in Fig. 2. When dislocation intersects the bubble it loses a certain amount of dislocation line length. This is energetically favorable for the dislocation line energy inside the bubble can be set to 0 (a similar effect is demonstrated for a void in [13].) At State 3, the dislocation crosses the bubble along its diameter and therefore loses the longest possible segment. This is the minimum energy and a zero stress state. It is equivalent to the point when τ(ε) curve intersects zero stress level at about ε=0.25 in Fig. 2. Further straining leads to dislocation glide over the bubble surface, restoring the dislocation line in the crystal and creating a step on the exit surface of the bubble. During this process the shear stress increases and dislocation line curve due to glide of the segments in the crystal. State 4 in Fig. 5 shows the critical shape of the dislocation just before it breaks out. The considered obstacle is “strong” and the initial edge dislocation creates a relatively long dipole of screw segments with a near-zero angle between them. As mentioned above, the dislocation is similar to that obtained by the Orowan mechanism for impenetrable

obstacles. The only difference between this and the true Orowan mechanism is the distance between dipole segments. In the case of impenetrable obstacles, this is equal to the obstacle diameter in the dislocation slip plane. In the case of bubbles and voids, this can be much shorter due to the dislocation glide over the bubble surface and the screw segments cross-slip. The State 4 in Fig. 5 is characterized by the maximum value on the τ(ε) curve. Finally, State 5 occurs when the dislocation is released from the bubble and glides through the crystal.

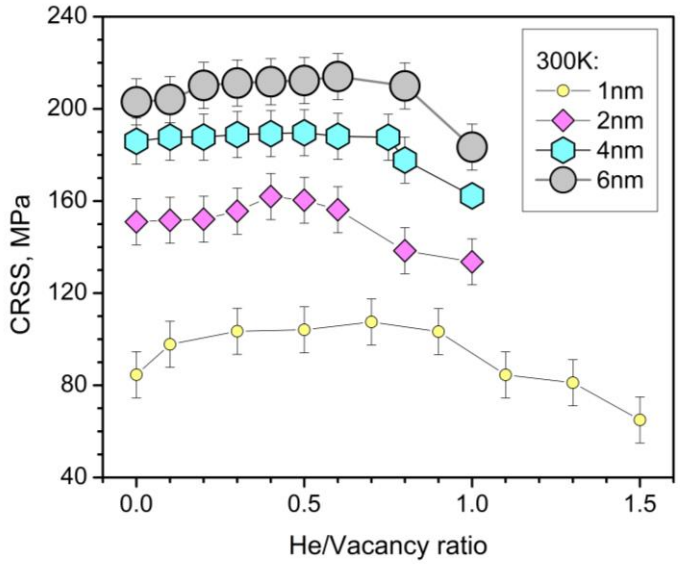

Figure 4. Dependence of the critical resolved shear stress versus He/Vac ratio for bubbles of 1, 2, 4 and 6 nm in diameter

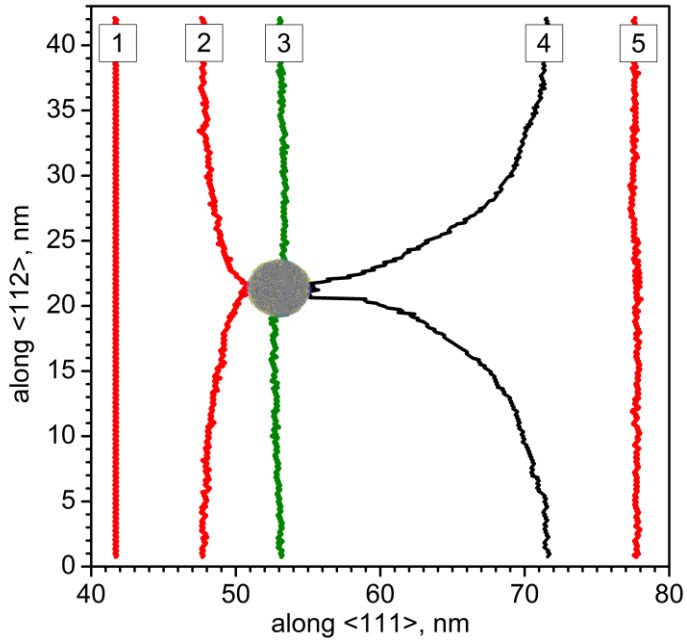

Figure 5. Shape of the dislocation line in the {110} slip at different stages during interaction with 4 nm bubble with He/Vac=1. Stages 1 to 5 are explained in the text.

The mechanism described above was observed for all the bubbles with He/Vac≤1. According to Fig. 5, and considering the uncertainty in the CRSS value definition of >10 MPa, the dependence of CRSS is rather weak for He/Vac≲0.8. However, we observed some differences between the interactions with low- and high- He content bubbles. One example of these differences is demonstrated in Fig. 6 which shows the dislocation line shape after it is released from a 4 nm bubble with different He/Vac. At He/Vac=0, i.e. a void, the line eventually climbs up absorbing vacancies from the obstacle. Visualization of this interaction has shown that one of the two screw segments that terminate at the void surface (see i.e. State 4 in Fig. 5) cross-slips up creating the corresponding superjog after the dipole is released from the void. A similar mechanism for other voids in Fe was discussed in [29]. However, a monotonic increase in He/Vac ratio, reduces the number of absorbed vacancies, and at He/Vac=1, the dislocation line absorbs more atoms and climbs down (see the corresponding dislocation line in Fig. 6). In this case one of the two screw dislocation segments climb down declines rather than up at lower He/Vac values.

As was pointed out in [30] such climb reduces the CRSS; however, the mechanism is not yet understood. The data obtained here, e.g. the CRSS (Fig. 4) and dislocation line shapes (Fig. 6) are in principle consistent with the maximum CRSS values usually being correlated with the minimum climb (and therefore the weakest cross-slip). However, this conclusion should be verified on other examples because of the high uncertainty in CRSS values. The only confident conclusion we can make is that at the highest He content studied here, He/Vac=1, all the bubbles are weaker than the corresponding voids.

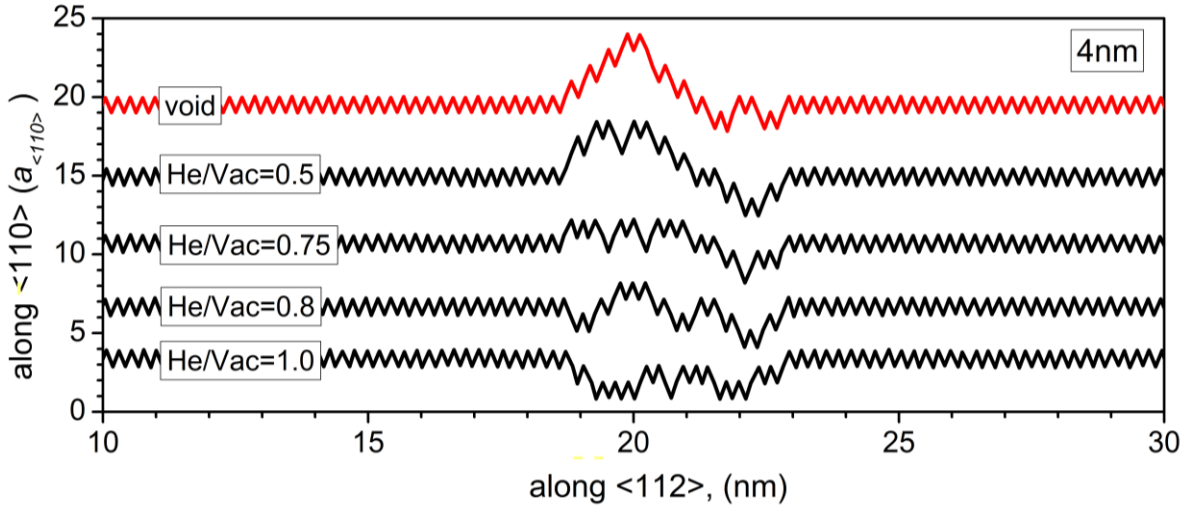

Figure 6. Shape of the dislocation line viewed along the Burgers vector after interaction with 4 nm bubbles with different He/Vac ratios.

To explore the effect of high He concentration, we modeled a 2 nm bubble with He/Vac=2. The τ(ε) curves for some He/Vac values are presented in Fig. 7 and the corresponding dislocation line shapes in Fig. 8. Obvious qualitative differences are observed in the both figures. In Fig. 7 the τ(ε) curve for He/Vac=2 is completely different from all the others with He/Vac≤1. The corresponding line shape demonstrates a significant amount of climb down that is equivalent to 36 atoms absorbed by the line. This means that the 2 nm bubble, that occupies 339 vacancy sites, increased its volume by more than 10%. Visualization of the interaction mechanisms has confirmed that it is qualitatively different from all other cases considered so far. During the equilibration process the bubble shape changed from the high symmetric sphere to some irregular shape that expanded locally. This occurred because for He/Vac=2 at T=300K the bubble is strongly over-pressurized and the bubble surface is deformed significantly outwards toward the Fe matrix but no clear punching of interstitial atoms was observed at this stage. However, when the dislocation approached the bubble it “emitted” an interstitial cluster that attracted the dislocation. This can be seen as a sudden drop on the corresponding τ(ε) curve on Fig. 7. The cluster was absorbed by the line creating a superjog and the dislocation was repelled from the bubble. At this state the

corresponding τ(ε) curve on Fig. 7 abruptly increased. At the next stage, due to continuous straining the jogged dislocation was pushed towards the bubble. However, unlike the other cases when the straight dislocation line intersected the bubble in the equatorial plane, the heavily jogged line just touches the periphery of the deformed bubble. As a result, the dislocation line now does not shear the whole bubble and the CRSS decreases by almost 40%. It is obvious that the over-pressurized bubble state arising from such a high He/Vac ratio is responsible for this change in the interaction mechanism.

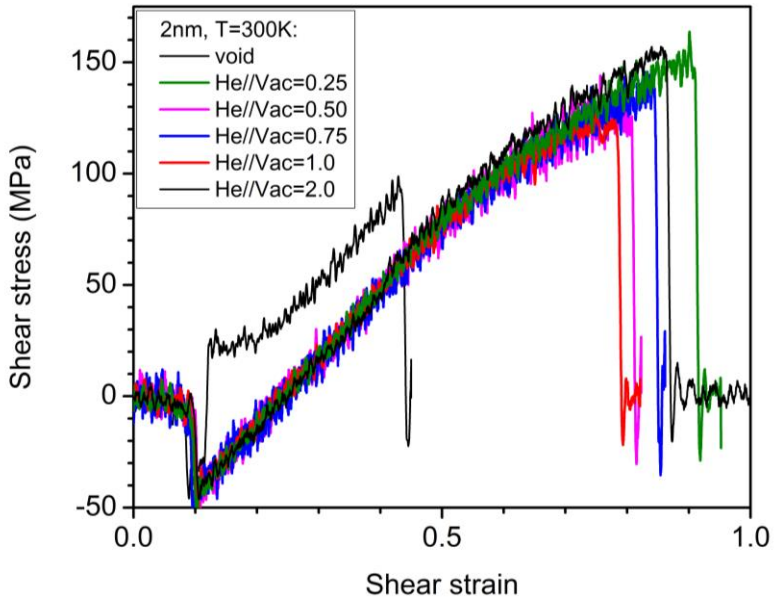

Figure 7. Stress-strain curves obtained during dislocation interaction with 2 nm bubbles with different He/Vac ratios.

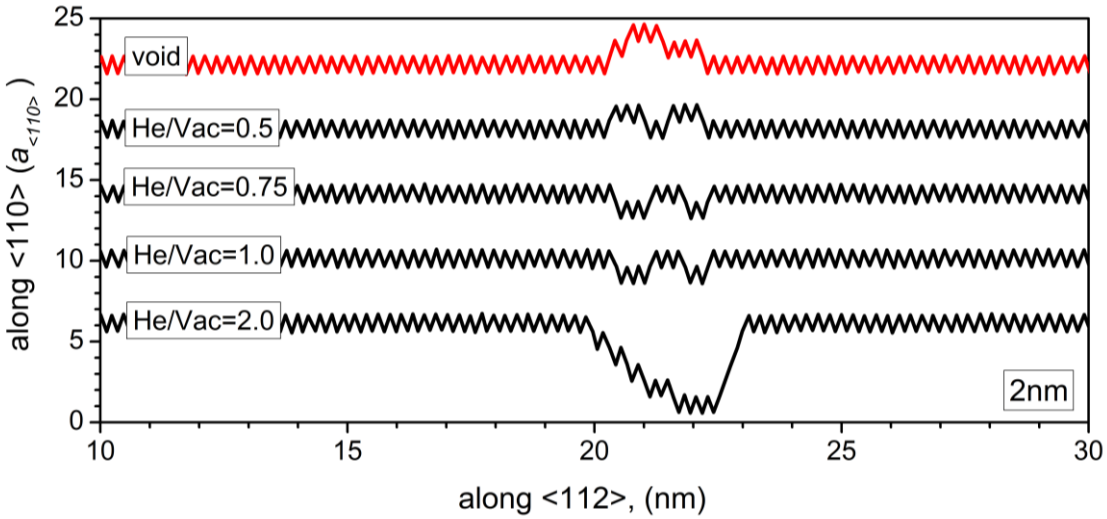

Figure 8. Shape of the dislocation line viewed along the Burgers vector after interaction with 2 nm bubbles with different He/Vac ratios.

We should note that CRSS decrease at He/Vac ≃ 2 as was reported earlier in [15-17]; however, the detailed mechanism and the difference with lower He-content bubbles was not described. Here we

confirm the drop in CRSS and identify the mechanism for the case of 2 nm bubble with He/Vac=2 at T=300K. We expect a similar decrease in CRSS for other sizes, which should be temperature dependent. The higher He-content bubbles studied in [15-17] demonstrated a significant increase in CRSS for up He/Vac=2-5, however the interacting mechanisms were not described. We expect that at such a high He-content a bubble should punch out interstitial clusters well before the dislocation approaches it, and in this case the interaction mechanism could be quite different than we observed with He/Vac=2. The difference is that in the present case the interstitial cluster was released from the bubble due to the strain fields from the approaching dislocation. It was released, a) in the place and b) with the orientation corresponding to the minimum interaction energy. These are, a) the negative pressure volume below the dislocation slip plane, and b) interstitial atom orientation along the dislocation Burgers vector. This correlated formation of an interstitial cluster from the over-pressurized bubble is the mechanism that reduces CRSS for a given size within a certain He/Vac and temperature range. However, if the He/Vac is much higher a strongly over-pressurized bubble may punch single interstitials or interstitial clusters out during its equilibration independent of the dislocation. In these cases interstitial clusters should be much larger (due to a much higher pressure) and their position and direction do not correlate with the dislocation stress fields. Therefore, dislocation-bubble interaction mechanism may be different for it may now involve interaction with the separate large interstitial cluster at the same time. The key issue here is the behavior of strongly over-pressurized bubbles and how the He/Vac ratio, temperature and bubble size affect the interstitial cluster punching, i.e. cluster size, formation geometry and crystallography. Once these mechanisms are understood their effect on dislocation-bubble interactions can be rationalized using a computational approach similar to that applied here. This work is now in progress.

We should also note that the size scale of dislocation-bubble interaction mechanisms is, in principle, compatible with direct transmission electron microscopy *in situ* straining experiments. It may be possible to study different mechanisms by performing *in situ* straining at different temperatures and therefore change the bubble pressure. Large scale atomistic simulations could then reproduce experimental conditions (except for the strain rate) to help in understanding the mechanisms observed. A similar direct modeling experiment comparison was made in previous studies of dislocation interactions with stacking fault tetrahedra when new mechanisms were discovered [30].

Summary

A large-scale atomistic study using molecular dynamics simulations was carried out to investigate the detailed interactions of moving edge dislocations with helium bubbles in iron. The important physical parameters of the computational model and their effects on the accuracy and uncertainty of simulation results were studied. Some of these issues are general, such as the accuracy of the shear stress definition, while others are specific to the behavior of gas-filled bubbles, such as the required equilibration time. The study focused on the interaction between a moving ½<111>{110} edge dislocation, and bubbles in the size range of 1 to 6 nm diameter, with the physically-relevant but so-far unexplored range of He-to-vacancy ratio from 0 to 1 at a temperature of 300K. The primary results include:

1. These bubbles demonstrate qualitatively the same hardening mechanism as that obtained earlier for voids,
2. The strength of these bubbles was found to be weakly dependent on. He/Vac ratio within the range of 0 to ~0.8. At higher He/Vac ratios the bubble strength decreases.
3. The over-pressurized 2 nm bubble with He/Vac=2 has demonstrated a completely different strengthening mechanism which i about 40% weaker. In this mechanism the over-pressurized bubble emits an interstitial cluster under the influence of the approaching dislocation strain fields. Correlated emission of interstitial clusters minimizes the dislocation-bubble intersection and the maximum shear stress.
4. The results are compared with those available in the literature and the possible mechanisms for strongly over-pressurized bubbles are discussed.

References.

[1] R. E. Stoller, Journal of Nuclear Materials 174 (1990) 289-310..

[2] H. Schroeder, P. Batfalsky, *J. Nucl. Mater.* 117 (1983) 287.
[3] T. Yamamoto, G.R. Odette, P. Miao, D.T. Hoelzer, J. Bentley, N. Hashimoto, H. Tanigawa, and R.J. Kurtz, *J. Nucl. Mater.* 367-370 (2007) 399-410.
[4] B.D. Wirth, G.R. Odette, J. Marian, L. Ventelon, J.A. Young-Vandersall, L.A. Zepeda-Ruiz, *J. Nucl. Mater.* **103** (2004) 329.
[5] N. M. Ghoniem, J. Nucl. Mater. 174 (1990) 168-177.
[6] R. E. Stoller and G. R. Odette, "The Effect of Helium on Swelling: Influence of Cavity Density and Morphology," Effects of Radiation on Materials, ASTM STP 782, H. R. Brager and J. S. Perrin, Eds., American Society of Testing and Materials, Philadelphia, 1982, pp. 275-294.
[7] J. B. Adams and W. G. Wolfer, J. Nucl. Mater. 166 (1989) 235-242.
[8] A. Caro, J. Hetherly, A. Stukowski, M. Caro, E. Martinez, S. Srivilliputhur, L. Zepeda-Ruiz, M. Nastasi, J. Nucl. Mater. 418 (2011) 261-268.
[9] R.E.Stoller and Y.N.Osetsky, *J. of Nucl. Mat.* **455** (2014) 258–262.
[10] Y. Wu, G.R. Odette, T. Yamamoto, J. Ciston, P. Hosemann, "An Electron Energy Loss Spectroscopy Study of Helium Bubbles in Nanostructured Ferritic Alloys," Fusion Reactor Materials, Semiannual Progress Report DOE/ER-0313/54, Oak Ridge National Laboratory (2013) 173–179.
[11] S. Fréchard, M. Walls, M. Kociak, J.P. Chevalier, J. Henry, D. Gorse, *J. Nucl. Mater.* **393** (2009) 102.
[12] M.I. Baskes, M.S.Daw, "The Effects of Impurities on Dislocation Dynamics and Fracture: An Atomistic Study", 4th International Conference on Hydrogen Effects on Material Behavior (Jackson Lake Lodge, WY: 1989), Published: Tms (September 1989), ISBN-10: 0873391500.
[13] R. Schaublin and Y.L. Chiu, *J. Nucl. Mater.* **362** (2007) 152.
[14] S S.M. Hafez Haghighat and R. Schaeublin, "Molecular dynamics modeling of cavity strengthening in irradiated iron", Proceedings of Third International Conference of Multiscale Materials Modeling, Freiburg, Germany, September 2006, p.729.
[15] S.M. Hafez Haghighat and R. Schaeublin, *J. Comput. Aided Mater. Des.* **14** (2008) 191.
[16] S.M. Hafez Haghighat and R. Schaublin, *Philos. Mag.* **90** (2010) 1075.
[17] G.J. Ackland, D.J. Bacon, A.F. Calder and T. Harry, *Phil. Mag.* A **75** (1997) 713.
[18] M.I. Mendelev, S. Han, D.J. Srolovitz, D.Y. Sun and M. Asta, *Phil. Mag.* **83** (2003) 3977.
[19] S.L. Dudarev and P.M. Derlet, J. Phys. *Condens. Matter.* **17** (2005) 7097.
[20] W.D. Wilson and R.A. Johnson, in Rare Gases in Metals, P.C. Gehlen, J.J. Beeler and R.J. Jaffe, eds., Premium Press, NY, 1972, 375.
[21] N. Juslin and K. Nordlund, *J.Nucl.Mater.* **382** (2008) 143.
[22] Yu.N. Osetsky and B.J. Bacon, Model. *Simul., Mater. Sci. and Eng.* **11** (2003) 427.
[23] T. Seletskaia, Yu.N. Osetskiy, R.E. Stoller and G.M. Stocks, *J. Nucl. Mater.* **361** (2007) 52-61.
[24] R.E. Stoller, S.I. Golubov, P.J. Kamenski, T. Seletskaia, Yu.N. Osetsky, *Philos. Mag.* **90** (2010) 923.
[25] R.A. Aziz, A.R. Janzen and M.R. Moldovan, *Phys. Rev. Let.* **74** (1995) 1586.
[26] T. Seletskaia, Yu.N. Osetsky, R.E. Stoller and G.M. Stocks, *J. Nucl. Mater.* **351** (2006) 109-118.
[27] D.M. Stewart, Yu. N. Osetskiy, R.E. Stoller, *J. Nucl. Mater.* **417** (2011) 1110.
[28] D.M. Stewart, Yu.N. Osetsky, R.E. Stoller, S. I. Golubov, T. Seletskaia, P.J. Kamenski, *Philos. Mag*. **90** (2010) 923.
[29] Yu.N. Osetsky and D.J. Bacon, *Philos. Mag*. **90** (2010) 945.
[30] Yu.N. Osetsky, Y. Matsukawa, R.E. Stoller and S.J. Zinkle, *Philos. Mag. Lett.* **86** (2006) 511.

8.5 MOLECULAR DYNAMICS MODELING OF ATOMIC DISPLACEMENT CASCADES IN 3C-SiC: COMPARISON OF INTERATOMIC POTENTIALS - G. D. Samolyuk, Y. N. Osetskiy and R. E. Stoller (Oak Ridge National Laboratory)

[This contribution is derived from a paper submitted for open-literature publication.]

OBJECTIVE

The objective of this work is to characterize the nature of primary radiation damage in SiC to provide a basis for understanding the experimentally observed fluence-temperature map of the irradiated microstructure. Recently reported results demonstrated that the most commonly used interatomic potentials (Tersoff) are inconsistent with *ab initio* calculations of defect energetics. In order to demonstrate the sensitivity of cascade recombination to the value of barrier recombination additional cascade simulations have been done with the newly developed Gao-Weber potential.

SUMMARY

Molecular dynamics modeling of cascades characterized the primary radiation damage in 3C-SiC, demonstrating that commonly used interatomic potentials are inconsistent with *ab initio* calculations of defect energetics. Both the Tersoff potential and a modified embedded-atom method potential reveal a barrier to recombination of the carbon interstitial and carbon vacancy much higher than the density functional theory (DFT) results. The barrier obtained with a newer Gao and Weber potential is closer to the DFT result, with significant differences in point defect production. Both 10 and 50 keV cascades were simulated in 3C-SiC at a range of temperatures. In contrast to the Tersoff potential, the Gao-Weber potential produces almost twice as many C vacancies and interstitials at the time of maximum disorder (~0.2 ps) but only about 25% more stable defects at the end of the simulation. Only about 20% of the carbon defects produced with the Tersoff potential recombine during the in-cascade annealing phase, while about 60% recombine with the Gao-Weber potential. Gao-Weber appears to give a more realistic description, with some shortcomings compared to the *ab initio* results.

Introduction

The outstanding physical, chemical and mechanical properties of silicon carbide (SiC) have stimulated significant technological and scientific interest for its use in electronic devices and neutron irradiation environments [1]. When subjected to high energy neutron irradiation, the microstructure and hence the mechanical properties of 3C-SiC (cubic phase of SiC) are changed. Understanding the details of this process is necessary for predicting these changes, and estimating the material's usable lifetime. Experimental studies have demonstrated that depending on the structural material's composition and other particular conditions, phenomena such as amorphization [2-7] and swelling [8-10] are observed.

Currently, the molecular dynamics approach with the atom-atom interactions described by empirical interatomic potentials appears to be the main tool for simulating atomic displacement cascades. In this approach, the results of cascade modeling significantly depend upon the accuracy of the description of the main defect properties by the interatomic potential. In the present paper we give a detailed comparison of the results of atomic displacement cascades in SiC obtained using the popular Tersoff [11] potential, with the parametrization proposed by Devanathan *et al.* [12] with the more recent Gao-Weber (GW) potential [13]. Despite having reasonably good agreement with the native defect formation energies obtained from *ab initio* density functional theory (DFT) calculations [14], the Tersoff potential predicts a very high interstitial migration energy [13]. We demonstrate that such high barrier also significantly suppressed the recombination of the carbon interstitial-vacancy defect pair, even when separated by distances as small as one lattice parameter. It is shown that this difference in barrier recombination also leads to a different temperature dependence for the number of stable defects at the end of cascade evolution.

Simulation Method

We used the LAMMPS code (Large-scale Atomic/Molecular Massively Parallel Simulator; see http://lammps.sandia.gov) for atomistic molecular dynamics simulations [15]. The interactions between atoms were described by either the Tersoff [12] or GW [13] empirical potentials. In order to improve the weak repulsion of these potentials at short distances, they are typically joined with the well-established Ziegler, Biersack and Littmark (ZBL) potential [16] at 0.95 Å using a Fermi-like function, as realized in LAMMPS, see Figure 1.

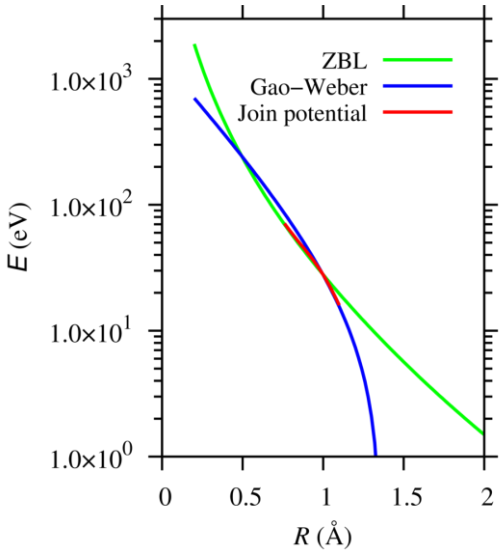

Figure 1. Repulsive Si-C atoms interaction. The GW potential is shown by blue color, the ZBL by green color and the resulting join potential is shown by red color line.

Simulations involving 80x80x80 unit cells (409,600 atoms) were used for 10 keV primary cascades and 150x150x150 unit cells (22,070,021 atoms) for 50 keV cascades. The initial system was equilibrated for 2 picoseconds with time steps of 0.1 femtoseconds. Each cascade was initiated by giving a Si atom the kinetic energy of 10 or 50 keV in a direction close to <135> while holding zero total momentum. The cascades evolved for 20 ps and the time step is modified such that the distance traveled by the fastest particle in the system is less than 0.014 Å per timestep. Constant volume is maintained throughout the simulation and the lattice parameter is chosen maintain zero system pressure in equilibrium at a particular temperature. The Wigner-Seitz cell analysis method was used to determine defects in the modeling system.

The *ab initio* recombination barrier within the DFT was calculated using the Quantum ESPRESSO (QE) package [17]. The calculations have been done using a plane-wave basis set and an ultra-soft pseudo-potential [18] optimized in the Rappe-Rabe-Kaxiras-Joannopoulos (RRKJ) scheme [19] (Si.pbe-n-rrkjus.UPF, C.pbe-n-rrkjus.UPF from the QE pseudopotentials database). We used the exchange-correlation functional parametrization according to Perdew, Burke, and Ernzerhof [20]. The Brillouin zone summations were carried out over a 4x4x4 Brillouin zone grid for the system with 64 atoms in the supercell. The electronic smearing with a width of 0.02 Ry was applied according to the Methfessel-Paxton method. Using a plane wave energy cut-off of40 Ry and charge density of 400 Ry allows reaching an accuracy of 0.2 mRy/atom. Atomic structure was optimized until the forces were smaller than 0.001 Ry/Å.

Results and Discussion

The 10 keV cascade simulations with the Tersoff potential were carried out for a range of temperatures and indicated that in-cascade recombination in SiC seemed to be much lower than in metals. In Figure 2, we show the number of defects as a function of time in 50 keV cascade in SiC (Figure 2a) and 10, 20 and 40 keV in Fe (Figure 2b).

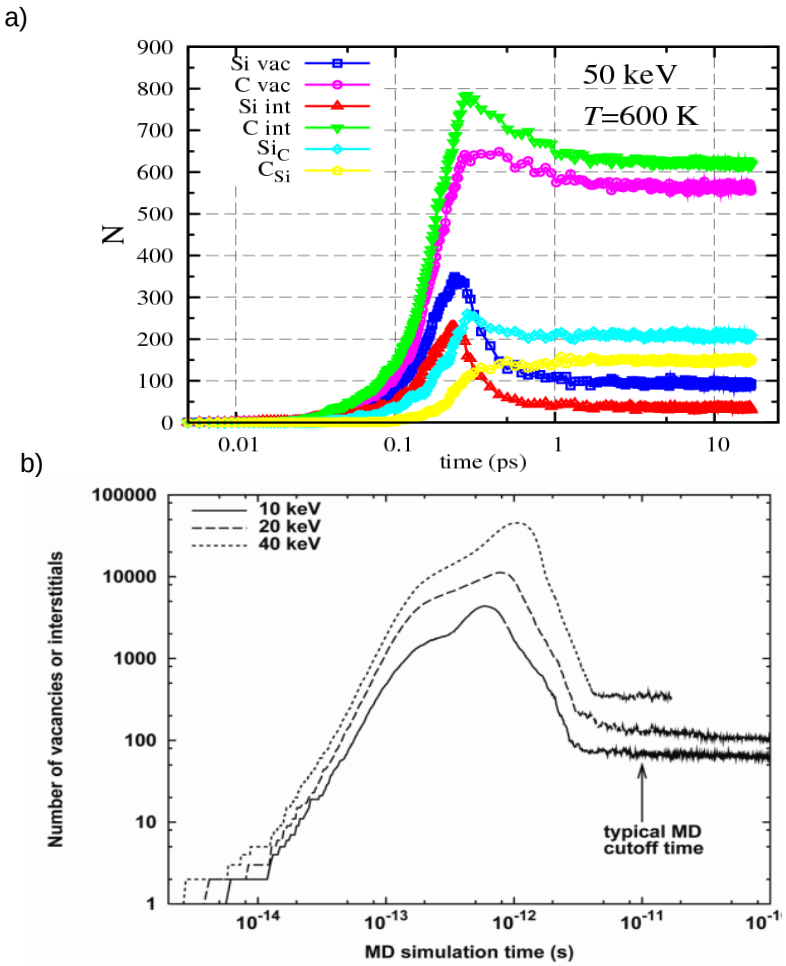

Figure 2. Time dependence of the number of point defects observed in MD displacement cascade simulations: (a) 50 keV SiC cascade at 600 K with Tersoff potential and (b) 10, 20, and 40 keV cascades in iron.

The ratio of the peak defect count to the stable defect count at t>10 picoseconds is less than a factor of two in SiC and almost two orders of magnitude in iron. Such a significant difference between SiC and Fe is due to specific properties of the Si-C interaction. In SiC, a strong-bond oriented interaction allows creation of a stable structure if each atom has four nearest neighbors. The second neighbors are placed at distances which are 60 % greater when compared to the nearest neighbors. As a result, the amorphous phase is very close in energy to the crystalline one and it's very easy to create metastable interstitial-vacancy pairs with a sizable recombination barrier. In the case of Si these interstitial and vacancy pairs produce the so-called I-V complex [21-24].

Point defects in SiC consist of interstitials (denoted as C(I) and Si(I)) and vacancies (C(V) and Si(V)) of both carbon and silicon, as well as anti-site defects of C on a Si site (C_{Si}) and Si on a C site (Si_C). Similar

to previous results [25, 26], it was observed that carbon defects predominate for both the Tersoff and GW potentials, as shown by the green line with up triangles (C(I)) and purple line with open circles (C(V)) symbols in Figure 3a,b for 10 keV cascades at temperature 300 K. The GW result (Figure 3b) is qualitatively similar to that obtained with the Tersoff potential (Figure 3a).

a)

b)

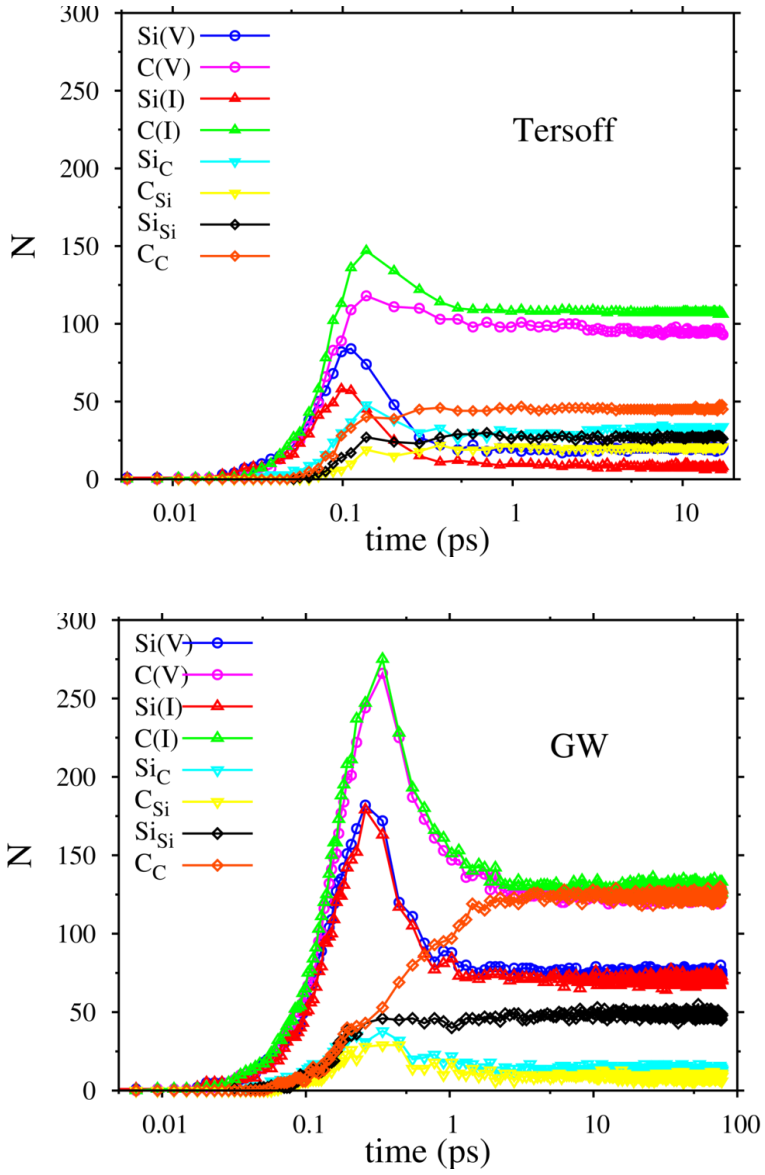

Figure 3. Time dependence of the number of point defects observed in MD displacement cascade simulations at 10 keV pka at 300 K: (a) Tersoff potential, (b) GW potential.

However, in contrast to the simulations with the Tersoff potential, the simulations with the GW potential produces almost twice as many C vacancies and interstitials at the time of maximum disorder (~0.2 ps), but has only about 25% more stable defects at the end of the simulation. As a result, the ratio of peak-to-stable defects is much higher for the GW. This result is more similar to that observed in metals. Only about 20% of the carbon defects produced with the Tersoff potential recombine during the in-cascade annealing phase, while about 50% recombine with the GW potential.

In order to investigate the source of the stability of carbon atom I-V pairs in modeling using the Tersoff potential, we calculated the barrier to C atom migration from its initial position (1/4, 1/4, 1/4) to a metastable position (3/4, 3/4, 3/4) along the [111] direction shown in (Figure 4a). The resulting configuration corresponds to a C(I)-C(V) distance between the I-V pair of $\sqrt{3}/2\ a_o$. The DFT results are close to that presented in references [27, 28]. The recombination barrier, which corresponds to C atom migration from the (3/4, 3/4, 3/4) position to its initial (1/4, 1/4, 1/4) position obtained has a very large value (~ 10 eV) for both Tersoff (shown green in Figure 4b) and another popular modified embedded atom method(MEAM; red color) potential [29], whereas the first principles calculations give a value equal to 0.2 eV (shown in purple). This large barrier suppresses any migration in the modeling system. The GW potential more reasonably describes interstitial diffusion in SiC; however, the migration barrier calculated with this potential (blue line in Figure 4b) is much less that the first principles result.

a)

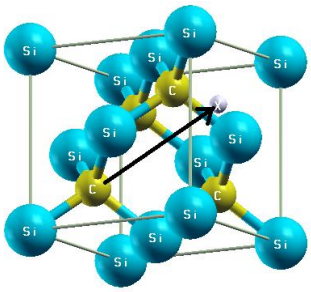

b)

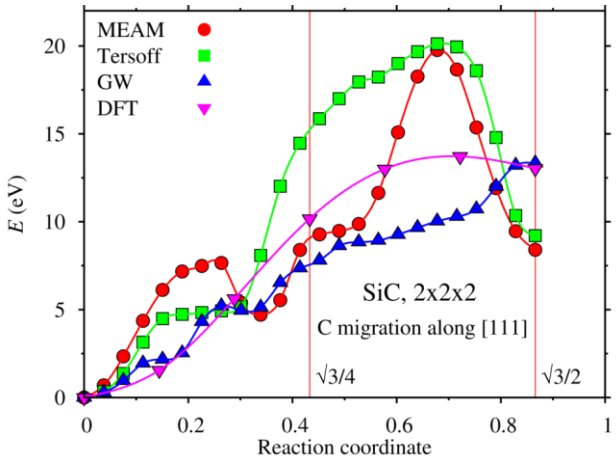

Figure 4. a) Carbon atom migration path along [111] direction to the <111> dumbbell configuration, b) corresponding migration barrier

A significant difference is also found between the two potentials for large size cluster distributions. The results for cluster size distributions obtained at the end of 10 keV simulations for both potentials are presented in Figure 5a, b. In our analysis we defined a group of point defects as a linked cluster if any of the defects are within the distance of one lattice parameter. A simulation with either potential produces a significant amount of pair clusters with ~ 75 % of these clusters correspond to the same atom type I-V pair. However, in the case of the Tersoff potential, all I-V pair clusters correspond to carbon atoms, while in the case of GW potential a significant fraction of these clusters correspond to silicon. Another difference is observed in large-size clusters distribution where in the case of Tersoff potential (Figure 5a),

there are only two relatively large clusters containing 19 and 21 defects, while in the case of the GW potential, there are four clusters containing 21, 30, 35 and 51 defects.

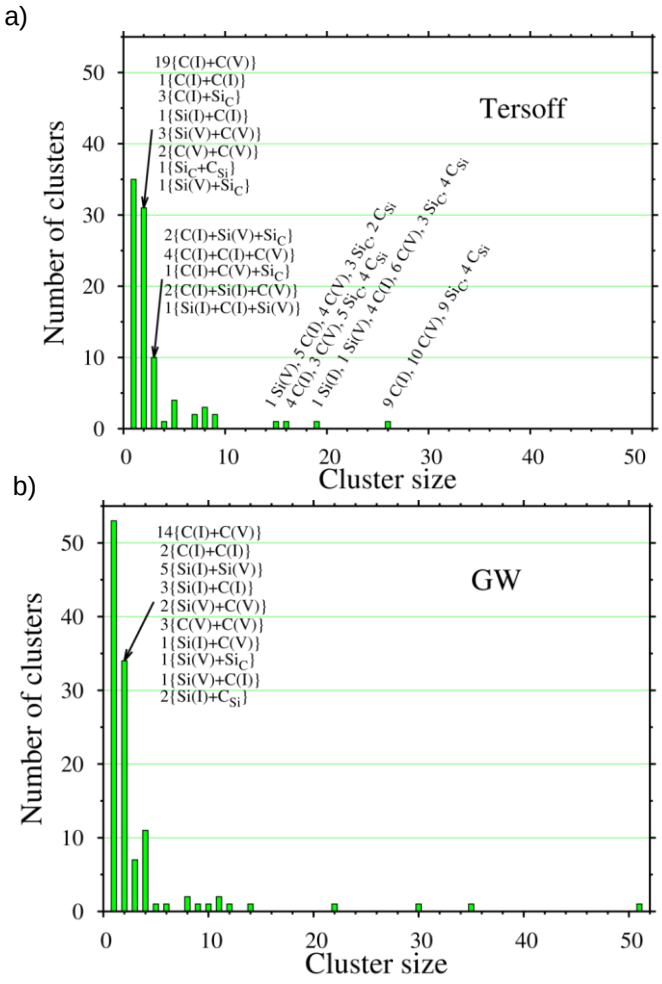

Figure 5. Cluster size distribution at the end of 10 keV Si recoil event in SiC at 300 K: (a) Tersoff potential, (b) GW potential.

These large size clusters are traditionally discussed as a potential candidate for amorphization domains [26]. One of these clusters containing 51 defects is presented in Figure 6. The carbon defects predominate as shown by the green (C) and purple (Si) symbols.

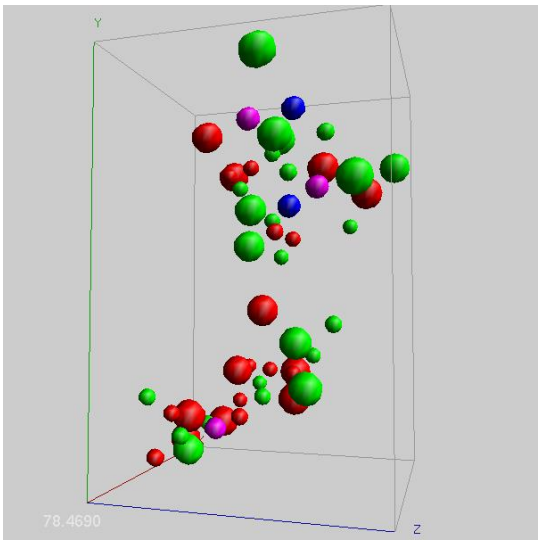

Figure 6. Carbon (green) and silicon (red) interstitials (large spheres) and vacancies (small spheres) at the end of 10 keV Si recoil event in SiC. Blue and purples spheres correspond to Si_C and C_{Si} anti-sites, respectively.

In Figure 7, we show the number of defects and mean-square displacements (MSD) of Si and C atoms as a function of time obtained with the GW potential in a 10 keV cascade at an elevated temperature (1200 K). After about 15 picoseconds, the number of remaining defects becomes approximately constant. At longer times, some further reduction in the number of vacancies and interstitials occurs and is accompanied by an increase in atomic mixing as shown by the number of antisite defects (Si_{Si} and C_C defects in Figure 7) and a significant rise in MSD values.

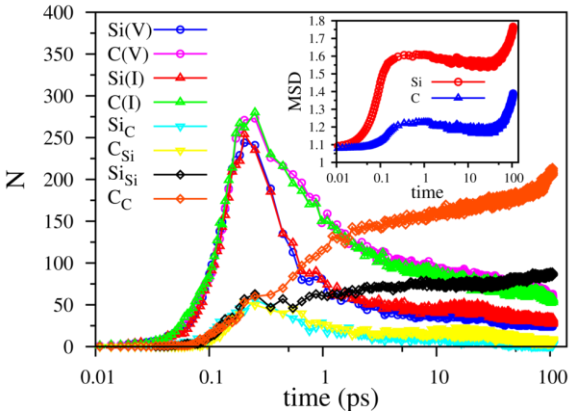

Figure 7. Time dependence of the number of point defects observed in MD displacement cascade simulations at 10 keV PKA at 1200 K with GW potential. The inserted figure corresponds to mean-square displacement of Si (red circles) and C (blue triangles) atoms as a function of time.

This stage of cascade evolution corresponds to in-cascade annealing and is normally not explored in MD calculations. It is can be observed at relatively short times here because of the high temperature. The Tersoff potential results don't demonstrate any annealing and the number of defects remain constant value after the initial saturation. In order to compare the number of stable defects at the end of cascade evolution between the two potentials, we have taken the GW values at 20 picoseconds.

The number of stable defects observed at the end of cascade evolution has been calculated as an average value from 8 cascades. The number for 10 keV cascades is weakly temperature dependent when using the Tersoff potential (Figure 8a), and increases slightly with temperatures. In contrast, for the results from the GW potential (Figure 8b) have much stronger temperature dependence and decrease with temperature.

a)

b)

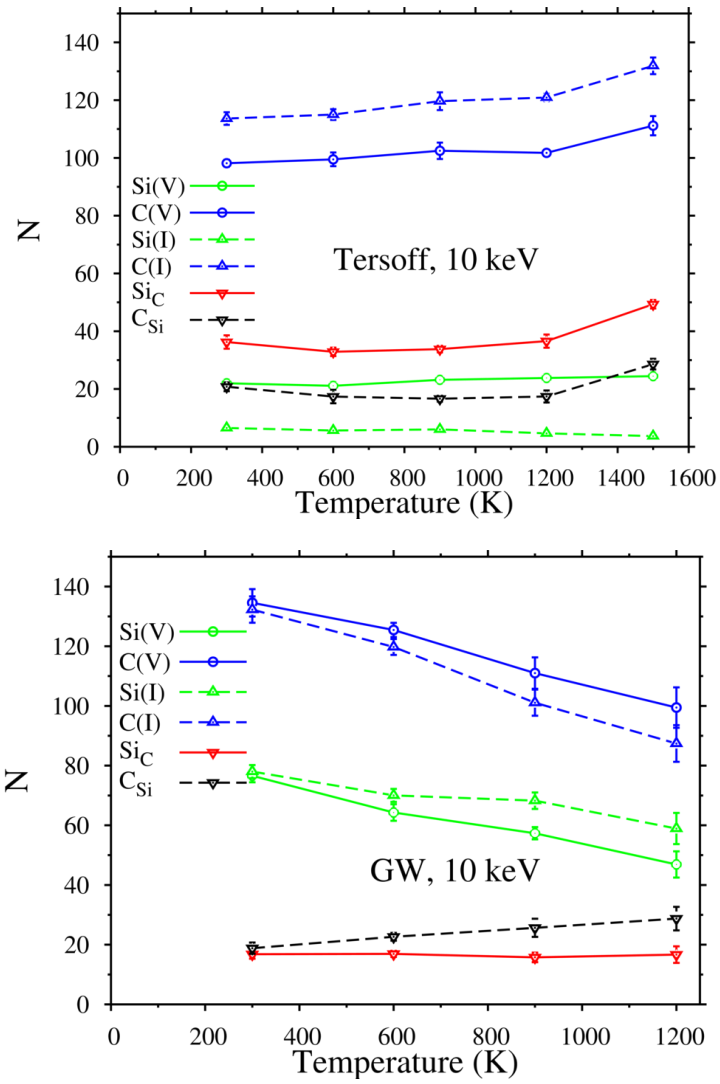

Figure 8. The number of defects at the end of cascade evolution in SiC for 10 pka (a) Tersoff, (b) GW interatomic potentials.

The temperature dependence with GW is more similar to that observed in metals, although it is stronger [30]. The difference between the Tersoff and GW potentials is due to the artificially large migration barriers obtained from the Tersoff potential. An increase in temperature naturally leads to more diffusion of carbon vacancies and interstitials. As a result, more carbon vacancies and interstitials recombine and the number of defects at the end of cascade evolution is reduced as the temperature increases. In contrast, the defect migration barriers using the Tersoff potential are so large that diffusion is suppressed, even at temperatures as high as 1600 K, and the number of defects is only weakly temperature

dependent. The number of defects obtained in 50 keV cascades calculated with both the GW and Tersoff potentials are shown in Figure 9, and exhibits a similar temperature dependence to the 10 keV cascades.

a)

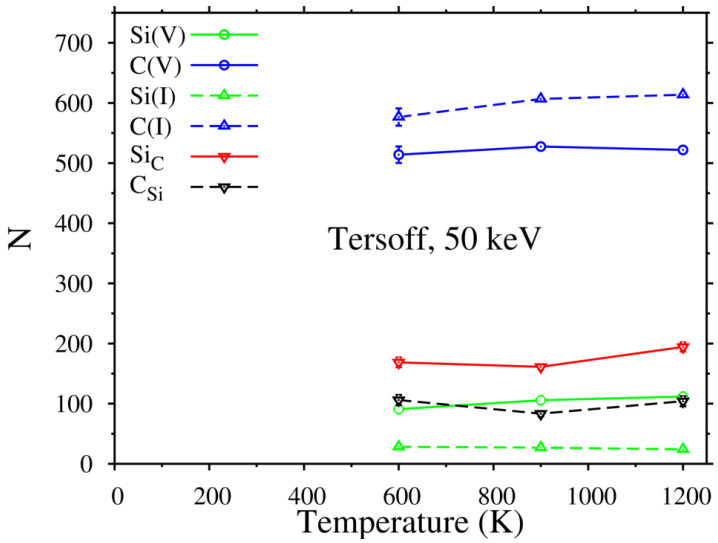

b)

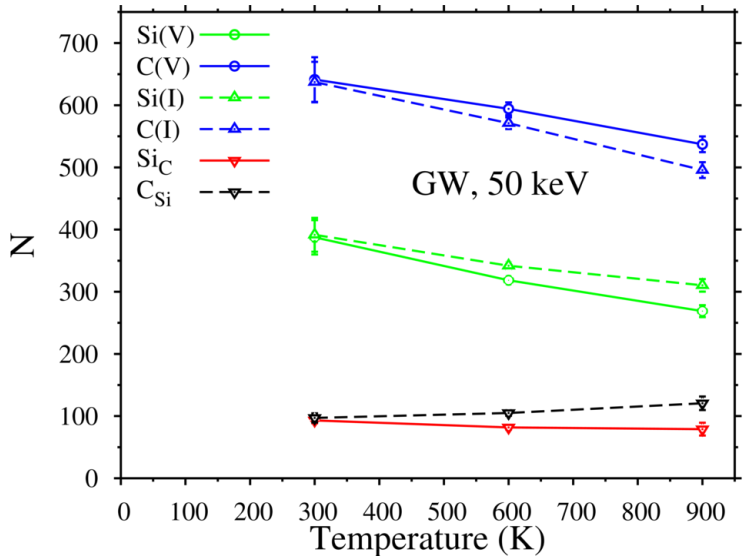

Figure 9. The number of defects at the end of cascade evolution in SiC for 50 pka (a) Tersoff, (b) GW interatomic potentials.

Conclusions

We demonstrated that two of the most commonly used interatomic potentials for SiC (Tersoff and MEAM) are inconsistent with *ab initio* calculations of defect energetics. This results in a significant difference in the cascade production and stability of points defects. To compare the Tersoff [12] and Gao-Weber [13] potentials, we have completed both 10 keV and 50 keV cascade simulations in 3C-SiC at temperatures of 300, 600, 900 and 1200 K in 3C-SiC. The primary results can be summarized as follows:

- The ratio of peak-to-stable defects is much higher for the GW potential than for the Tersoff potential;

- The primary reason for the difference is that the Tersoff potential predicts a barrier to carbon atom vacancy-interstitial recombination which is much higher than DFT results, while the GW potential barrier is much closer to DFT.
- The temperature dependence of the number of stable defects produced (Tersoff: weak and increasing with temperature; GW: stronger and decreasing with temperature) is also caused by the recombination barrier difference.
- The GW potential appears to give a more realistic description of cascade dynamics in SiC, but still has some shortcomings when the defect migration barriers are compared to the *ab initio* results.

Acknowledgments

We are grateful to Dr. L. K. Béland for useful discussions. This work was supported by the US Department of Energy Office of Fusion Energy Sciences. Additional computational resources have been used for this work through collaboration with the Japan Atomic Energy Agency.

References

[1] M.A. Capano, R.J. Trew, MRS Bull. 22 (1997) 19.
[2] H. Inui, H. Mori, and H. Fujita,. Philos. Mag. B 61 (1990) 107.
[3] H. Inui, H. Mori, T. Sakata, and H. Fujita, Philos. Mag. B 65 (1992) 1.
[4] E. Wendler, A. Heft, and W. Wesch, Methods Phys. Res., Sect. B 141 (1998) 105.
[5] Y. Zhang, F. Gao, W. Jiang, D.E. McCready, and W.J. Weber, Phys. Rev. B 70 (2004) 125203.
[6] W. Jiang, H. Wang, I. Kim, I-T. Bae, G. Li, P. Nachimuthu, Z. Zhu, Y. Zhang, and W.J. Weber, Phys. Rev. B 80 (2009) 161301.
[7] L.L. Snead and J.C. Hay, J. Nucl. Mater. 273 (1999) 213.
[8] R. Blackstone and E.H. Voice, J. Nucl. Mater. 39 (1971).
[9] J.E. Palentine and J. Nucl. Mater. 61 (1976) 243.
[10] A.I. Ryazanov, A.V. Klaptsov, A. Kohyama, H. Kishimoto, J. Nucl. Mater. 307– 311 (2002) 1107.
[11] J. Tersoff, Phys. Rev. B 39 (1989) 5566.
[12] R. Devanathan, T. Diaz de la Rubia, W.J. Weber, J. Nucl. Mater. 253 (1998) 47.
[13] F. Gao and W. J. Weber, Nucl. Instr. And Methods in Phys. Research B 191 (2002) 504.
[14] F. Gao, E. J. Bylaska, W. J. Weber, and L. R. Corrales, Nucl. Instr. and Methods in Phys. Research B 180 (2001) 286.
[15] S. Plimpton, J. Comp. Phys. 117 (1995) 1.
[16] J.F. Ziegler, J.P. Biersack, U. Littmark, The Stopping and Ranges of Ions in Solids. vol. 1, Pergamon, 1985.
[17] P. Giannozzi, S. Baroni, and N. Bonini, J. of Physics: Condens. Mat. 21 (2009) 395502.
[18] D. Vanderbilt, Phys. Rev. B 41 (1990) 7892.
[19] A.M. Rappe, K.M. Rabe, E. Kaxiras, and J.D. Joannopoulos, Phys. Rev. B 41 (1990) 1227.
[20] J.P. Perdew, K. Burke, and M. Ernzerhof, Phys. Rev. Lett. 77 (1996) 3865.
[21] M. Tang, L. Colombo, J. Zhu, and T. Diaz de la Rubia, Phys. Rev. B 55 (1997) 14279.
[22] F. Wooten, K. Winer, D. Weaire, Phys. Rev. Lett. 54 (1985) 1392.
[23] L.K. Béland, and N. Mousseau, Phys. Rev. B 88 (2013) 214201.
[24] L.K. Béland, Y. Anahory, D. Smeets, M. Guihard, P. Brommer, J.-F. Joly, J.-C. Pothier, L.J. Lewis, N. Mousseau, and F. Schiettekatte. Phys. Rev. Lett. 111(2013) 105502.
[25] D.E. Farrell, N. Bernstein, and W.K. Liu, J. Nucl. Mater. 385 (2009) 572.
[26] W.J. Weber, and F. Gao, J. Mater. Res., 25 (2010) 2349.
[27] G. Lucas, and L Pizzagalli, J. Phys.: Cond. Matter. 19 (2007) 86208.
[28] M.-J. Zheng, N. Swaminathan, D. Morgan, and I. Szlufarska, Phys. Rev. B 88 (2013) 54105.
[29] H. Huang, N.M. Ghoniem, J.K. Wong, M.I. Baskes, Modeling Simul. Mater. Sci. Eng. 3 (1995) 615.
[30] R. E. Stoller, "Primary Radiation Damage Formation," in Comprehensive Nuclear Materials, R. J. M. Konings, T. R. Allen, R. E. Stoller, and S. Yamanaka, Eds., Elsevier Ltd., Amsterdam, 2012, pp. 293-332.

9.1 FUSION MATERIAL IRRADIATION TEST STATION (FMITS) AT SNS – Mark Wendel, Phil Ferguson (Oak Ridge National Laboratory)

OBJECTIVE

The Fusion Materials Irradiation Test Station (FMITS) is a plan for an irradiation facility at the Spallation Neutron Source (SNS). The objective of the FY15 effort is to address comments by the reviewers of the 2014 feasibility study and to reduce the technical risks to a potential project by analysis and by building and testing hardware mockups. The 2014 effort produced a Feasibility Study Report, 30% Design Review, and a Preliminary Safety Assessment. The 2014 estimate for implementation of the FMITS at SNS was $13.4 M including a 25% contingency.

SUMMARY

The Fusion Materials Irradiation Test Station (FMITS) is a design concept for installation at the Spallation Neutron Source (SNS) Facility. The project has received funding from OFES during FY15 for (1) performing a mockup test on an FMITS-type target seal, (2) augmenting the safety assessment based on the 2014 technical review, (3) analyzing thermal-hydraulic off-normal transients with a full 3D model, and (4) remote-handling electrical connector operational mock-up. The main goals of the effort are to remove the project technical risks and prepare for a potential upcoming viability review by DOE.

PROGRESS

Seal mockup

FMITS-type (double-pillow) seal hardware (Fig. 1) is on order. Finite element analysis was completed and the design specification was approved and archived. The fabrication contract was awarded to bellows manufacturer KSM, Inc., and should be delivered to ORNL in March, 2015. This seal is a prototype of the assembly that could be used between the target module and the core vessel flange for an FMITS installation. It would replace the single-sided version currently in use at SNS. Once the prototype seal is received, it will be tested in the seal test tank (Fig. 2) at SNS to determine it operates to required specifications, shows robust and repeatable performance, and compares favorably to the quality of the original design. If these mockup test results are positive, then the technical risk to a proposed FMITS project would be greatly reduced, according to the Feasibility Study Report of 2014.

Safety assessment

Two meetings have been held to discuss the 30% Design Review comments on safety. The outstanding issues are: possible tungsten/water reaction and subsequent detonation of hydrogen, removing the rupture tube mitigation concept to avoid complicating the fabrication, and radiolysis and shock wave risks. The hydrogen production due to the tungsten water reaction is limited by tungsten availability, and a simple calculation should provide an acceptable bound. A deterministic analysis that can rule out possible tube rupture severe consequences does not seem feasible. It is likely that the FMITS plan will have to keep the engineering control safeguard of a calibrated containment tube with directional failure bias.

Finite element analysis (FEA) model of FMITS test section

The FMITS team met on December 17, 2014, to discuss the off-normal analysis plan for 2015. The purpose of the analysis is to comply with recommendation of the 30% Design Review Committee to strengthen the case for operational reliability by understanding how the proposed sensor array protects the SNS facility. These concerns will be addressed by thermal modeling of an actual FMITS experiment with inclusion of realistic thermocouple details. Transient conditions will be performed with a three-dimensional transient model. The sensitivity of each thermocouple to the changing thermal conditions will be quantified, thus providing the necessary information to optimize a machine protection voting logic that would be effective to protect the SNS facility.

The team selected 5 off-normal events to consider:

- beam/power generation drift
- diminished or loss of flow
- flow redistribution or flow blockage
- primary gas transients (e.g., 100% argon flow)
- startup and shutdown sequences

A representative three-dimensional FEA model of the FMITS has been constructed. A simple, but commonly used, specimen configuration of bend bars was selected, as shown in Fig. 3. Figure 4 shows this same configuration contained inside a specimen holder.

Currently, there are 5 holder assemblies contained within a single FMITS capsule. Figure 5 shows the complete FMITS capsule with the 5 holder assemblies.

As shown in Fig. 5, a TCAT assembly runs through the center of the capsule and is used to measure temperature at various locations in the assembly. A close-up view of the TCAT is shown in Fig. 6. This device is a combination of seven individual thermocouples into one wire. Each of the seven thermocouples will measure the temperature at whatever location the wires come together: nominally, one at the center of each assembly, plus two that can be located at arbitrary points. It is necessary to model the TCAT in detail in order to get the proper thermal time response from the transient conditions.

Currently, the Creo solid model is about 98% complete. The next stage is to import the design into the ANSYS FEA software and begin the process of meshing and defining contact between parts.

Remote-handling connector mockup

A wooden mockup was created of the electrical connector pocket that is located at the front of the target carriage (Fig. 7). This pocket houses the fixed half of the mercury leak detector jumper connector, which is very difficult to access remotely due to its location relative to the shoulder joint of the thru-wall-manipulators. Implementing FMITS would require a second connector in this region, and perhaps a third, so the mockup was developed using the proposed electrical connectors. Initial tests showed the first mockup configuration was manageable, but a lower connector location within the pocket could enhance the ability to remotely manipulate the connectors. Because the proposed FMITS-style electrical connectors have more pins than the current connector, the insertion force required to mate the connectors will increase. The next step is to procure some prototype connectors with identical pin configurations and test them with the manipulators. Once the mockup is complete, the results can be used in a preliminary design for the FMITS-specific Vent Line Shield Block.

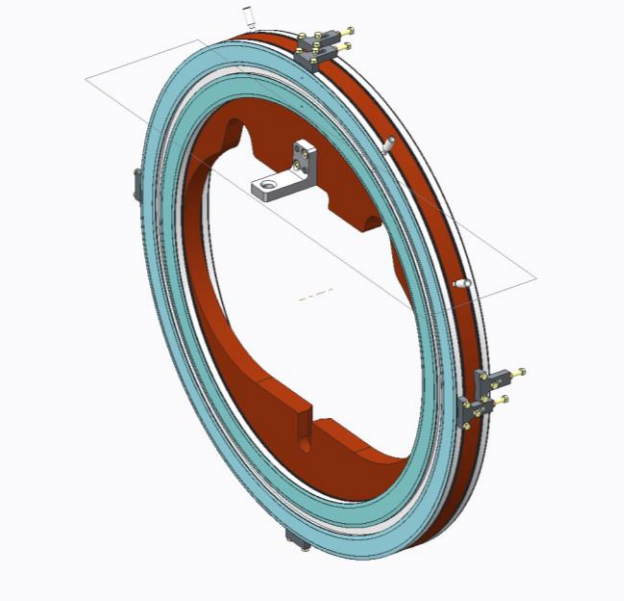

Figure. 1. Double-inflatable seal ring under fabrication.

Figure 2. Target seal test tank which will be adapted to test FMITS-type core vessel seal.

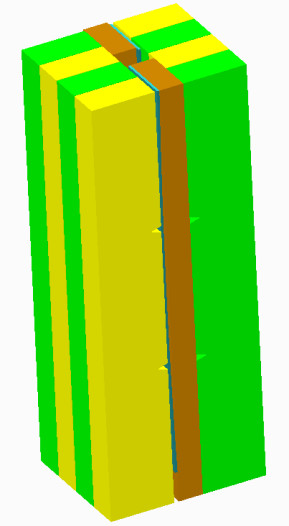

Figure. 3. Specimen configuration showing 8 bend bars (yellow and green), 2 thermometry elements (brown) and springs (blue).

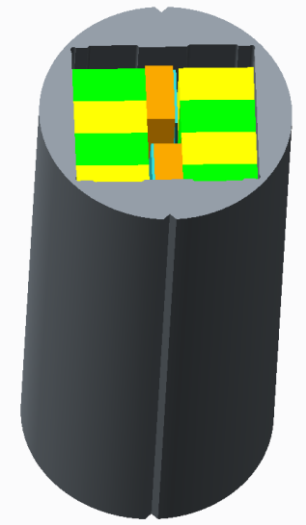

Figure 4. Standard specimen configuration shown inside a holder**.**

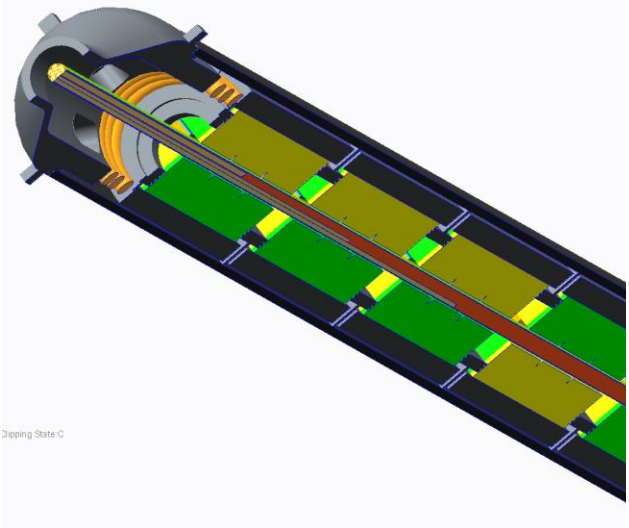

Figure 5. FMITS Assembly

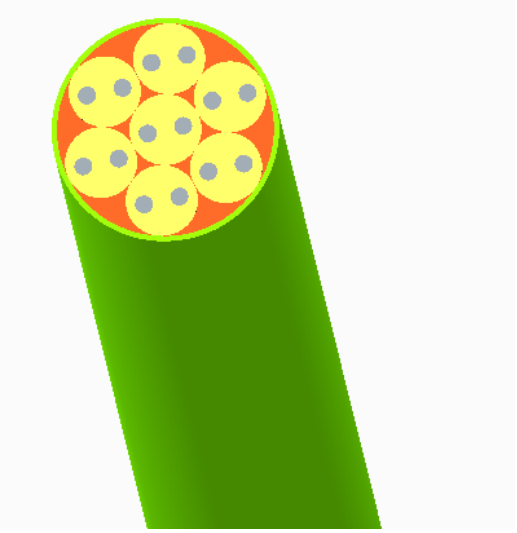

Figure 6 . TCAT Assembly Showing 7 Individual Thermocouples

Figure 7. Remote handling mockup for FMITS electrical connections.

9.2 HFIR IRRADIATION EXPERIMENTS

Status of the Reactor

HFIR completed 3.5 cycles during the second half of 2014. Cycle 454 started in June but ended July 12, 2014. Complete cycles 455, 456 and 457 all occurred in the reporting period.

The reactor operated seven full cycles during the calendar year 2014.

Summary of Recent, Current and Planned Fusion Materials Program Experiments

Experiment Designation	Primary Materials	Specimen Types*	Irradiation Temperature (°C)	Max Exposure (dpa)	Number of Reactor Cycles	Irradiation Period (month/year)		
Beryllium reflector (RB) irradiation positions								
RB-15J	F82H	T, F, FT	300, 400	6	10	6/08	–	12/09
Target zone full-length capsules								
JP-25	F82H	T, FT	300, 500	20	10	2/99	–	1/01
JP-26	F82H	T, FT	300,400,500	9	5	12/03	–	11/04
JP-27	F82H	T, FT	300, 400	21	13	12/03	–	1/08
JP-28	F82H	T, FT	300,400,500	80	46	4/05	–	7/13
JP-29	F82H	T, FT	300,400,500	80	46	1/05	–	7/13
12-DCT	F82H	DCT	50	1.6	1	8/11	–	8/11
JP-30	F82H	T, FT	300,400,650	20	~10	11/11	–	8/13
JP-31	F82H	T, FT	300,400,650	20	~10	11/11	–	8/13
Target zone rabbit capsules (DOE-JAEA)								
F8A1	F82H	T, FT	300	50	29	2/09	–	7/13
F8A2	"	"	"	"	"	"	–	"
F8B1	"	"	"	"	"	"	–	"
F8B2	"	"	"	"	"	"	–	"
JCR-1	SiC/SiC	Bend bars	800	30	15	10/04	–	1/09
JCR-2	"	"	"	"	"	"	–	"
JCR-3	"	"	"	"	"	"	–	"
JCR-4	"	"	"	"	"	"	–	"
JCR-5	"	"	"	>50	>25	10/04	–	2/11
JCR-6	"	"	"	"	"	"	–	"
JCR-7	"	"	"	"	"	"	–	"
JCR-8	"	"	"	"	"	"	–	"
JCR-9	"	"	500	30	15	10/04	–	1/09
JCR-10	"	"	"	"	"	"	–	"
JCR-11	"	"	"	"	"	"	–	"
JCR-12	"	"	"	"	"	"	–	"
F11A3	F82H	T, FT	300	20	12	5/11	–	2/13
F11A4	"	"	"	"	"	"	–	"
F11B3	"	"	"	"	"	"	–	"
M4-TEN	F82H	DCT	50	1.6	1	8/11	–	8/11
JCR11-01	SiC/SiC	Bend bars	950	50	25	11/12	–	
JCR11-02	SiC/SiC	Bend bars	950	10	5	10/12	–	8/13

Continued

Experiment Designation	Primary Materials	Specimen Types*	Irradiation Temperature (°C)	Max Exposure (dpa)	Number of Reactor Cycles	Irradiation Period (month/year)		
JCR11-03	SiC/SiC	Bend bars	950	30	15	5/13	–	
JCR11-04	SiC/SiC	Bend bars	950	30	15	5/13	–	
JCR11-05	SiC/SiC	Bend bars	950	50	25	10/12	–	
JCR11-06	SiC/SiC	Bend bars	950	10	5	10/12	–	7/13
JCR11-07	SiC/SiC	Bend bars	950	100	50	10/12	–	
JCR11-08	SiC/SiC	Bend bars	950	100	50	10/12	–	
JCR11-09	SiC/SiC	UDMC	950	4	2	6/13	–	11/13
JCR11-10	SiC/SiC	UDMC	950	10	5	6/13	–	
JCR11-11	SiC/SiC	UDMC	950	30	15	6/13	–	
JCR11-12	SiC/SiC	UDMC	950	100	50	6/13	–	
F13A5	F82H	T, FT	300	10	9	1/14	–	
F13A6	F82H	T, FT	300	20	18	1/14	–	
F13B4	F82H	T, FT	300	10	9	1/14	–	
F13B5	F82H	T, FT	300	20	18	1/14	–	
SCF6	SiC/SiC	Bend bars	600	10	6	11/14	–	
SCF7	SiC/SiC	Bend bars	600	30	14	11/14	–	
SCF8	SiC/SiC	Bend bars	600	100	45	11/14	–	
SCF9	SiC/SiC	Bend bars	600	200	90	11/14	–	
SCF10	SiC/SiC	Bend bars	950	10	5	1/15	–	
SCF11	SiC/SiC	Bend bars	950	30	14	1/15	–	
SCF12	SiC/SiC	Bend bars	950	100	45	1/15	–	
Target zone rabbit capsules (DOE-NIFS)								
T8A1	SiC	BSR	300	0.01	HT**	10/09	–	10/09
T8A2	SiC	BSR	300	0.1	HT	10/09	–	10/09
T8B1	SiC	BSR	500	0.01	HT	10/09	–	10/09
T8B2	SiC	BSR	500	0.1	HT	10/09	–	10/09
T8C1	SiC	BSR	500	~1	1	5/09	–	6/09
T8D1	SiC	BSR	800	0.1	HT	3/11	–	10/09
T8E1	SiC	BSR	800	~1	1	8/09	–	8/09
T8F1	SiC	BSR	1200	~1	1	8/09	–	8/09
T9A1	W, Ni	Discs	90	0.1	HT	1/09	–	10/09
T9A2	W, Ni	Discs	90	1.2	1	1/09	–	1/09
T9C1	Steels	T, MC	500	5.5	3	11/09	–	2/10
T9C2	Steels	T, MC	500	9.6	5	11/09	–	6/10
T9G1	Steels	T, MC	300	1.2	1	6/09	–	8/09
T9G2	Steels	T, MC	300	9.6	8	6/09	–	8/11
MTTN01	Steels	T, MC	300	4.8	4	1/12	–	8/11
300-LD-1	Steels	SSJ, MC	300	2	1	5/12	–	6/12
300-HD-1	Steels	SSJ, MC	300	12	6	5/12	–	2/13
500-LD-1	Steels	SSJ, MC	500	2	1	5/12	–	6/12
500-HD-1	Steels	SSJ, MC	500	12	6	5/12	–	2/13
500-HD-2	Steels	SSJ, MC	500	12	6	5/12	–	2/13
500-HD-3	Steels	SSJ, MC	500	12	6	5/12	–	2/13
650-LD-1	Steels	SSJ, MC	650	2	1	5/12	–	6/12
650-LD-2	Steels	SSJ, MC	650	2	1	5/12	–	6/12
650-HD-1	Steels	SSJ, MC	650	12	6	5/12	–	2/13
650-HD-2	Steels	SSJ, MC	650	12	6	5/12	–	2/13
300-LD-2	Steels, W	SSJ, MC	300	2	2	7/12	–	8/12
300-MD-1	Steels, W	SSJ, MC	300	7	4	7/12	–	2/13

Continued

Experiment Designation	Primary Materials	Specimen Types*	Irradiation Temperature (°C)	Max Exposure (dpa)	Number of Reactor Cycles	Irradiation Period (month/year)		
500-LD-2	Steels, W	SSJ, MC	500	2	2	1/13	–	7/13
300-LD-3	Steels, W	SSJ, MC	300	2	2	7/12	–	11/12
300-HD-2	Steels, W	SSJ, MC	300	12	8	7/12	–	2/14
500-LD-3	Steels, W	SSJ, MC	500	2	1	7/12	–	8/12
500-HD-4	Steels, W	SSJ, MC	500	12	6	7/12	–	7/13
650-LD-3	Steels, W	SSJ, MC	650	2	2	10/12	–	7/13
650-HD-3	Steels, W	SSJ, MC	650	12	8	7/12	–	11/13
PC1	Various	SSJ, MC	80/100	0.02	HT	6/12	–	6/12
PC1A	Various	SSJ, MC	80/100	0.02	HT	6/12	–	6/12
PC2	Various	SSJ, MC	80/100	0.1	HT	6/12	–	6/12
PC2A	Various	SSJ, MC	80/100	0.1	HT	6/12	–	6/12
PC3	Various	SSJ, MC	80/100	0.5	HT	6/12	–	7/12
PC3A	Various	SSJ, MC	80/100	0.5	HT	6/12	–	7/12
PC4	Various	SSJ, MC	80/100	2	1	6/12	–	7/12
PC4A	Various	SSJ, MC	80/100	2	1	6/12	–	7/12
PC5	Various	SSJ, MC	80/100	20	9	6/12	–	11/13
TB-300-1	Steels, W	SSJ, MC	300	0.02	HT	8/12	–	8/12
TB-300-2	Steels, W	SSJ, MC	300	0.1	HT	8/12	–	8/12
TB-300-3	Steels, W	SSJ, MC	300	0.5	HT	8/12	–	8/12
TB-300-4	Steels, W	SSJ, MC	300	7	5	7/12	–	6/13
TB-500-1	Steels, W	SSJ, MC	500	0.1	HT	8/12	–	8/12
TB-500-2	Steels, W	SSJ, MC	500	0.5	HT	8/12	–	8/12
TB-500-3	Steels, W	SSJ, MC	500	7	4	7/12	–	2/13
TB-650-1	Steels, W	SSJ, MC	650	0.1	HT	8/12	–	8/12
TB-650-2	Steels, W	SSJ, MC	650	0.5	HT	8/12	–	8/12
TB-650-3	Steels, W	SSJ, MC	650	7	5	7/12	–	6/13
TB-650-4	Steels, W	SSJ, MC	650	20	11	7/12	–	7/14
TTN09	SiC	Joint	500	3.4	2	8/11	–	11/11
TTN10	SiC	Joint	500	4.1	2	8/11	–	11/11
TTN11	SiC	Joint	800	4	2	3/12	–	5/12
TTN01	SiC	BSR	300	1	1	2/11	–	3/11
TTN02	SiC	BSR	300	10	6	2/11	–	12/11
TTN03	SiC	BSR	300	20	11	2/11	–	8/13
TTN04	SiC	BSR	500	10	6	5/11	–	4/12
TTN05	SiC	BSR	500	20	11	5/11	–	8/13
TTN06	SiC	BSR	800	10	6	5/11	–	4/12
TTN07	SiC	BSR	800	20	11	5/11	–	8/13
TTN08	SiC	BSR	1200	10	6	5/11	–	8/12
TTN16	SiC	Fiber BSR	500	1	1	11/11	–	12/11
TTN17	SiC	Fiber BSR	500	10	6	8/11	–	6/12
TTN18	SiC	Fiber BSR	500	20	11	8/11	–	8/13
TTN19	SiC	Fiber BSR	1200	1	1	3/12	–	4/12
TTN20	SiC	Fiber BSR	1200	10	6	3/12	–	11/12
PXW1	W	Discs	800	2	1	1/15	–	2/15
PXW2	W	Discs	800	2	1		–	
PXW3	W	Discs	800	6	3		–	
PXW4	W	Discs	1100	2	1	1/15	–	2/15
PXW5	W	Discs	1100	2	1		–	
PXW8	W	Discs	1100	6	3		–	

Continued

Experiment Designation	Primary Materials	Specimen Types*	Irradiation Temperature (°C)	Max Exposure (dpa)	Number of Reactor Cycles	Irradiation Period (month/year)		
Target zone rabbit capsules (US-NIFS-JAEA)								
T11-01J	V-4Cr-4Ti	BTC	425	2	1	11/12	–	12/12
T11-02J	V-4Cr-4Ti	BTC	425	6	3	1/13	–	7/13
T11-03J	V-4Cr-4Ti	BTC	425	2	1	11/12	–	12/12
T11-04J	V-4Cr-4Ti	BTC	425	6	3	1/13	–	7/13
T11-05J	SiC	BTC	600	2	1	11/12	–	12/12
T11-06J	SiC	BTC	600	6	3	1/13	–	7/13
T11-08J	SiC	BTC	600	6	3	1/13	–	7/13
T11-09J	SiC	BTC	600	2	1	11/12	–	12/12
T11-11J	SiC	BTC	600	2	1	11/12	–	12/12
T11-13J	Graphite	BTC	600	2	1	11/12	–	12/12
T11-14J	Graphite	BTC	600	6	3	1/13	–	7/13
J12-01	F82H	BTC	300	1.5	1	1/13	–	2/13
J12-02	F82H	BTC	300	6	3	5/13	–	7/13
J12-03	F82H	BTC	300	1.5	1	5/13	–	2/13
J12-04	F82H	BTC	300	6	3	1/13	–	6/13
J12-05	F82H	BTC	300	1.5	1	1/13	–	2/13
J12-06	F82H	BTC	300	6	3	5/13	–	6/13
Target zone rabbit capsules (US-IMR)								
MX-1	Ceramics	Various	400	2	1	7/13	–	8/13
MX-2	Ceramics	Various	400	6	3	7/13	–	3/14
MX-3	Ceramics	Various	400	10	6	7/13	–	7/14
MX-4	Ceramics	Various	700	2	1	7/13	–	8/13
MX-5	Ceramics	Various	700	6	3	7/13	–	2/14
MX-6	Ceramics	Various	700	10	5	7/13	–	5/14
MX-7	Ceramics	Various	1000	2	1	7/13	–	8/13
MX-8	Ceramics	Various	1000	6	3	7/13	–	3/14
MX-9	Ceramics	Various	1000	10	5	7/13	–	5/14
IMR1	Various	Various	200	2	1		–	
IMR2	Various	Various	200	2	1		–	
IMR3	Various	Various	200	2	1		–	
IMR4	Various	Various	200	2	1		–	
IMR5	Various	Various	200	2	1		–	
IMR6	Various	Various	600	2	1		–	
IMR7	Various	Various	600	6	3		–	
IMR8	Various	Various	600	10	5		–	
IMR9	Various	Various	1000	2	1		–	
IMR10	Various	Various	1000	6	3		–	
IMR11	Various	Various	1000	10	5		–	
Target zone rabbit capsules (US)								
SCJ2-10	Ceramics	Joint	500	3	2	5/14	–	7/14
SCJ2-11	Ceramics	Joint	500	>10	10	5/14	–	
SCJ2-12	Ceramics	Joint	500	3	2	5/14	–	7/14
SCJ2-16	Ceramics	Joint	1000	3	2	6/14	–	8/14
SCJ2-17	Ceramics	Joint	1000	3	2	6/14	–	8/14

*T = Tensile, F = Fatigue, FT = Fracture Toughness, MC = Multipurpose Coupon, BSR = Bend Stress Relaxation Creep, DCT = Disc Compact Tension, BTC: Bellows-loaded Tensile Creep, UDMC: Uni-directional Mini-composite. Most experiments also contain TEM disks, other special purpose specimens, and monitors occupying small spaces.
**Hydraulic tube – fractional cycle exposures.